Heat release and performance studies using monolithic ceramic piston caps in a Petter AV1 diesel engine

Shams, Omar Mohammad Abdulla

Award date:
1991

Awarding institution:
University of Bath

Heat Release and Performance Studies Using Monolithic Ceramic Piston Caps in a Petter AV1 Diesel engine

submitted by

Omar Mohammad Abdulla Shams

for the degree of Ph.D. of the

University of Bath

1991

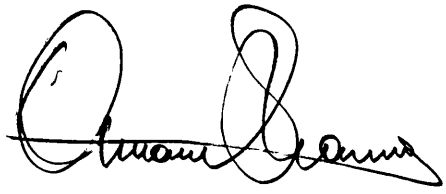

ProQuest LLC
789 East Eisenhower Parkway
P.O. Box 1346
Ann Arbor, MI 48106-1346

To my Mother, Father,
Dunia, Hayat and Ammar
with love.....again.

ACKNOWLEDGEMENTS

The author wishes to thank very sincerely the following people and establishments for their support during the course of this work.

H.E. Mr. M.M.Al-Tajir
Prof. F.J.Wallace
The Embassy of the United Arab Emirates (London)
Dubai Natural Gas Company
Scimitar Oils S.A.

Dr. S.J.Charlton
Dr. C.Chen
Dr. D.Dang
Dr. Y.Rasihhan
Dr. M.B.Wilson

Mr. D.Barker
Mr. G.Bonwick
Mr. E.Brain
Mr. A.Cox
Mr. R.Hassan
Mr. M.McLaren
Mr. G.J.McKenzie
Mr. I.Marsh
Mr. M.H.A.Porter
Mr. V.Rajput
Mr. D.Rushton

Miss. J.Greener
Mrs. M.Greenhalgh

SUMMARY

A single cylinder indirect injection four stroke 550cc watercooled diesel engine was the subject of an engine insulation exercise where the only component to be considered was the piston. The method of insulation was the use of two different glass ceramic monoliths namely Cordierite and Lithium Aluminium Silicate.

The monoliths were produced by Pilkington PLC in several shapes and varying dimensions which were then attached to the piston bodies using a variety of fixing methods developed at Bath. The most successful fixing technique was found to be the "glueline" method with Cordierite as the mechanically more reliable of the two materials.

Initially, the piston assemblies were subjected to inertial and moderate mechanical and thermal loading in a motored engine simulation rig. This was an identical engine to it's firing counterpart but had no fuel system and a slightly higher compression ratio. This rig was designed to check the mechanical integrity of the assemblies but its use was later eliminated when it became clear that the ceramics were failing due to thermal stresses rather than mechanical loading.

Several piston assemblies were built and failures in the firing engine ranged from breakage at engine assembly to catastrophic failure after a few minutes running time. To reduce the chance of failure, the fuel injection timing was substantially retarded and the injector cracking pressure reduced from 210 bar (3000 psi) to 126 bar (1800 psi). With these "softer" conditions, a piston assembly survived for over 60 hours. In this time sufficient data was recorded to compare a standard engine to the insulated one.

The ultimate aim of the exercise was to build four ceramic capped pistons and fit them into a four cylinder Ford 1.6 litre IDI diesel engine, but time restraints halted the research after the pistons had been constructed.

Two different analysis programs were written in order to transform the recorded pressure into meaningful heat release results, one relying on a single cylinder pressure record (main or pre-chambers), and the other on pressure records taken from both main and pre-chambers. Only the former program could be used as it became clear that it was not possible to record pressures in both main and pre-chambers with sufficient accuracy.

It was concluded from this research that Cordierite is not sufficiently durable as a material for diesel engine application while Lithium Aluminium Silicate was found to be even weaker mechanically. It was also concluded that insulation of one component merely redirects heat loss to other components but there is a significant increase in exhaust temperature. The effects of insulation or emissions was not considered in this study.

CONTENTS

NOTATION

A	constant	-
B	constant	-
b	bore	m
BMEP	brake mean effective pressure	bar
C	constant	-
C_d	coefficient of discharge	-
C_p	specific heat at constant pressure	J/KgK
cp	mean piston speed	m/s
C_v	specific heat at constant volume	J/KgK
D	cross setional area of throat	m^2
F	equivalence ratio	-
f	fuel fraction	_
FMEP	friction mean effective pressure	bar
F_s	stoichiometric fuel air ratio	-
g	bumping clearance	m
h	enthalpy	J/Kg
h	throat length	m
K_p	orifice plate calibration constant	-
l	connecting rod length	m
LCV	fuel lower calorific value	J/kg
m	mass	Kg
$\dot{m}$	mass flowrate	Kg/s
N_e	engine speed	rev/min
P	pressure	N/m^2
Q	heat release	W
R	gas constant	J/KgK
r	crank radius	m
T	temperature	k
T	torque	Nm

t	time	s
u	internal energy	W
V	volume	m^3
$\dot{V}$	volume flowrate	m^3/s
γ	gas constant ratio	-
Δh	manometer height differential	m
ΔP	change in pressure	N/m^2
η	efficiency	%
θ	crank angle	degrees
ρ	density	Kg/m^3

ABBREVIATIONS

ATDC	after top dead centre
AIVC	after inlet valve closure
BMEP	brake mean effective pressure
BTDC	before top dead centre
C.A.R.E.	ceramic applications in reciprocating engines
CR	compression ratio
Cr_2C_3	chromium carbide
DI	direct injection
DSS	digital storage scope
EVC	exhaust valve closure
EVO	exhaust valve opening
FE	finite element
FMEP	friction mean effective pressure
IDI	indirect injection
IDIPA	indirect injection pressure analysis program
IVC	inlet valve closure
IVO	inlet valve opening
LAS	lithium aluminium silicate
LCV	fuel lower calorific value
LED	light emitting diode
LHR	low heat rejection
NOx	nitrous oxides
PSZ	partially stabilised zirconia
RBSN	reaction bonded silicone nitride
SAC	specific air consumption
SFC	specific fuel consumption
SPA	single pressure analysis program
TDC	top dead centre
TDCF	firing top dead centre
ZrO_2	Zirconia

CHAPTER1
INTRODUCTION

1.1 General Background

The reciprocating internal combustion engine in its two main forms, viz

a) the spark ignition (usually gasoline) engine

b) the compression ignition (or diesel) engine

has firmly established itself as the dominant form of prime mover for land transportation by road and rail.

Whereas the former is used predominately in passenger cars where its wide speed range and great flexibility are outstanding advantages, the latter occupies an equally dominant position in the field of heavy road vehicles and rail traction, on account of its high efficiency and reliability.

The diesel engine, in spite of the very advanced stages of development which it has now reached, is still the subject of intensive research and development, in order to achieve further gains in

a) economy
b) power density
c) reliability
d) reduction of emissions, under the pressure of increasingly stringent legislation.

Had it not been for legislation in first world countries, emission control would not have enjoyed the intense research it does today. The more we develop, the bigger the demand for power and thus the heavier the contamination of the atmosphere. It is this problem of severe atmospheric pollution in certain geographical locations that first alerted the world to the need for legislation against pollutants. Cities such as Los

Angeles, Tokyo and Mexico City are but a few of the better known examples.

Compared to gasoline engines, the diesel engine emits less carbon monoxide and is considered more environmentally sound, even though it suffers from a smokier and more odorous exhaust. Within the diesel engine divide of direct and indirect injection (DI and IDI), it is the IDI design that benefits from lower exhaust emissions (and noise).

With regard to the other main areas listed under a to c above, economy is still of overriding importance in view of the very high mileages covered by commercial vehicles and locomotives, and the resultant high proportion of fuel costs as a function of the operating costs.It has long been established by leading researchers worldwide, that diesel engine insulation results in a more economical and versatile unit.The full adiabatic engine has always been the hypothetical target of these researchers and the main route towards nearing the target has been through thermal insulation.The insulating materials considered to date range from sophisticated steel alloys to air gaps and ceramics.

The two main routes to achieving such thermal insulation by the use of ceramic materials are :

a) deposition of thin coatings, the preferred material being Partially Stabilised zirconia (PSZ)
b) the use of monolithic components for such parts as piston caps, liner inserts, prechambers etc.

Although research in the field of diesel engine insulation with respect to ceramics is still inconclusive, Jackson and Wotton (ref. 1) have proved that ceramic insulation has a detrimental effect on NOx emission. They conclude somewhat pessimistically that future work in this field is "not promising in view of current and future legislation." This view is also echoed (although not as negatively) by Shephard et al (ref. 2).

It has to be made clear that the author based his work on ceramic insulation and the effects on engine performance rather than emission control. In fact no work associated with the monitoring of exhaust emissions was conducted in this study although its importance has been acknowledged.

1.2 Engine Insulation for Low Heat Rejection (LHR) Engines

Exploration into the use of ceramics in structural components of reciprocating engines began around 1970 when Godfrey et al (ref. 3) pioneered the use of reaction bonded silicon nitride (RBSN) in producing a piston for a Villiers 0.9 kw gasoline engine. By 1975 Gibson et al (ref. 4) had achieved significant running time on a single cylinder Gardner 9 kw diesel engine. The time was now ripe for more intensive research to create the necessary impression on diesel engine insulation.

By 1978, the Cummins engine company in association with the U.S. Army described a scheme which yielded a smaller engine with superior performance (ref. 5). The scheme involved using newly developed ceramic materials (hot pressed silicon nitride and glass ceramics) to insulate the engine thermally resulting in a higher power to weight ratio. The dedication of this team was such that a year later they had built a fully insulated engine using ceramics (ref. 6). These papers and subsequent literature from this establishment has led almost every major diesel manufacturer to invest in researching the "insulated engine".

In Bath, Wallace et al (ref. 7) simulated a semi-adiabatic six cylinder four stroke Perkins engine using a simplified one-dimensional Fourier representation of the heat flux at the wall surface. The intention was to determine how close to the ideal adiabatic insulation was the behaviour of reaction bonded silicon nitride. The conclusion was that the engine behaved in much the same way as a standard one except for an increase in exhaust enthalpy. The obvious extension to this work was to introduce turbocharging and turbocompounding (ref. 8) the latter resulting in an improvement of three to four percentage points in thermal efficiency and torque for

a given fuelling.

The above work by Wallace et al did however reveal significant improvements in engine performance for a hypothetical fully adiabatic engine. This was to be the basis for engine insulation work at Bath University.

It soon became clear that higher combustion chamber temperatures in insulated engines facilitated the burning of low cetane number fuels and coal derived fuel (SRC II). Yoshimitsu et al (ref. 9) realised the benefits of insulation but ran into the difficulties still restricting work to this day: namely, ceramic material quality and lubrication of high temperature components. Ceramic components used for this work had to undergo stringent screening prior to their use in the test engine. Even after screening, the test engine only covered 250 hours with much doubt of it ever achieving 10,000 hours.

A year later, the same team reported significant advantages using ceramic coatings instead of the monoliths used previously (ref. 10). The problem of lubrication still remained but the six cylinder turbo-charged unit was converted to run with zirconia coated combustion chamber components and without water cooling. It was found that the liner and top rings had to be plasma spray coated with chromium carbide and titanium carbide respectively to avoid scuffing and abnormal wear. Heat rejection was reduced by 35% and the overall thermal efficiency of the engine was increased by 6% to a claimed 48%. This was claimed to be the result of heat insulation and turbocompounding.

With such a high performance system, turbocharging and turbocompounding becomes almost a necessity and the need for optimised turbomachinery is now of paramount importance. In fact it was seen in this study (ref. 10) that turbocompounding made fuel consumption insensitive to fuel injection timing. This was due to the fact that a retarded engine produces higher exhaust temperatures (and hence enthalpy) which is recovered in a turbocompounded configuration. The effect was that NO_x emission could be reduced by retarding the fuel injection timing without too great a loss in fuel

consumption due to energy recovery through compounding.

The alternative of using all metallic components with air gap insulation was pursued at Bath by Wallace et al (ref. 11) who experimented with an "air gap piston" which replaced a standard piston in a single cylinder Petter PHIW engine. The "air gap piston" was made up of four components assembled to give a 1mm air gap under a Nimonic crown. The results were encouraging, piston crown temperatures reaching a maximum of approx 750°C and exhaust temperatures increasing by approximately 100°C.

Until the mid eighties, there was little or no opposition to the concept of insulation being a forward step in the development of the diesel engine. In 1987, however, Woschni et al (ref. 12) introduced a note of scepticism by claiming that a standard engine returned better fuel economy than its insulated counterpart, be it naturally aspirated, turbocharged or even turbo compounded, as a result of higher rather than lower heat transfer.

This appeared to contradict totally the work done thus far by previous researchers who used similar engine configurations to Woschni's. In a further publication in 1988, Woschni et al (ref. 13) reported a detailed validation of his previous findings, both experimentally and by computer modelling. This prompted great discussion from leading researchers such as Borman, Morel, Wallace, Alkidas and many others.

Startling as it was, this contribution by Woschni et al did not result in the termination of research into insulated engines. Morel et al (ref. 14) proved that "insulation and increasing wall temperatures led to a decrease in heat transfer and thus contributed positively to thermal efficiency." The hypothesis due to Woschni et al (ref. 12) made researchers aware of the fact that not every insulated engine produced better results (see refs. 1 and 2). The type of insulation, materials and baseline engine used for comparison have a large bearing on the overall effect of insulation.

The unfortunate situation with international research into diesel engine insulation is

highlighted by Churchill et al (ref. 15). The lack of cooperation and the desire to plunge into the marketplace of advanced engines is the root cause of inconsistency in findings thus far. Churchill and his co-workers summarise the research in LHR engines by suggesting that "no one company will capture the art and develop the science" and that "we all have a long way to go, and if we are to get there in an effective manner it will occur best in an open and cooperative environment".

1.3 Experimental Studies

Work at Bath University has over the years contributed significantly towards the goal of achieving a production LHR diesel engine. As early as 1979, Wallace et al (refs. 7 and 8) devoted much of their attention to the field of diesel engine insulation. Perhaps the most significant contribution of the Bath research team was the air gap piston used by Wallace et al (ref. 11).

In 1987, work started at Bath in conjunction with Pilkington PLC on LHR engines using ceramic components sponsored by the Department of Trade and Industry (DTI). The programme code named CARE (Ceramic Applications in Reciprocating Engines) brought together industry and various Universities nationwide united in their quest for success in this hitherto less than encouraging field.

The connection between Bath and Pilkington PLC was such that Pilkingtons produced ceramic monoliths specifically for piston caps. The materials used were glass ceramics, Cordierite (magnesium aluminium silicate) and LAS (lithium aluminium silicate). A simple IDI system was chosen (Petter AV1 engine) characterised by the use of a completely flat piston crown. The general aim was to implement the following sequence of events :

a) Make a ceramic cap to fit on a standard Petter AV1 piston
b) Run the piston assembly in a motored engine to prove its integrity
c) Run the firing engine with the ceramic piston assembly

d) Run the Ford 1.6 litre four cylinder production car diesel engine with ceramic piston cap assemblies.

Unfortunately, the final part of this goal was never realised due to time constraints.

Prior to any building of piston assemblies, a detailed finite element study was undertaken by Wilson (refs. 16 and 17) to establish whether or not the concept of securing a ceramic on an aluminium body was a feasible one. Wilson established from his detailed work, that the assembly would be thermally and mechanically capable of withstanding the pressure and temperature fluctuations experienced during assembly.

To verify this work, Alexander (ref. 18) designed and built a thermal shock rig, which basically consisted of a high density quartz halogen lamp concentrating its thermal power on and off a ceramic specimen on a traversing table. The thermal loading on the ceramic specimen was such that surface temperature fluctuations between 200°C and 700°C were achieved in only 50 seconds. This test was repeated over many cycles resulting in very few failures and then only in the Cordierite material. These failures were attributed to defects in the manufacturing process associated with internal and surface cracks.

Having been satisfied by the results so far, designs for securing the ceramic caps to the piston body were investigated by Alexander (ref. 18). This led to a complicated combination of material, fixing method and cap type configuration to be devised. The reason for this was that there were two materials to choose from, two types of cap to consider (Petter and Ford) and four methods of fixing. The overall objective of this rather complex ceramic to aluminium assembling exercise was to choose an optimum method of assembly. The method ultimately chosen was to secure a Cordierite cap (of either Ford or Petter design) to the aluminium body by using an adhesive known as "Aremco-Bond 568".

The plan was to produce a satisfactory piston assembly and subject it to a motored test

in the engine simulation rig prior to running in a firing engine. The simulation rig was a replica of the firing rig with the exception of the fuel system which did not feature in this rig at all. The only modification to the engine itself was the blanking off of the prechamber to increase the compression ratio and carry a pressure probe. To subject the piston caps to thermal loading, an air heater was introduced upstream of the inlet manifold which was capable of maintaining inlet temperatures of up to 150°C. Another feature of this rig was the closed inlet and exhaust loop which was so designed to be able to simulate boost and backpressures associated with a turbocharged engine. Boost pressures of up to 5 bar were achievable using this system.

Once again due to time constraints, the simulation rig was only used for one piston assembly. The result, although encouraging at first, led to failure in the firing rig. The piston assembly having successfully completed 60 hours in the simulation rig at speeds of up to 2000 rev/min and 1.8 bar boost, failed in the firing rig after only thirty minutes under low speeds (1000 rev/min) and ¾ load. At this stage the simulation rig was abandoned due to its lack of useful contributions to the exercise. There was evidence to suggest that failures can occur instantaneously, and when they do, it is generally catastrophic.

The firing rig was subject to five total engine rebuilds due to four catastrophic ceramic piston failures before a change in operating conditions resulted in a successful outcome. It was found that by reducing the fuel injection pressure and retarding the fuel injection timing, the peak cylinder pressures were reduced by some 20 bar. The overall effect on the performance of the engine was clearly detrimental (except for noise which was significantly reduced). At this stage of the exercise, performance was not as important as obtaining comparable results for the engine operating either with its standard or the ceramic piston cap assembly. This was achieved satisfactorily and after 61 hours of running time, the piston was removed and examined visually to reveal the propagation of a hairline crack, which would have almost certainly resulted in a catastrophic failure had the piston continued in service. Having obtained results for an engine running with a ceramic piston crown over the entire operating range of

speed and load, corresponding results were obtained for an equivalent engine with a standard piston.

Due to the failures encountered, the programme was considerably slowed down. As a result no work could be achieved on the Ford 1.6 litre engine although four pistons were produced with ceramic caps ready for assembly in such an engine.

1.4 Theoretical Work

Theoretical studies in the present research were mainly based on two heat release analysis models adapted specifically to the determination of instantaneous heat release in an IDI engine. The difference between the two models was that one relied on two pressure measurements and the other only on one. These two models will be described briefly in this section and in more detail in Chapter 5.

Many programs have been run during the course of this research but only the cycle analysis models will be explained here. A separate data reduction program was run during engine testing which was capable of converting the input data into performance figures. This program was written by Cole (ref. 19) and relied on a large bank of input information to determine parameters such as BMEP, Air fuel ratio, SFC, Volumetric efficiency, Brakepower, etc. This was very useful as instantaneous performance figures were available to establish whether running conditions were suitable or not.

In the past, a high speed data acquisition system was used by Cole (ref. 19) which due to technical obsolescence has become difficult to connect to the University mainframe system. This meant that an alternative data acquisition system had to be considered. A simple and somewhat limited system was employed whereby a digital storage scope (DSS) with a two channel facility was used as a data acquisition unit. The biggest drawback of this system was that only one cycle could be captured and no averaging or sampling was possible. With this system repeatability becomes a major stumbling

block. Another drawback of this system was that only two input channels could be stored at any one time. It was hoped that as well as pressure, a trace for injector needle lift could be stored. This was not possible as a TDC marker was more critical to the analysis work.

The DSS was connected to the cylinder pressure piezo output and engine TDC trigger. This stored data was then transferred to a BBC computer and disk drive using a package prepared by Barker (ref. 20). Once on disk, this rather randomly stored data was trimmed using a separate program to establish cylinder pressure in bar and valve opening and closing points. Having arranged the data in a more uniform manner, it was stored and then transferred to the University mainframe system (Gould) for processing. Once on the Gould, the data was smoothed and then fed into the single pressure model. The results from this model were finally plotted using a plotting routine.

Although only one pressure transducer was used in the engine, it was thought early in the research programme that a two pressure (main and prechamber) system could possibly be employed. This would have been a much better system to use but several criteria ranging from time to cost to transducer accuracy swayed the decision in favour of a single transducer system. Another system considered was that of a differential pressure transducer whereby the two probes in the main and pre-chambers would register the instantaneous difference in pressure between the two chambers throughout the operation of the cycle. Apart from the problems of having to locate and watercool the two probes, a third probe would have been necessary to obtain an absolute value for pressure.

Although it was known early on in the research that a two chamber pressure measuring system was unlikely to be employed, a computer model was written based on main and prechamber pressure values as the only inputs to the program. This program employed a rather simplistic approach to the two chambers,making it possible to obtain a value for the total heat release from both chambers using gas properties, engine geometry data and the two cylinder pressures. To establish the individual heat

releases, i.e. main and prechamber distribution, it was important to know the flow between the two chambers. This was not very easy as in practice the coefficient of discharge plays a complex role during flow transfer through the throat.

It was the single pressure measurement system that had to be developed during the analysis of the results. In this case where only the prechamber pressure is known, a compromise between accuracy and practicability was reached. It was assumed that both chambers are treated as one, and according to Heywood (ref. 21) the loss in accuracy of calculating heat release is large during the initial stages of combustion but later on (i.e. after 20° ATDC) the errors become negligible.

In order to analyse the heat release fully, a heat transfer term had to be introduced. Heat transfer in the cylinder was calculated using the expression due to Woschni (ref. 22) the value of which was assumed to be uniform throughout the cylinder. Energy absorbed through heat transfer to the walls was calculated assuming fixed wall temperatures that had been previously calculated using a cycle simulation program (ODES) due to Chen (ref. 23). Chen's simulation program (ODES) also served as a very useful tool in determining the initial trapped conditions of the author's analysis program. ODES is a very sophisticated program capable of simulating virtually any engine configuration be it single or multicylinder, naturally aspirated or double turbocompounded, two stroke or four etc. The program relied heavily on a large data bank specific to the engine it was to simulate. It employed a filling and emptying system treating the engine as several control volumes connected by a series of orifices. Output from this package was divided into sections of performance, heat loss analysis, trapped conditions and conditions in each of the control volumes specified (four in the case of the Petter AV1 engine).

The single pressure analysis program used gas properties which were calculated using instantaneous inputs for pressure temperature and equivalence ratio. The drawback here was the difficulty in pinpointing precisely the start of injection and burning in order to establish a starting point for equivalence ratio calculations to commence. It was assumed that the heat release calculations had to distinguish between fuel burnt

and heat transfer and thus the fuel component could be isolated and converted to a known quantity by using the fuel lower calorific value. This yielded an equivalence ratio which together with the recorded pressure and calculated temperature made possible the instantaneous calculation of gas properties.

The heat release analysis was used to highlight differences in the behaviour of the engine, operating either with the ceramic cap piston or the standard piston over a wide range of speeds and loads.

1.5 Breakdown of work undertaken in this reaearch

The tasks undertaken in this research can be broken down into two main categories. Firstly the work done by the project team, and secondly the work done by the author. Among the work done by the team were the following:

1) Finite element analysis of ceramic and aluminium piston assemblies using both LAS and Cordierite as the main ceramic monoliths.
2) Building and running a thermal shock rig to test the ceramics under high cyclic thermal loadings.
3) Designing a satisfactory method of securing a ceramic cap to an aluminium piston body capable of withstanding the adverse conditions experienced in a diesel engine.
4) Build two engine rigs, one firing and the other motored to test the compound piston assemblies.

Work carried out by the author involved the following:

1) Completing the building, and commissioning of both firing and motored engine rigs.
2) Running the simulation rig with a ceramic piston assembly over a timed trial period.

3) Running the firing rig both boosted and naturally aspirated to obtain baseline performance results.
4) Running the "detuned" firing rig both insulated and in standard form to establish both performance and heat release data for the two engine builds.
5) Writing two heat release analysis programs based on both two chamber pressures, and prechamber only pressure measurements as the only input.
6) Modifying a previously written data reduction program to calculate performance parameters.
7) Writing a series of programs to convert pressure signals in voltage form to smoothed results capable of transfer between various proprietary computer systems.
8) Running a simulation program and matching the results to both the standard and insulated engine builds.

CHAPTER 2
THE APPLICATION OF CERAMIC MONOLITH CAPS TO DIESEL ENGINE PISTONS.

2.1 Introduction

This chapter is divided into two main sections; the first, sections 2.2 to 2.5 dealing with ceramic caps and their use in diesel engines, and the second sections 2.6 and 2.7 dealing with the results obtained from running both simulation and firing rigs using these ceramic caps.

At this stage, it is important to define the terms "simulation" and "firing" rigs to eliminate any confusion. The "simulation rig" is used as a motoring facility and is based on the same standard Petter AV1 engine as the firing rig except for the elimination of the fuel injection system and all associated components, and the use of a 4KW 3 phase AC motor as the source of power. In addition, the prechamber passage has been blocked off to increase the effective compression ratio, thereby ensuring high motored peak cylinder pressures. It is intended to simulate, as far as possible the conditions in the firing engine, at least with respect to pressure and inertia forces.

The "firing rig" uses the fully instrumented Petter AV1 engine complete with fuel injection equipment and a D.C. dynamometer.

From the beginning, work on low heat loss engines at Bath had mainly concentrated on the insulation of pistons. Kao (refs. 22 and 23) studied the effects of thermal and pressure loading on air gap pistons used in semi-adiabatic engines. These studies led to the production of an air gap piston to be used by Wallace et al (ref. 11). The next step from the air gap piston was the extension of previous analysis and experimental work to ceramics. The author joined the research program sponsored by C.A.R.E. in

1987 when much of the groundwork had been completed by Alexander (ref. 18). In conjunction with Pilkington PLC, the team embarked on a research programme to replace standard production pistons with modified ceramic monolith capped designs. The ultimate aim was to run a Ford 1.6 litre 4 cylinder IDI automotive diesel engine of 80 mm bore and 80 mm stroke with such a piston, the bore being identical with that of the Petter AV1 engine. Although this aim was not fully achieved due to time constraints, four complete piston assemblies were produced but not tested in the engine.

2.2 Ceramic Materials Considered

Ceramic materials have been researched for many years with particular regard to diesel engine applications. The U.S.A., Japan, Germany and Great Britain have been leading the world in this research and to date have produced scores of papers in this field.

The attractions of ceramic materials are their superior properties in certain respects compared to conventional metals currently used. Ceramics offer high temperature strength, good wear and corrosion resistance, high hardness, low friction and density, and low conductivity. Apart from these reasons, relative abundance and low cost of basic elemental constituents make engineering ceramics even more attractive. The elements that make up these high performance ceramics include aluminium, carbon, nitrogen, oxygen, silicon and zirconium.

There are however many disadvantages, especially their brittleness and poor reliability characteristics which can lead to sudden and catastrophic failure. The study of ceramics, unlike the study of diesel engines, is still in its infancy and great strides with respect to mechanical properties will have to be made before any large scale applications can be considered.

The application of ceramics in reciprocating engines can be divided into two

techniques. Firstly, the depositing of thin insulating coatings usually by plasma spraying, and secondly the introduction of ceramic monoliths in the body of the components to be insulated.

When this project was initiated, the research team at Bath and Pilkington PLC focused on monoliths only and more specifically, the use of ceramic piston caps. The use of glass ceramics as opposed to such materials as zirconia, silicon nitride or sialon was considered to be of particular interest in view of their unusual combination of low thermal conductivity, considerable mechanical strength and resistance to thermal shock. Figure 2.1 shows the most important physical properties of the two candidate materials used, viz magnesium aluminium silicate (Cordierite) and lithium aluminium silicate (L.A.S.) which were both produced by Pilkington PLC.

2.3 Finite Element Studies on Ceramic Caps

The finite element work done since the start of this research by various workers has generated a large volume of results. The person who began this work was Rentsch (ref. 26) who in 1987 modelled a rather basic piston/ceramic combination which highlighted the need to alter the shape to prevent the build up of high local stresses. This work was then developed further by Kassens (ref. 27) who modelled a different shaped cap free of high stress concentration points. Unfortunately Kassens was not able to accurately model the interface element between the piston and ceramic cap; this led to less than reliable results. This work was then continued by Wilson (refs. 16 and 17) who changed the shape of the cap twice and finally established an accurate model of the assembly.

The aim of the analysis was to ascertain both the thermal stresses and the mechanical stresses on the ceramic caps during assembly. Figure 2.2a shows the shape of the assembly for the original Kassens (ref. 27) design and fig. 2.2b shows the revised shape of the assembly due to Wilson. Note the difference in shape of the underside of the ceramic cap which had the effect of reducing the mass of the ceramic.

For the material Cordierite, FE analysis revealed acceptable temperature levels which were well within the material specifications (see fig. 2.3). The hoop stress, however, was considered too high at the ceramic/aluminium interface (see figure 2.4). The radial and axial stresses showed dangerously high stress points at the clamping annulus (see figs. 2.5 and 2.6 respectively). In the second report by Wilson (ref. 17) based on a lightweight design for the Ford engine, the ceramic cap is modified further to show a greater reduction in mass and the introduction of a compliant layer between the ceramic and the aluminium body (fig. 2.7). The compliant layer was introduced to absorb the stresses due to shrinkage in the assembly process. Due to the high stress levels previously experienced in this region, more elements were introduced to facilitate closer inspection of results and higher resolution (fig. 2.8).

The analysis with this new geometry once again revealed high stress concentrations (fig. 2.9). To rectify this problem, the model was modified yet again by limiting the region under investigation to the cap and clamping ring only. This simplified the model, but according to the displacement results (fig. 2.10) the ceramic cap would almost certainly break during cooling.

The final modification was to introduce an interface of 45° (see fig. 2.11) to improve the displacement properties. This gave more reasonable results (fig. 2.12) but all the indications were that the tensile stresses at the interface were in the order of 150% that of the maximum permissible value.

The F.E. exercise yielded unfavourable results partly due to possible unrealistic boundary constraints and partly due to uncertainties concerning gap element empirical input. This statement can be justified as it was possible to build a few working examples of ceramic capped pistons which actually ran in both motored and firing engines.

2.4 The Design and Fixing of Ceramic Piston Caps

The means of attaching a ceramic monolith to an aluminium piston was a major design problem. Alexander (ref. 18) had the task of solving this problem before the author joined the research team. Due to the properties of the two materials to be joined (ceramic and aluminium) (see fig. 2.1), elaborate fixing strategies had to be considered. The conditions that the assembly had to endure presented another design constraint. The finished product would have to withstand high instantaneous accelerations and very large temperature and pressure fluctuations.

As stated earlier, the final phase of the programme (which could not be executed due to time constraints) was to run a Ford 1.6 litre 4 cylinder engine with ceramic monolith piston caps. This meant that two cap arrangements had to be designed; a Ford and a Petter fixing system.

Pilkington chose two types of ceramics to base the investigation on and they were;

a) Titania nucleated magnesium aluminium silicate giving Cordierite as the crystal form.
b) Lithium aluminium silicate (LAS) nucleated with zirconia and titania.

Some basic physical properties of these materials are shown in fig 2.1.

The final outcome from the ceramic cap designing exercise was to produce two basic geometries, viz.

a) The Ford Cap, type F (fig 2.13a)
b) The Petter Cap, type P (fig 2.13b)
with either plain or scalloped boss.

Figure 2.14 shows the three types of cap relative to each other. Note the difference in thickness of the crown face to piston top of the Ford type F cap relative to the

Petter type P caps. The latter were consistently heavier and hence potentially stronger in view of the much lower speed of the Petter engine (1500 rev/min compared to 4500 rev/min).

Both types of cap were produced in Cordierite as well as LAS, with either plain boss (type A) or scalloped boss (type B). To identify the various caps the codes PAC, PBC, FAC, FAL etc. were used in which the first letter P or F, refers to the basic type (i.e. Petter or Ford), the second letter, A or B, to the type of boss (i.e. plain or scalloped respectively), and the third letter, L or C, to the material, (i.e. LAS or Cordierite).

In all, four different methods of attachment were used these are shown in fig. 2.15, 2.16 and 2.17. The methods of fixing are detailed in the following subsections.

2.4.1 Mechanical Attachment

Figure 2.15 shows a sectional view of this method of attachment. It is evident that this method of fixing involves a rather complex assembly. Furthermore, the final product was very difficult to assemble due to the spring retaining clip jamming. Unfortunately the clip had to have a certain stiffness below which the cap would "rock" about the piston body. The split retaining ring was a very difficult object to machine, especially to the tolerances which had to be observed. To overcome the problem of tolerance build up, it was thought useful to include a compliant layer of graphite above the piston body. This was omitted due to doubts of the long term integrity of the graphite layer and the fear of sealing problems, which could cause the assembly to break up under pressure.

2.4.2 Casting Technique

Figure 2.16 shows a sectional view of this method of fixing and fig. 2.18 shows the

jig used to produce the composite pistons. A split annular stainless steel ring is first assembled around the boss of a ceramic crown. Aluminium alloy is then melted around the ring and a premachined piston body is brought into contact with the molten pool with the aid of the jig shown in fig. 2.18.

This method of cap fixing is not without its faults. The quantity of molten metal has to be carefully measured such that precise filling of the gap around the boss and the stainless steel ring is ensured. Another problem is the need to carry out post-casting sealing to ensure a good piston-to-crown seal. A further disadvantage of this system is the need to machine the ring to a very tight tolerance to ensure no molten alloy escapes into the gap between it and the boss during casting. Figure 2.19 shows the result of an incorrectly calculated quantity of molten aluminium.

2.4.3 Shrink Fit Attachment

Figure 2.17 shows a cross sectional view of this method of fixing which attempts to overcome most of the major difficulties of the two previously described methods. This design was produced for use with the Ford type ceramic crown which was of thinner top section and narrower boss diameter (figs. 2.13 and 2.14) than the Petter design.

The shrink fit spring design essentially comprises a split circular ring of cantilever beam cross section, probably better described as a coned disk type spring. The boss section of the ceramic cap has a section which is essentially conical and at 45°. The spring section which is intended to surround this is therefore an extreme case of the coned disk type spring. The annular ring which surrounds this sprung section acts against it on a smaller angle conical section. The purpose of this section is roughly to equalise the radial and axial expansions, which are in the opposite sense, and thus achieve a reasonably constant clamping force throughout the operating temperature range. Another factor here was that some consideration of the tolerances of the components had to be taken into account. The annular ring is adhesively bonded back

together after fitting to the coned spring section, and machined to provide a degree of interference, (at the lowest temperature expected), with the hole in the piston body. Fitting of the cap assembly is achieved by heating the piston body to a temperature of around 200°C, and then inserting the room-temperature crown coned spring sub-assembly.

Although more satisfactory, this method is still complex and suffered from excessive shrinkage stresses.

2.4.4 Glueline Method

This method of producing a ceramic cap piston is almost identical to the shrink fit technique (2.4.3 above) but instead of an interference fit, the assembly is held together using an adhesive bond. The adhesive used was a product known as "Aremco-Bond 568" which was made by Aremco, U.S.A. A sample piston assembly utilising this method of attachment was subjected to severe tensile tests up to an equivalent inertia stress at 4000 rev/min without failure.

It must be pointed out that this method was the only one to result in a functional piston which actually ran in the firing engine over a period exceeding 60 hours to give the results reported in Chapters 4 and 6.

2.5 The Behaviour of Ceramics as Engineering Materials

The use of ceramics as an engineering material where they are expected to endure hostile environments led to a series of tests in order to establish their durability.

Prior to their use in engines, ceramic disc samples were subjected to instantaneous thermal cycling, ranging from 150 to 750°C in 50 seconds. This was done approximately 1000 times (or 2000 thermal cycles) for the two materials considered

(Cordierite and LAS). Details of the thermal shock rig and results using it are found in Alexander's thesis (ref. 18). In general, Cordierite and LAS survived thermal cycling in what could be described as a hypothetical situation where pressure effects are ignored.

This test was then extended to observe the effects of localised thermal loading comparable to heat emitted from a prechamber on a piston crown. This was done rather crudely by positioning ceramic caps on a hollow tube and applying an oxy-acetylene torch to the centre of the top face. The Cordierite caps tested, failed by catastrophically cracking within two or three minutes whereas the LAS cap withstood the flame test for nine minutes. The estimated maximum face temperatures exceeded 1300°C and in the case of LAS, the cap cracked explosively on cooling. An example of a fractured Cordierite specimen can be seen in fig. 2.20.

To observe the effects of inertial loading an adaptor was adhesively bonded to the crown of a fully assembled ceramic cap piston and the whole assembly placed in a standard tensile testing machine. The assembly was subjected to loads somewhat higher than the inertial loads expected to occur in a running engine (equivalent to an engine speed of 4000 rev/min). The result of one such test is shown in fig. 2.21 using a Cordierite cap. In another test, Pilkington PLC devised a method of mounting ceramic caps on an annular ring and applying a downward force through a spherical ball in the centre of the specimen. The results yielded lower than expected failure loads which were put down to the quality of the surface finish after machining. More information on these tests are detailed in a confidential report by Pilkington PLC (ref. 28). A sketch showing some fractures from this test are shown in fig. 2.22.

Analysis of fractured ceramic caps were carried out by Pilkington PLC and it is clear that failures occurred in regions of material inconsistency within the caps. The main causes of failure are the casting and machining of the components where impurities or rough finishes propagate these failures. Figure 2.23a shows an iron inclusion at the source of a crack magnified 25 times using optical microscopy. Figures 2.23b and 2.23c show the same inclusion magnified 72 and 288 times respectively using a

scanning electron microscope. From these figures it is easy to see the inconsistency of the material due to a foreign body and hence a weak point in the structure of the chemical composition of the host material. To obtain a clinically cast and carefully machined specimen free of any imperfections is an extremely difficult task which has not been mastered yet.

2.6 Simulation Rig Results Using a Cordierite Cap Piston

The simulation rig is fully detailed in Chapter 3 and will therefore not be described in this section. Due to time constraints and poor reliability, the simulation rig did not receive as much use as originally intended. It was hoped to try every ceramic cap destined for the firing rig in this rig first, but the lack of available time made this impossible. There was, however, one piston with a ceramic cap that did perform in this rig, albeit for a total of only 60 hours. The 60 hours were achieved over a period of three months due to drive mechanism failures.

The ceramic cap used was Cordierite which was fitted to the aluminium body by the casting technique detailed in 2.4.2 above. The simulation rig was run at various conditions during the 60 hours and they were:

1) Speeds ranging from 750 to 2000 rev/min
2) Inlet and exhaust pressures varying from 1 bar to 1.8 bar
3) Inlet temperatures varying from 50 to 100°C.

For these conditions various recorded pressure traces were obtained but in the interest of brevity only three such records will be shown. Figures 2.24 and 2.25 show cylinder and exhaust manifold pressures while figure 2.26 shows cylinder and inlet manifold pressures. The conditions for figures 2.24, 2.25 and 2.26 are, 100°C inlet temperature, 1.8 bar boost and speeds of 1000, 1750 and 2000 rev/min respectively.

As expected the cylinder pressure trace rises to a maximum at TDCF with one peak

every other revolution. The inlet and exhaust pressure traces do show some interference and resonant pulsations but in general a drop in inlet, and a rise in exhaust pressures at their corresponding valve openings is as expected.

It is interesting to see that the maximum recorded cylinder pressure was 80 bar, suggesting that the piston could withstand the pressures and inertial forces expected from it in the firing rig. Unfortunately the piston failed in the firing rig after only half an hour's running time at 1000 rev/min and ¾ load. This result was instrumental in bypassing the simulation rig as a standard procedure in the research programme.

Prior to installing this piston in the firing rig, it was photographed to show the effects of hot compressed air at elevated pressures on Cordierite. Although the photographs were lost, they showed clearly the charring of particles that had found their way into the combustion chamber during the 60 hours of operation. It is assumed that oil from the engine made up the majority of the accumulated particles and the discolouration is mainly due to the effect of temperature on Cordierite.

2.7 The Use of Ceramic Capped Pistons in the Firing Rig

As mentioned earlier in section 2.6, the one piston assembly that had been used in the simulation rig having survived 60 hours running, failed in the firing rig after only 28 minutes running time. The fact that this piston assembly survived 60 hours in the simulation rig proved that failure was due to thermal, and not pressure or inertial influences.

The sequence of events that led to the catastrophic failure was as follows:

1) engine preheated to operating temperature using the external water heater.
2) engine started up at 750 rev/min, no load.
3) speed increased to 1000 rev/min (still no load) after ten minutes idling at 750 rev/min.

4) loading applied to 25% of maximum value, still at 1000 rev/min. Time elapsed: twenty minutes after start up (maximum load = 23 Nm).
5) Loading increased slowly, maintaining speed at approximately 1000 rev/min.
6) After 25 minutes running time, load applied was 75% of maximum value.
7) Three minutes later, the engine came to an abrupt halt. Catastrophic failure had taken place.

Due to the nature of the failure, very little could be inferred from the collection of ceramic pieces which had spread themselves all over the engine internals. The extent of the damage caused to the engine was such that a total rebuild was necessary. The piston, connecting rod, and liner were all beyond salvage, and as can be seen in fig. 2.27, both valves and their seats had to be replaced. The cylinder head had to be skimmed and oil passages had to be freed from the dust which had clogged them. The powdery dust that had reached small oil galleries within the engine is clearly visible in fig. 2.28. Having removed the debris in the cylinder, it was possible to see the area around which the ceramic cap had failed (see fig. 2.29). Figure 2.30 shows a side view of the piston where the ceramic cap appears to be intact around the boss area. This prompted suspicion that the failure was not only thermal in origin but that there was also a stress component, possibly due to the process of assembly. On sectioning the piston body, it was seen that excessive quantities of aluminium alloy melt had been used which had completely filled the region around the stainless steel ring instead of partially filling it.

It was therefore necessary to modify the piston assembly design in the attachment area. As mentioned in section 2.4, four methods of piston attachment had been explored and the two materials used in the two cap designs resulted in a large number of combinations of piston assemblies. In all, seven functioning piston assemblies were built and they are briefly tabulated in fig. 2.31. The eighth piston assembly is a Ford cap in Cordierite, mounted in the Petter piston for future running in that engine.

Additionally at the very end of the programme, a complete set of four Ford type piston caps in Cordierite mounted in the Ford 1.6 litre IDI engine pistons, was produced but unfortunately could not be run in that engine (see figure. 2.37).

Having experienced a large scale failure, a change of tactics was considered and a shrink fit Ford type Cordierite cap assembly was proceeded with (number 4 in fig. 2.31). This cap failed during the building of the engine where the force from compressing a lead wire used to measure the bumping clearance fractured the Cordierite, as can be seen in fig. 2.32.

Another attempt was made at using the shrink fit system but once again failure resulted only minutes after the engine had fired (piston number 5). This failure took place under idling conditions, suggesting that the shrink fit method introduced large stresses in the ceramic caps.

A further change to the fourth fixing method i.e. the glueline method (see section 2.4.4) was now indicated. Two caps were produced, one in Cordierite and the other in LAS with Petter and Ford designs respectively. These were attached to the aluminium bodies using the adhesive already refered to. To use the convention in fig. 2.31, the two assemblies were pistons 7 and 6 respectively.

Piston 7 was first assembled into the engine and this time a precaution of "easy running conditions" was introduced. To minimise the pressure and temperature effects on the fragile caps, the fuel injection timing was retarded to 7.5 degrees before TDC from the original 18 degrees. It had been observed that combustion with its original timing had been extremely harsh, with an extremely rapid pressure rise following the delay period. By retarding injection, initiation of combustion was delayed until just after TDC, with a much lower rate of pressure rise and without any of the harshness previously observed. Another precautionary measure was to reduce the injector cracking pressure from 3000 to 1800 PSI. Before starting the engine, it was motored for approximately two minutes with the fuel rack in the off position. The engine was then started up with minimum fuelling and no load. After 45 minutes of successful

running at 1000 rev/min and 25% load, the engine was voluntarily stopped for the first time.

Successful starting and stopping of this engine configuration continued for 27 hours during which speeds of up to 1500 rev/min and 25% load were achieved. Although the engine load was increased to half load at 1000 rev/min it was felt unnecessary to try running at 1500 rev/min full load at this stage.

At this point piston 7 was replaced by piston 6 to observe the difference in behaviour between Cordierite and LAS. After only half an hour of running, the torque indicator showed a rapid drop and the engine note changed. At this stage the engine was shut down having achieved a speed of 1000 rev/min and 25% load. On engine stripdown it was observed that the LAS cap had broken as can be seen in fig. 2.33.

The engine was rebuilt again using piston number 7. After running a total of 61 hours the engine had successfully covered every operating condition from 25% to full load over the entire speed range of 1000 to 1500 rev/min.

The piston was removed for inspection and as can be seen from figure 2.34 the crown appeared to be intact, albeit discoloured from the somewhat rich fuellings it was subjected to. Having cleaned up the sooty deposits, the Cordierite exhibited some interesting wear phenomena. As can be seen from fig. 2.35 a permanent discolouration directly below the prechamber throat was associated with an erosion of the surface of the Cordierite. The once smooth glazed surface was now roughened in the darkened area to the consistency of 400 grade abrasive paper. The discolouration in this area and its outer boundary show the centre of heat emission in the cylinder opposite the prechamber passage very clearly.

Another interesting feature here is the imprint of the exhaust valve on the surface of the piston crown. Although the two never made contact, the heat emitted by the hotter exhaust valve was enough to discolour the Cordierite in that region. The inlet valve running obviously much cooler, has not had such a pronounced effect, although

a small segment of its circumference nearest to the exhaust valve (where it is the hottest) has made a token impression.

The reason for the erosion is not fully known and by the time this piston was available for inspection, the C.A.R.E. programme had been concluded. This made it impossible to obtain full laboratory analysis on the cause of this erosion or indeed the cause of the hairline crack which is highlighted in fig. 2.36. Although minor, this crack was not visible during assembly which leads to one of two conclusions viz:

a) the crack only propagated after the engine was run,
b) the crack was always there but not observed due to the bright monochromatic colour of the clean Cordierite.

From past experience of failures using Cordierite, it is unlikely that the crack propagated itself whilst the engine was running. The inference from previous failures would suggest by extrapolation that it would have continued into catastrophic failure. Catastrophic failure of ceramics has been known to occur when defects in the material were not detectable by any visual means other than x-ray. It has been observed that the crack is geometrically opposite the prechamber and in the direction of "rock" of the small end of the piston. It is possible that the cause of this crack is mechanical loading brought about by the action of rock over many firing cycles.

The last piston assembly produced for use in the Petter engine (number 8 in fig. 2.31) never received any testing due to time constraints, as was the case for the four piston assemblies produced for the Ford 1.6 litre engine.

Having spent many hundreds of hours designing and finally producing the rather complex Ford 1.6 piston assemblies (see fig. 2.37), it will never be known whether the intricate "cloverleaf" cut outs on the top face are a potential failure area or otherwise. These cut outs were a necessity for the swirl and combustion characteristics of the Ford engine and to replace them with a gradual stress free curved shape would have drastically reduced the performance of the engine.

Physical Property	Cordierite	Lithium Aluminium Silicate (LAS)	Aluminium	Cast Iron
Young's Modulus (GN/m^2)	143 - 148	90-91	68.9	200
Thermal Expansion ($X10^{-7}$ per °C)	20.3 - 23.2	6.0-8.0	230	120
Thermal Conductivity (W/mK)	2.0	1.5	170	49
Vickers Hardness Number	860 - 890	540	50	160
Density (Kg/m^3)	2600	2500	2750	7850
Specific Heat capacity (KJ/KgK)	1.06	1.08	0.880	0.544
Modulus of Rupture MOR (MN/m^2)	121 - 217	91 - 120	--	--

Figure 2.1 : Physical properties of ceramics used compared to conventional materials

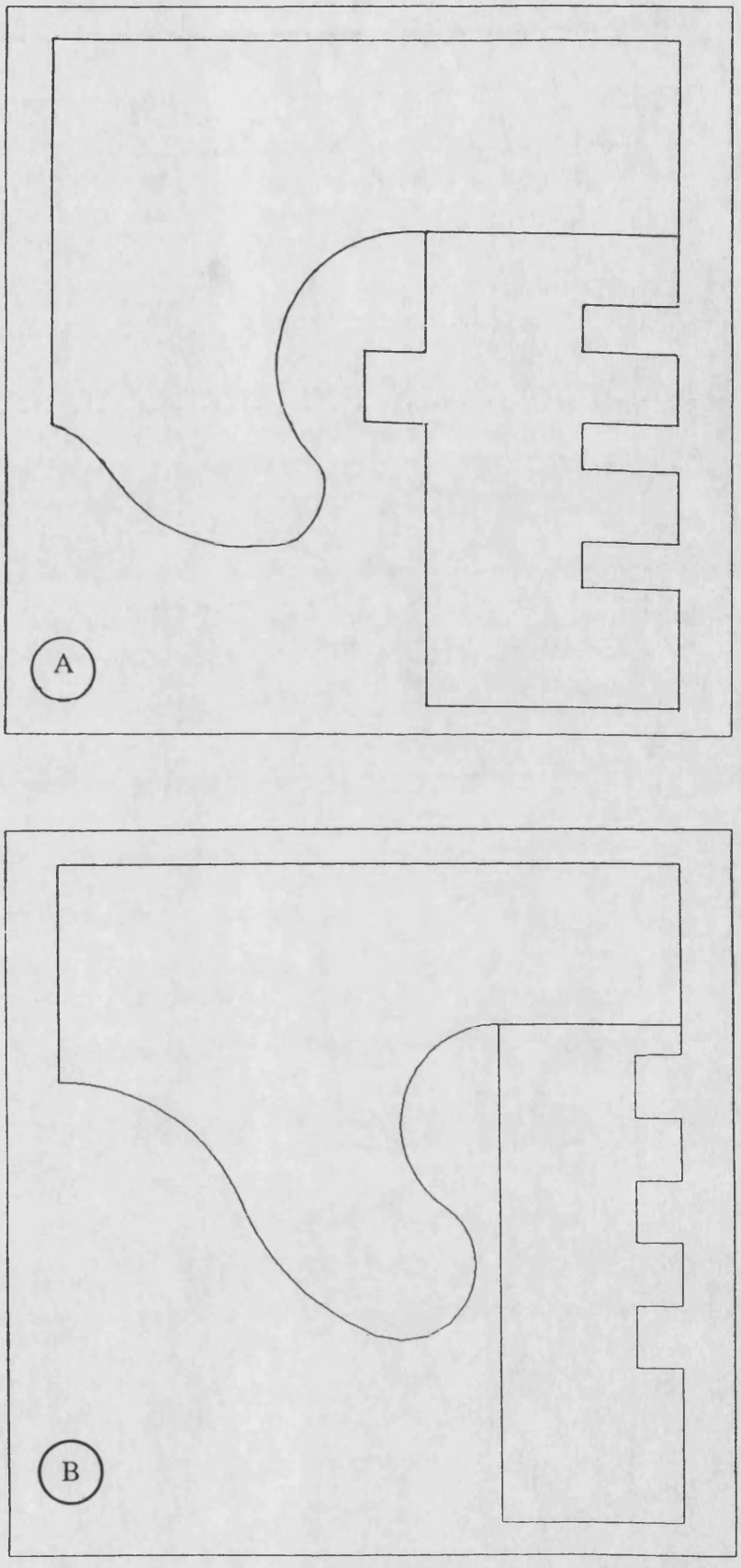

Figure 2.2 : Outline of ceramic cap and piston assembly considered for analysis.

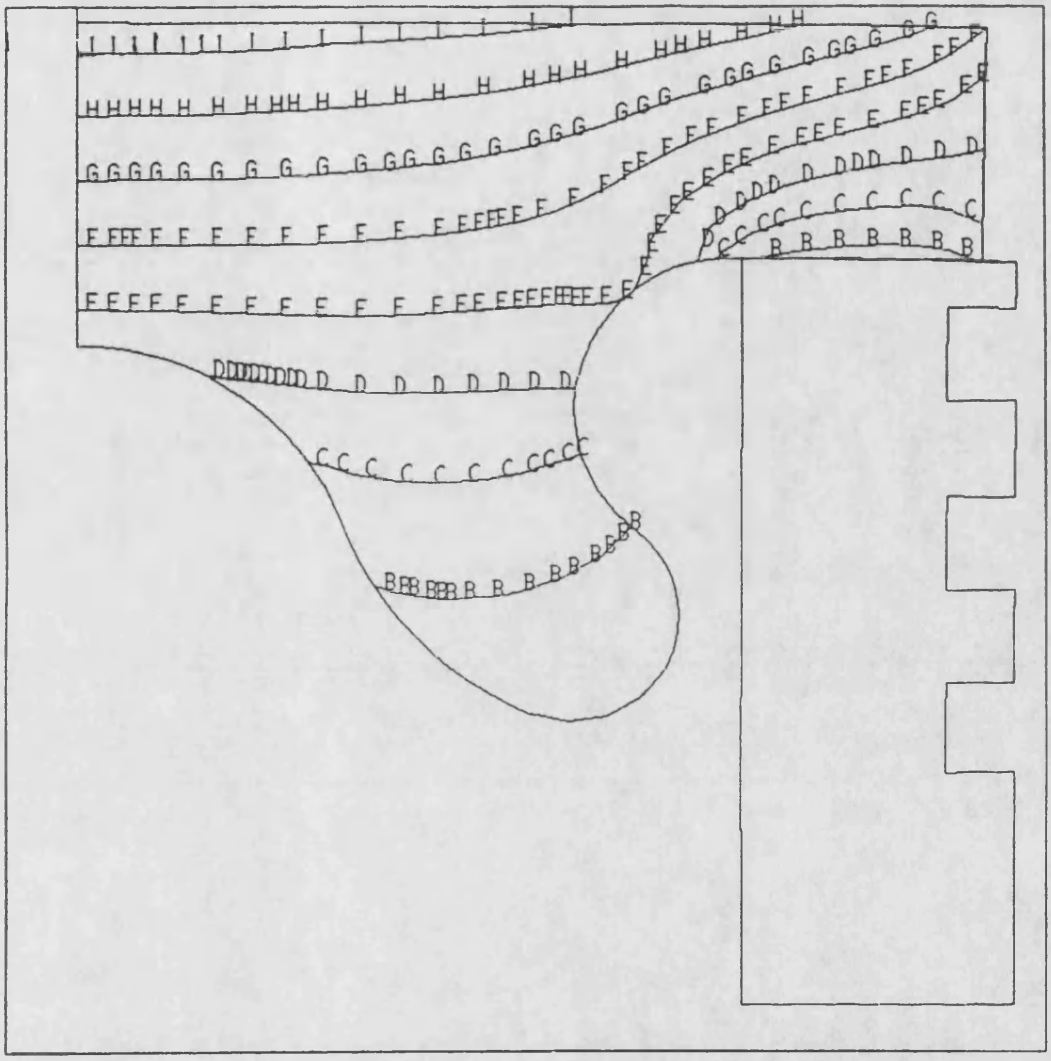

Maximum temperature	=	735.971°C
Minimum temperature	=	127.685°C
A	=	161.479°C
B	=	229.066°C
C	=	296.654°C
D	=	364.241°C
E	=	431.828°C
F	=	499.415°C
G	=	567.003°C
H	=	634.590°C
I	=	702.177°C

Figure 2.3 : Finite Element analysis on Cordierite cap piston assembly showing temperature distribution.

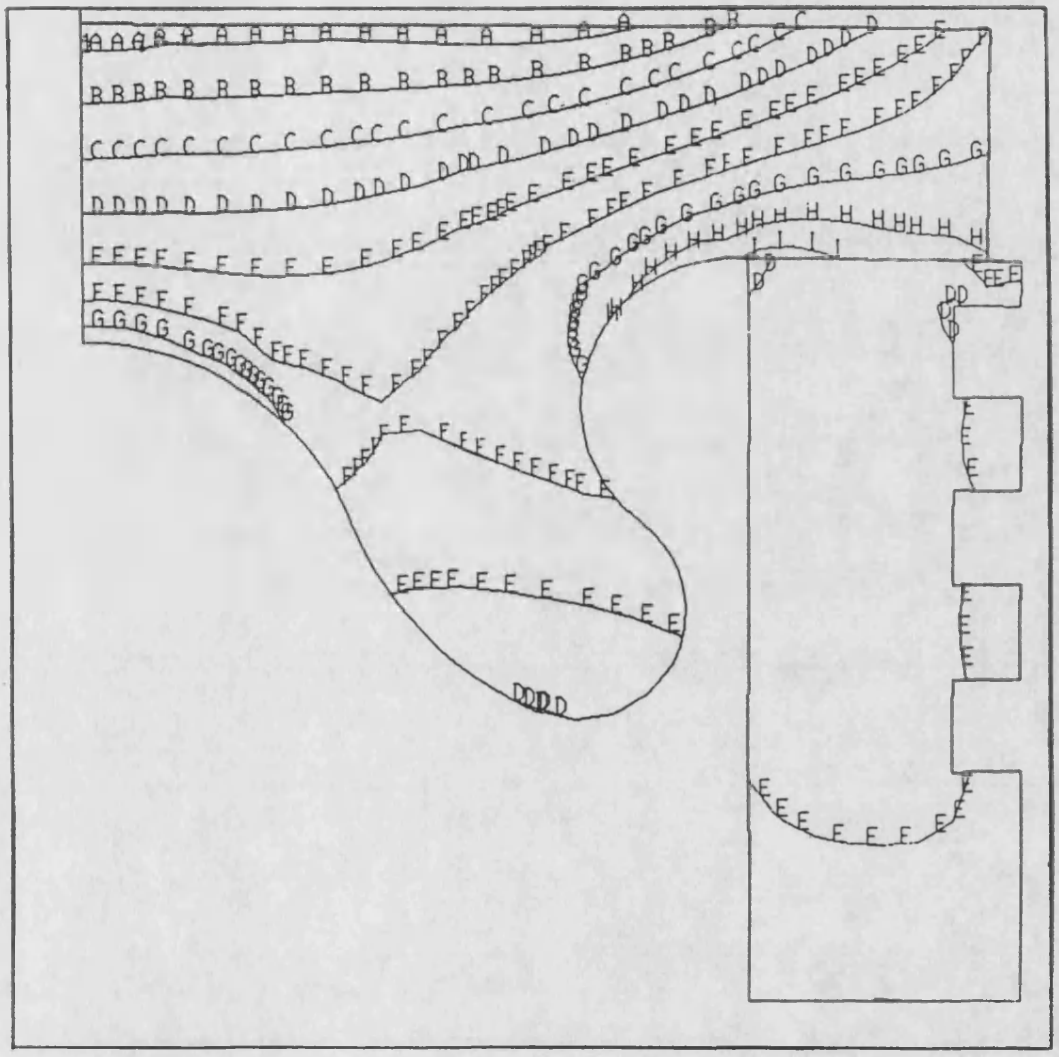

Maximum displacement	=	0.135 mm
Maximum hoop stress	=	0.705E+08 N/m2
Minimum hoop stress	=	-0.660E+08 N/m2
A	=	-0.584E+08 N/m2
B	=	-0.432E+08 N/m2
C	=	-0.280E+08 N/m2
D	=	-0.129E+08 N/m2
E	=	0.228E+07 N/m2
F	=	0.174E+08 N/m2
G	=	0.326E+08 N/m2
H	=	0.478E+08 N/m2
I	=	0.629E+08 N/m2

Figure 2.4 : Finite Element analysis on Cordierite cap piston assembly showing effects of hoop stress.

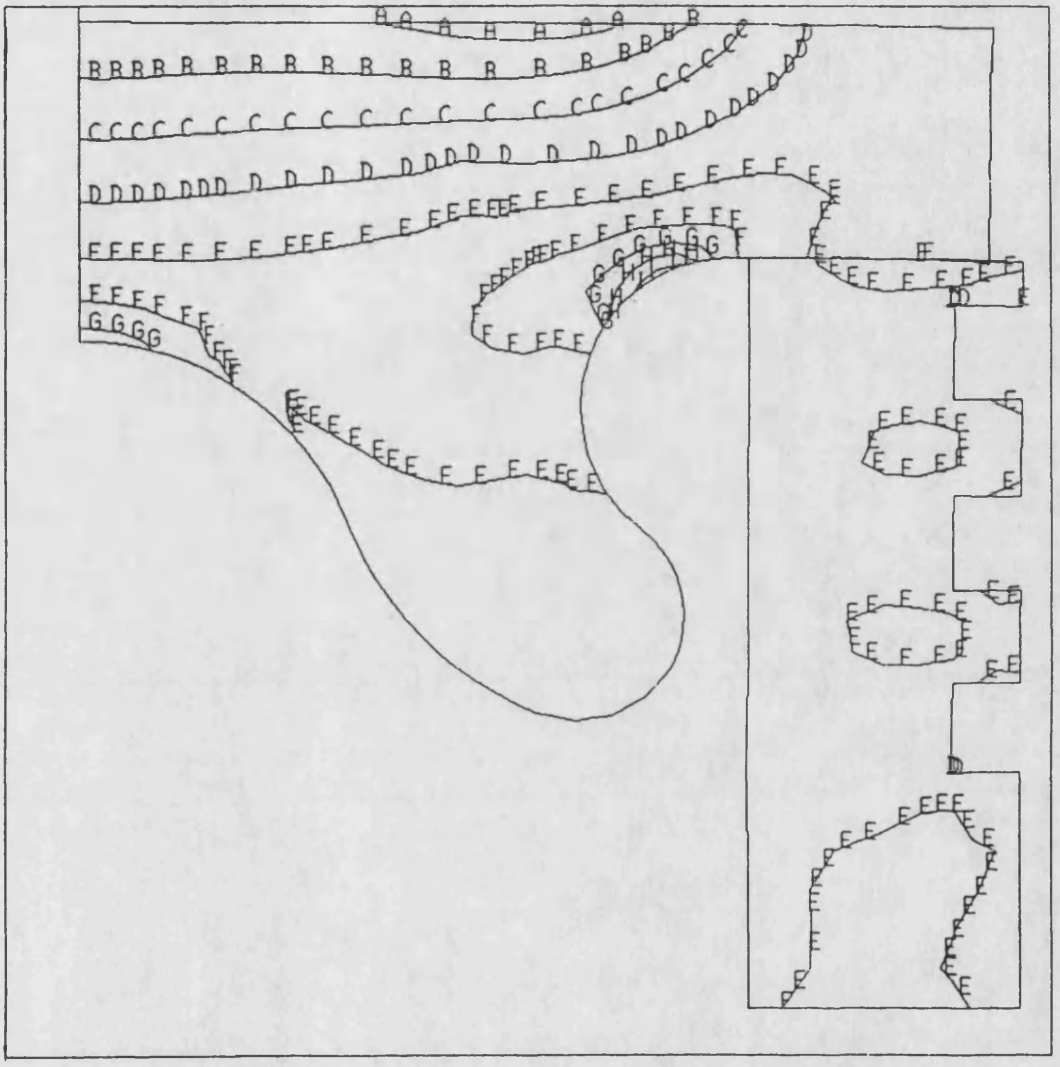

Maximum displacement	=	0.135 mm
Maximum radial stress	=	0.777E+08 N/m2
Minimum radial stress	=	-0.755E+08 N/m2
A	=	-0.670E+08 N/m2
B	=	-0.500E+08 N/m2
C	=	-0.330E+08 N/m2
D	=	-0.159E+08 N/m2
E	=	0.110E+07 N/m2
F	=	0.181E+08 N/m2
G	=	0.352E+08 N/m2
H	=	0.522E+08 N/m2
I	=	0.692E+08 N/m2

Figure 2.5 : Finite Element analysis on cordierite cap piston assembly showing effects of radial stress.

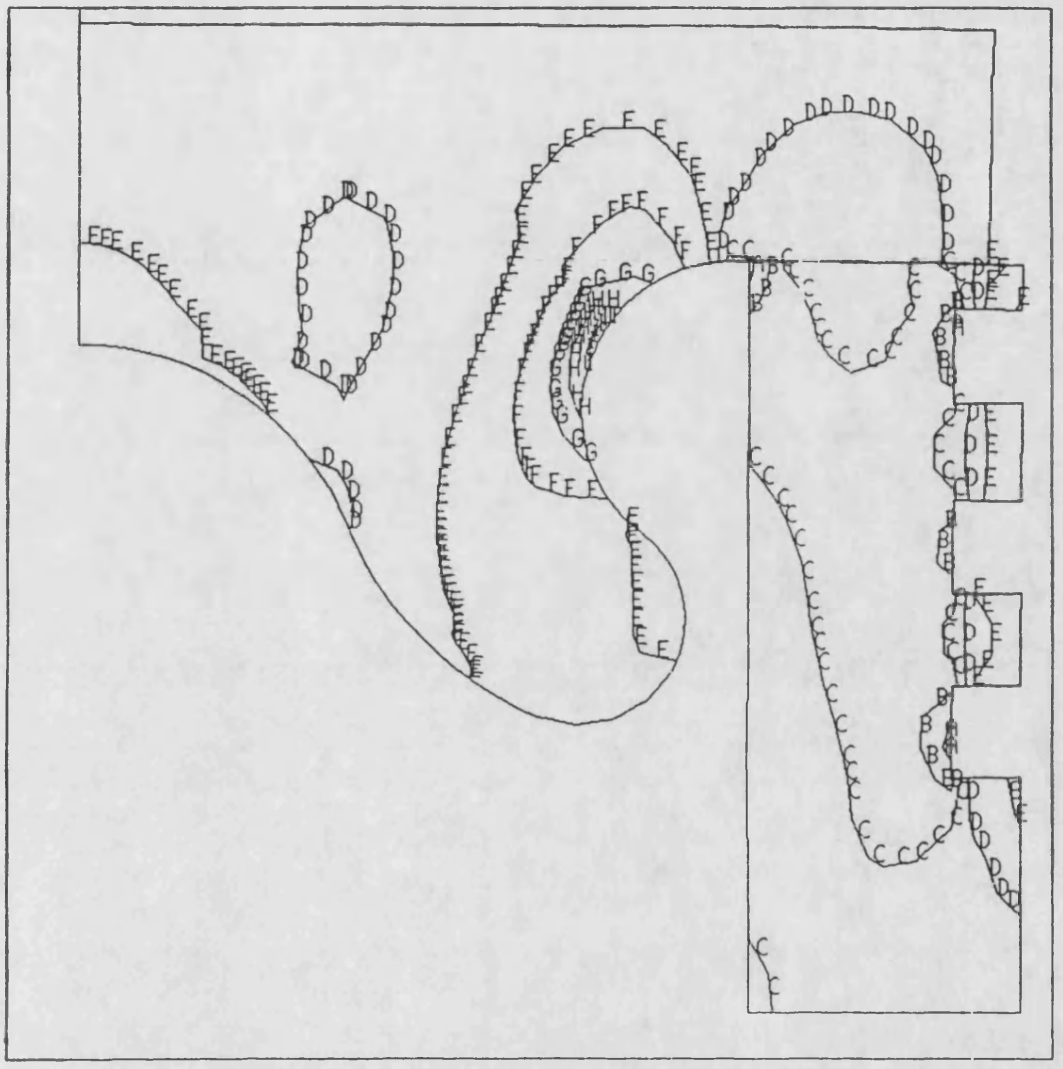

Maximum displacement	=	0.135 mm
Maximum axial stress	=	0.696E+08 N/m2
Minimum axial stress	=	-0.722E+08 N/m2
A	=	-0.643E+08 N/m2
B	=	-0.486E+08 N/m2
C	=	-0.328E+08 N/m2
D	=	-0.170E+08 N/m2
E	=	-0.129E+07 N/m2
F	=	0.145E+08 N/m2
G	=	0.302E+08 N/m2
H	=	0.460E+08 N/m2
I	=	0.617E+08 N/m2

Figure 2.6 : Finite Element analysis on cordierite cap piston assembly showing effects of axial stress.

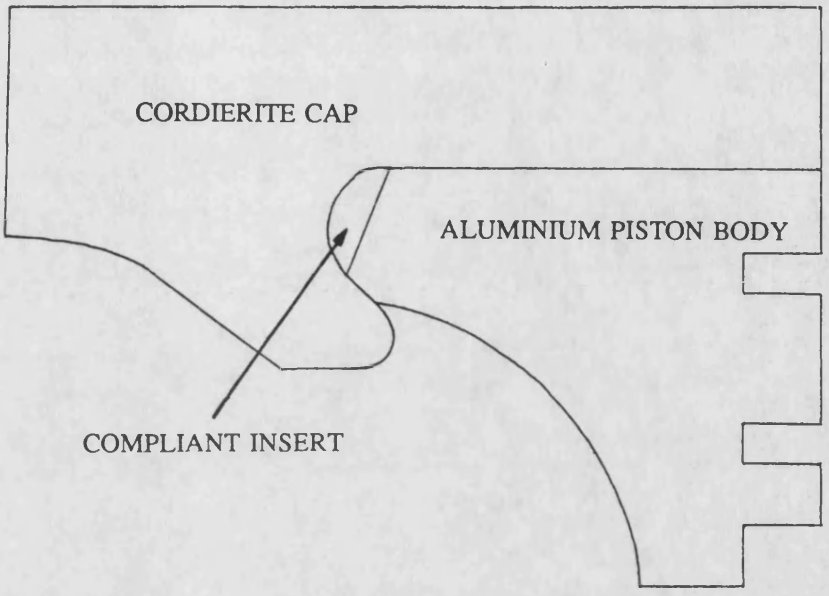

Figure 2.7 : Geometric outline of the revised design.

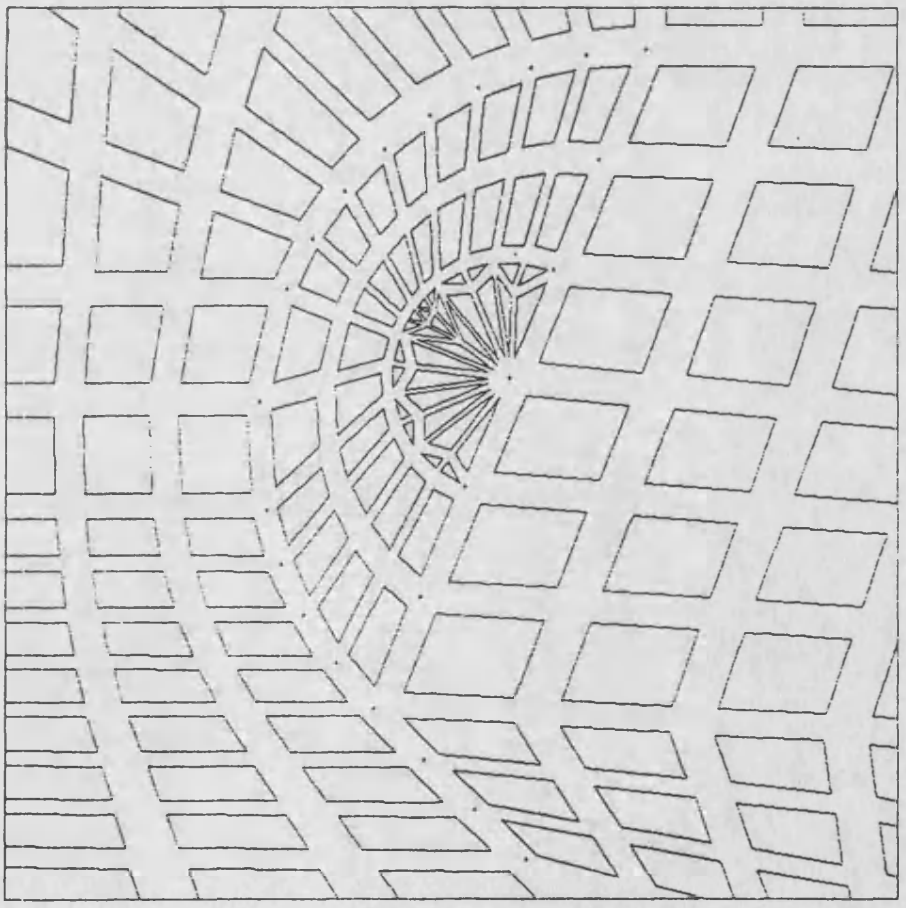

Figure 2.8 : Finite Element mesh for the compliant insert.

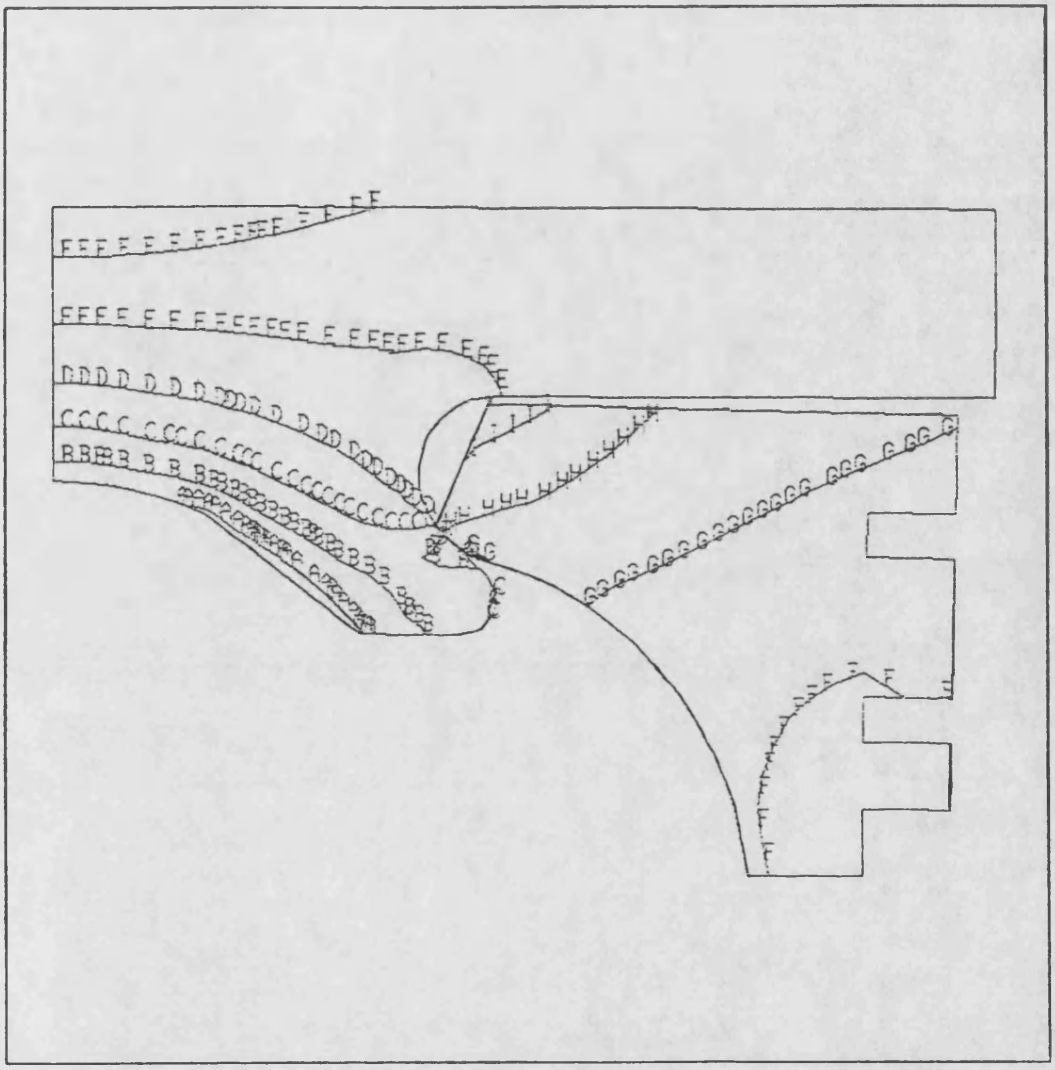

Maximum displacement	=	0.364 mm
Maximum hoop stress	=	0.307E+09 N/m2
Minimum hoop stress	=	-0.401E+09 N/m2
A	=	-0.361E+09 N/m2
B	=	-0.283E+09 N/m2
C	=	-0.204E+09 N/m2
D	=	-0.125E+09 N/m2
E	=	-0.468E+08 N/m2
F	=	0.318E+08 N/m2
G	=	0.110E+09 N/m2
H	=	0.189E+09 N/m2
I	=	0.268E+09 N/m2

Figure 2.9 : Finite Element analysis for a revised cordierite cap design showing effects of hoop stress.

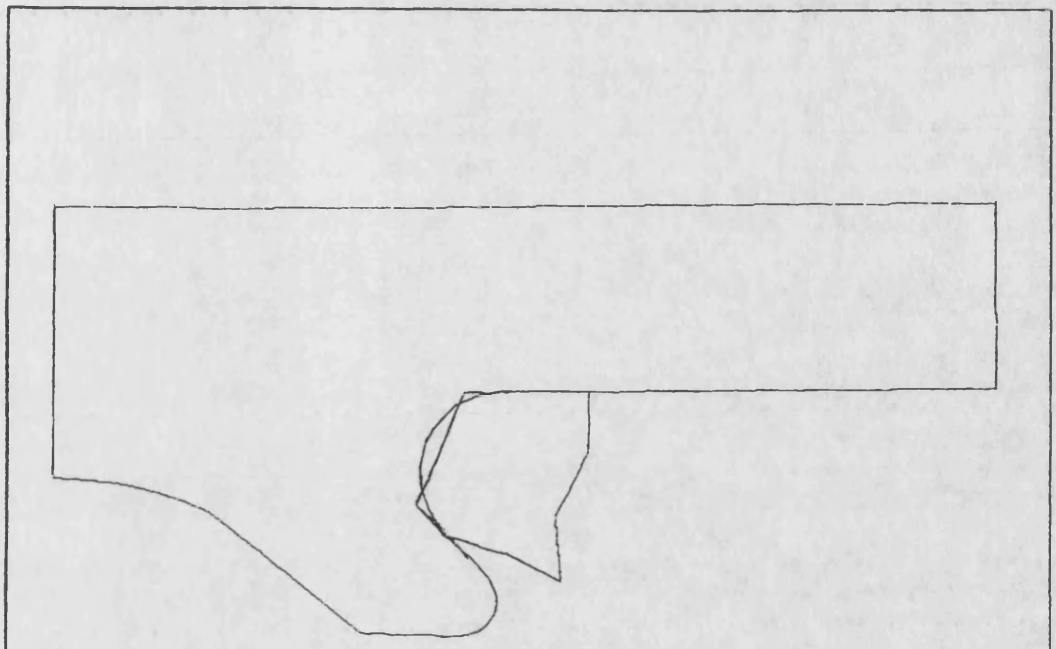

Figure 2.10 : Finite Element analysis for a revised Cordierite cap design showing displacement due to shrink fit assembly.

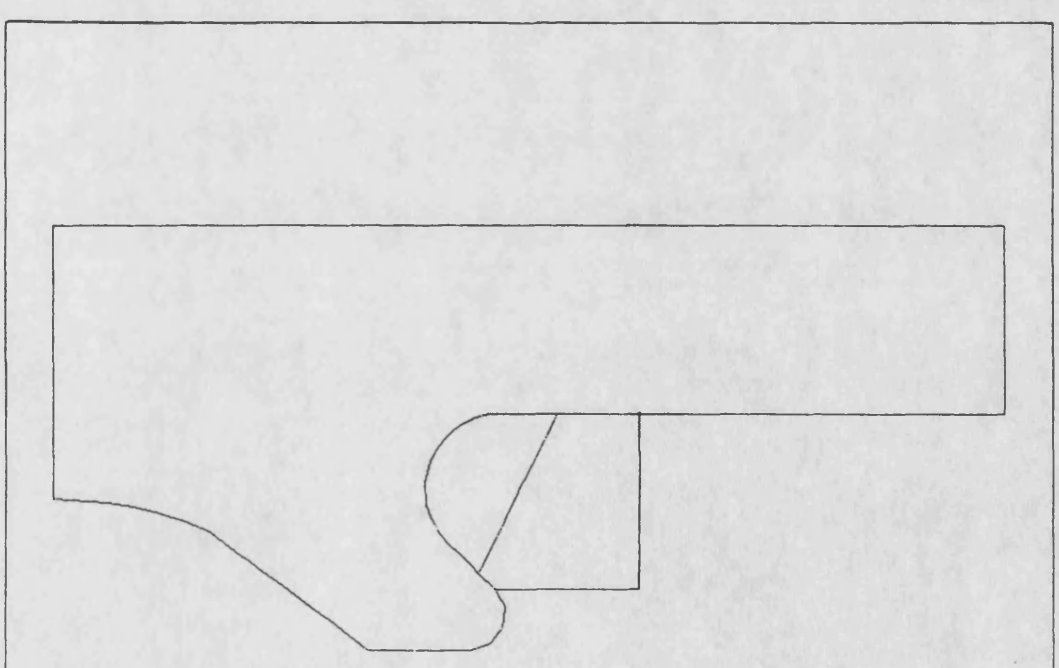

Figure 2.11 : Outline of the model hith revised smaller 45° interface.

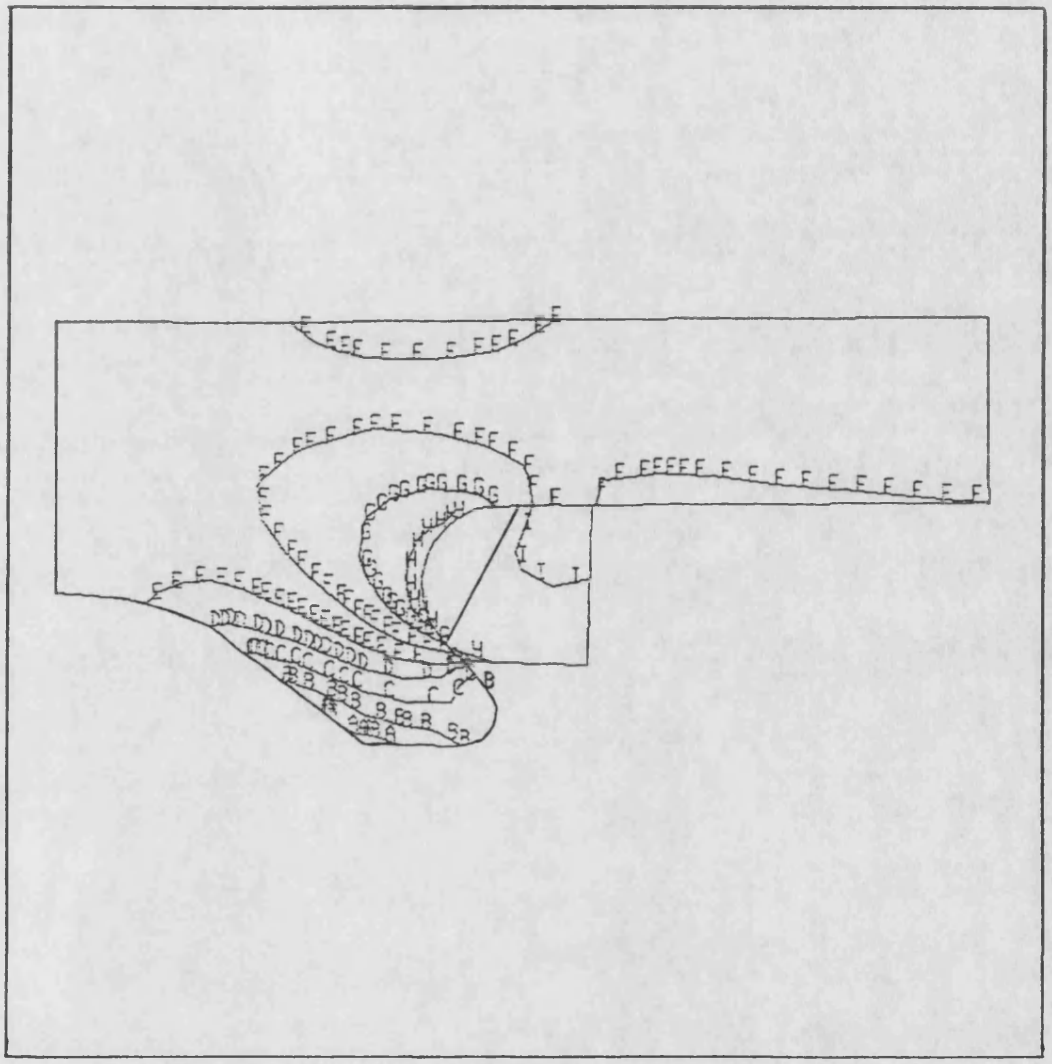

Maximum displacement	=	0.209 mm
Maximum hoop stress	=	0.125E+09 N/m2
Minimum hoop stress	=	-0.179E+09 N/m2
A	=	-0.162E+09 N/m2
B	=	-0.128E+09 N/m2
C	=	-0.944E+08 N/m2
D	=	-0.606E+08 N/m2
E	=	-0.268E+08 N/m2
F	=	0.703E+07 N/m2
G	=	0.408E+08 N/m2
H	=	0.746E+08 N/m2
I	=	0.108E+09 N/m2

Figure 2.12 : Finite Element analysis on revised cordierite cap piston assembly showing effects of hoop stress.

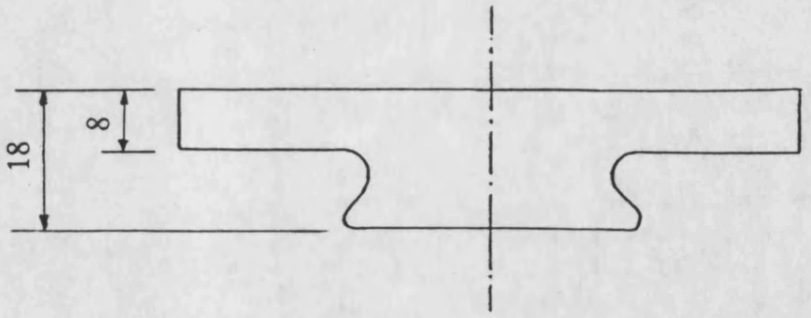

Figure 2.13 (A) : Half cross sectional view of Ford type F ceramic cap.

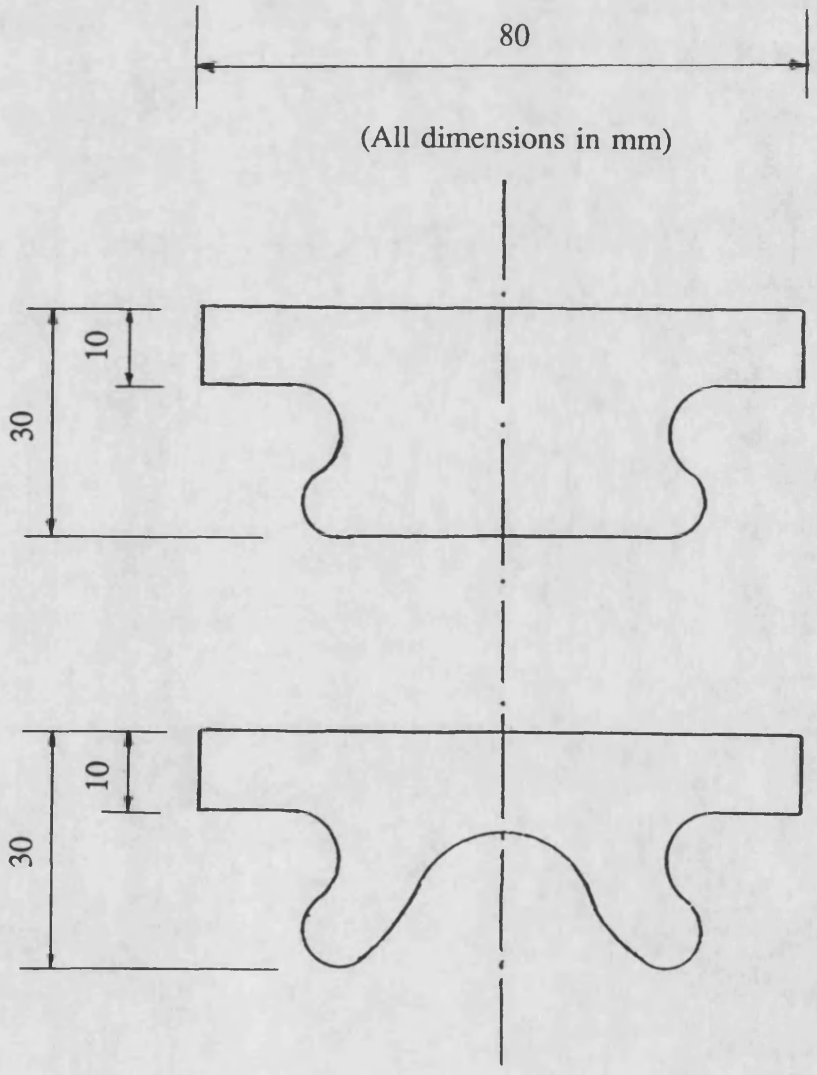

Figure 2.13 (B) : Half cross sectional views of the two Petter type P ceramic caps.

Figure 2.14 : Overall view of the three types of ceramic cap used relative to each other.

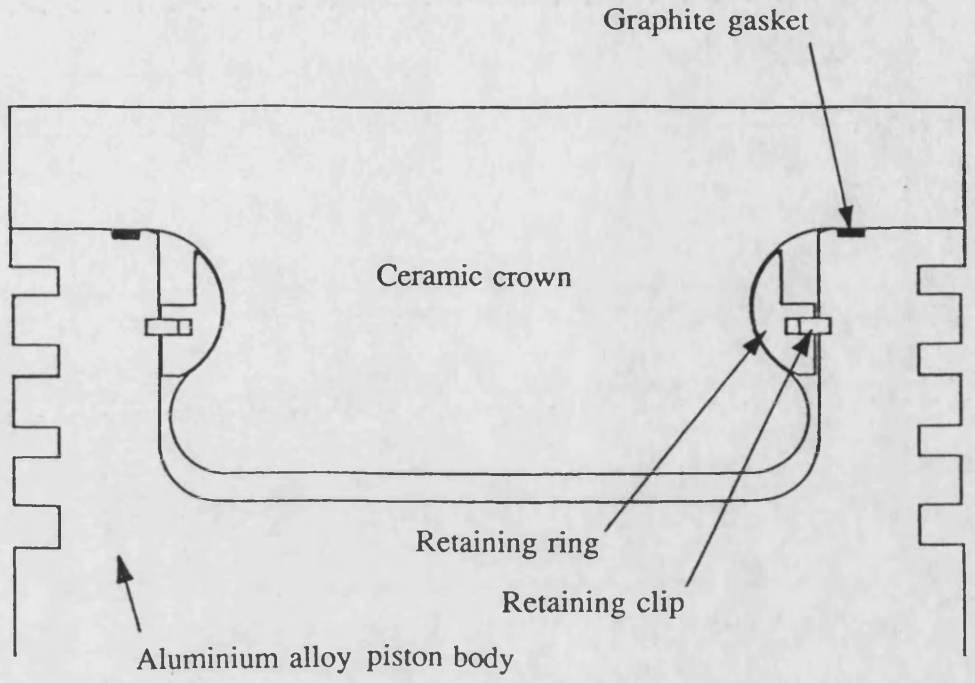

Figure 2.15 : half sectional view of mechanical cap attachment.

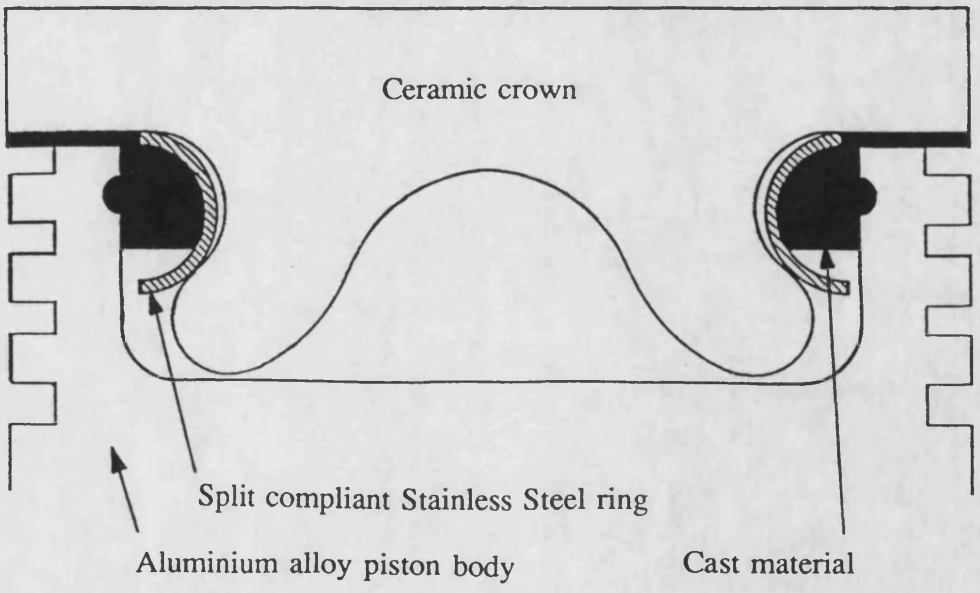

Figure 2.16 : Half sectional view of cast cap attachment.

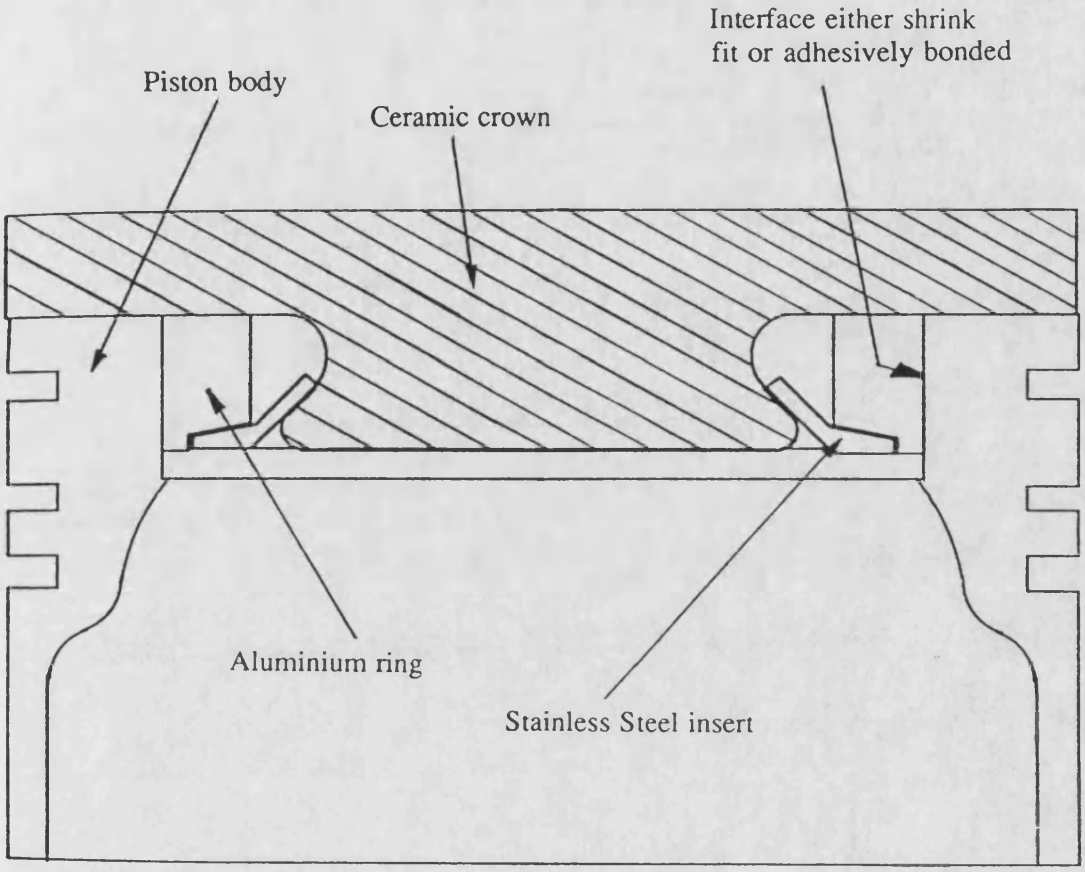

Figure 2.17 : Half sectional view of shrink fit or glueline cap attachment.

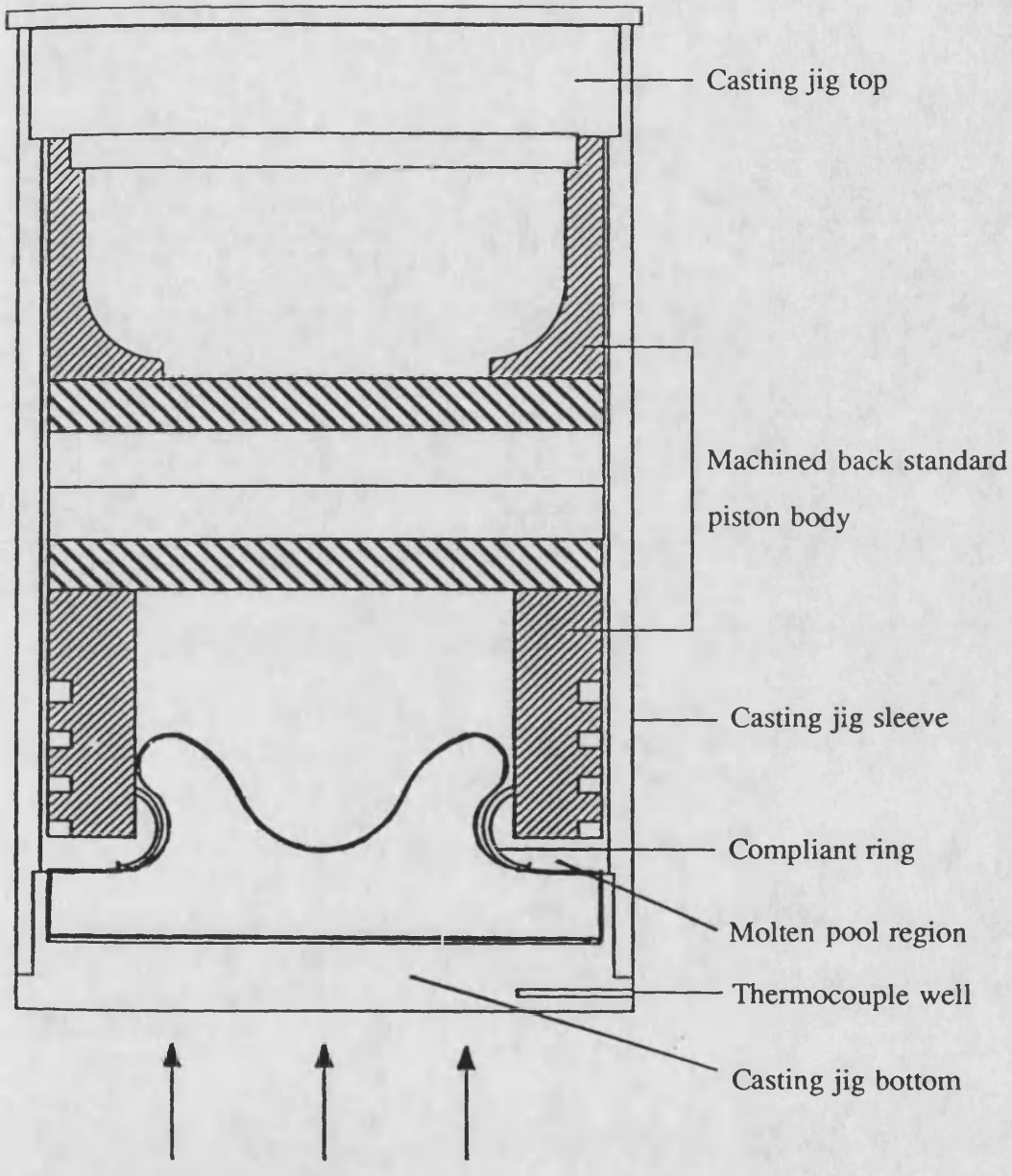

Figure 2.18 : Jig used to cast formed Ceramic caps into machined piston bodies.

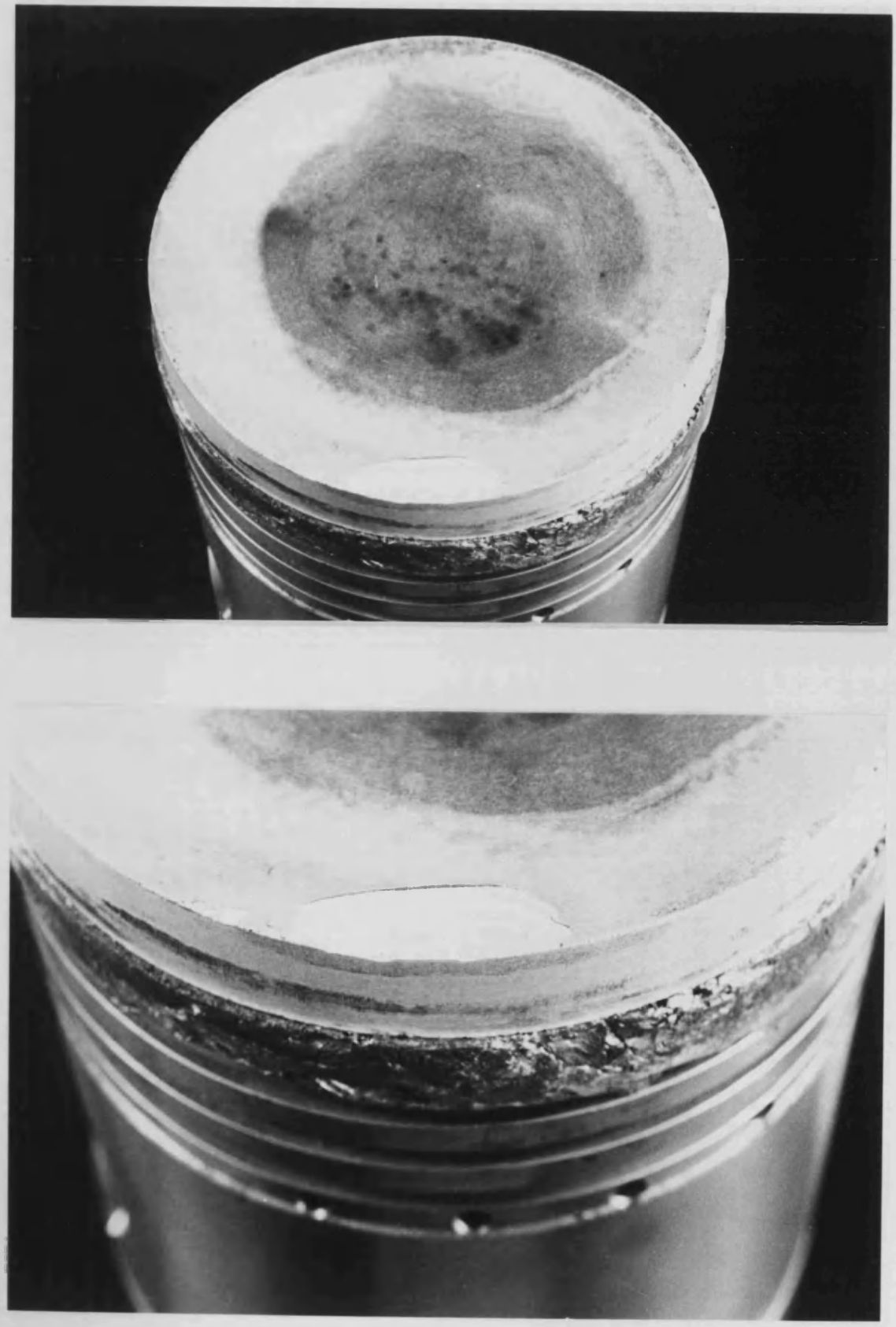

Figure 2.19 : The effects of incorrectly calculated filler material needed during the casting process.

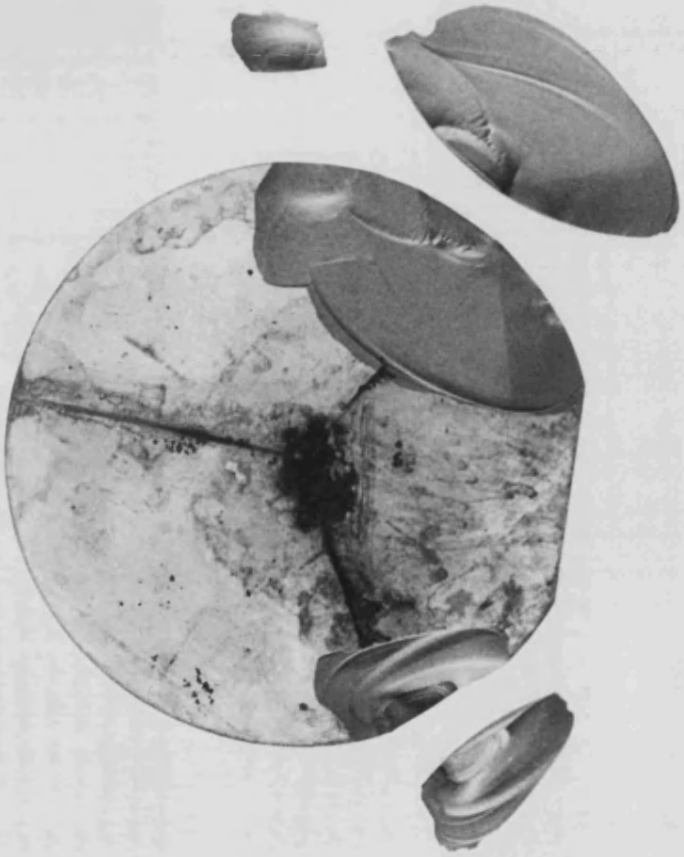

Figure 2.20 : The effect of an Oxy-Acetylene test on a Cordierite specimen.

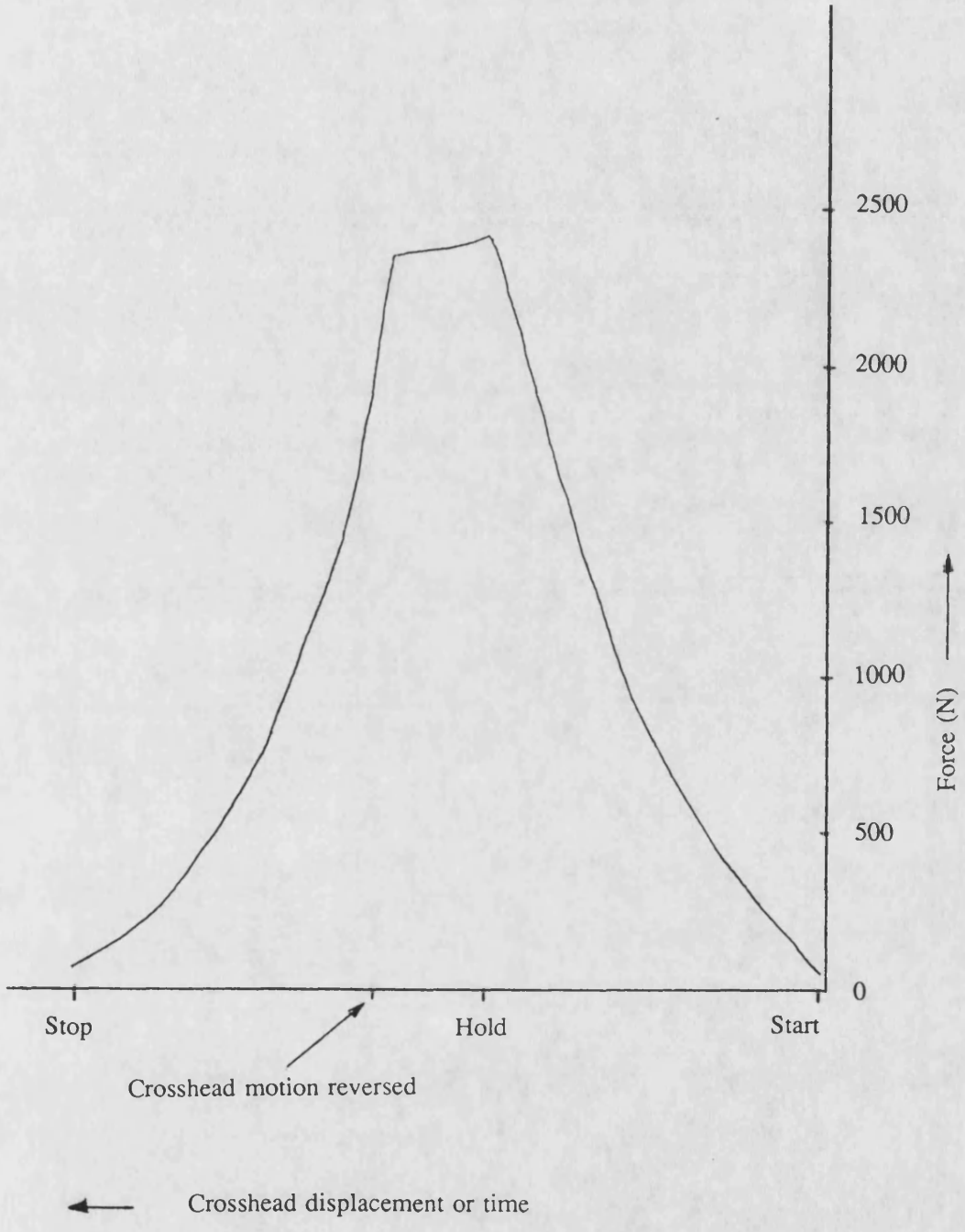

Figure 2.21 : The resuls of a tensile test on a piston assembly with a Cordierite cap.

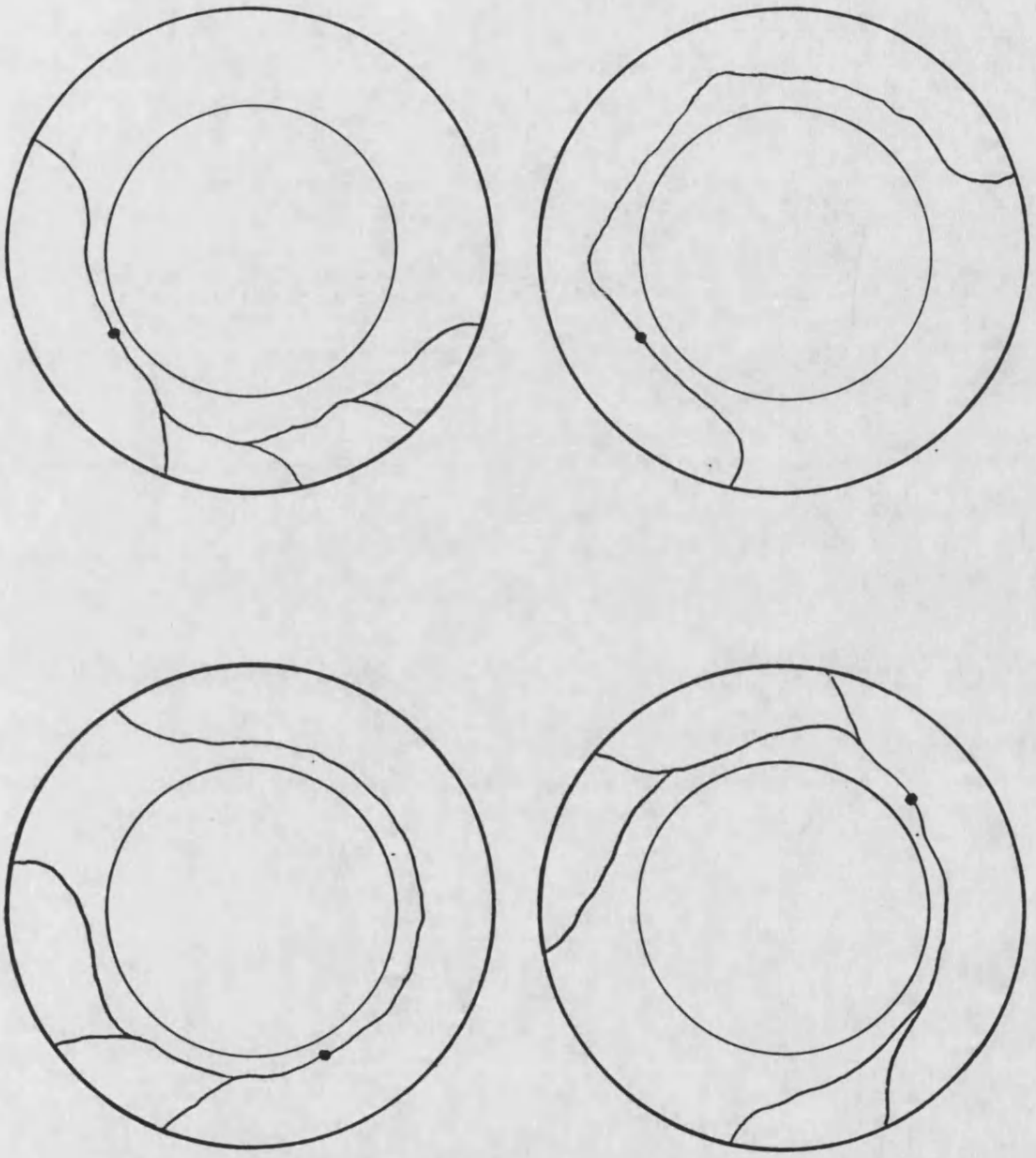

• Failure origin

Figure 2.22 : Sketch showing fracture patterns for Cordierite ceramic piston caps.

A) Surface inclusion bisected by failure crack (magnification 25x).

B) Partially dissolved Iron inclusion (magnification 72x).

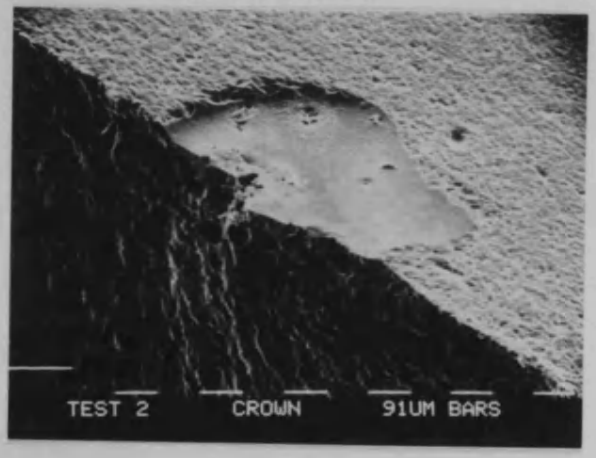

C) Foaming and bubbling inside and around inclusion (magnification 288x)

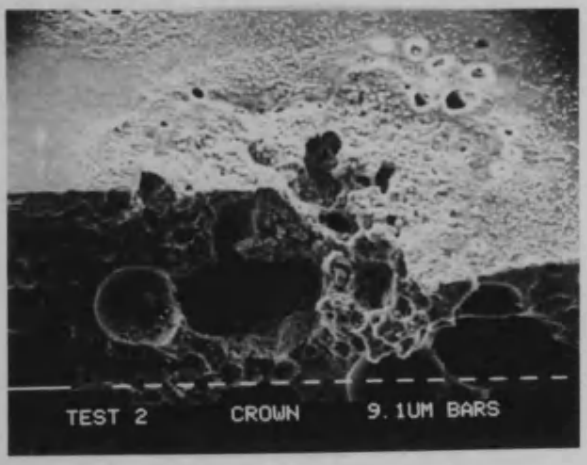

Figure 2.23 : Showing the result of a fracture due to an Iron inclusion.

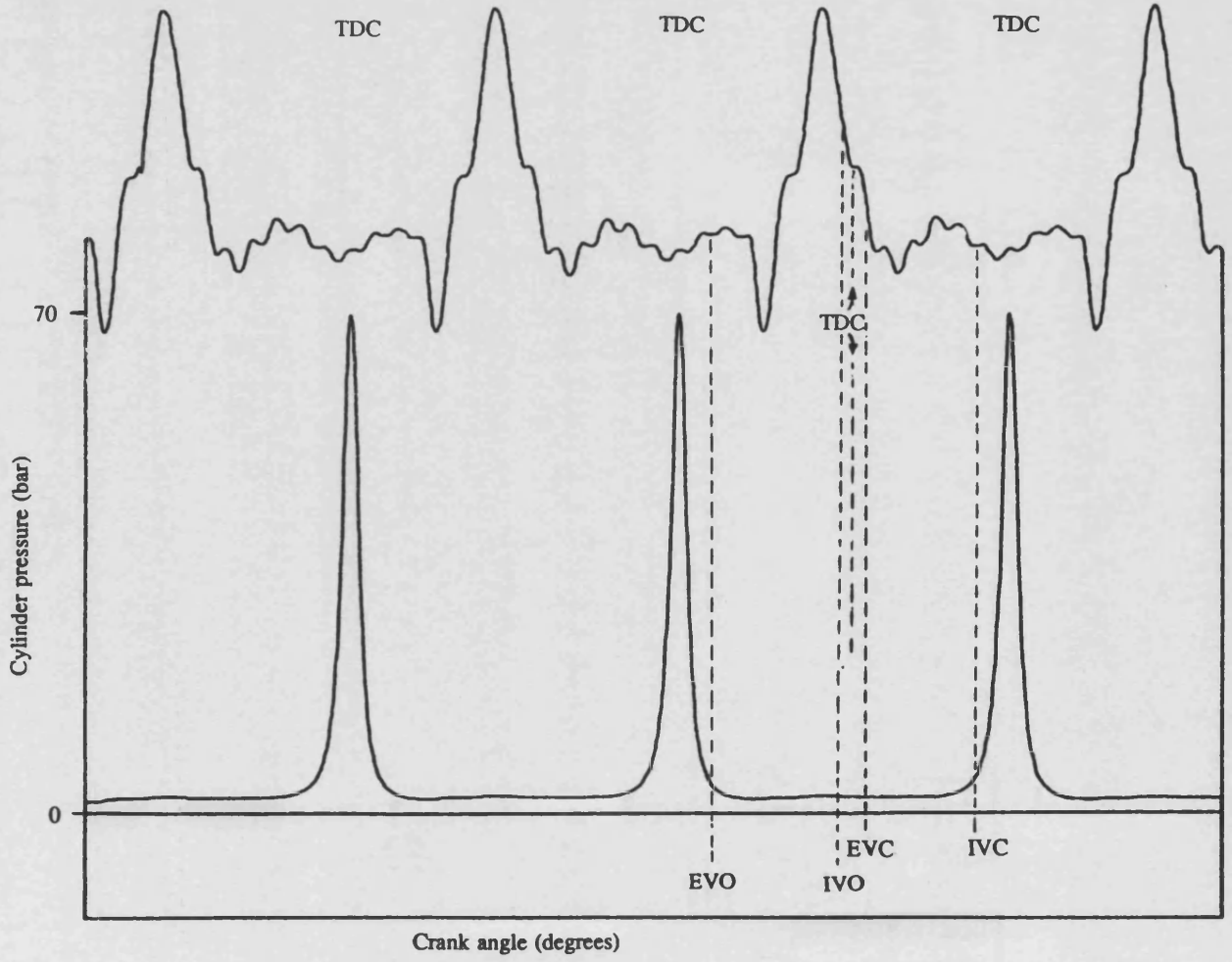

Figure 2.24 : Exhaust manifold and cylinder pressure traces for the simulation rig running at 1000 rev/min, 1.8 bar boost and 100°C inlet temperature.

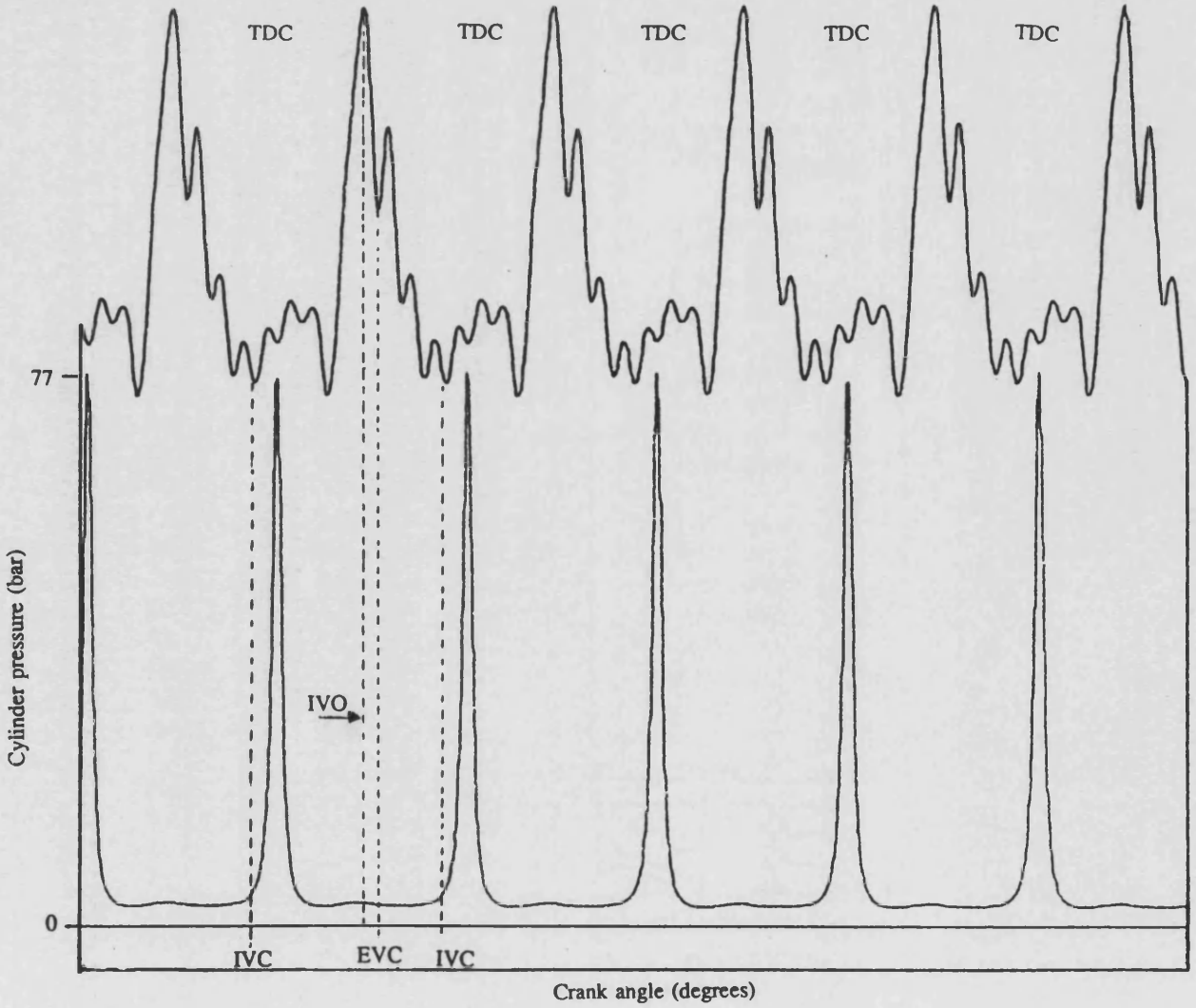

Figure 2.25 : Exhaust manifold and cylinder pressure traces for the simulation rig running at 1750 rev/min, 1.8 bar boost and 100°C inlet temperature.

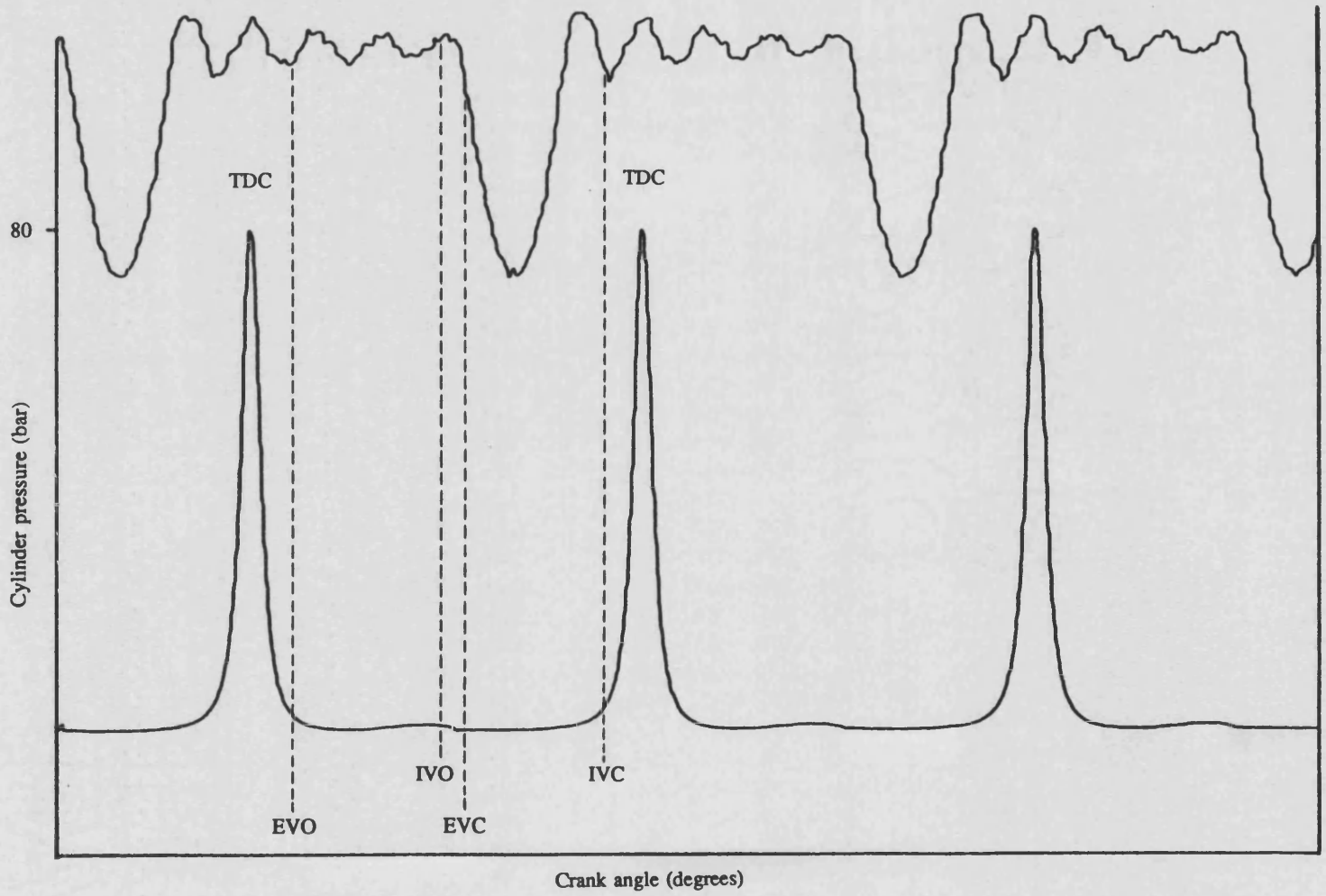

Figure 2.26 : Inlet manifold and cylinder pressure traces for the simulation rig running at 2000 rev/min, 1.8 bar boost and 100°C inlet temperature.

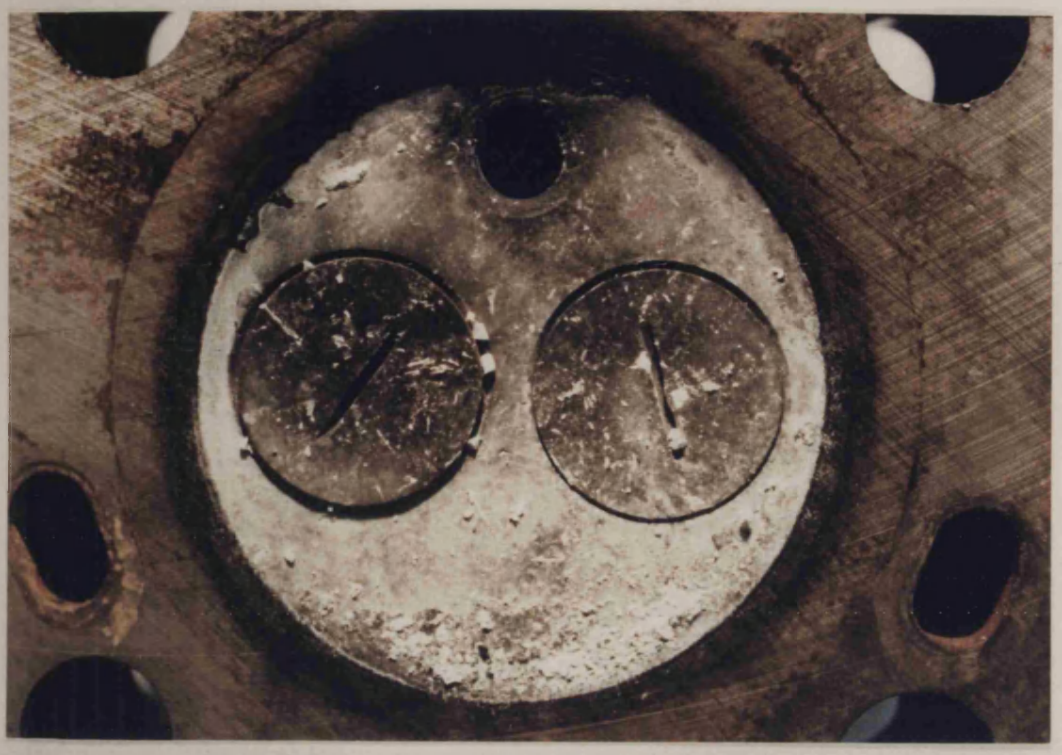

Figure 2.27 : View of cylinder head face and valves after failure.

Figure 2.28 : View of failed Cordierite piston cap in situ. (looking into bore).

Figure 2.29 : View of failed Cordierite piston cap in situ. after removal of debris (looking into bore).

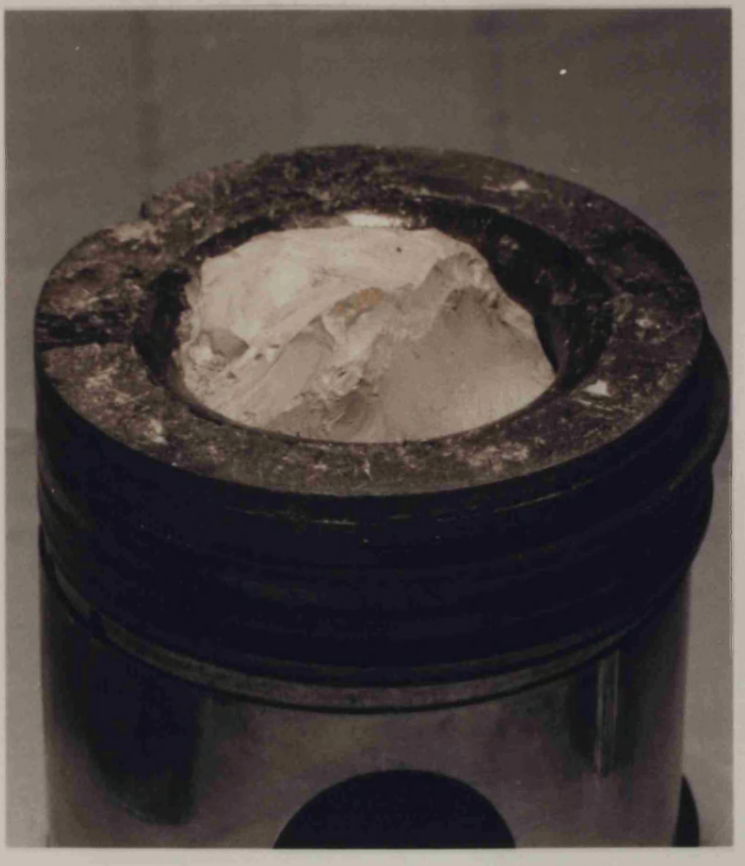

Figure 2.30 : Side view of failed piston.

Piston number	Code	Fixing method	Comments
1	PAC1	Mechanical	Difficult to assemble.
2	PBC2	Cast in	Ran in simulation rig for 60 hours, failed in firing rig after ½ hour running at 1000 rev/min 75% load.
3	FAC3	Shrink fit	Subjected to tensile test in Instron machine.Held up to 1200N equivalent to 4000 rev/min.
4	FAC1	Shrink fit	Bumping clearance failure.
5	FAC2	Shrink fit	Failed in engine almost immediately after start up.
6	FAL1	Glueline	Failed at light load after 30 minutes in firing rig.
7	PBC3	Glueline	Covered over 60 hours in firing engine reaching speeds up to 1500 rev/min at full load.Removed for inspection to find propagation of hairline crack.
8	FAC4	Glueline	Ready for testing.

Figure 2.31 : Showing the piston combinations used.

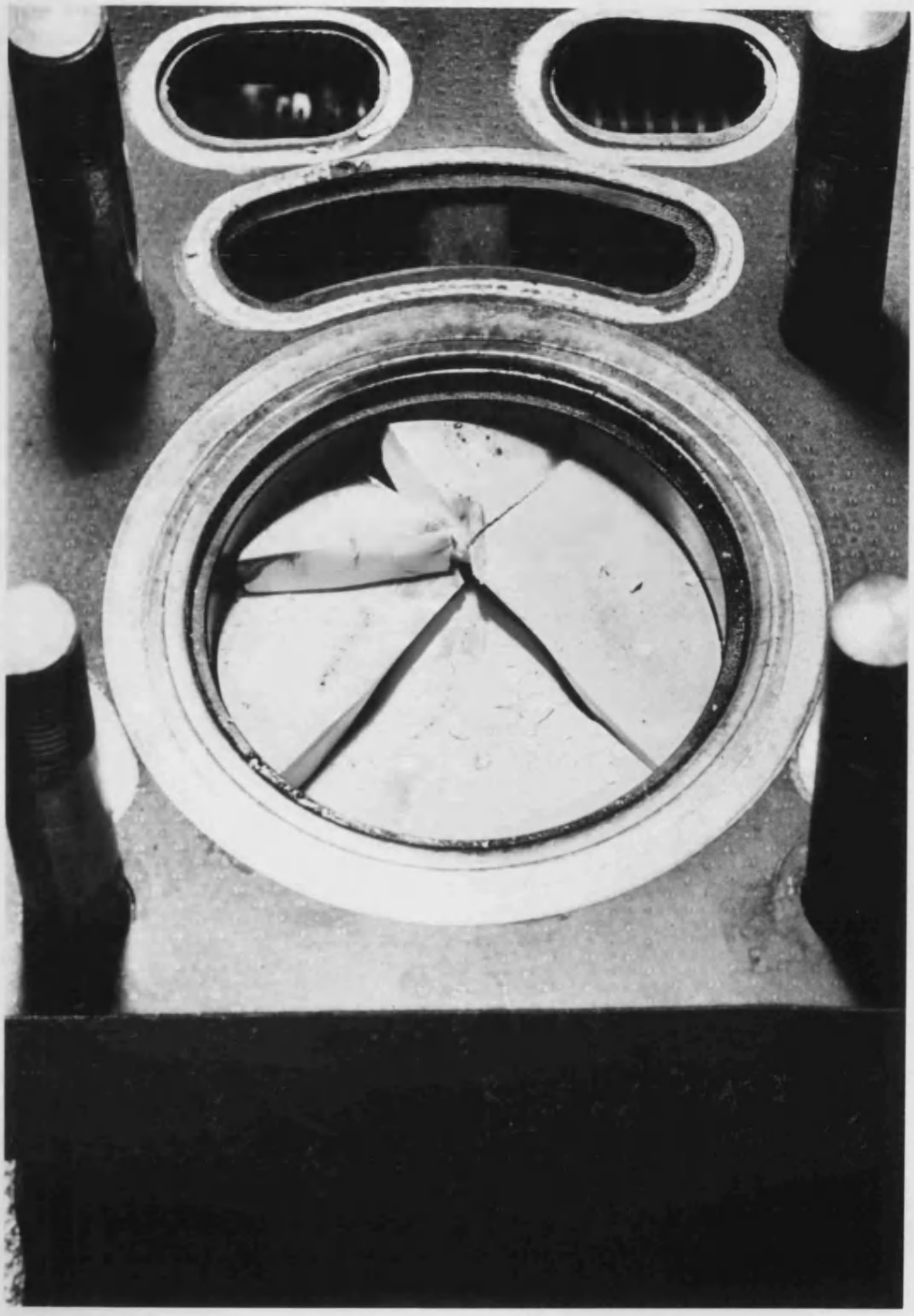

Figure 2.32 : Bumping clearance failure on Cordierite cap.

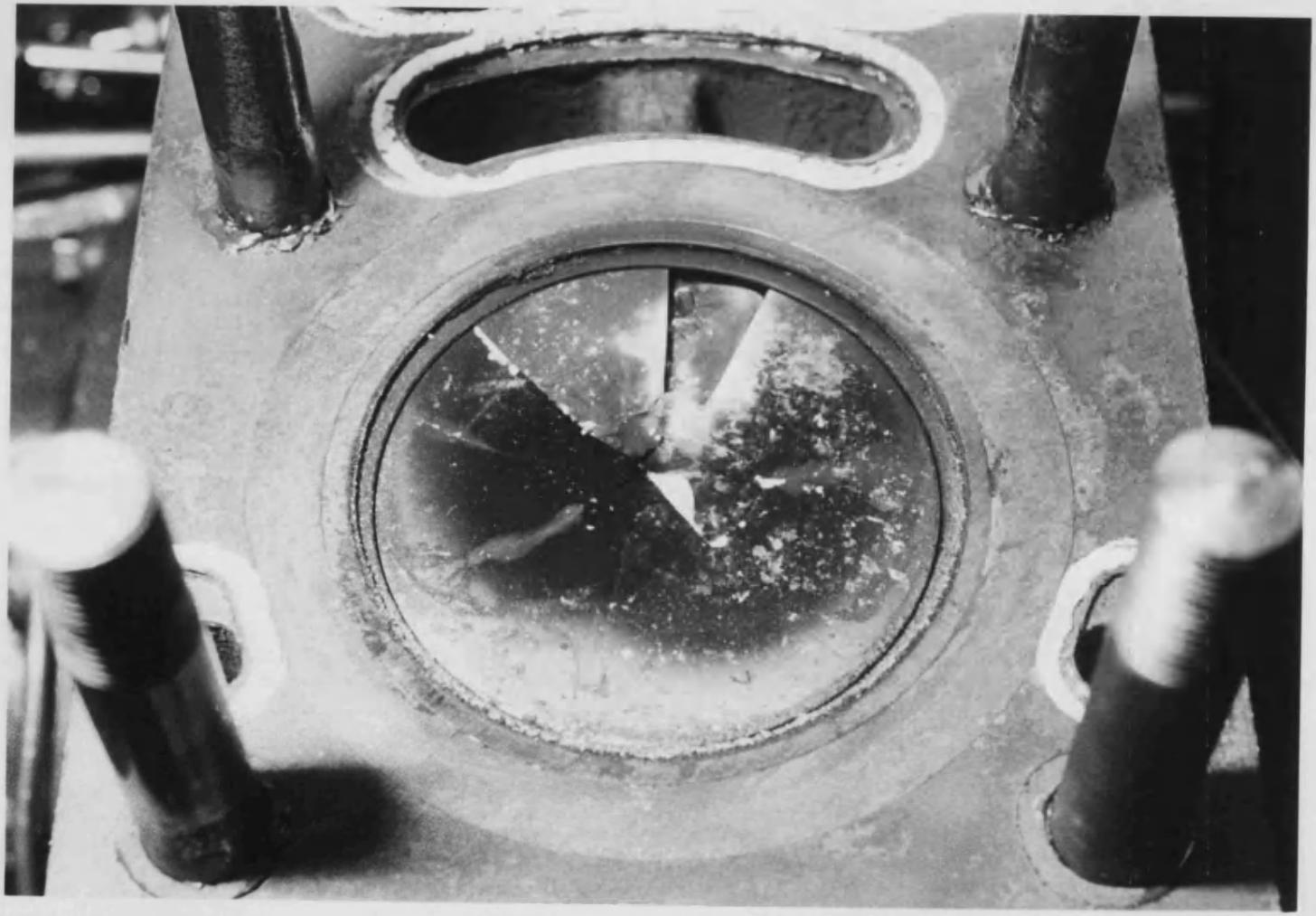

Figure 2.33 : Failed LAS crown in situ.

Figure 2.34 : Piston assembly with Cordierite cap as extracted from the firing engine.

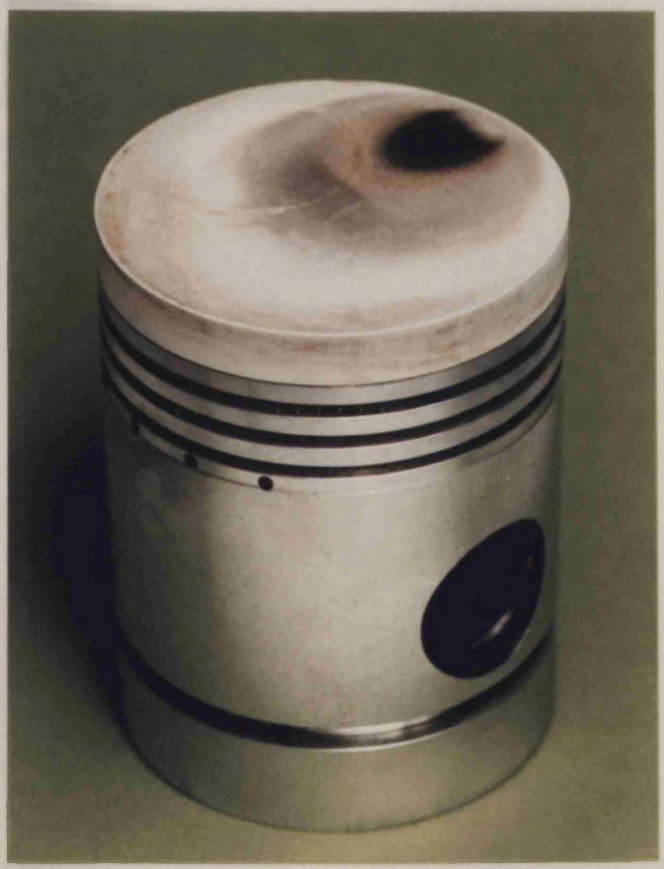

Figure 2.35 : Cleaned piston assembly with Cordierite cap after running in the firing rig.

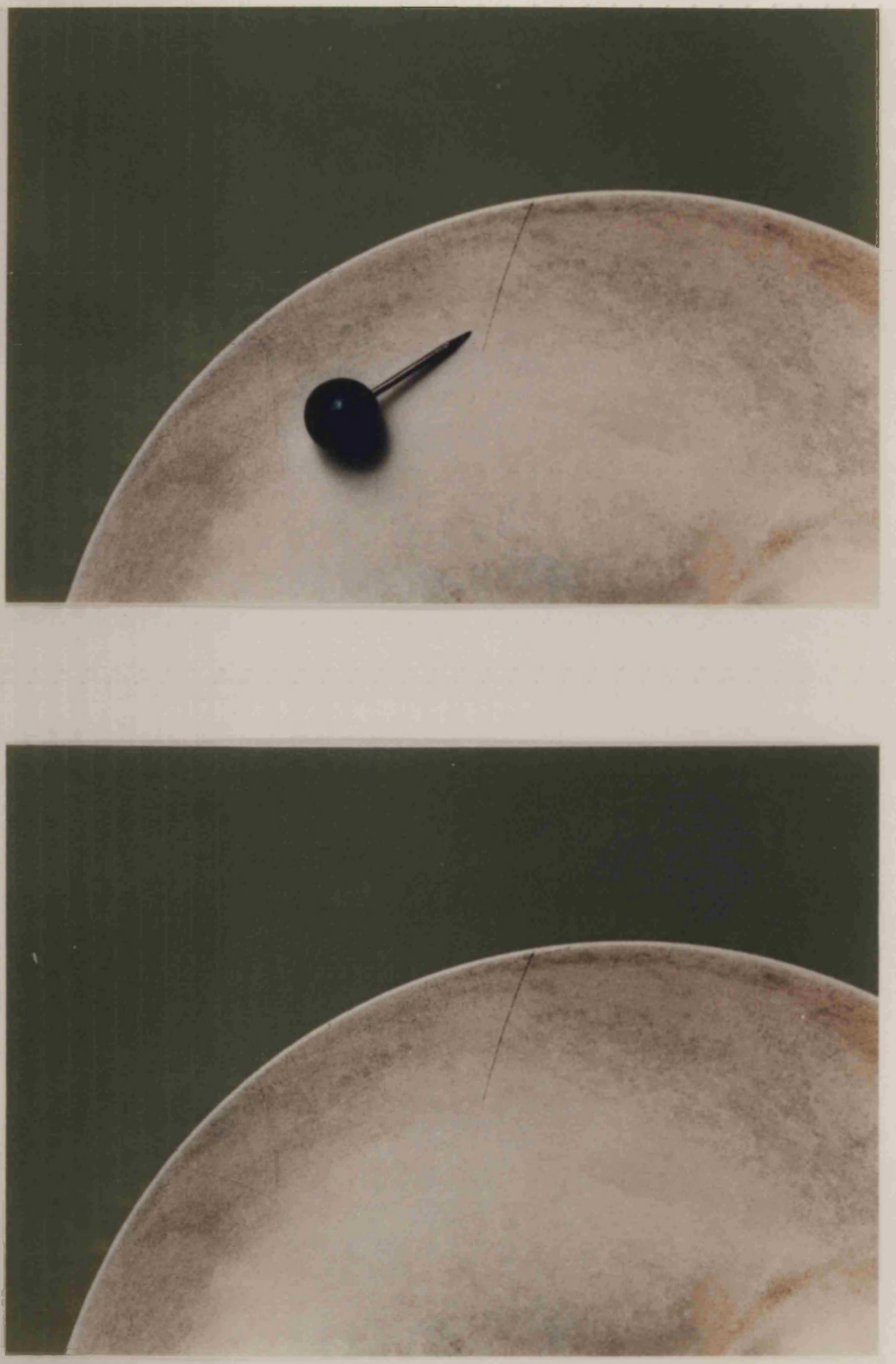

Figure 2.36 : Close-up view of a hairline crack in the cordierite cap.

Figure 2.37 : Ford 1.6 litre piston assembly using a Cordierite cap.

CHAPTER 3
THE SIMULATION AND FIRING ENGINE RIGS

3.1 Introduction

This chapter is divided into two parts, the former (sections 3.2 and 3.3) dealing with the motored engine simulation rig and the latter (section 3.4 and 3.5) with the firing engine rig.

The simulation rig was inherited from a previous research by Manton (ref. 29) which required a single cylinder engine of high reliability and versatility to be modified in such a way that it could simulate as far as possible the in-cylinder conditions of a diesel engine without the process of combustion.

Manton's work involved completely redesigning the cylinder head to facilitate stationary mounting of ceramic components within the new design to minimise the level of secondary damage sustained in the event of a failure.

Whilst Manton was using the simulation rig, Cole (ref. 19) had already set up a firing version of that engine (also used by the author, see ref. 30) for work based on insulated pistons. This same firing engine used by Cole was also used by the author as the basis of the firing rig. However for a number of reasons it was converted from direct injection (DI) to indirect injection (IDI) operation.

The engine chosen by Cole and Manton was a Petter PHIW direct injection single cylinder four stroke 650cc engine. The difference between this D.I. engine and its IDI counterpart, the AV1, was confined to the cylinder head, piston and liner.

At the outset of this research, Alexander (ref. 18) converted both existing engines to the AV1 design, thus having to change only cylinder heads, pistons and liners. This

AV1 design was considered more suitable than the PHIW configuration due to its flat topped piston. A flat topped piston was preferred in order that ceramic shapes could be produced more easily and with less chance of failure due to high stress concentration points, both during production and running.

Having effected the conversions, the simulation and firing engines were now considered to conform to the standard AV1 design except for obvious differences, such as fuelling in the case of the simulation rig and bolt-on instrumentation in both cases.

When the author joined the research team, the simulation and firing rigs had already been converted to IDI operation but had not been commissioned or refined to their final form. The simulation engine was intended to be a proof test rig for ceramic piston assemblies prior to their operation in the firing engine.

3.2 Description of Simulation Rig

Figures 3.1 and 3.2 show the overall view of the simulation rig layout while fig. 3.3 shows it in schematic form. The rig is based on a development of the Kamo and Bryzik design (ref. 6). The single cylinder IDI engine of 80 mm bore and 110 mm stroke was chosen for reasons highlighted earlier, especially for its flat top piston arrangement. Apart from the compression ratio of 25:1 the engine was completely standard. Detailed specifications of the AV1 engine are shown in table 3.1. The original Kamo and Bryzik design concept was developed a stage further by introducing an air pre-heater to achieve peak cylinder temperatures, under motored conditions of the order of 1200K, combined with peak pressures of the order of 70 to 80 bar to simulate both thermal and mechanical loading conditions for a firing engine.

The rig had the capacity to achieve speeds up to 2000 rev/min albeit for short periods only, due to high wear rates of driving belts at elevated speeds.

The airflow circuit of the rig was designed as a closed system where air was drawn from a large volume receiver into the engine via an air heater. The exhaust air from the engine was then pumped back into the air receiver to go through the engine again.

Inlet and exhaust pressures of up to 5 bar were achievable through an accurate pressure regulating valve, downstream of a moisture absorbing filter. The external air supply needed for this was standard "shop air" available in the test cell. Although 5 bar was available, the maximum pressure used was only 1.8 bar (abs). A pressure relief valve (item 7 in fig. 3.3.) ensured the system did not overpressurise.

The inlet temperature was also variable up to 200°C to provide high in-cylinder temperatures. This was achieved using an external electrical heater (fig. 3.3) connected to a thermostatic controller to ensure the temperature was kept constant, at a predetermined level, during operation.

The engine was cooled using a closed water system consisting of a reservoir, pump, immersion heater and heat exchanger. With this system, rapid steady state operation was possible at start up. The cooling of the heat-exchanger was from an external water supply drawn from a very large reservoir.

Drive to the engine was from a three phase electric motor with star and delta switching for easy starting. The motor had a rated power of 4 kw at 1420 rev/min. The manually operated variable speed belt drive system used to motor the engine proved to be severely underdesigned for the application. At the time of designing the rig, Manton (ref. 29) never intended the engine speed to exceed 700 rev/min. The change in engine construction and the nature of the research meant that speeds up to 2000 rev/min were now needed. The weak link in achieving these speeds was the variable pulleys which could neither sustain speeds over 1400 rev/min nor transmit the power needed at elevated cylinder pressures. Although it was possible to reach speeds of 2000 rev/min and 1.8 bar (absolute) inlet pressure at 100°C, the belts soon deteriorated and the pulleys chattered, resulting in "fretting" of the bearings. After running the rig at these conditions for only 45 minutes the belts had to be changed

and pulley bearings remachined.

3.3 Simulation Rig Instrumentation

In the interest of longevity and minimal damage, the rig was instrumented in a manner whereby most monitoring devices were connected to an overall system shutdown circuit.

To install a pressure probe into the engine, a means of accessing the cylinder was necessary. As this engine was never intended to fire, the prechamber could be sealed by an instrumented plug (fig. 3.4) which was designed by Alexander (ref. 18) to carry both a pressure transducer and a heat flux probe. The plugging of the prechamber increased the engine compression ratio to 25:1 thus making possible peak cylinder pressures of up to 80 bar. A Kistler 6121 pressure transducer was used to observe the cylinder pressure. Section 3.5.10 deals with the transducer and associated equipment in full detail.

Inlet and exhaust pressures were monitored by a Farnell SA, high gain, strain-gauge, pressure transducer. As there was only one transducer, either exhaust or inlet pressure could be monitored at any one time, but not both. The inlet and exhaust pipes were modified by T pieces to enable the pressure transducer to be mounted on either pipe. A dummy plug was used in the pipe which was not being monitored. The disadvantage of this system was the need to stop the engine to monitor the plugged line.

The transducer was neatly connected to the control panel (fig. 3.5) the output of which was taken directly to the digital storage scope.

Oil pressure and water coolant temperature were measured by gauges with inbuilt cut outs to trigger the failsafe circuit. The automatic shutdown circuit was to prove a useful device in that the rig could not be started until every switch was activated. The

circuit included the following shutdown facilities:

1. low engine speed
2. high inlet air temperature
3. low engine oil pressure
4. high cooling water temperature
5. low coolant water flow
6. low coolant water level (primary circuit)
7. low coolant water level (secondary circuit)
8. spare

If a failure was indicated by an open circuit, then the power to the electrical motor would be cut. The failure detection panel (fig. 3.5) would then indicate exactly which of the eight possible circuits caused the shutdown.

It was possible to override any of these failure detection channels so that spurious signals caused by faulty switches could be ignored. This facility was also used during start up to override the low speed and low oil pressure cut outs.

NOR gates were used to combine inputs in the desired fashion as can be seen in figures 3.6 and 3.7. If any of the switches (S) in fig. 3.7 were opened, the accompanying input would be ignored. Light emitting diode (LED) displays, (F) and (D), were used to indicate whether any of the circuits had failed or been overridden. Figure 3.5 shows the arrangement of diodes (F) and (D) above and below the switches respectively.

A latching relay was used to ensure that a failure would stop the motor until the circuit was manually reset. The relay could then be reset with a switch mounted on the control panel (see fig. 3.5). If the 12 volt power supply to the detection circuit failed then the input to the electrical motor would also fail, and the motor would stop. Similarly, if the three phase supply failed, the motor would only restart if it was manually switched on.

3.4 Description of the Firing Rig

Figure 3.8 shows the engine and associated ancillaries as they appear in the test cell, and figure 3.9 shows the overall layout in schematic form. The rig was based on the Petter AV1 single cylinder IDI engine, details of which are shown in table 3.1. The firing engine was mainly used in non-standard operating mode for reasons highlighted in Chapter 2. The deviations from standard operation are shown in table 3.2.

3.4.1 Engine Loading

A DC compound wound dynamometer with trunnion mountings was used as a means of loading the engine, and the current generated from it was directed to a series of water heating elements. The ability to use the dynamometer in "reverse", i.e. as a motor, meant that it could be used as a means of starting the engine thus eliminating the standard starter motor. The torque measuring system is described in section 3.5.2.

3.4.2 Inlet Manifold and Associated Components

Figure 3.10 shows a schematic view of the whole of the "induction system", which can be used for both naturally aspirated and boosted conditions.

Under naturally aspirated conditions, the pipework is disconnected at point A and filtered fresh air is drawn in from the test cell. When running under boost, the whole set up is used as shown in fig. 3.10 without the break at A. For this case, compressed air from the main laboratory compressor is supplied at a constant pressure of 5.3 bar. To maintain a given pressure within the manifold, a pressure regulator and dome valve is used (B in fig. 3.10). Boosted conditions also require the inlet air to be at elevated temperatures. This is done by passing the compressed air through a heater (H in fig. 3.10) which raises the air temperature to a preset level. The heater consists of conventional domestic cooker elements housed in a stainless steel casing and regulated by a proportional /integral/differential temperature controller via a thyristor switching

unit. To prevent the heater casing from overheating on engine shutdown, the power to the elements is switched off for a short period prior to stopping the engine, thus allowing cooling of the heater system by the flow of cool compressed air into the engine.

The air receiver (R in fig. 3.10) is a necessary item in air flow measurement for a single cylinder low speed engine. Without it, the pulsations at the inlet manifold would make flow measurement of the air highly inaccurate. A "damping" effect is therefore necessary; this is obtained with the large receiver making accurate measurements at the orifice plate (O in fig. 3.10) possible.

3.4.3 Exhaust Manifold and Associated Components

The exhaust system is designed in much the same way as the induction system with the obvious exception of the heater. Exhaust back pressure is controlled with the aid of a 25mm diameter gate valve, located downstream of the relatively smaller damping receiver. Unlike the induction system, however, the same set-up is used for either naturally aspirated or boosted conditions, the gate valve being wide open for naturally aspirated operation and partly shut under boosted conditions. The design of the exhaust system was not found to be wholly satisfactory as the 90° and 180° bends in the pipe immediately before the receiver itself set up undesirable pressure reflections.

3.4.4 Fuel System

The fuel system is a very simple one in that the light diesel oil (class A1, (BS141A), measured s.g. 0.8) is supplied to the tank in the test cell from the main fuel store. Fuel from the tank is gravity fed to the on-engine fuel filter and pump. The rack has two control levers attached to it, one for fine adjustment and another for rapid fuel cut off in the case of emergency engine shutdown. The fine adjustment screw opens or closes the rack by discrete amounts making accurate fuelling control possible to

establish a given speed or load.

3.4.5 Cooling System

The cooling system may also be classed as an initial preheating system in that it contains a 3 kw heating element which serves as a means of preheating the engine prior to starting up. This greatly reduces warming up time and enables tests to be carried out more rapidly.

The system consists of a two stage circuit incorporating a closed primary circuit cooling the engine and a secondary circuit cooling the primary circuit (fig. 3.11). The primary circuit is supplied by an SMC Commodore pump and controlled by a 1" diameter needle valve. When possible, the coolant water flow is kept to a minimum, thus maximising the coolant temperature differential across the engine. Coolant flow rates below the minimum result in errors in flow measurement exceeding any potential increase in temperature differential accuracy.

The secondary circuit is gravity fed from a storage tank (within the test cell) and cools the primary circuit through a shell and tube heat exchanger. The flow is regulated by a thermostatically controlled valve within the circuit, effectively controlling the engine coolant inlet temperature. The mercury switch used to operate the valve is positioned in the primary circuit and has the capability of maintaining coolant inlet temperature to 59°C $\pm$ 1°C under all operating conditions.

3.4.6 Oil Cooling System

For a standard engine, the conventional method of cooling oil (through the sump and crankcase) is adequate, but in this case, the various semi-insulated engine configurations are potentially a source of elevated oil temperatures and hence engine failure. Additional oil cooling is therefore necessary.

A heat exchanger was added to the lubrication system after a few simple modifications were made to the internal oil galleries at the on-engine filter (see fig. 3.12). Appropriate positioning of the cooler meant that the existing oil pump could handle the additional load. The design of the oil cooler and interconnecting pipes is such that they are fully insulated, thus enabling the external circuit's flowrate and temperature gain to be used to assess the heat rejection to oil (under steady state conditions). The external circuit is in fact the same as that of the engine coolant secondary circuit and is attached through a spur connection.

3.4.7 Injector Cooling System

The standard Petter AV1 engine, when used as a naturally aspirated unit, can be run continuously for days on end. Supercharging the unit (or running the engine under simulated boost conditions) results in the injector nozzle clogging up after only a few hours. On one occasion the injector nozzle actually seized rendering it useless. It was therefore critical to watercool the injector to achieve satisfactory running under boosted conditions. This involved boring the cylinder head injector hole to incorporate a watercooled plug. Figure 3.13 shows the watercooled assembly which was connected to a peristaltic pump capable of delivering from 0 to 1 litre/min.

3.5 Firing Rig Instrumentation

This section deals with the various instruments used on the test rig detailing the specification, installation and method of calibration.

3.5.1 Engine Speed

Engine speed is measured by a non-contact inductive transducer positioned above the flywheel starter motor teeth. Each tooth "breaking" the magnetic field induces an

e.m.f. which is then amplified using a d.c. amplifier. The amplified pulses are counted by an Orbit tachometer (Model 74A610) and displayed as revolutions per minute digitally after the appropriate multiplying conversion.

3.5.2 Engine Torque

The applied torque is measured as the reaction force between an earth point and a torque arm on the external casing of the dynamometer (fig. 3.14). This force is measured by a strain gauge load cell (Novatech F241 30Kgf): signal processing is by means of an A.C. carrier signal (i.e. a phase comparison is made between the original signal and that returned by the load cell). After rectification, the D.C. signal is amplified and displayed on the control panel as a voltage proportional to engine torque. Static calibration is undertaken using calibration weights applied to an additional arm on the dynamometer casing. The resultant calibration line (fig. 3.15) shows good linearity throughout the operating range as well as good repeatability under subsequent calibrations.

3.5.3 Fuel Delivery Rate

Fuel flow rate is measured using a simple burette and stop watch. Fuel specific gravity and temperature are measured regularly in order that flowrates can be determined accurately. The obvious disadvantage using this system is that it requires constant attention during the measurement time interval (up to two minutes). Other systems were considered to replace the rather crude burette and stop watch arrangement but it was found that they were either too expensive or unable to measure the lower fuel flowrates accurately (< 0.4 litres/hour).

3.5.4 Engine Coolant Flowrate Measurements

Primary circuit coolant flowrate is measured using a bevel edged orifice plate and differential water manometer connected to corner tappings within the plate carrier (A in fig. 3.11). Coolant flow is guided in accordance with BS1042 using 38 mm diameter of 1" i.d. seamless pipe upstream of the plate and 24 mm diameter downstream. Particular attention was paid to keeping the orifice plate's faces and edges free from scale deposits which could affect the calibration. Calibration of the installation was carried out simply by opening the primary circuit at inlet (B in fig. 3.11) and measuring a range of timed deliveries into a calibrated balance. Obviously this procedure is difficult to conduct over a range of temperatures, so a temperature relationship in accordance with BS1042 was incorporated in the calibration.

3.5.5 Engine Coolant Temperature Measurement

Coolant temperature is measured at engine block inlet and cylinder head outlet by two groups of three 1mm diameter sheathed chromel-alumel thermocouples each being located within a machined housing. The group thermocouples are connected in parallel to the cold junction/display unit, thus giving a mean temperature of the water through each housing.

The connections are checked by comparing each group with boiling and freezing points standards. The cold junction/display unit was a Keithley 870 with twin thermocouple entry facility, 0 to 100°C range and 0.1°C resolution.

3.5.6 Oil Coolant Flowrate Measurement

Oil coolant flowrate is measured using a turbine meter giving a flow dependent pulsed signal output over flow range 0.025 to 1.66 litres/min (RS Components LTD, catalogue no 304 431). A simple four digit display frequency counter is used to

convert the pulses into a flow related frequency. Calibration of the instrumentation is by weighted deliveries over time periods.

3.5.7 Oil Coolant Temperature Measurement

Oil coolant temperature measurement, at oil cooler inlet and outlet is measured by 1/16" diameter sheathed chromel-alumel thermocouples. Each thermocouple is connected to a 12 way Jenway thermocouple unit.

3.5.8 Induction System-Flow, Temperature and Pressure Measurement

A bevel edged orifice plate located upstream of the damping receiver is used to measure air flowrate (O in fig. 3.10).

Two different plate/pipe assemblies are used to cover the expected flow range from naturally aspirated to boosted conditions; the pipe bores being 1" and 1½" diameter for the naturally aspirated and boosted applications respectively. Both plates are installed in accordance with BS1042, in corner tapping carriers, the differential pressure being measured by vertical water manometers. Direct calibration of the air flow installation is not feasible, therefore the manufacturer's quoted plate performance (at the specified design point) is used within the BS1042 relationship, i.e.

$$V = K_p \sqrt{\Delta h / \rho_a}$$

V = volume flowrate (m^3/s)
Δh = pressure differential (N/m^2)
ρ_a = air density (Kg/m^3)
K_p = plate constant = 0.62 and 0.99 for 1" and 1½" plates respectively

Air temperature at the point of flow measurement is the mean of the downstream air receiver temperature (i.e. engine inlet temperature) and an upstream temperature at the start of the flow straightening pipe. Both temperatures are recorded using the Jenway unit and sheathed chromel-alumel thermocouples.

Air pressure is measured using a static tapping on the air receiver connected to either a water or mercury manometer depending on receiver pressure (i.e. naturally aspirated or boosted conditions).

3.5.9 Exhaust Temperature and Pressure Measurement

The exhaust gas temperature is measured at the exhaust duct using a stainless steel 1/16mm diameter sheathed thermocouple connected to the Jenway thermocouple unit previously mentioned. The thermocouple within the exhaust gas stream, records the equilibrium temperature based on the nett convective heat transfer between the gas and the junction and the combined radiation - conduction heat transfer from the junction to its surroundings (i.e. mounting point and duct walls). Under steady state conditions the difference between the true gas temperature and this thermocouple equilibrium temperature is due mainly to radiation from the probe. Because of this radiation influence, lagging is required around the system to raise the wall temperatures.

It is with the objective of minimising both the radiative and convective errors that the steady state probe design of Moffat (ref. 31) is adopted as shown in figs. 3.16a and 3.16b. Ideally, exhaust gas temperature should be measured in the exhaust damping receiver, but in practice this presents problems in fully insulating the receiver and interconnecting pipework to withstand potentially high exhaust temperatures when the engine is run under high boost conditions.

In order to obtain mass average temperatures given the above constraints, the probe is positioned near the exhaust port and the value inferred from the time average

temperature using the work of Caton (ref. 32). Caton uses a single cylinder spark ignition engine of similar bore/stroke/geometry. By using a matched computer cycle simulation program with a flow related exhaust duct heat transfer model, Caton has shown that the time-averaged exhaust temperature is consistently about 92.5% of the mass-averaged temperature. This then provides an empirical method of approximating the mass-averaged temperature from the measured thermocouple temperature.

Exhaust pressure measurement is by a static pressure tapping with a piezometric ring downstream of the damping receiver designed to BS1042 specifications. Despite following their guidelines, frequent blockage of the tapping with carbon deposits occurs, necessitating regular checking and maintenance.

3.5.10 Cylinder Pressure Measurement

The development of piezo-electric pressure sensitive transducers has enabled engine cylinder pressure to be measured thus yielding potentially accurate pressure Vs. crank angle diagrams. This type of transducer relies on the electric charge generation property of a piezo crystal when it is subjected to a change in applied load. The change in signal produced by the transducer is amplified by a charge amplifier which produces a voltage signal either for oscilloscope display or data logging. Conventional transducers have temperature limits of about 150°C (determined by the crystal). This type of transducer, therefore, needs to be watercooled and hence requires a pump driven cooling circuit supplying a steady flow of distilled water plus the necessary alarms in the case of emergencies. In an investigation such as this where cylinder temperatures in the order of 1500K are expected, it is considered wise to seek an alternative device with a higher temperature limit such as the Kistler "Poly crystal" device with an operating maximum temperature of 620K. Although the extra cooling circuit cannot be avoided, there is a greater chance of survival of a very costly piece of equipment in the event of a failure in the cooling circuit.

A further complication in the use of transducers in I.C. engines is the sensitivity to the

advancing combustion flame. Shielding the transducer using a silicon rubber coating over the transducer face to minimise the effect of the resultant "thermal shock" (ref. 33) requires extreme care in preparing the transducer and applying the coating. Such transducers are restricted to a limited operational life which suggests the use of purpose built transducers such as those made by Kistler.

The unit chosen for this research was a Kistler 6121a which has all the necessary shielding to operate under these harsh conditions with good repeatability. Ideally, the determination of heat release rates in IDI engines, which was one of the primary objectives of this work, should be based on the use of two transducers; one in the prechamber and one in the main chamber (see Chapter 5). This allows the separate heat release rates in the main and pre-chambers to be calculated. Unfortunately there are many practical difficulties in the use of two transducers. Primarily, the relatively small pressure difference across the prechamber passage, relative to the high absolute pressure level, and secondly, the practical problems of accommodating two transducers in a very confined space. Hence it was decided to fit a single transducer to the prechamber and adopt a calculation procedure similar to that for single chamber DI engines.

Figure 3.17 shows the remachined prechamber housing, modified to carry a Kistler 6121a transducer at the same time as retaining the prechamber bowl shape and volume. The assembly is predominantly mild steel with the two part watercooled core made of free machining stainless steel and brazed together. The design of the assembly is such that the transducer can be removed and re-installed without disturbing any other part of the engine except the rocker cover.

Water cooling of the transducer is totally separate from the main engine cooling system. It consists of a small peristaltic pump on a 240v a.c. supply connected to a five litre water reservoir which is continuously pumped around the transducer cooling gallery at the rate of one litre/minute.

Several means of calibration were considered in order that a truly acceptable and

repeatable procedure could be adopted throughout this programme. Kistler recommend frequent calibration checks on their instruments; such checks were indeed carried out using a special hydraulically operated static tester, which in turn was calibrated against a precision gauge. A dynamic calibration device used by Cole (ref. 19) resulted in poor repeatability due to the ageing apparatus suffering from small leaks which were amplified, resulting in unreliable readings.

A "dead weight tester" was also considered but due to the time available to read the signal having applied the load, the repeatability was greatly marred.

The system eventually chosen was similar in principle to a dead weight tester i.e. based on the use of pressurised oil. Pressurisation of the oil in a small reservoir was effected by a high precision piston under manual position control, the pressure being read on a suitably accurate pressure gauge. The device had a disadvantage in that results depended on the rate at which pressure was applied. This was overcome by using a charge amplifier with a long time constant and suitable low noise cabling. Another important factor was the absolute cleanliness of every electrical contact using degreasing solvents.

An attempt was made to add a dynamic facility to the calibration device by the introduction of rapid opening valves. This produced pressure drops as the valves were opened giving instantaneous increments of pressure which were unacceptable. The valves were positioned such that the transducer was subjected instantaneously to the built up pressure upstream of the valve. Unfortunately the small volumes of oil and high pressures resulted in a severe drop in pressure as the valves were opened. The valves were then removed and the standard facility used.

The calibration graph of figure 3.18 shows a good linearity over the entire 140 bar range which proved very repeatable.

3.5.11 Engine Top Dead Centre

The engine crankshaft (non-flywheel end) is used to drive a Moore-Reed optical encoder (350P122). The encoder's output consists of three square wave channels; amplitude 3.5V, width ½ degree. One channel produces a pulse every 360° crank degrees, whereas the remaining two channels produce pulses every ½ crank degree, though at a ¼ degree out of phase with each other.

The 360° pulse is statically synchronised with the engine top dead centre position. This position was determined by observing a rising and falling column of oil, contained within the engine cylinder. Verification of this synchronisation method was demonstrated (dynamically) using the cylinder pressure transducer under motored conditions.

3.5.12 Data Acquisition System

Previous work on the test rig detailed above had been conducted by Cole and the author (refs. 19 and 30 respectively). The high-speed data acquisition system used by Shams and Cole proved somewhat dated, in that experimental data was stored on a "Commodore PET" computer for analysis. The problem was in transferring stored data from the PET to the mainframe computer for detailed analysis. Due to changes in the mainframe computer at Bath, it was no longer possible to achieve a link from the PET to the "Gould" mainframe.

A rather simple approach was taken to resolve the problem by using a portable digital storage scope capable of storing up to 4000 points of data per channel of input.The "Nicolet 3091" digital storage scope had two major limitations, which were :

a) Only two channels could be monitored at any one time.
b) The stored picture on the screen was the signal being processed at the time of freezing. This meant that there was no means of sampling or averaging of

signals whatsoever. Any signal fluctuations were either recorded, or missed depending on when the "freeze" button was activated.

The limitations of the Nicolet 3091 digital storage scope are fully discussed in chapter 4, section 3.2 .

The Nicolet 3091 is equipped with an extremely useful RS232 interface which is capable of linking it to most desk top computers. As was the case in the early 80's (which was when the Nicolet was purchased by the Department of Mechanical Engineering) the most versatile and popular desk top computer was the "BBC micro computer". The fact that the Nicolet could be interfaced with a computer led Barker (ref. 20) to write a software package to transfer to disk, two channels of captured information from the Nicolet scope. The program also had the facility of screen dumping, superimposing other captured data and digitising numerically stored data. Due to the incompatibility of the BBC computer with more common desk top computers, it was not possible to use this extensive program of Barker's on any other device. It was either a case of completely rewriting an already working program or accepting the limitations of a dated, slow machine using BBC Basic as its only language. Due to time limitations, it was thought best to use Barker's package and write a smaller package to refine the captured Nicolet data for analysis on the mainframe.

The way in which the BBC/Nicolet coupling worked presented a small problem in that the BBC computer would only record the information available on the Nicolet's screen. The Nicolet in turn had no facility for simultaneously storing a cylinder pressure and TDC traces which would have reasonable resolution and start at the same point in the engine cycle every time. It was for this reason that the previously mentioned "refining" program had to be written.

The refining program locates a randomly stored TDC point, and relative to the next TDC point, divides the captured cylinder pressure trace into one degree intervals. The pressure trace is then tabulated between inlet valve closure and exhaust valve opening.

This "refined" trace is then stored on disk and transferred to the "Gould" mainframe computer ready for analysis and direct comparison with other stored traces. Figure 3.19 shows a schematic diagram of the sequence of events involved in obtaining fully analysed results from pressure transducer voltages.

Engine type	:	Petter AV1 Water cooled single cylinder stationary IDI Diesel
Speed range	:	1000-2000 rev/min
Rated power	:	5 bhp (3.73 Kw) at 1500 rev/min
Cylinder Bore	:	80 mm
Stroke	:	110 mm
Cubic Capacity	:	553 cm^3
Compression ratio	:	19:1
Fuel Injection pressure	:	2850-3150 PSI (200-221 Kg/cm^2)
Fuel Injection timing	:	18°BTDC
Valve timing	:	IVO 4.5 BTDC IVC 35.5 ABDC EVO 35.5 BBDC EVC 4.5 ATDC
Bumping clearance	:	0.91 - 1.02 mm
Valve rocker clearance	:	0.25 mm cold
Prechamber volume	:	2.569 x $10^{-5}m^3$
Swept Volume	:	5.529 x $10^{-4}m^3$

Table 3.1: Standard Petter AV1 engine specification.

ENGINE TYPE : Petter AV1 Water cooled single cylinder stationary IDI Diesel

PARAMETER	STANDARD ENGINE	NON-STANDARD ENGINE	BOOSTED ENGINE
Fuel injection pressure	2850-3150 PSI (200-221 Kg/cm^2)	1800 PSI (126 Kg/cm^2)	2850-3150 PSI (200-221 Kg/cm^2)
Fuel Injection timing (spill)	18°BTDC	7.5°BTDC	24°BTDC
Bumping clearance	0.91-1.02 mm	1.42 mm	0.91-1.02 mm (0.056")
Compression ratio	19:1	18:1	19:1

Table 3.2 : Variation on standard engine build parameters.

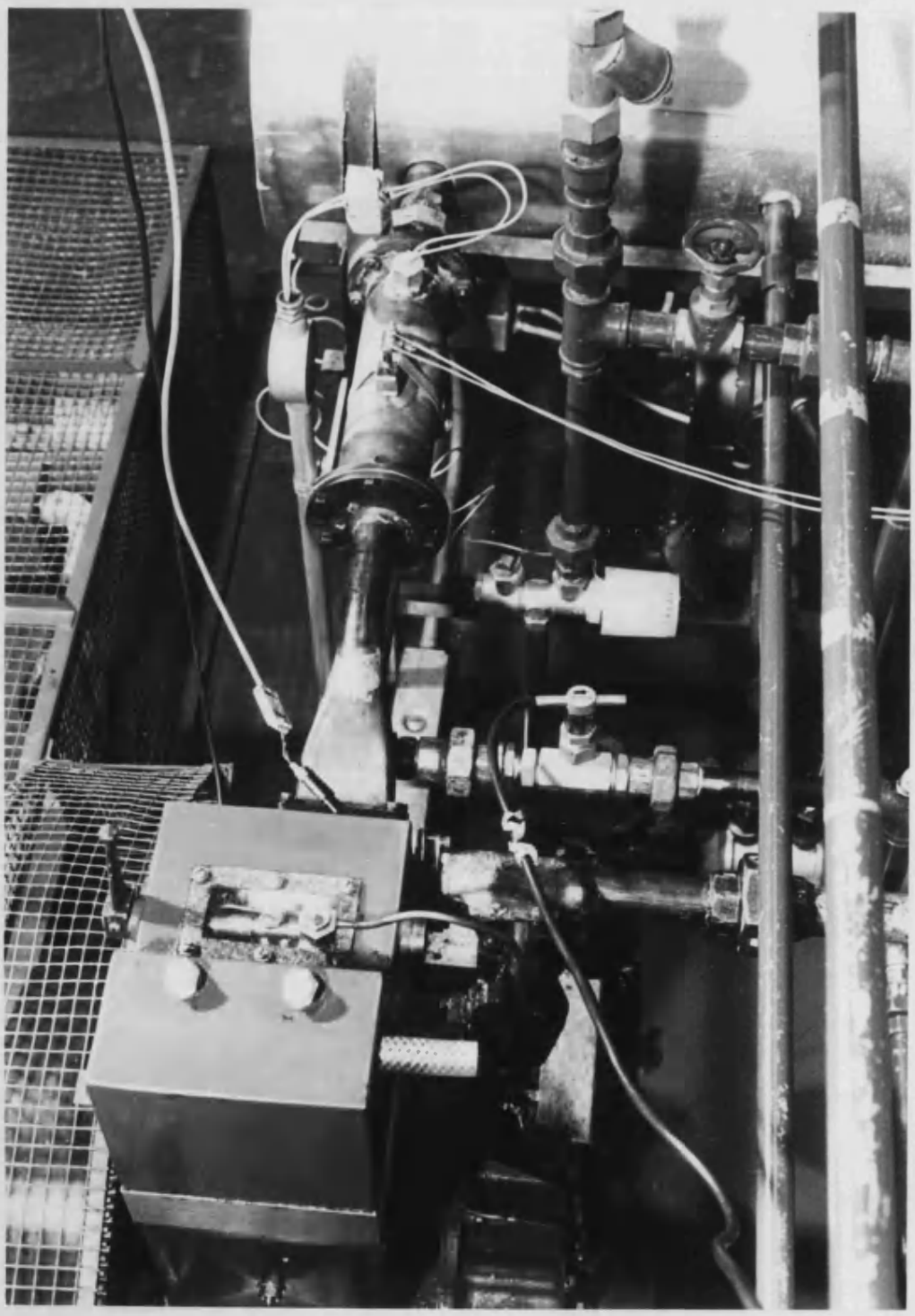

Figure 3.1 : Overall view of simulation rig.

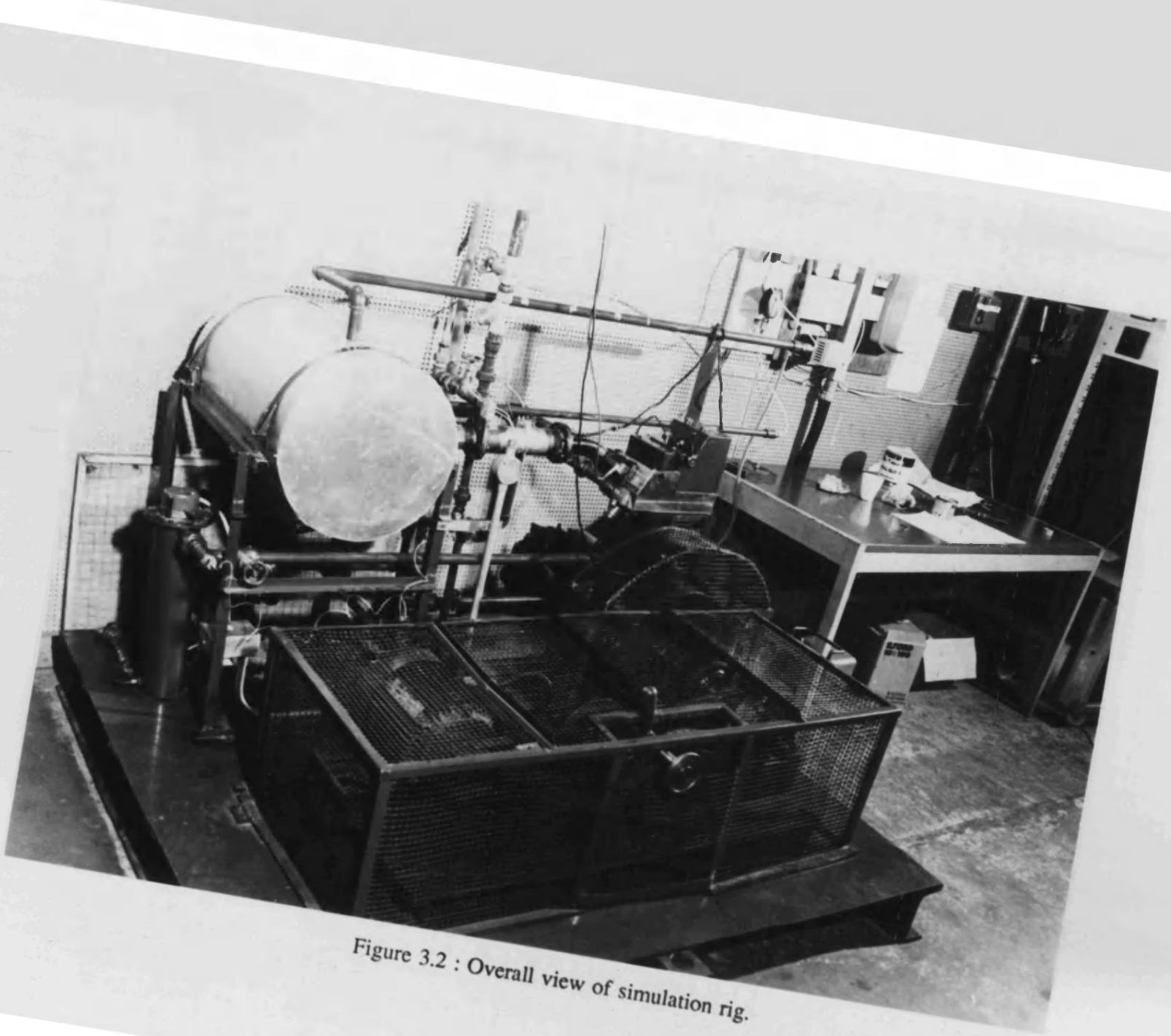

Figure 3.2 : Overall view of simulation rig.

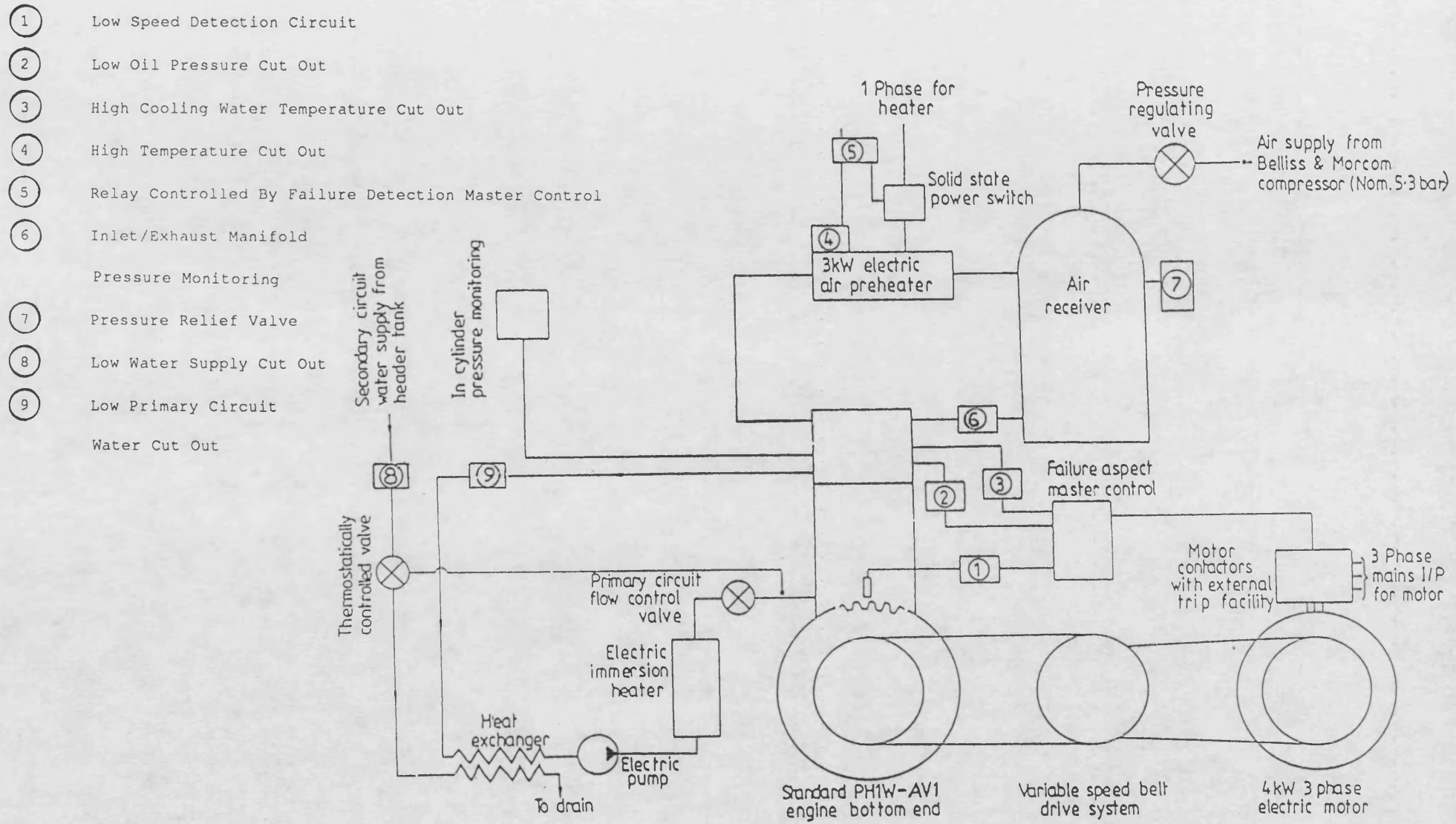

Figure 3.3 : Simulation rig schematic diagram.

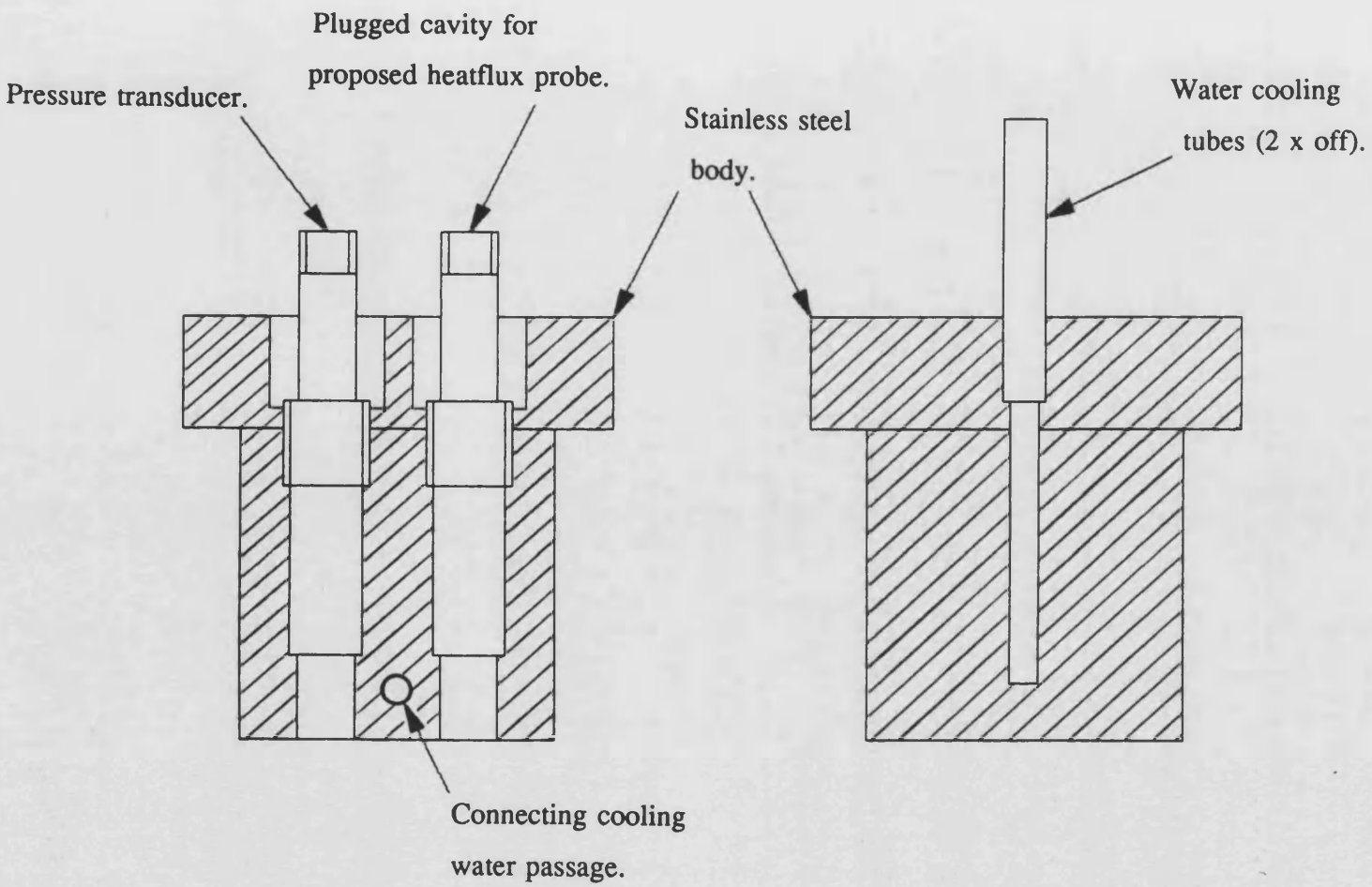

Figure 3.4 : Orthogonal cross section of the pressure transducer plug used in the engine simulation rig.

Engine speed indicator & cut out

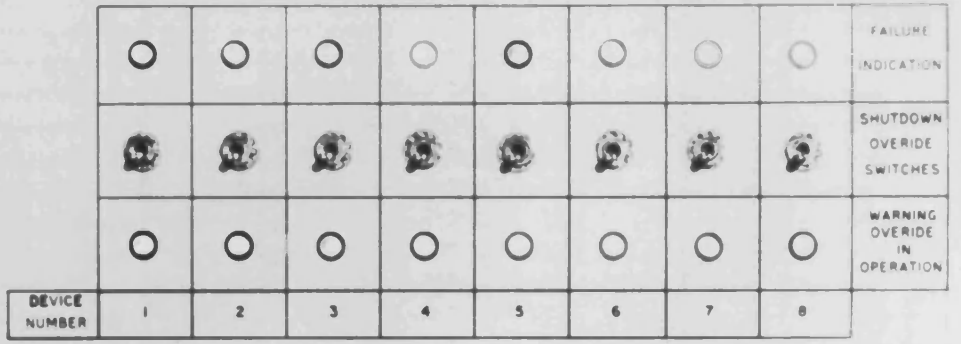

Air inlet temperature indicator & cut out

System reset switch

Figure 3.5 : Failure detection and control panel for engine simulation rig.

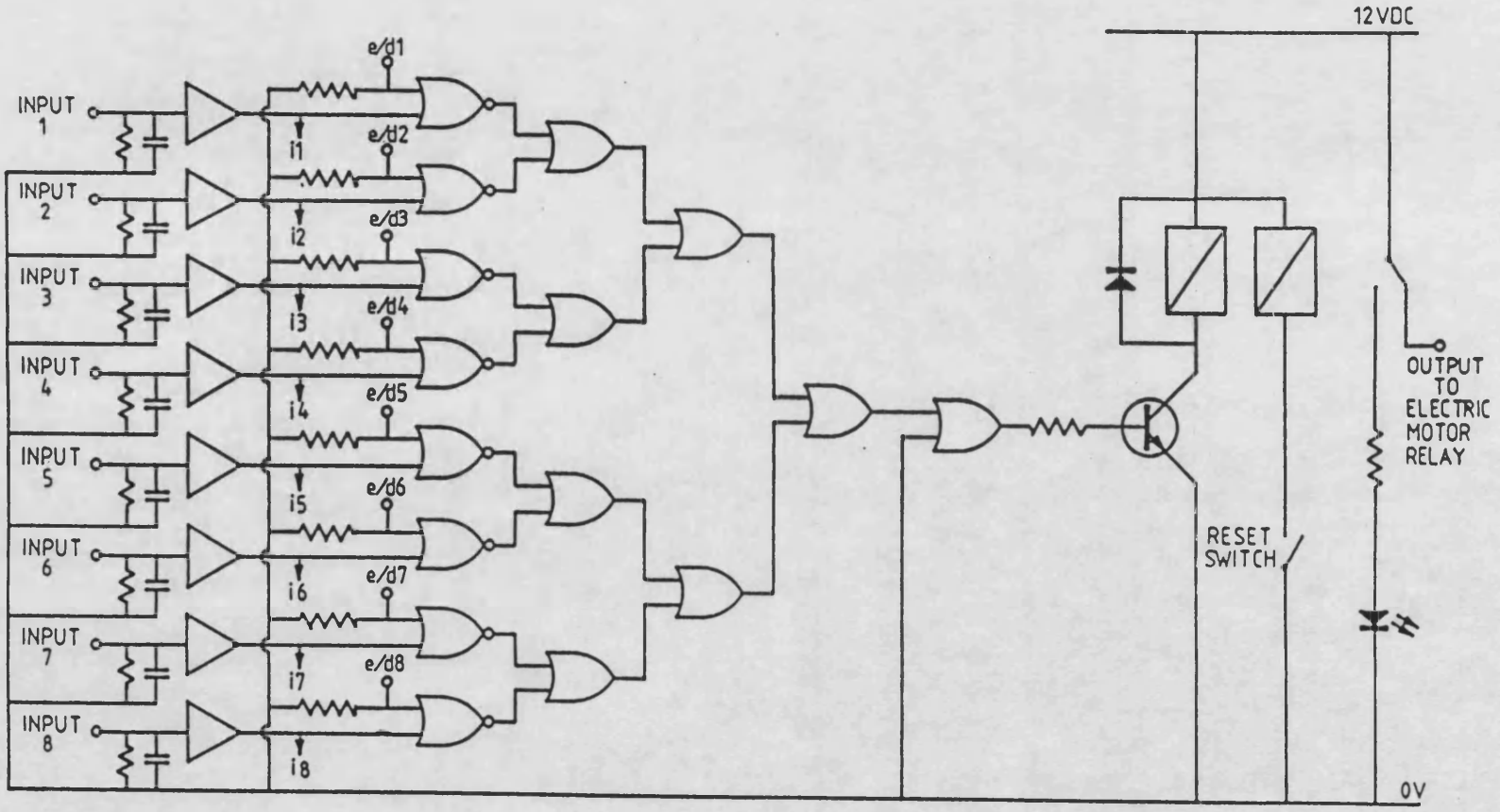

Figure 3.6 : Automatic shutdown circuit diagram.

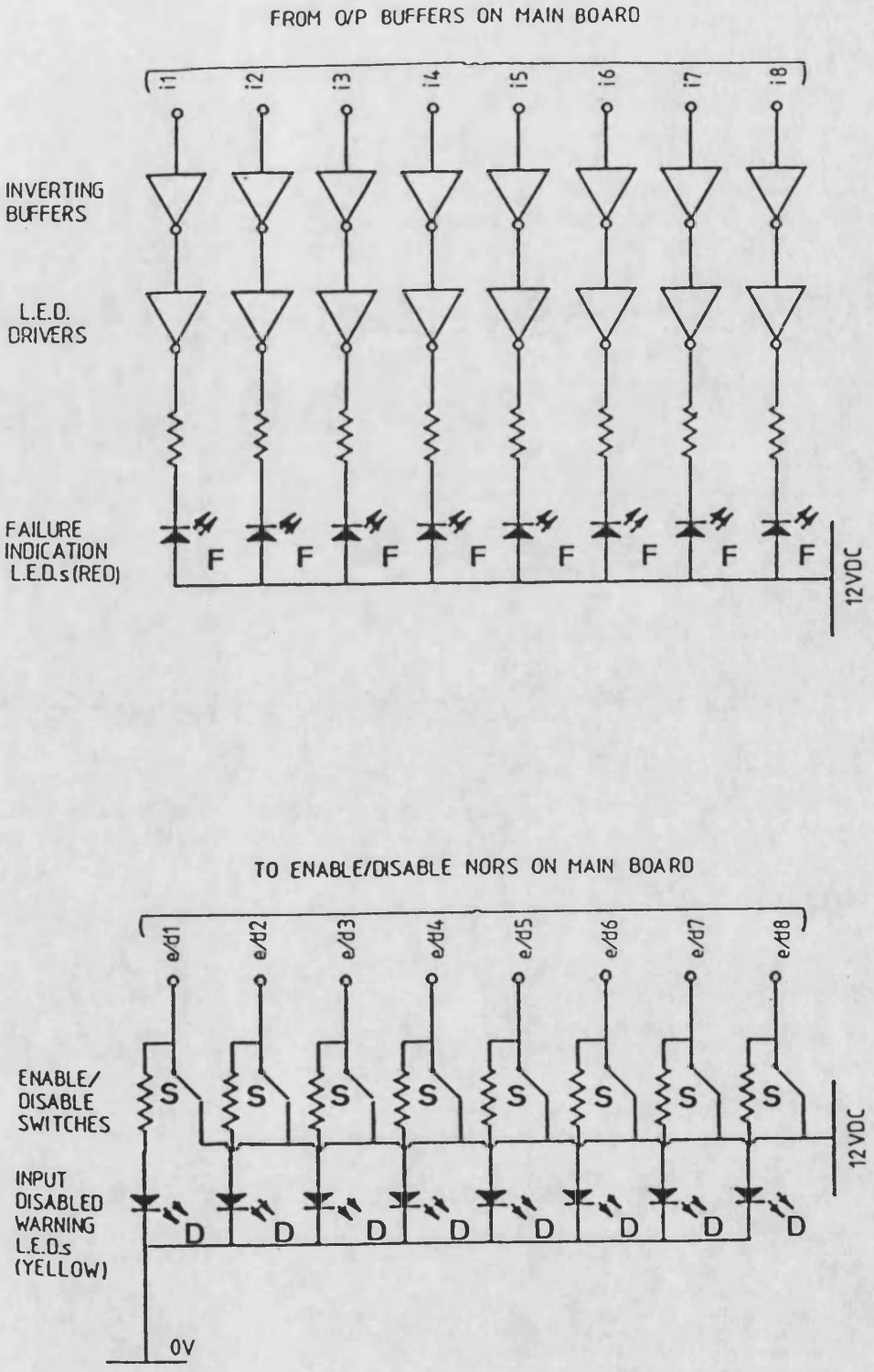

Figure 3.7 : Automatic shutdown system display circuits.

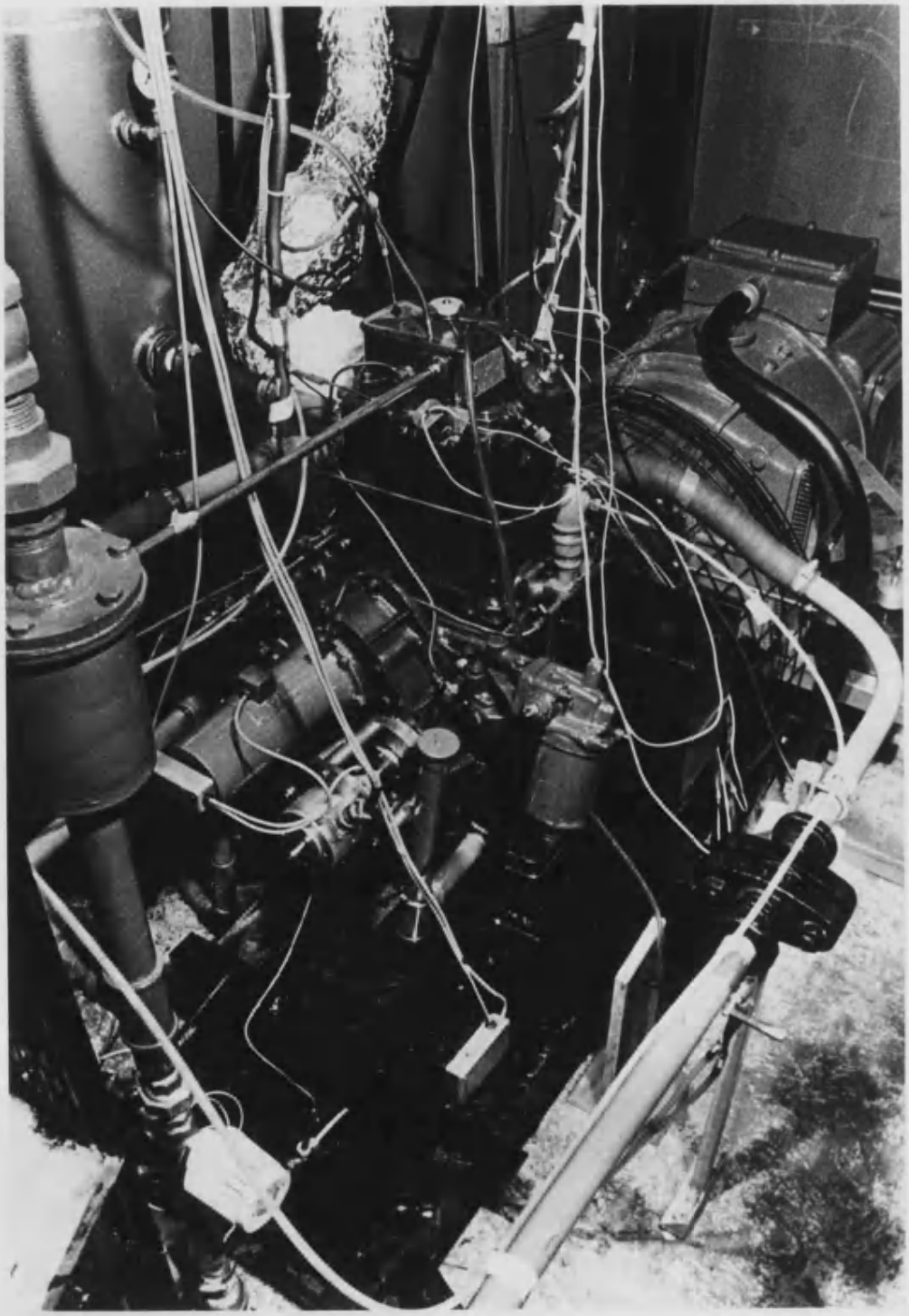

Figure 3.8 : Overall view of the firing engine rig.

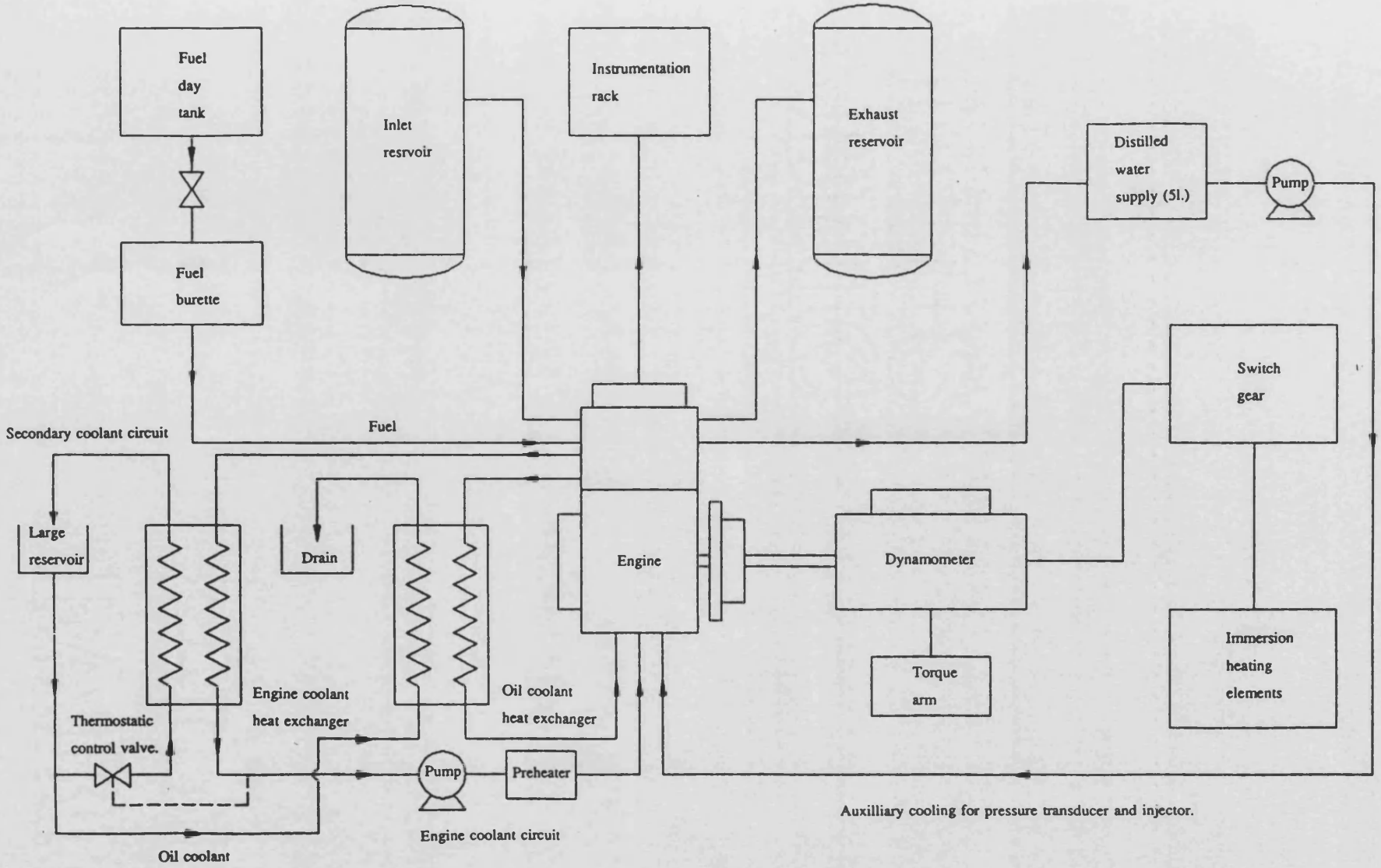

Figure 3.9 : Firing engine rig schematic.

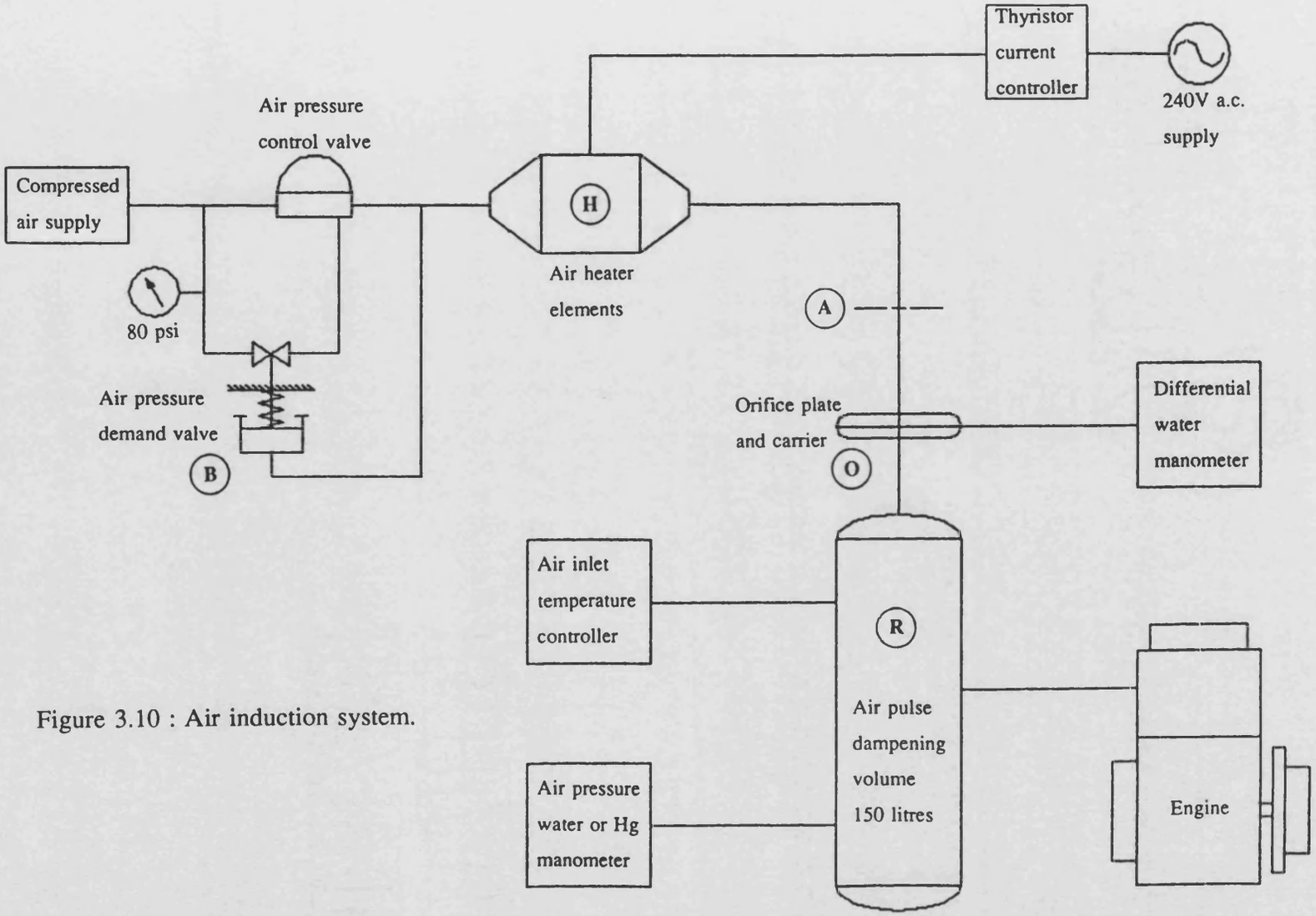

Figure 3.10 : Air induction system.

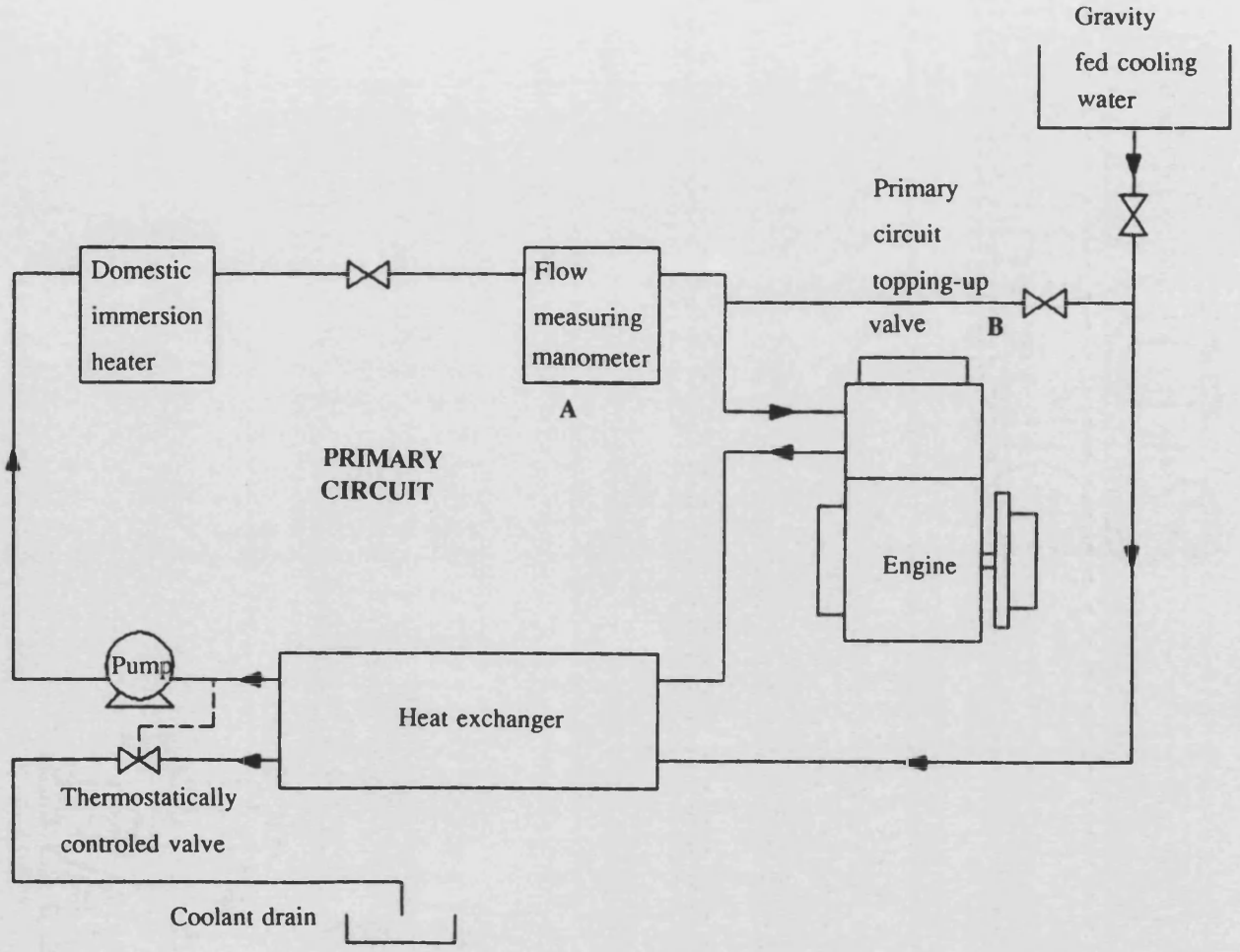

Figure 3.11 : Engine water cooling system.

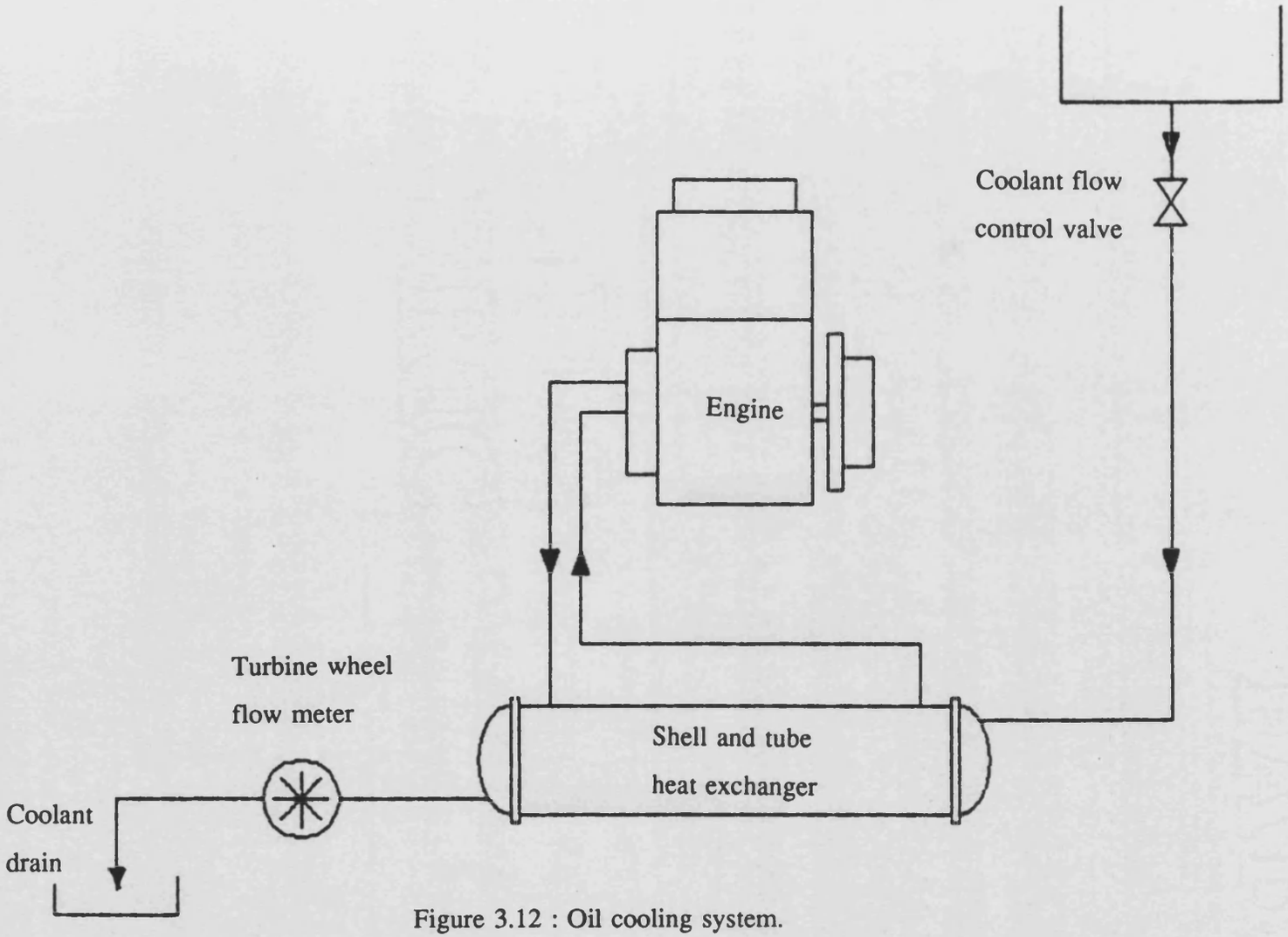

Figure 3.12 : Oil cooling system.

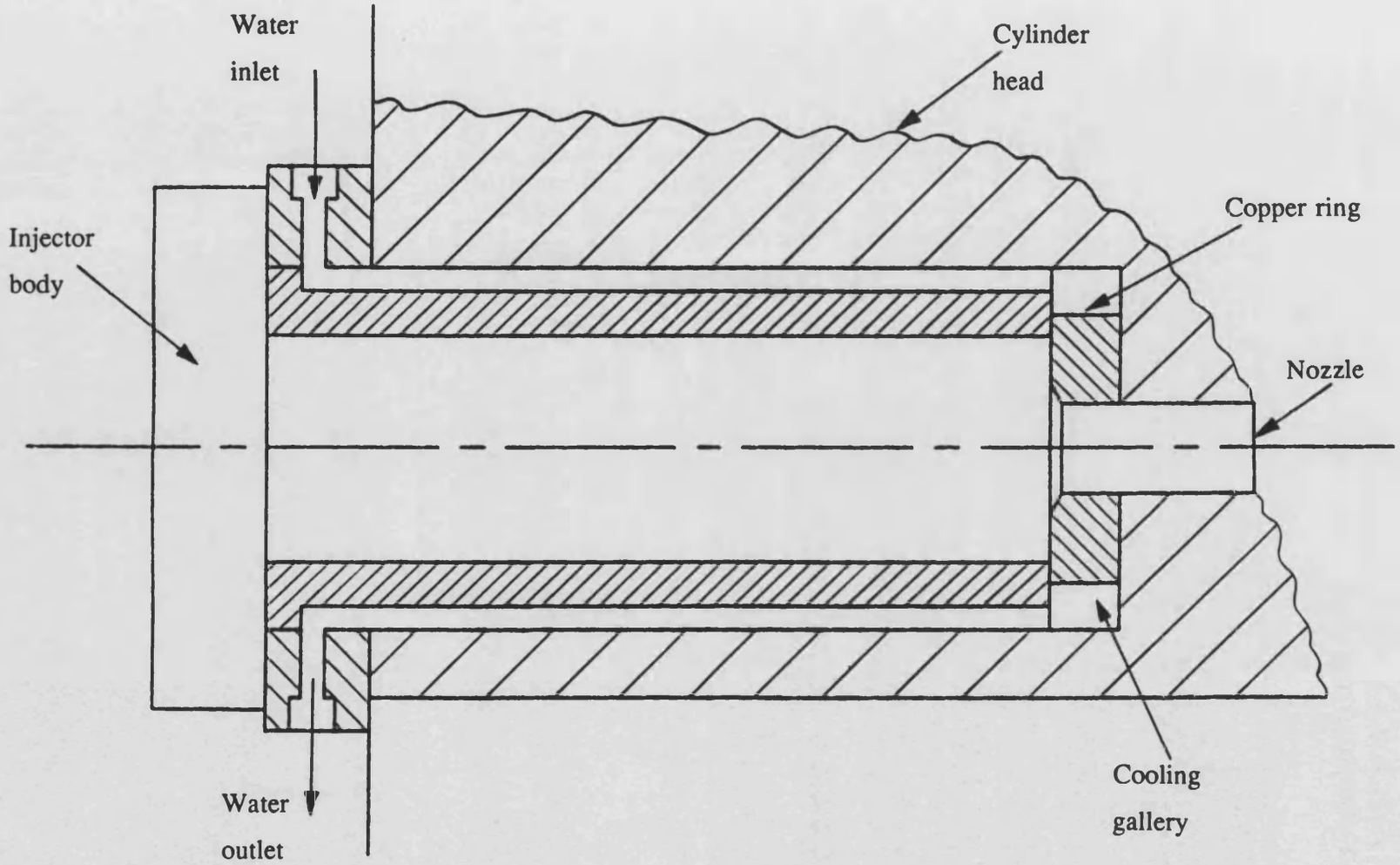

Figure 3.13 : Watercooled injector assembly.

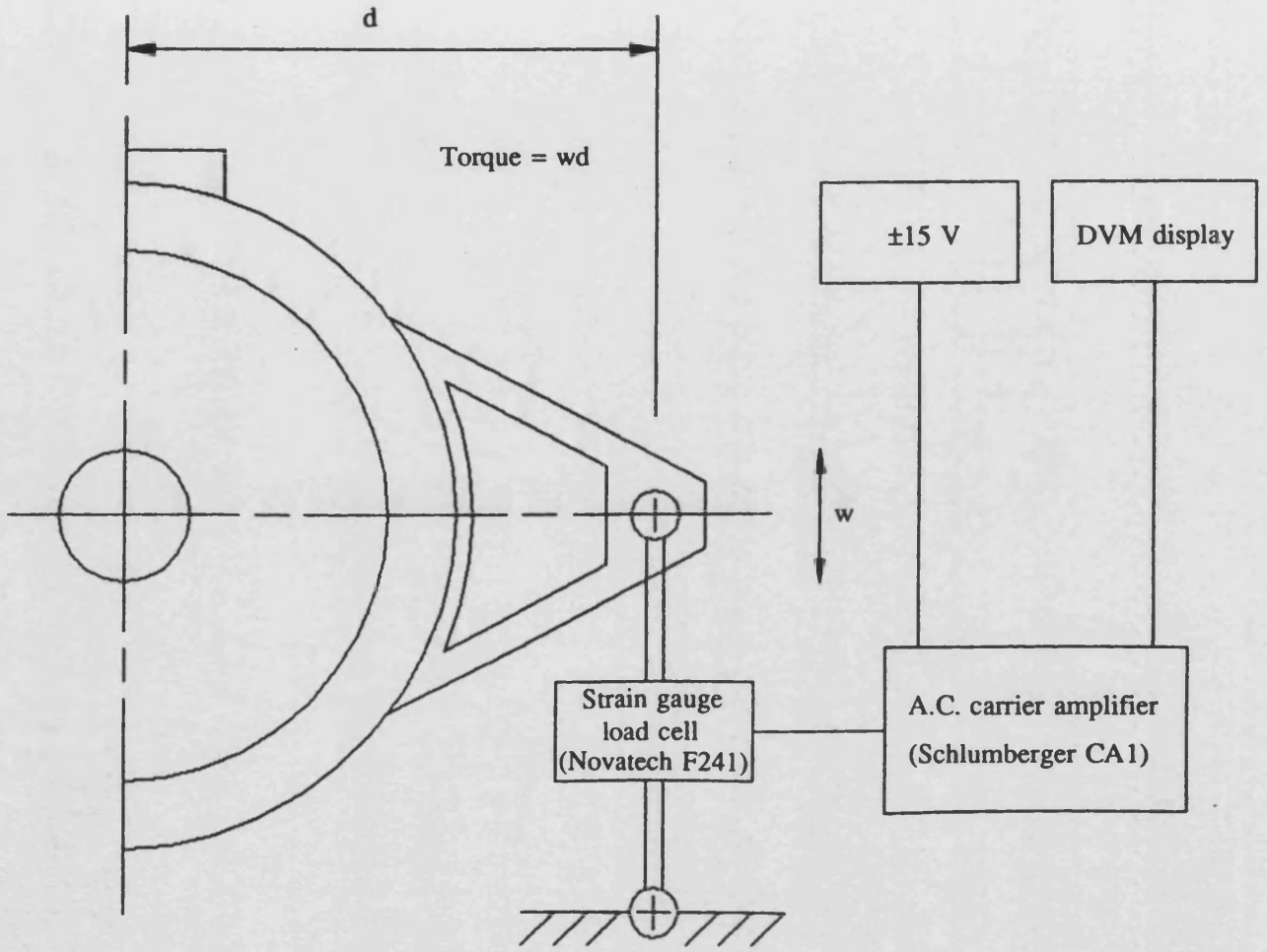

Figure 3.14 : Torque transducer installation.

FIGURE 3.15 : LOAD TRANSDUCER CALIBRATION
FOR PETTER AV1 FIRING ENGINE.

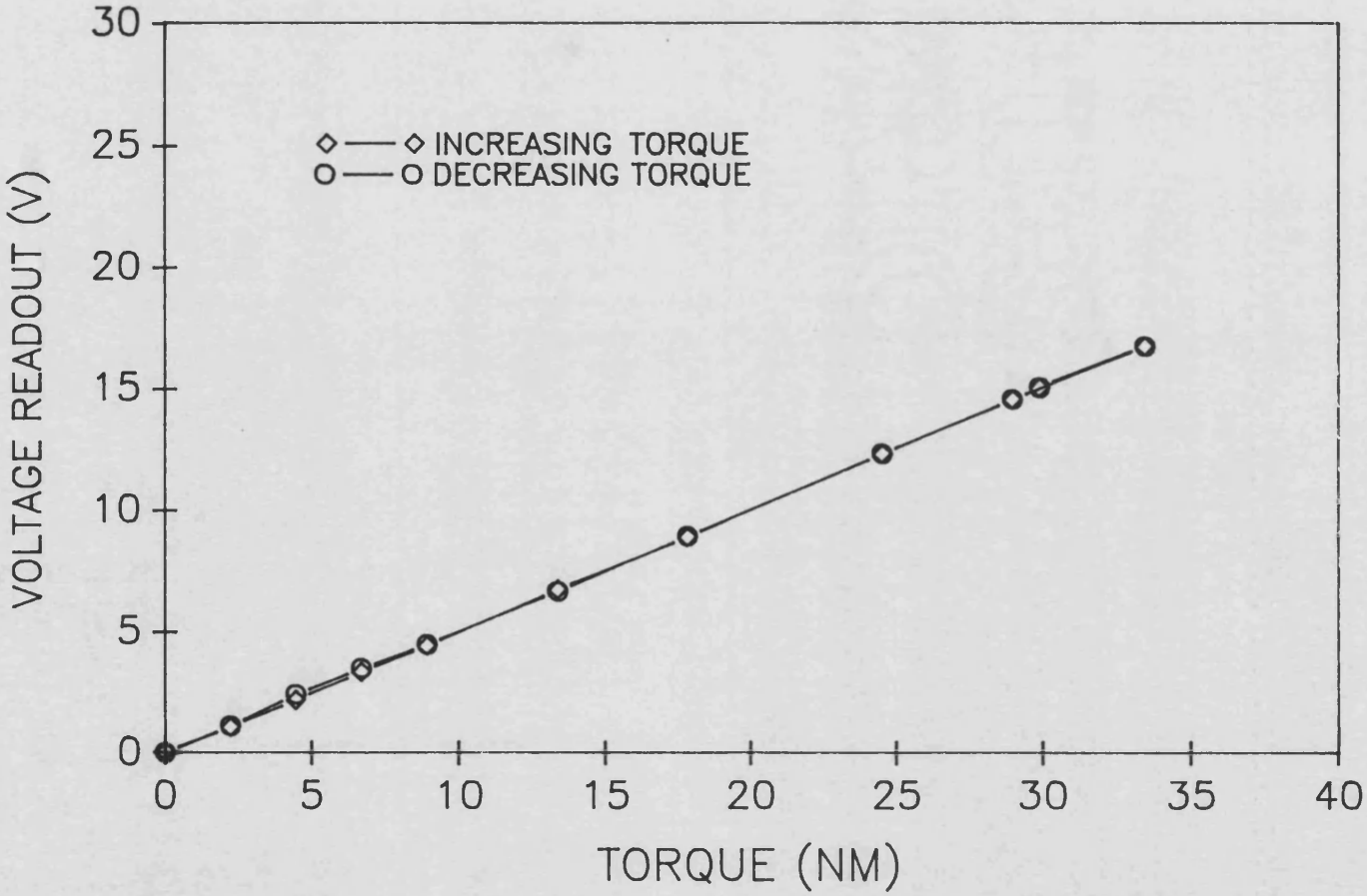

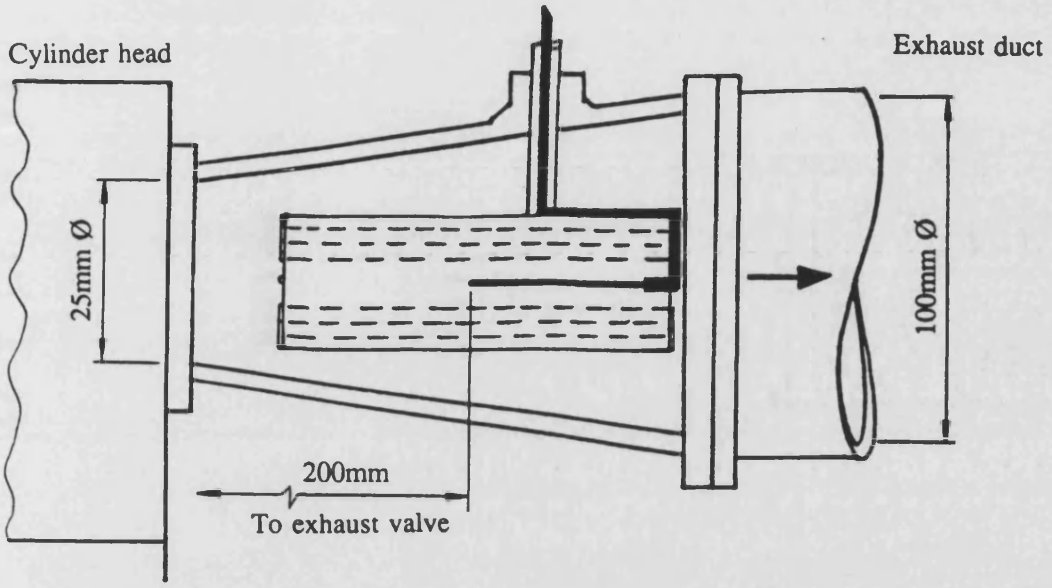

Figure 3.16a : Exhaust temperature probe installation.

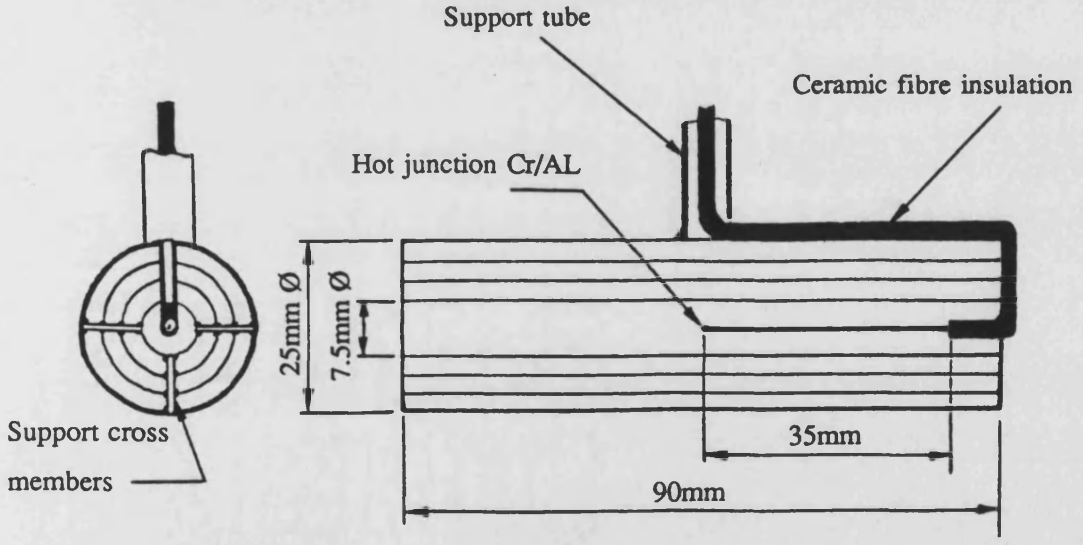

Figure 3.16b : Exhaust gas temperature probe.

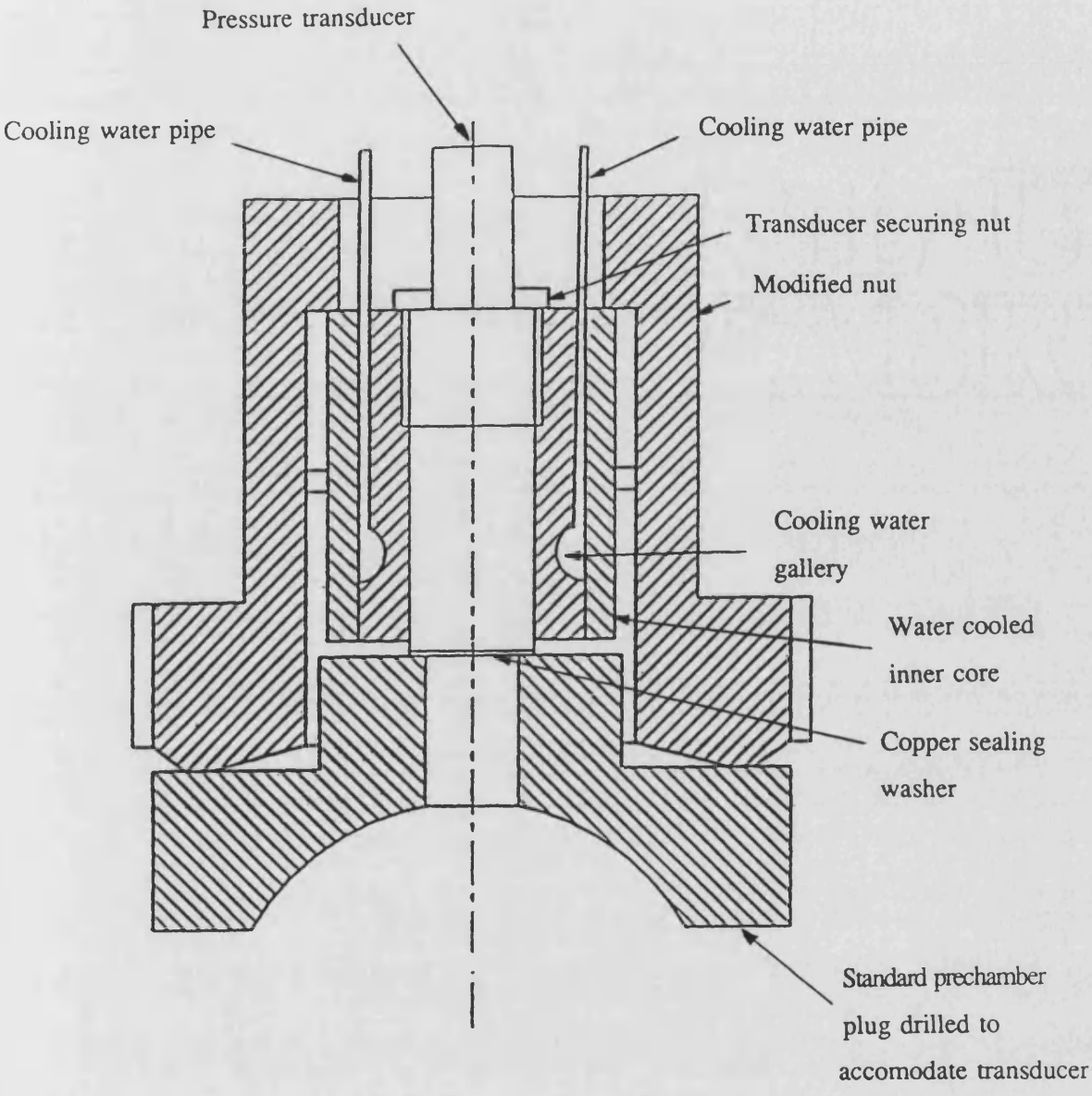

Figure 3.17 : Prechamber pressure transducer arrangement.

FIGURE 3.18 : PRECHAMBER PRESSURE TRANSDUCER CALIBRATION.

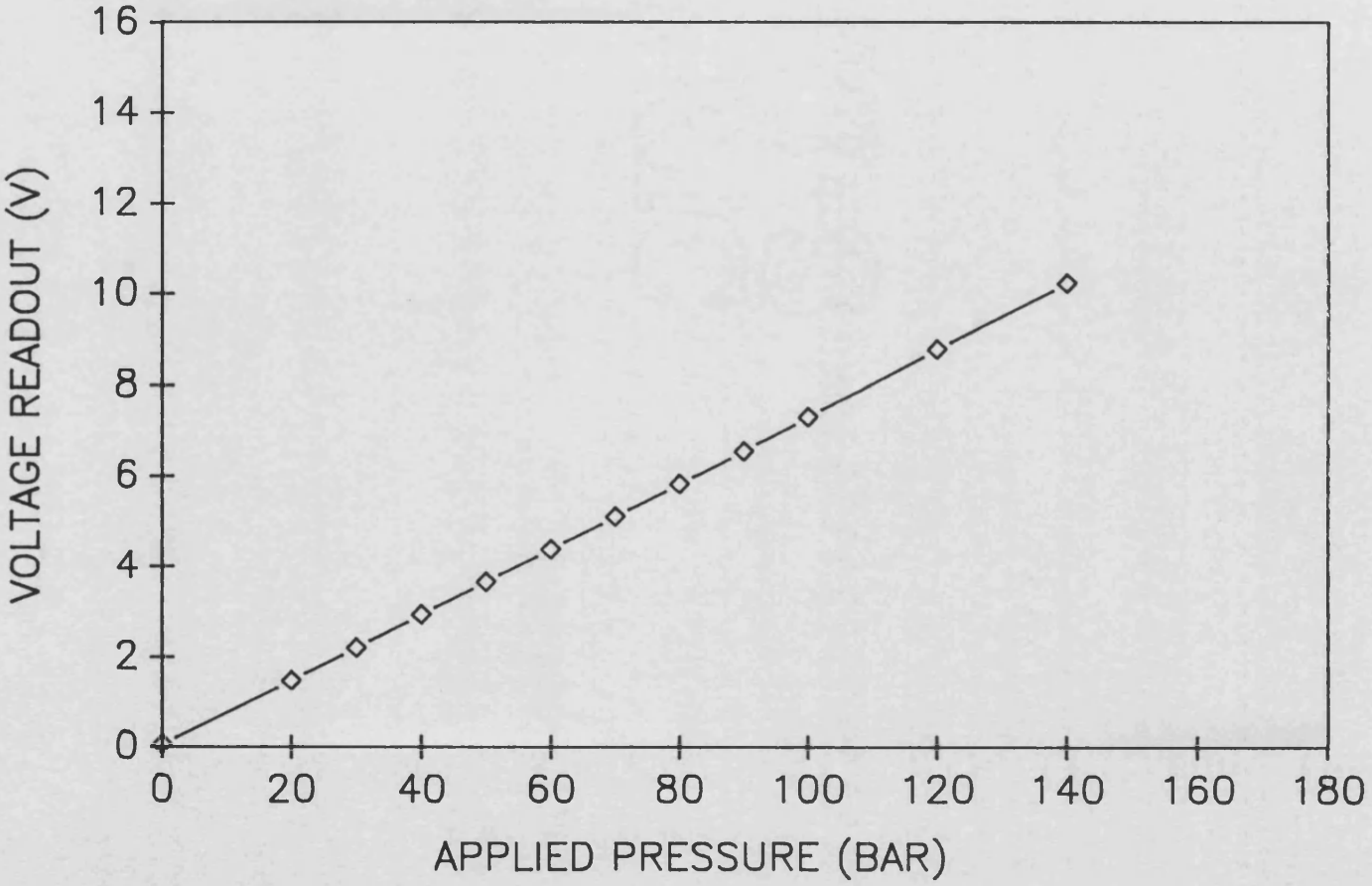

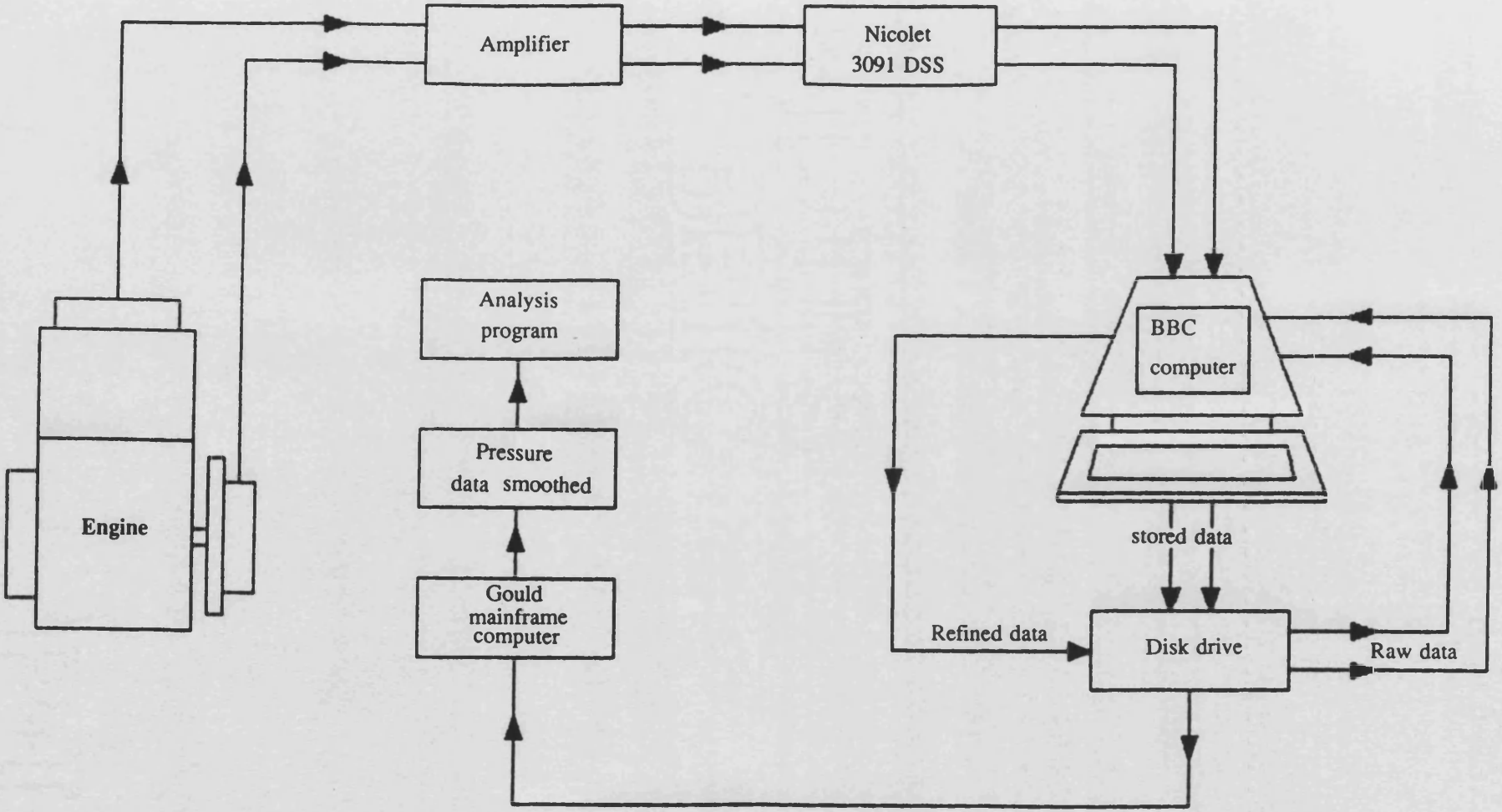

Figure 3.19 : Data acquisition-analysis schematic.

CHAPTER 4
EXPERIMENTAL RESULTS

4.1 Introduction

The achievement of the objective of this research viz. to obtain detailed comparisons of the performance and combustion characteristics of the Petter AV1 engine, both in standard form and with ceramic piston caps, proved extremely difficult in view of the many problems, including repeated catastrophic failures resulting from the use of ceramic components in the firing engine.

At the start of the project, the standard AV1 engine was run both naturally aspirated and boosted at 1.5 bar in order that a full spectrum of baseline results may be available for comparison with ceramic piston engine build results. This process alone took several months to conclude due to the problems associated with running at high levels of fuelling.

Another time consuming task was establishing a value for the bumping clearance in order that the valves could be prevented from "kissing" the piston top at speeds exceeding 1750 rev/min. Two designs of head gaskets were used and a range of tightening torques experimented with until the problems associated with the cylinder head were finally eradicated. The two types of head gaskets were so different from one another that the bumping clearance was changed, simply by changing a head gasket, by 0.5 mm (0.020").

In commissioning the firing rig, fundamental quality control mishaps wasted valuable time. These included incorrectly fitted pushrods, poorly seated inlet and exhaust valves and a leaking prechamber, amongst others.

During boosted running, it was noticed that the injector would foul up after only one

or two hours operation. After several recurrences of this problem, the cylinder head was removed and the injector body bored out to accept a cooling jacket. The brass cooling jacket (shown in fig. 3.13) was made from three separate sections and took a total of four weeks to design, build and install.

Changing the engine build from naturally aspirated to boosted operation involved altering the fuel injection timing and connecting an alternative pipe system to the main compressor. This job was initially delayed by having to rebuild the top half of the engine several times due to blown head gaskets when running the engine boosted. This problem was finally rectified when the right combination of gasket and tightening torques were empirically found.

Having established a reliable engine build, the ceramic piston assemblies were ready to be installed in the engine. After many failures and several engine rebuilds, the standard engine was detuned (see table 3.2) to create a "less harsh" operating environment for the fragile ceramic caps. This made all the previous engine running redundant and added several months of lost time onto the schedule. The original plan of running a boosted engine was dropped and all further runs were carried out under the newly established "detuned" conditions, essentially operating with greatly retarded injection timing in order to reduce the extreme harshness associated with standard timing (see also chapter 2, section 2.7).

4.2 Calibration of Standard Engine

The AV1 engine in standard form was initially run in using the Hepworth and Grandage schedule shown in table 4.1. This schedule was considered the most suitable as it was comprehensive and least time consuming. In previous work, Cole (ref. 19) had also used this schedule satisfactorily. Owing to the number of engine rebuilds, the Hepworth and Grandage running in schedule was curtailed to that shown in table 4.2. This modified running in procedure was substituted after the second failure of a ceramic crown to save time.

Frequent engine rebuilds, although necessary, do contribute to some deviations from the intended "standard" build. Table 3.1 shows the standard engine specifications and table 3.2 gives the difference in specifications observed for the purpose of this research. It is usually assumed that every engine rebuild results in an identical engine, so that performance should not be affected. However, in practice changes in clearances etc. following a rebuild are unavoidable. The factors that do influence the performance of an engine following a full rebuild are detailed in the sections below.

4.2.1 Bumping Clearance

This is the term used to designate the gap between the piston crown at TDC and cylinder head flame face. A standard procedure for carrying out the measurement of this gap in IDI engines is to introduce a length of soft lead wire through the prechamber and measure its new thickness after the piston compresses it at TDC. The thickness of the compressed lead wire is the "bumping clearance" which is rarely the same for two engine rebuilds. There is a large element of human judgement in making this measurement which may occasionally be influenced by the need to dismantle both the cylinder head and block to rectify. This very critical parameter determines the compression ratio (and hence energy distribution to shaft, exhaust and coolant) and as can be seen below, only a small difference in bumping clearance can be acceptable.

$$\text{compression ratio } CR = \frac{\text{maximum cylinder volume}}{\text{minimum cylinder volume}}$$

$$CR = \frac{V_s + V_c}{V_c}$$

$$\text{or} \qquad = \frac{V_s}{V_c} + 1 \qquad (1)$$

For the engine specified in table 3.1 and assuming a bumping clearance of 1 mm, equation (1) becomes

$$CR = \frac{5.529 \times 10^{-4}}{3.0717 \times 10^{-5}} + 1$$

$$CR = 19.0 : 1$$

If a bumping clearance of 0.9 mm is used, the compression ratio becomes 19.3:1. It can therefore be seen that an insignificant (and often difficult to measure accurately) 0.1mm change in bumping clearance produces a significant change in compression ratio.

4.2.2 Fuel Injection Timing

The injection timing is set by the fuel "spill" method at the fuel pump. Calibrated timing marks on the flywheel enable the timing to be altered to within ± ½ crank angle degree. In practice, the layout of the rig is such that the spill timing cannot be set to within this accuracy and a compromise of ± 1½ degrees is considered acceptable. By carefully setting the spill using one person to adjust the crank angle and another the fuel pump, accuracy to within one degree is possible. Having set the timing it can remain in this "set position" regardless of whether a cylinder head is being overhauled, or even of a complete piston, block and head overhaul.

4.2.3 Valve Lift

From Table 3.1, the rocker clearance of 0.25 mm is set for both valves when the engine is cold. Errors in this measurement can result in incorrect maximum valve opening, valve opening and closing times, and valve overlap. Wear in the cams due to grit from catastrophic ceramic cap failures could also influence the three parameters outlined above, regardless of whether the valve clearance was accurately set or not.

The analysis programs described in Chapter 5 rely heavily on pressure readings at IVC

to be precisely at the specified point of 35.5°ABDC. If this is any more than 0.5° either side of the manufacturer's value, large errors are built up in the program due to assumptions made at the trapped conditions.

4.2.4 Instrumentation Calibration

Chapter 3 details the instrumentation used on this rig. The instruments are calibrated as often as recommended by the manufacturers. The orifice plates around the engine are cleaned every three months, and the transducers calibrated every time they are disturbed, or after 10 hours running time, whichever occurs first. The fuel specific gravity is measured every time there is a fuel delivery to the University.

It is in the interest of the research team to ensure the equipment is as accurate as possible to eliminate the possibility of errors. For this reason much time is devoted to calibration, in particular the cylinder pressure transducer and the torquemeter.

4.3 Obtaining Experimental Results

Experimental results are divided into two main categories;

1) Performance data
2) Cylinder Pressure data

Different experimental procedures had to be employed, depending on which of the two investigations was being conducted. These categories are detailed in the following subsections. It must be pointed out that the two types of investigation had to be conducted separately for any one running condition. It was not possible to carry out both activities simultaneously (although that would have been ideal) as a watchful eye had to be kept on the engine at all times. The staggering of two banks of results is a large potential source of error as it is almost impossible to reset the engine to run under a fixed set of boundary conditions, previously recorded. Apart from changes

in atmospheric pressure, temperature and relative humidity, another problem is the time taken to record a test. The fact that a particular fuelling can be preset by the operator does not necessarily mean that the engine operating under fuel pump governor control may not experience "random" fluctuations in engine speed and hence performance.

4.3.1 Performance Testing

In an effort to save time, a previously written (and well tested) data reduction program due to Cole (ref. 19) was used rather than writing a totally new program. This program had been previously used on a Petter PHIW DI engine and therefore had to be modified in certain key areas to make it suitable to use in conjunction with the AV1 IDI engine. The program written in BASIC for a Commodore CBM 4032 minicomputer is used to convert the experimental readings into meaningful engine performance data (eg. thermal efficiency, shaft power, etc.).

The program requires the experimental data to be keyboard entered during the actual test. Its virtually instantaneous output is used to assess the acceptability of each test with respect to engine stabilisation, instrumentation mis-readings, etc. The input structure is such that a number of instruments are read more than once (e.g. cooling water temperatures and speed) so that an average of the particular reading can be used within the main program.

A sample output result sheet using the data reduction program can be seen in table 4.3. Having obtained families of these output sheets for several operating conditions, the more important parameters were tabulated for easy analysis, as can be seen in tables 4.4, 4.5, and 4.6.

4.3.2 Cylinder Pressure Recording

In a previous research, Cole (ref. 19) used a data acquisition system that had been initially developed for the purpose of measuring transient signals from a combustion bomb (ref. 34). This system, using a CBM microcomputer, recorded digitally the transient data and transferred it to a tape cassette. The data from this cassette was then transferred to the University mainframe computer for detailed analysis. Although rather primitive, this system was considered feasible due to high costs of purchasing a proprietary data acquisition unit. Unfortunately the system became obsolete in that there was no longer any possible way of transferring captured data from the data acquisition system to the current mainframe computer short of tailoring an expensive network of cables which was economically impossible.

In the absence of a modern proprietary data acquisition system, an alternative method of capturing voltage signals from a piezo pressure transducer was required. A two channel digital storage scope (DSS) was tried and the result was favourable. After conducting a trial test it was observed that the DSS could satisfactorily record with reasonable accuracy a complete four stroke cycle or any part thereof.

The biggest drawback of this method of data acquisition was the lack of sampling or averaging so very necessary to data of this nature. With this arrangement only one cycle could be captured at any one time. Nevertheless, this avenue was the only realistic one under the given circumstances.

The captured pressure signal, along with one other trace, could be simultaneously recorded by the DSS. Initially this facility was stretched by coupling both needle-lift and TDC triggers on one channel and cylinder pressure on the other (see figure 4.1). Although this would have been an extremely useful combination, the idea had to be abandoned when the digitally stored voltages were analysed. It became clear that the digitally stored values corresponding to both needle-lift and TDC traces were intermingled in such a way that it was impossible to isolate them for analysis. Having tried all three possible combinations of input connections, the limitation of the Nicolet

3091 became clear.

Since the TDC trace was more important to the analysis than needle lift, it was considered good policy to store only the cylinder pressure and TDC traces. Figure 4.2 shows two traces where the needle lift has been completely omitted in both cases.

The method of determining IVC and EVO events of the captured data was complicated by the limitations of the DSS. It had to be inferred from the TDC points as to where the closed period was on any captured trace. This meant that at least two separate TDC points had to be captured as well as an entire closed period trace for the valve events to be calculated. For the slowest speed of 1000 rev/min it was not possible to capture both closed period and two TDC points simultaneously without sacrificing resolution. Figure 4.1b shows an output at 1000 rev/min where only one TDC point could be stored on an otherwise clear closed period pressure trace. This trace was of no use, as no analysis was possible due to the lack of information regarding valve events. This further limitation meant that resolution had to be sacrificed in order that satisfactory 1000 rev/min signals could be stored.

Figure 4.2b shows the loss in resolution which unfortunately applied to both the TDC and pressure traces. As can be seen from figure 4.2b, only three TDC points out of a total of four could be stored, as the poor resolution often missed the somewhat faint TDC points. As a consequence many runs at 1000 rev/min had to be carried out in order that clear traces with enough information could be captured.

Having captured a satisfactory set of pressure and TDC traces, the process of transferring the data from the DSS to the mainframe was conducted in the following manner:

1) The necessary pressure and crank angle data were stored in the DSS memory.
2) The stored data was transferred to a BBC computer using a package prepared by Barker (ref. 20).

3) The stored BBC data was trimmed using a separate program in order to locate IVC and EVO. This program also converted voltage levels into pressure including an adjustment for an assumed pressure at IVC.
4) This trimmed data was then stored and transferred to the University mainframe system (Gould) for processing.
5) The pressure data was then smoothed on the mainframe computer using a series of NAG subroutines.
6) Analysis of the smoothed data resulted in numerical output.
7) Numerical output from the analysis program was then plotted.

The above process is shown in schematic format in fig. 3.19.
The reasons a BBC computer was chosen instead of a more versatile and up to date PC compatible machine was the need to have to rewrite a fully functional (and rather complex) package to interface the Nicolet DSS to the PC compatible computer. It was fortunate that Barker (ref. 20) had already written a comprehensive package which would have taken months to finalise had it been necessary to write it ab initio.

The full set of processed pressure records for both the standard and insulated builds of the engine was used to obtain the heat release results described in Chapter 6.

4.4 Engine Performance Results

It is important to reiterate the fact that the baseline engine is not a factory original engine running under the marker's recommended settings. The modifications as per table 3.2 apply throughout the course of this study and reference to a "standard" engine or "standard build" apply to an engine running with a standard piston and not standard fuel injection timing or cracking pressure.

Although a wide range of results were obtained for the engine running as per the manufacturer's settings, and under boosted conditions, these are not included here. Due to the volume of information produced during each test, the only "standard build"

results presented will be those for which a "ceramic engine" is also available, ie with retarded timing and reduced fuel cracking pressure.

Results from the data reduction program presented in the format shown in table 4.3 are compressed into the more meaningful data shown in tables 4.4, 4.5, and 4.6. Plotting the values of these tables results in the graphs shown in figures 4.3 to 4.18 for the "standard " engine and figures 4.19 to 4.34 for the "ceramic cap engine".

All performance results are presented on a base of fuel energy input at four different torque levels (¼, ½, ¾ and full load at a series of fixed speeds). By this means, comparisons between standard and insulated engine performance, especially with respect to energy balances, can readily be made. "Full load" is defined as the torque developed by the engine at 1500 rev/min and an air/fuel ratio of 25:1.

4.4.1 Standard Engine Performance

Shaft performance

As expected, the engine produces more power at the flywheel, as more fuel is fed to it; figures 4.3, 4.4 and 4.5 confirm this. Since BMEP is proportional to torque it is to be expected that both figures 4.4 and 4.5 show identical trends. It is interesting that the torque curves of this engine become less steep with increasing speed, suggesting higher frictional losses (and hence FMEP) with increasing speed.

Figure 4.6 for brake thermal efficiency versus fuel energy input confirms the above statement by showing an increase in thermal efficiency with decreasing speed at all load levels. In addition, there is evidence for an increase in friction with increased fuelling reflected in reduced slope of the efficiency curves at the highest load levels.

The specific fuel consumption curves shown in figure 4.7 are obviously inversions of the brake thermal efficiency curves.

Flow through engine

In figures 4.8 for air flow and especially figure 4.9 for volumetric efficiency, the breathing capability of the engine is clearly shown to reach a peak in the progressive increase of air flow at speeds up to 1400 rev/min. This is the point where volumetric efficiency levels off and any increase in speed (and fuel) will not increase volumetric efficiency, although air flow will continue to increase.

The rate at which the air-fuel ratio trends become less steep (figure 4.10) with increasing fuel input reflect a rectangular hyperbola relationship. This is due to the relatively constant air flow and volumetric efficiency for a given speed (see figures 4.9 and 4.8). Since air flow is fairly constant for any one speed, the fuel input increases with load resulting in the air-fuel ratio to be inversely proportional to fuel flow viz

$$A/F = \frac{m_a}{m_f} = \frac{\text{constant}}{m_f}$$

Which results in a rectangular hyperbola relationship reinforced by the specific air consumption trends shown in figure 4.11.

Heat rejection to coolant and exhaust

It is difficult to gain a full breakdown of information from the coolant energy plots of figures 4.12 and 4.13. The more irregular trends in figure 4.13 can be explained by the small inaccuracies in heat loss to coolant measurements being amplified with respect to the quantity of fuel injected. Heat loss to coolant is measured indirectly by flow and temperature rise measurements in the water and oil heat exchangers. These quantities are small and therefore difficult to measure. Furthermore, they require a long time to stabilise. Hence high accuracy is difficult to achieve. As a means of reducing the possible errors incurred by such small quantities, several readings are taken and averaged over the test period.

It can be seen from figure 4.12, showing absolute heat rejection to coolant, i.e. combined heat rejection to coolant water and oil heat exchangers, that more energy is rejected as the engine is loaded for obvious reasons, while figure 4.13 shows a reduction at any one speed in percentage heat rejection to coolant (ie water plus oil) with increased load. This latter trend is also confirmed by analysis (see section 4.5).

Obviously the objective of having a cooling system is to preserve the engine components and by maintaining a set cooling jacket temperature, any extra heat energy input will be channelled to the exhaust. Figures 4.14, 4.15 and 4.16 show precisely this effect as well as the fact that more energy is passed onto the exhaust at higher speeds due to less available time for heat transfer to take place between combustion gases and cylinder walls. Exhaust energy is defined as the enthalpy of the gas in the exhaust system relative to that of the inlet manifold.

$$\text{Exhaust energy} = m_{ex}\, Cp_{ex}\, T_{ex} - m_a\, Cp_a\, T_a$$

Although the temperature of the inlet air is not shown in tables 4.4, 4.5, and 4.6, it was constant at around 21°C $\pm$1°C.

Figure 4.17 shows a trend towards more heat rejection to oil, as speed and to a lesser extent as load, increases as a result of greater loading of the bearings and general heat transfer.

Ideally the heat balance on any set of calculations should be 100%, but as can be seen in figure 4.18, the lower fuelling rates show more unaccountable heat losses. This is mainly due to lack of accuracy of the heat lost to coolant measurements explained previously and the fact that radiation losses are not accounted for.

4.4.2 Ceramic Cap Engine Performance

The ceramic cap piston assembly was introduced into the engine with a new set of piston rings which under normal circumstances would require a running in period as per the schedules shown in tables 4.1 or 4.2. This running in period was dispensed with as it was certain that this engine would not be expected to run for hundreds of hours.

The results obtained from running the Cordierite piston cap assembly can be seen in tabulated form in tables 4.4 and 4.5 and graphically in figures 4.19 to 4.34. The comments previously made regarding the performance analysis of the standard engine in section 4.4.1 also apply to this engine except for the obvious differences which will be discussed in this section.

Shaft performance

Although the differences in brake power trends of figures 4.19 and 4.3 are not immediately obvious, close examination of the tabulated values of tables 4.4 and 4.5 reveals that more fuel is required to produce the same power output in the case of the insulated engine.

The amount of additional fuel needed to produce the same torque (or BMEP) in the insulated engine increases with load, as can be seen in tables 4.4 and 4.5 and figures 4.20, 4.21 (and their equivalent 4.4 and 4.5).

Comparison of figures 4.22 and 4.6 and of tables 4.4 and 4.5 shows that the insulated engine is always less efficient than the standard engine, the difference approaching two percentage points at the highest loads and speeds. The absolute level of efficiency always remains below 30%. This is not surprising in view of the combination of large mechanical losses in single cylinder engines and of the thermodynamic losses associated with IDI engines as well as retarded injection.

The geometric shift of the specific fuel consumption trends of figures 4.23 and 4.7

show the insulated engine to be less efficient at converting fuel input into useful work and especially so at the higher speeds. This is seen as a direct result of the higher energy loss to coolant at higher loads and speeds, and to exhaust, at all loads and speeds.

Flow through engine

The air flow figures of 4.24 and 4.8 and of tables 4.4 and 4.5 show the standard engine to induce much more air than the insulated engine, this is also reflected by better volumetric efficiency (see figures 4.25 and 4.9). It is noted in figures 4.24 and 4.25 that small errors in airflow measurements at the 1000 rev/min condition are amplified greatly in the corresponding volumetric efficiency plots.

The reason for the poorer volumetric efficiency (and low air flow) of the insulated engine relative to the standard engine shown in figures 4.25 and 4.9 and tables 4.4 and 4.5, is charge heating due to the much hotter piston cap. The piston draws approximately the same volume of air into the cylinder on the induction stroke but because the ceramic cap is at a much higher temperature than the standard aluminium one, the induced air is heated up thus reducing its density and hence its mass. This means that the mass of air available for combustion in the standard engine is substantially greater resulting in a higher relative air-fuel ratio for a fixed fuelling.

This is clearly seen in figures 4.26 and 4.10, and tables 4.4 and 4.5 where for a given load at any one speed,the air-fuel ratio is higher for the standard engine than the insulated one.

The specific air consumption (SAC) trends of figures 4.27 and 4.11 follow the same general pattern with the insulated engine always showing a lower SAC than the standard engine at the same level of fuelling.

Heat rejection to coolant and exhaust

The heat loss to coolant parameters of figures 4.28 and 4.12, and tables 4.4 and 4.5, show a higher loss at higher loads for the insulated engine and lower loss at lower

loads with a break-even point near the half load condition. This half load break-even point also applies to the percentage energy lost to coolant (figures 4.29 and 4.13) but due to congestion of data points on these plots, figures 4.28 and 4.12 showing absolute heat loss to coolant will be discussed. It can be seen from figures 4.28 and 4.12 (and tables 4.4 and 4.5) that the higher speeds of 1400 and 1500 rev/min lower the break-even point discussed earlier to near quarter load. An explanation for this "cross-over" point could be related to heat transfer. The insulated engine running at low loads loses less heat to coolant since the metallic combustion chamber walls are relatively cool and heat loss through the insulated piston is reduced. The same engine at full load, however, will find it easier to direct a higher percentage to coolant since the temperature of the metallic components will now have increased significantly. These results confirm the findings of other researchers that heat transfer can increase in a partially insulated engine rather than decrease, under certain circumstances (ref. 12,13), and insulation does not always produce a total improvement or deterioration in an operating parameter (ref. 35,36).

The simplest physical explanation is that with the higher in-cylinder gas temperature of the insulated engine, due to the charge heating effects already discussed,the rate of heat flow actually increases through those parts of the combustion chamber wall which are not insulated (namely cylinder head, valves,and cylinder liner). The simulation program ODES, on the other hand, fails to predict this cross over condition (see figure 4.46). It gives excellent agreement with the experimental heat rejection to coolant for the standard engine, (figure 4.38) but underpredicts heat loss at high speeds for the insulated engine (figure 4.44). The behaviour of ODES in the way it predicts the performance of the Petter AV1 engine is further explained in section 4.5 of this chapter.

The fact that exhaust energy in general increases in an insulated engine is proved in figures 4.30, 4.31 and 4.14, 4.15 and tables 4.4 and 4.5. This increase in exhaust energy never exceeds 0.5 KW which for this low BMEP engine is nevertheless over 15% of the maximum useful power the engine can produce.

The exhaust temperatures for a given fuelling level are higher by up to 100°C (see figures 4.32 and 4.16, and tables 4.4 and 4.5) for the insulated engine. The temperature difference between exhaust and inlet temperature of the insulated engine is consequently also higher than that of the standard engine with the greatest differences at the higher loads.

The heat rejection to oil does not seem to be greatly affected by insulation; the plots of figures 4.33 and 4.17 do not show significant differences with both engines rejecting similar amounts of heat to the oil.

Figure 4.34 shows the heat balance defined as the sum of;

a) percentage heat to useful work
b) percentage heat to water
c) percentage heat to oil
d) percentage heat to exhaust (relative to inlet)

It can be seen that the full load results significantly exceed 100% which is due to errors in obtaining experimental data; on the other hand, at lower fuellings there are very high, unaccountable heat losses. This is mainly attributed to the general heat transfer from the whole engine as a unit (including exhaust system, cooling system etc.) to the surroundings. The greatest error, particularly at light load is thought to occur in connection with the calculation of heat rejection in the water and oil heat exchangers. The temperature rise at low loads is of the order of 5°C which is also subject to fluctuations of ±1°C. Clearly in spite of every care taken in making the various measurements, considerable errors remain.

4.5 Comparison of Experimental and Simulation Results Using ODES

An engine simulation package was written by Chen (ref. 23) based on earlier work by Tarabad (ref. 37). This comprehensive package is based on a step by step filling and emptying method which treats individual engine and turbomachinary components as

separate control volumes. The program is capable of simulating a wide range of engine configurations from a basic single cylinder four stroke naturally aspirated 550cc unit, to a sophisticated 12 cylinder two stroke highly rated turbocompounded system.

The control volumes defined by the user are connected to each other by a series of orifices or valves. Heat transfer correlations due to Annand (ref. 38) or Woschni (ref. 22) are both available as options. Valve geometry and discharge coefficient values are used in the data file such that it is possible to vary or scale any aspect of the flow through the valves from physical size and shape, to directional discharge coefficient.

A typical output from ODES can be seen in table 4.7. The way in which the results are laid out is very comprehensive and any comparison between experimental and simulation results will have to be limited to those aspects of performance covered by the experimental work.

As a consequence, it was decided to compare only BMEP, thermal efficiency, air-fuel ratio, coolant energy and exhaust temperature. The following two subsections deal with the "standard" and "insulated" engines respectively. The condition chosen to match the program to experimental results was the 1500 rev/min ½ load case. This condition was chosen because the engine was originally rated at 1500 rev/min by the manufacturer. Having found a matched result, the only parameters that were varied were, engine speed and fuel energy input.

4.5.1 Standard Engine

The results of matching the standard engine are shown in figures 4.35 to 4.40. The basic overall pattern shows the BMEP (fig. 4.35) to be well predicted, but as with the thermal efficiency plots of figure 4.36, the general trend is for a lower prediction at the higher fuellings and a higher one at the lower fuellings. Although the BMEP shows this trend, it is more pronounced in the thermal efficiency plots.

This inaccuracy is attributed to the way in which the package models the overall friction. Clearly the model does not accurately simulate the behaviour of the overall engine friction throughout it's operation range. The friction model used in ODES is that due to Chen and Flynn (ref. 39) where the FMEP is represented as follows:

$$FMEP = A + B\ P_{max} + C\ cp$$

Where A, B and C are constants,

P_{max} is the maximum cylinder pressure,

and cp is the mean piston speed.

An attempt was made at rectifying the influence of the FMEP on the results by varying the A constant. In hindsight it would have been more appropriate to vary the B constant as this would have resulted in a change in FMEP gradient and hence an improved overall match. As the matching exercise was rather time consuming, a line was drawn to prevent endless attempts at matching some 32 operating conditions. It was found during the matching exercise that many runs had to be executed for every changed parameter in order that the whole "engine" could be made to respond in the intended manner.

Had there been more time, an empirical relationship for the FMEP could have been obtained in order that the engine could be perfectly matched over it's entire operating range. The relationship would have been based on previous work by Cole (ref. 19) who ran the very engine in question (in D.I. form) under motored conditions. Cole found that the friction and auxiliary power absorbed by the engine represented 0.6KW at 1000 rev/min and 1.1KW at 1500 rev/min. The relationship was found to be non linear over this range. Although this work by Cole gives an indication of the order of magnitude for FMEP, it is by no means a basis for an empirical relationship since the engine used for this research had a higher compression ratio and smaller bore resulting in a different pumping work characteristic.

The air-fuel ratio of figure 4.37 shows an excellent match for the 1500 rev/min and

1200 rev/min speeds and a good match for the other two speeds. It is interesting to note that the valve geometry and flow behaviour of the air into the engine is more comprehensively modelled than that for friction. By inference the volumetric efficiency would also match as closely as the air-fuel ratio which is why it was not included in this exercise.

Figure 4.38 shows a rather congested heat loss to coolant plot suggesting that a good match was found, and as in the previous plot (for air-fuel ratio), the match is consistent over the entire operating range*. The reason for including the percentage heat loss to coolant (fig. 4.39) in the comparison exercise is obviously not based on any geometric patterns that the experimental results portray (see section 4.4.1 under "Heat rejection to coolant and exhaust" for reasons regarding irregular percentage heat loss to coolant patterns). The superimposition of the experimental and matched results shows that the simulation program has realistically apportioned the fractions of the injected fuel energy to useful work, coolant (water and oil) though, as can be seen from figure 4.40, rather less so in the case of exhaust.

The exhaust temperature trends of figure 4.40, show a poor match between the experimental and predicted results. An explanation for this could be in the way ODES models the exhaust gas flow, but a more plausible explanation could be inaccuracies in the experimental results. It has always been difficult to measure a transient parameter such as exhaust temperature where the flow is pulsating and conduction from the walls is significant. Although every attempt has been made at measuring the exhaust temperature as accurately as possible (see chapter 3 section 5.9) this discrepancy has to be largely attributed to experimental errors. Had the problem been related to the simulation results, the predicted temperatures of figure 4.40 would have been higher not lower than the experimental values, for the following reason.

* Footnote

The heat loss to coolant as plotted in this chapter, excludes for reasons connected with the program output print-out, the heat loss from the prechamber which appears in a separate output block. The resultant overestimate of heat loss to coolant would then partly balance the underestimate of exhaust temperature at the higher loads. Figures 4.38, 4.39, 4.44, and 4.45 refering to heat loss to coolant have been replotted including the heat loss from the prechamber and are presented in appendix 1.

Since friction is underestimated at low loads and overestimated at high loads, one would expect to see an underestimate of heat loss to coolant at low load and the reverse at high load. Figure 4.38, however, shows a good match for heat lost to coolant suggesting the friction mismatch to be portrayed in the exhaust temperature. Since thermal efficiency is overestimated at low loads and underestimated at high loads (see figure 4.36), one would expect the heat loss to exhaust to show the reverse prediction, given that heat lost to coolant is correctly estimated. In fact the reverse is the case suggesting that indeed, the measurement of exhaust temperature must be called into question.

4.5.2 Ceramic Cap Engine

The results of figures 4.41 to 4.47 show to a large extent the same patterns and trends as those for the standard engine, and as such, the arguments made in section 4.5.1 apply to the analysis of the insulated engine predictions. Having changed the piston, the friction behaviour of the engine is not directly affected which is why the BMEP and thermal efficiency of figures 4.41 and 4.42 are similar to those of the standard engine. The only difference is in the absolute values and the relative difference of the predicted results to the experimental equivalents which is negligible.

The air-fuel ratio matching is not as accurate in the insulated case as the standard case (figures 4.43 and 4.37 respectively) with the lower speeds being worst affected. An explanation for this could be the charge heating phenomenon explained earlier where the hot cylinder draws a less dense charge resulting in a lower air-fuel ratio. The model overestimates the quantity of air at the lower speeds (and the higher loads) which is possibly due to the heat transfer model not simulating accurately the heat distribution in the cylinder over the entire cycle. Another theory is the possibility of a correct temperature distribution but an incorrect effect on the incoming charge.

Unlike the standard engine simulation results, the coolant energy distribution for the insulated engine is unsatisfactory (see figures 4.44 and 4.38). The fact that the engine

configuration has been altered by a significant change to a critical heat transfer component -namely the piston- has obviously thrown the matching significantly. Although the match was re-optimised at the 1500 rev/min 50% load condition, the overall match has not been very successful. The gradient of the matched results need to be rotated anticlockwise about a pivot point of approximately 2.5KW coolant energy and 7KW fuel input. The suggestion is therefore, that the program underestimates at the higher speeds and loads and overestimates at the other extreme.

When figure 4.45 for percentage coolant energy loss is studied, it becomes difficult to have full confidence in the experimental results. The problem with these results lies predominantly in the lower fuelling levels where both fuel input and power output are relatively low. At these low levels of fuelling and output, the very small flows and temperature differences in the oil and water heat exchangers amplify the slightest errors.

Figure 4.46 comparing computed coolant heat loss for the standard and insulated engine shows that ODES predicts a lower coolant heat loss for the insulated engine over the whole range of speeds and loads. This is obviously not reflected by the experimental results which suggest a "cross-over" point at approximately 3KW coolant energy (see section 4.4.2). The reason ODES shows no "cross-over" can be seen in fig. 4.44 where there is a marked discrepancy in the gradients, the heat loss at high loads and speeds being substantially underpredicted.

If ODES is to be believed, it can be said that insulation of piston only, results in a reduced heat loss to coolant. If however, the experimental findings are to be believed, it would appear that selective insulation results in more heat rejection to coolant at high loads and speeds and less at lower speeds and lower loads. Judging by the matching reflected by figures 4.42 to 4.45 it may be easier to accept that the experimental results are more credible.

The exhaust temperature trends for the insulated case are similar to those of the standard engine (see figures 4.40 and 4.47) and as such are explained using the same

arguments. No "cross-over" is evident in any exhaust temperature plots be it experimental or simulated.

To confirm the ability of ODES to sensibly simulate the two engine configurations, exhaust temperature is plotted for both engine builds using the predicted results in figure 4.48. Clearly the trends are as expected with the insulated engine showing higher exhaust temperatures for every condition, and the higher speeds and loads showing more significant increases.

4.6 Conclusions Based on the Analysis of Performance Results

In this section, all the observations made in this chapter will be highlighted in order to asses the general effects of selective insulation on the Petter AV1 engine.

It was observed that the insulated engine consumed more fuel to produce the same torque (or BMEP). This increase in fuel consumption appeared to increase with both load and speed.

The insulated engine showed all the expected trends of increased exhaust enthalpy and decreased volumetric efficiency but highlighted an interesting "cross-over" in coolant energy. It was found that the insulated engine shows a higher loss in coolant energy at higher loads and lower loss at lower loads with a break even point at the ½ load condition. Heat rejection to oil appears to be unaffected by insulation.

Time (mins)	Speed (rev/min)	Load (%)
90	1000	25
30	1200	25
60	1000	50
30	1400	50
15	1000	75
15	1200	75
15	1400	75
15	1000	100
15	1200	100
15	1400	50
15	1800	50
15	1500	75
15	1800	75
15	2000	75
15	1500	100
15	1600	100
15	1800	100
15	2000	100

Table 4.1 : Hepworth and grandage Running-in schedule.

Time (mins)	Speed (rev/min)	Load (%)
90	1000	25
30	1200	25
30	1000	50
30	1400	50
15	1000	75
15	1200	75
15	1400	75
15	1000	100
15	1200	100
15	1400	75
15	1500	75
15	1500	100
15	1600	100

Table 4.2 : Modified Hepworth and Grandage Running-in schedule

ADIABATIC PROJECT DATA REDUCTION - 1989

TEST NAME 1800 REV/MIN 1.5BAR BOOST FULL LOAD

PETTER AV1 SINGLE CYLINDER DIESEL

SPEED (RPM)	1800.00
POWER (KW)	5.86
TORQUE (NM)	31.11
BMEP (BAR)	7.07
THERMAL EFFICIENCY (%)	30.70
VOLUMETRIC EFFICIENCY (%)	96.35
AIR-FUEL RATIO	28.40
SFC (G/KW.HOUR)	273.43
SAC (G/KW.HOUR)	7767.79
AIR MAN PRESSURE (BAR)	1.46
EXHAUST MAN PRESSURE (BAR)	1.48
AIR INLET TEMP (C)	50.00
EXHAUST TEMP (C)	434.00
FUEL ENERGY INPUT (KW)	19.10
SHAFT POWER (KW)	5.86
COOLANT ENERGY (KW)	7.74
% COOLANT ENERGY	40.53
OIL ENERGY (KW)	.56
EXHAUST ENERGY 1 (KW)	5.35
% EXHAUST ENERGY	28.01
HEAT BALANCE (%)	102.18
AIR FLOW (LI/SEC)	7.98
AIR FLOW (G/SEC)	12.65
AIR DENSITY (KG/M3)	1.58
FUEL FLOW (G/SEC)	.44
FUEL PER INJECTION (MG/INJ)	29.69
ENGINE COOLANT FLOW (KG/SEC)	.08
OIL COOLANT FLOW (LI/HR)	53.93
OIL TEMPERATURE (C)	31.00
WATER INLET TEMPERATURE (C)	52.97
MEAN WATER TEMP RISE (C)	22.00

Table 4.3 : Sample output sheet using the data reduction program.

Engine configuration	1000 rev/min Standard build				1000 rev/min Insulated engine				1200 rev/min Standard build				1200 rev/min Insulated engine			
Test number	SB1	SB2	SB3	SB4	CP1	CP2	CP3	CP4	SB5	SB6	SB7	SB8	CP5	CP6	CP7	CP8
Load (%)	25	50	75	100	25	50	75	100	25	50	75	100	25	50	75	100
Engine speed (rev/min)	995.0	999.5	996.5	1002.5	997.5	1017	1004	1001.5	1197	1201	1198	1201	1200	1203	1205	1199
Brake power (KW)	0.54	1.08	1.64	2.22	0.54	1.12	1.65	2.2	0.65	1.31	1.97	2.67	0.65	1.33	1.98	2.63
Torque (Nm)	5.20	10.36	15.78	21.16	5.23	10.57	15.75	21.04	5.19	10.48	15.76	21.27	5.22	10.57	15.72	20.98
BMEP (bar)	1.18	2.35	3.58	4.81	1.18	2.4	3.57	4.78	1.17	2.38	3.58	4.83	1.18	2.4	3.57	4.76
Thermal efficiency (%)	16.17	22.32	26.97	29.86	15.5	22.07	26.08	27.62	15.84	22.05	26.44	29.57	15.15	21.81	25.7	27.66
S.F.C. (g/KW.Hr.)	519	376	311	281	554	380	322	304	530	381	317	284	554	385	327	304
Air flow (g/s)	4.6	4.58	4.62	4.55	3.95	4.65	4.02	4.25	5.73	5.73	5.65	5.54	5.72	5.58	5.18	5.20
Volumetric efficiency (%)	89.18	89.03	88.6	87.6	85.69	86.16	78.74	82.17	91.75	91.47	90.4	88.33	89.39	87.47	84.82	84.67
Air/Fuel ratio	58.86	40.48	32.49	26.26	54.57	39.10	27.17	22.81	59.89	41.13	32.43	26.27	56.67	39.22	28.83	23.44
S.A.C. (g/KW.Hr.)	30559	15222	10114	7385	30224	14875	8744	6933	31732	15662	10297	7459	31402	15096	9418	7115
* Water coolant energy (KW)	1.58	1.74	2.44	3.01	1.47	1.85	3.03	3.82	1.89	2.35	3.01	3.58	1.62	2.06	3.41	4.34
* Water coolant energy (%)	47.19	35.97	39.97	40.57	40.84	36.38	47.84	47.84	46.21	39.36	40.26	39.66	37.62	33.87	44.22	45.65
Exhaust energy (KW)	0.83	1.17	1.5	1.88	0.95	1.33	1.53	2.14	1.10	1.54	1.96	2.45	1.28	1.76	2.12	2.84
Exhaust energy (%)	17.28	18.37	19.43	20.57	19.12	20.24	19.41	22.28	19.05	19.71	20.87	22.22	21.81	22.75	22.32	24.97
Exhaust temperature (°C)	146	204	262	332	165	230	308	400	156	219	282	356	180	257	331	434
Oil energy (KW)	0.19	0.2	0.19	0.2	0.17	0.2	0.24	0.21	0.25	0.2	0.18	0.22	0.23	0.26	0.23	0.26
Heat balance (%)	94.19	88.53	94.79	98.51	87.29	88.69	101.9	105.0	95.34	90.59	95.43	98.86	87.83	88.89	100.5	106.0
Fuel flow (g/s)	0.07	0.11	0.14	0.17	0.08	0.11	0.14	0.18	0.09	0.13	0.17	0.21	0.10	0.14	0.17	0.22
Fuel per injection (mg/inj)	9.43	13.6	17.14	20.77	10.12	14.04	17.69	22.32	9.59	13.93	17.47	21.07	10.09	14.20	17.92	22.32
Fuel energy input (KW)	3.35	4.86	6.10	7.44	3.60	5.10	6.34	7.99	4.10	5.97	7.48	9.04	4.32	6.1	7.71	9.52

* Combined heat rejection to cooling water and oil heat exchanger (see fig. 3.9)

Table 4.4 : Performance results for engine speeds of 1000 rev/min and 1200 rev/min.

Engine configuration	1400 rev/min Standard build				1400 rev/min Insulated engine				1500 rev/min Standard build				1500 rev/min Insulated engine			
Test number	SB9	SB10	SB11	SB12	CP9	CP10	CP11	CP12	SB13	SB14	SB15	SB16	CP13	CP14	CP15	CP16
Load (%)	25	50	75	100	25	50	75	100	25	50	75	100	25	50	75	100
Engine speed (rev/min)	1401	1397	1399	1403.5	1399	1407	1399	1402.5	1497	1499	1500	1500	1493	1495	1503	1501
Brake power (KW)	0.77	1.54	2.3	3.1	0.76	1.52	2.34	3.09	0.81	1.65	2.46	3.31	0.81	1.64	2.46	3.30
Torque (Nm)	5.28	10.53	15.73	21.15	5.22	10.33	16.02	21.09	5.20	10.54	15.72	21.07	5.23	10.53	15.67	21.06
BMEP (bar)	1.19	2.39	3.57	4.80	1.18	2.34	3.64	4.79	1.18	2.39	3.57	4.78	1.18	2.39	3.56	4.78
Thermal efficiency (%)	14.20	21.78	26.45	29.50	14.34	22.94	25.29	27.31	14.22	21.89	26.27	28.26	13.74	19.87	24.69	26.59
S.F.C. (g/KW.Hr.)	591	385	317	295	585	401	332	307	590	383	320	297	611	422	340	316
Air flow (g/s)	6.99	6.92	6.82	6.74	6.71	6.54	6.16	6.15	7.38	7.35	7.25	7.09	7.19	6.82	6.65	6.62
Volumetric efficiency (%)	93.67	92.94	91.84	89.80	90.01	90.46	87.03	85.80	93.32	93.66	93.26	92.18	90.64	89.76	87.44	86.84
Air/Fuel ratio	55.02	42.0	33.57	26.52	53.91	38.60	28.50	23.28	55.21	41.69	33.08	25.99	51.82	35.27	28.54	22.83
S.A.C. (g/KW.Hr.)	32531	16190	10654	7811	31548	15474	9460	7157	32592	15986	10572	7720	31641	14903	9703	7210
* Water coolant energy (KW)	2.14	2.67	3.33	4.02	1.98	2.94	3.92	4.73	2.47	3.00	3.64	4.51	2.00	3.37	4.36	5.23
* Water coolant energy (%)	39.41	37.81	38.32	36.88	37.29	40.53	42.34	41.73	43.05	39.75	38.79	38.55	33.6	40.62	43.7	42.04
Exhaust energy (KW)	1.55	2.01	2.53	3.19	1.65	2.17	2.77	3.60	1.71	2.23	2.81	3.48	1.90	2.58	3.13	4.11
Exhaust energy (%)	20.9	22.15	23.37	24.22	23.37	23.62	24.57	26.47	22.27	23.13	24.19	24.62	24.41	25.07	25.92	27.67
Exhaust temperature (°C)	176	234	299	376	199	269	364	460	186	247	316	395	214	309	382	487
Oil energy (KW)	0.20	0.22	0.24	0.24	0.25	0.23	0.27	0.3	0.27	0.30	0.36	0.39	0.30	0.29	0.27	0.33
Heat balance (%)	85.75	91.29	96.62	96.96	87.43	94.51	100.5	103.5	92.09	95.25	98.86	99.91	84.44	95.21	102.6	104.4
Fuel flow (g/s)	0.12	0.16	0.20	0.25	0.12	0.16	0.21	0.26	0.13	0.17	0.21	0.27	0.13	0.19	0.23	0.29
Fuel per injection (mg/inj)	10.89	14.16	17.43	21.74	10.66	14.46	18.55	22.62	10.72	14.11	17.53	21.84	11.15	15.53	18.60	23.21
Fuel energy input (KW)	5.45	7.07	8.71	10.9	5.33	7.27	9.27	11.34	5.73	7.56	9.40	11.71	5.95	8.29	9.99	12.44

* Combined heat rejection to cooling water and oil heat exchanger (see fig. 3.9)

Table 4.5 : Performance results for engine speeds of 1400 rev/min and 1500 rev/min

Engine configuration	1600 rev/min Standard build				1800 rev/min Standard build			
Test number	SB17	SB18	SB19	SB20	SB21	SB22	SB23	SB24
Load (%)	25	50	75	100	25	50	75	100
Engine speed (rev/min)	1593	1600	1599	1597	1793	1798	1805	1803
Brake power (KW)	0.87	1.74	2.64	3.51	0.96	1.99	2.96	4.01
Torque (Nm)	5.22	10.44	15.78	21.03	5.14	10.62	15.70	21.25
BMEP (bar)	1.18	2.39	3.58	4.77	1.16	2.41	3.56	4.83
Thermal efficiency (%)	13.89	20.93	25.52	28.30	13.38	20.85	24.93	27.31
S.F.C. (g/KW.Hr.)	604	401	329	297	627	403	337	307
Air flow (g/s)	7.72	7.68	7.64	7.53	8.44	8.39	8.37	8.25
Volumetric efficiency (%)	93.95	92.56	91.65	90.35	90.53	89.64	88.71	87.90
Air/Fuel ratio	52.87	39.45	31.67	25.99	50.19	37.52	30.17	24.08
S.A.C. (g/KW.Hr.)	31953	15819	10417	7708	31482	15107	10159	7403
* Water coolant energy (KW)	2.63	3.16	3.90	4.68	2.89	3.58	4.52	5.47
* Water coolant energy (%)	42.05	37.87	37.70	37.71	40.15	37.39	38.00	37.24
Exhaust energy (KW)	1.88	2.51	3.18	3.86	2.24	3.02	3.86	4.81
Exhaust energy (%)	22.55	23.75	25.07	25.86	23.80	25.32	26.79	27.32
Exhaust temperature (°C)	200	267	337	410	217	294	372	459
Oil energy (KW)	0.44	0.44	0.42	0.48	0.53	0.52	0.51	0.51
Heat balance (%)	93.11	94.10	98.13	101.0	92.15	95.35	99.77	100.8
Fuel flow (g/s)	0.14	0.19	0.24	0.28	0.16	0.22	0.27	0.34
Fuel per injection (mg/inj)	11.01	14.61	18.12	21.77	11.26	14.92	18.45	22.80
Fuel energy input (KW)	6.26	8.35	10.35	12.42	7.21	9.58	11.90	14.70

* Combined heat rejection to cooling water and oil heat exchanger (see fig. 3.9)

Table 4.6 : Performance results for engine speeds of 1600 rev/min and 1800 rev/min.

```
  oo     ddd     eeee     sss
 o  o    d  d    e       s
 o  o    d  d    eeee     ss
 o  o    d  d    e          s
  oo     ddd     eeee    sss
 ================================

 THERMAL POWER ENGINEERING,SCHOOL OF ENGINEERING UNIVERSITY OF BATH
 DEVELOPED BY : C.CHEN
 ================================================================================
 AMBIENT CONDITIONS :
 Ambient Temp.(degK)295.0 Ambient Press(KN/M2)100.00 Back Press(KN/M2) 100.00
 Inlet Temp.(degK)  295.0 Inlet Press(KN/M2)  100.00
 --------------------------------------------------------------------------------
 SYSTEM PERFORMANE:
 Total Output Power (KW)          1.66   Overall Thermal Eff.           0.2196
 Overall B.S.F.C. (Kg/KW.H)     0.3830   Total Fuel Flow Rate (Kg/S)   0.00018
 --------------------------------------------------------------------------------
 SHAFT PERFORMANCE:
 Shaft Speed (REV/MIN)          1499.1   Shaft Power (KW)                 1.66
 Shaft Torque (N.M)              10.55
 --------------------------------------------------------------------------------
 MANIFOLD:
 Temperature  (degK) (t.a.)      295.0   Pressure  (KN/M2) (t.a.)         98.7
 Temperature  (degK) (m.a.)      295.0   Pressure  (KN/M2) (m.a.)         98.7
 Heat Loss (KW)                   0.00   Gas Temp (deg K) (htc a)        295.0
 Mean H.T.C.(KW/M2/K)           0.2840
 --------------------------------------------------------------------------------
 ENGINE SPECIFICATION:
 4 Stroke Divided Chamber Diesel Engine
 Bore (M)                       0.0800   Stroke (M)                      0.1100
 Connecting Rod Length (M)      0.2318   Compression Ratio               18.000
 Valve Timing (deg CA):
       EVC   364.50      IVC   575.50      EVO   144.50      IVO   355.50
 --------------------------------------------------------------------------------
 ENGINE PERFORMANCE:
 Engine Speed  (REV/MIN)          1499.   B.Power  (KW)                     1.7
 I.M.E.P. (KN/M2)                  277.   B.M.E.P. (KN/M2)                240.
 B.Torque   (N.M)                10.55   Charging Eff.  amb.0.8936  inl.0.9052
 Brake Thermal Efficiency       0.2195   Mechanical Efficiency          0.8639
 B.S.F.C. (KG/KW.HR)            0.3833   B.S.A.C. (KG/KW.HR)             15.77
 Air Flow  (KG/S)               0.0073   Air Volume Flow  (m3/S)        0.0061
 Trapped Air Fuel Ratio          42.44   Overall Air Fuel Ratio          41.34
 Delivery Ratio amb. 0.889  inl. 0.901   Charge Purity                  0.9858
 Max. Cyl. Pressure  (KN/M2)      4619.  Max. Cyl. Temperature (deg K)  1027.2
 Fuel/cyl/cyc  (G)              0.01411   Gas Heat Loss %                 36.73
 --------------------------------------------------------------------------------
 TRAPPED IN-CYLINDER CONDITIONS
 Temperature (deg.K)            342.95   Pressure (KN/M2)                110.47
 Equivalent Ratio              0.01195   Mass (KG)                      0.00058
 --------------------------------------------------------------------------------
 Pumping Work (KJ)             -0.0114   P.M.E.P. (KN/m2)                -20.6
 --------------------------------------------------------------------------------
 HEAT LOSS ANALYSIS:
 Thermal Resistance:(deg C/KW):R1,R2,R4,R5,R7,R8,R9,R10
     37.04     8.02     22.92     20.83     20.83    200.00     41.67    200.00
 Energy Input (KW)                 7.54   % Liner Heat Loss              17.08
 % Piston Heat Loss               11.21   % Head Heat Loss                8.44
 % Friction Loss                   3.46   % Output Shaft Energy          21.95
 Liner(mean) Temp. (deg K)        373.0   Piston Temp. (deg K)            431.2
 Head Temp. (deg K)               484.2   Cooling Water Temp. (deg K)     330.0
 Cooling Oil Temp. (deg K)        300.0   % Piston Heat Loss to Oil        6.81
 Gas Mean H.T.C (KW/M2.K)         0.786   Gas Mean Temp. (deg K)           533.
 Gas Temp (deg K) (htc a)         646.2   Piston Node Temp(K)              413.5
 % Heat Piston-Liner               4.40   % Total Heat to Water           30.78
 % Friction to Water               0.86   % Total Heat to Oil              9.41
 % Air-Enthalpy In                27.23   % Gas-Enthalpy Out               57.00
 --------------------------------------------------------------------------------
 COMBUSTION PARAMETERS: COMPRESSION IGNITION
 Static Injection (degree)        719.0   Dynamic Injection (degree)      719.0
 Ignition Delay (degree)           8.98   End of Burning (degree)         804.5
 Ignition Point (degree)          728.0   Mode of Burning                 0.534
 Mean Temp During Delay (degK)    818.    Mean Press Dur Delay (KN/M2)    4157.
 --------------------------------------------------------------------------------
 PRECHAMBER
 Max. Pressure (KN/M2)          4380.2   Max. Temperature (K)            1044.7
 Temperature  (degK) (t.a.)      558.2   Pressure  (KN/M2) (t.a.)         491.9
 Temperature  (degK) (m.a.)      726.2   Pressure  (KN/M2) (m.a.)        1800.2
 Heat Loss (%)                    5.71   Wall Temp (K)                   403.73
 Gas Mean H.T.C. (KW/M2.K)        0.473  Gas Temp (deg K) (htc a)         707.5
 --------------------------------------------------------------------------------
 MANIFOLD:
 Temperature  (degK) (t.a.)      520.8   Pressure  (KN/M2) (t.a.)         101.5
 Temperature  (degK) (m.a.)      520.8   Pressure  (KN/M2) (m.a.)         101.5
 Heat Loss (KW)                   0.06   Gas Temp (deg K) (htc a)         520.8
 Mean H.T.C.(KW/M2/K)           0.2840
 --------------------------------------------------------------------------------
 ORIFICE:
 Orifice Area (Sq.M)           0.00040   Flow Rate (Kg/S)                0.0073
 Exit Temp. (K) (t.a)            294.3   Exit Temp. (k) (m.a)             289.0
 --------------------------------------------------------------------------------
 VALVE:
 Flow Rate (Kg/S)               0.0073   Exit Temp. (K) (t.a)             302.3
 Exit Temp. (k) (m.a)            284.9
 --------------------------------------------------------------------------------
 ORIFICE:
 Orifice Area (Sq.M)           0.00011   Flow Rate (Kg/S)                0.0004
 Exit Temp. (K) (t.a)            545.4   Exit Temp. (k) (m.a)           -3886.1
 --------------------------------------------------------------------------------
 VALVE:
 Flow Rate (Kg/S)               0.0075   Exit Temp. (K) (t.a)             526.8
 Exit Temp. (k) (m.a)            532.8
 --------------------------------------------------------------------------------
 ORIFICE:
 Orifice Area (Sq.M)           0.00040   Flow Rate (Kg/S)                0.0073
 Exit Temp. (K) (t.a)            378.2   Exit Temp. (k) (m.a)             523.5
 --------------------------------------------------------------------------------
```

Table 4.7 : Sample output file using the analysis program ODES.

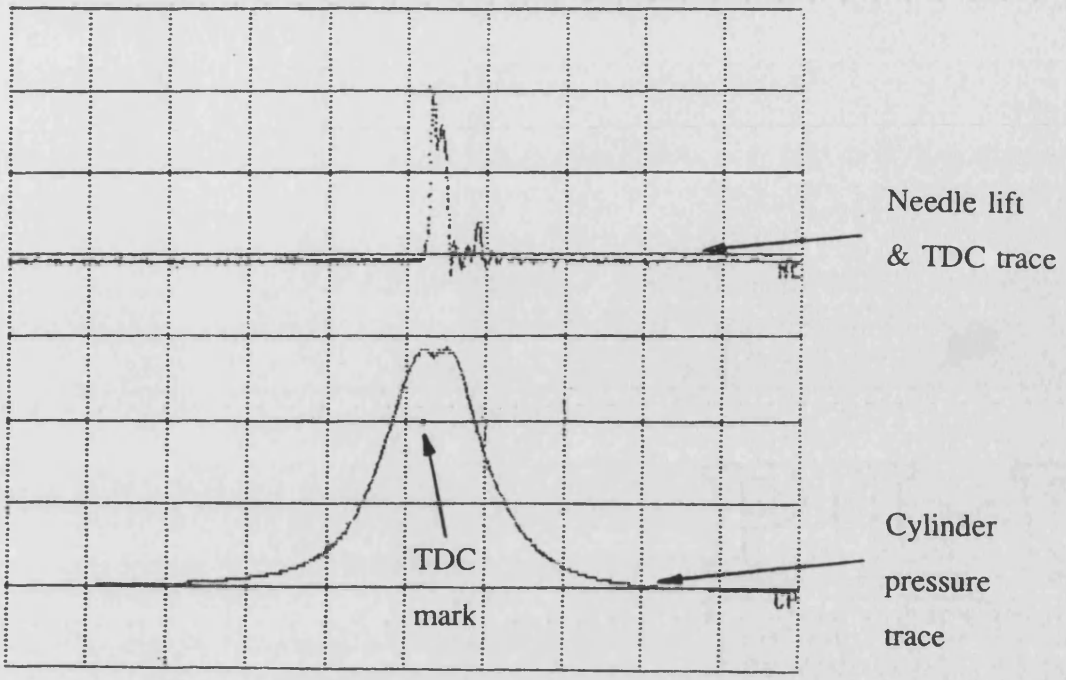

A) 1500 rev/min 25% load
insulated engine.

Figure 4.1 : Cylinder pressure, Needle lift and TDC traces as cptured by the Nicolet DSS.

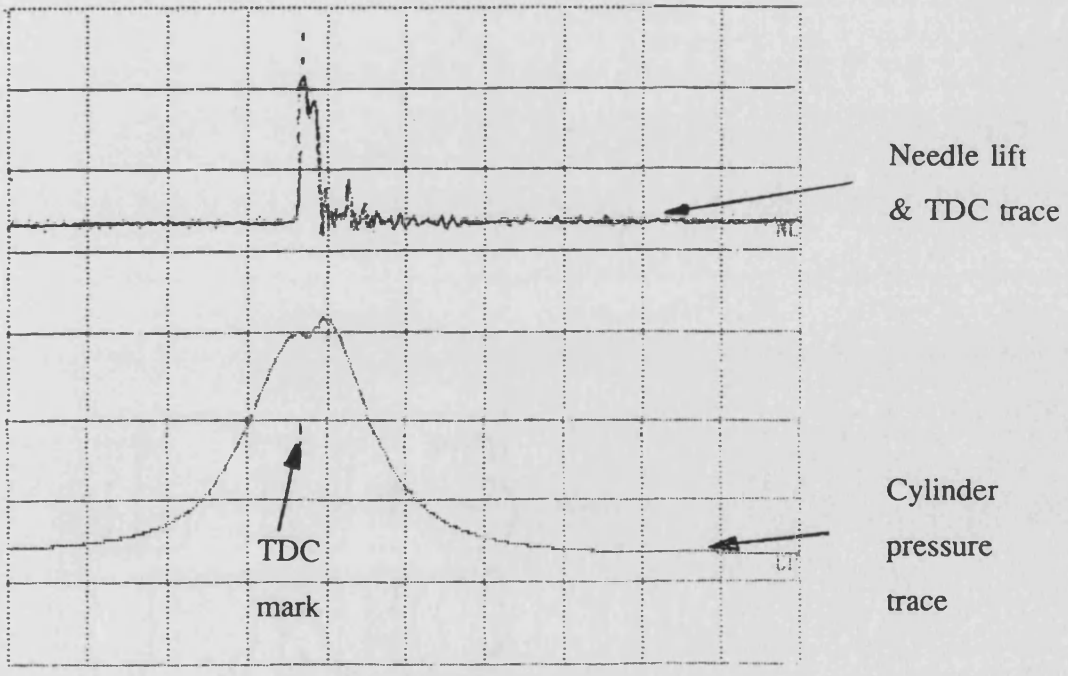

B) 1000 rev/min 25% load
insulated engine.

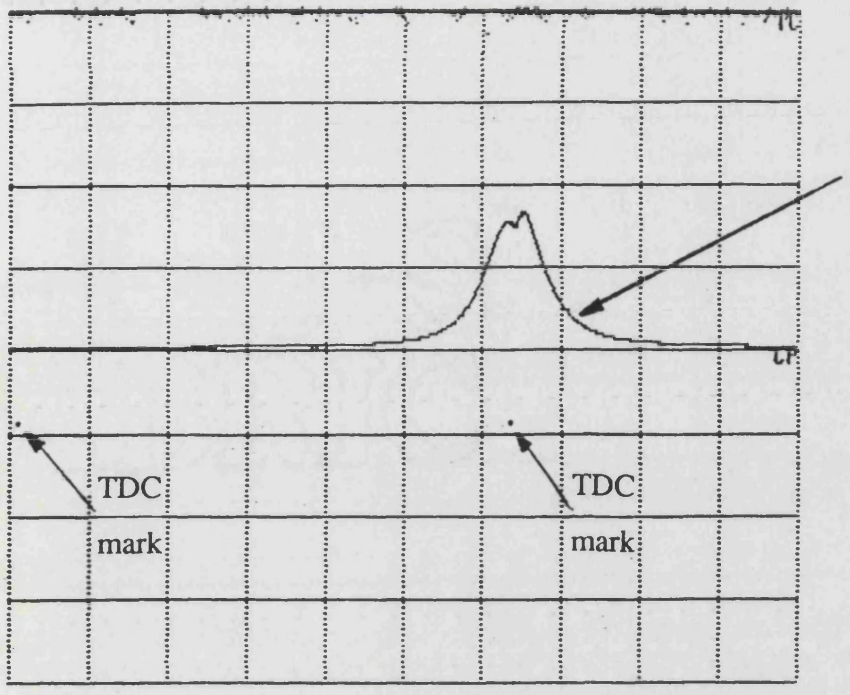

A) 1200 rev/min 25% load
insulated engine.

Figure 4.2 : Cylinder pressure and TDC traces for two timebases as captured by the Nicolet DSS.

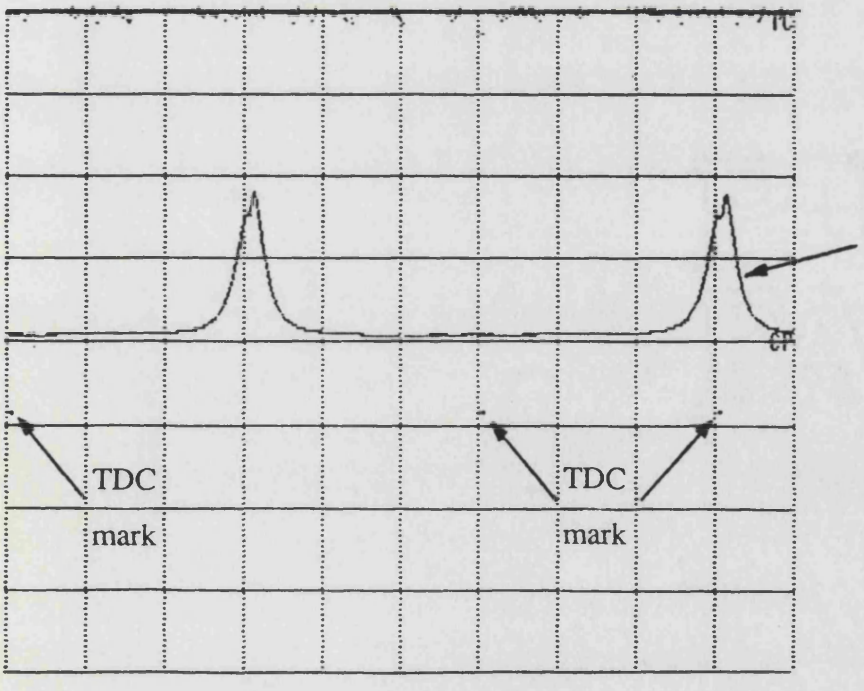

B) 1000 rev/min 25% load
insulated engine.

FIGURE 4.3 : BRAKE POWER VS. FUEL ENERGY INPUT FOR STANDARD ENGINE CONFIGURATION.

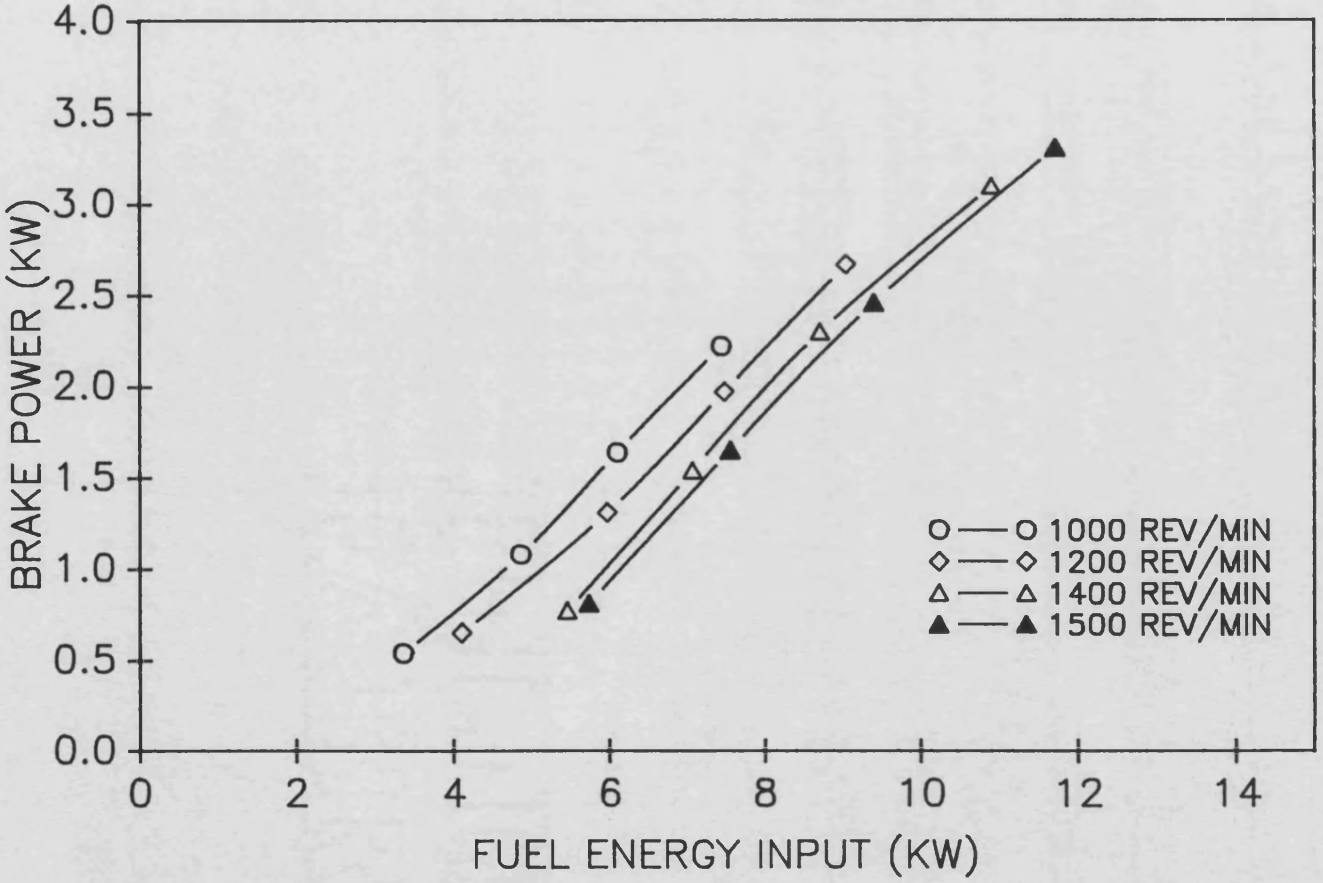

FIGURE 4.4 : ENGINE TORQUE VS. FUEL ENERGY INPUT FOR STANDARD ENGINE CONFIGURATION.

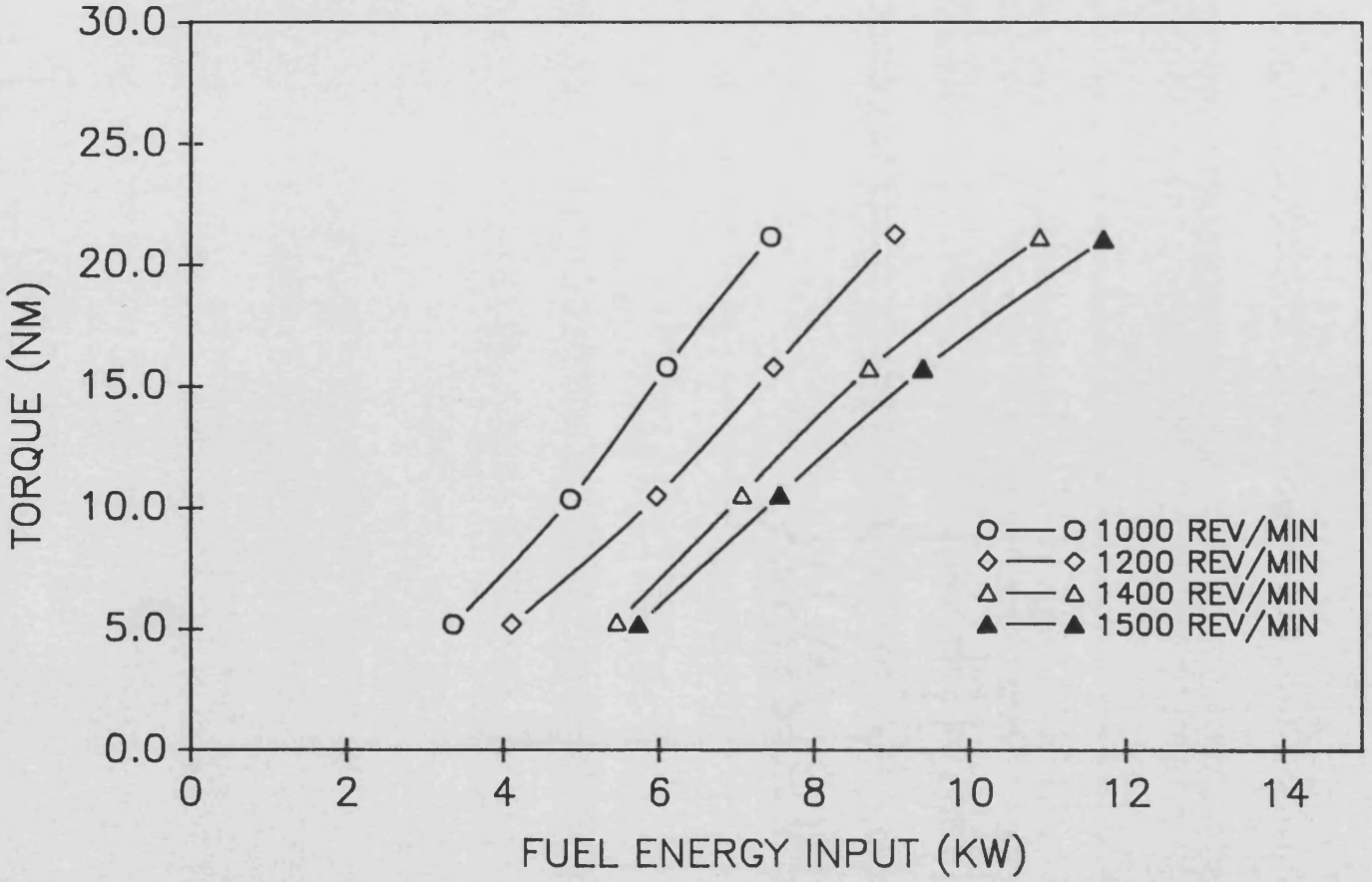

FIGURE 4.5 : BMEP VS. FUEL ENERGY INPUT
FOR STANDARD ENGINE CONFIGURATION.

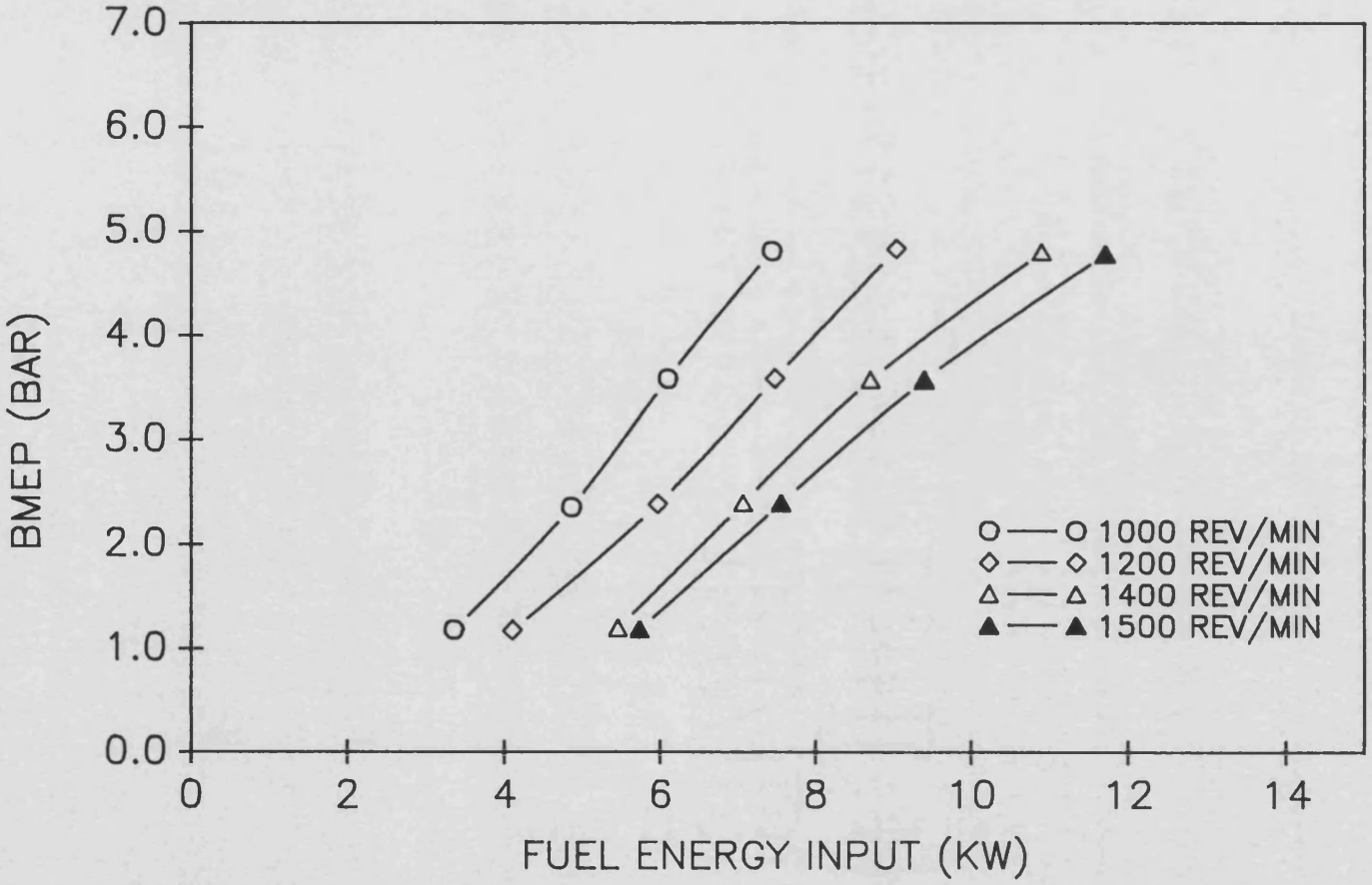

FIGURE 4.6 : THERMAL EFFICIENCY VS. FUEL ENERGY INPUT FOR STANDARD ENGINE CONFIGURATION.

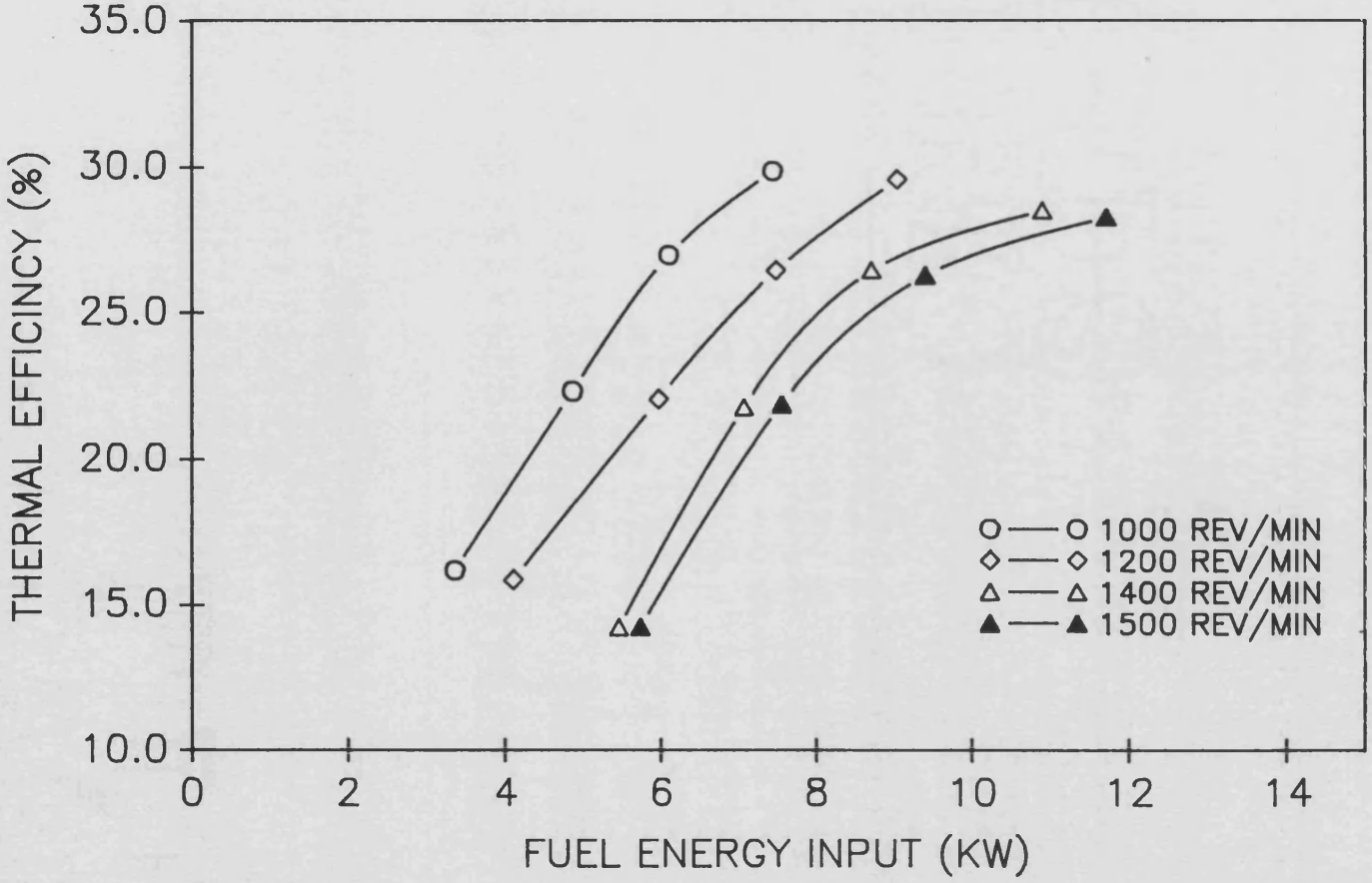

FIGURE 4.7 : SPECIFIC FUEL CONSUMPTION VS. FUEL ENERGY INPUT FOR STANDARD ENGINE CONFIGUATION.

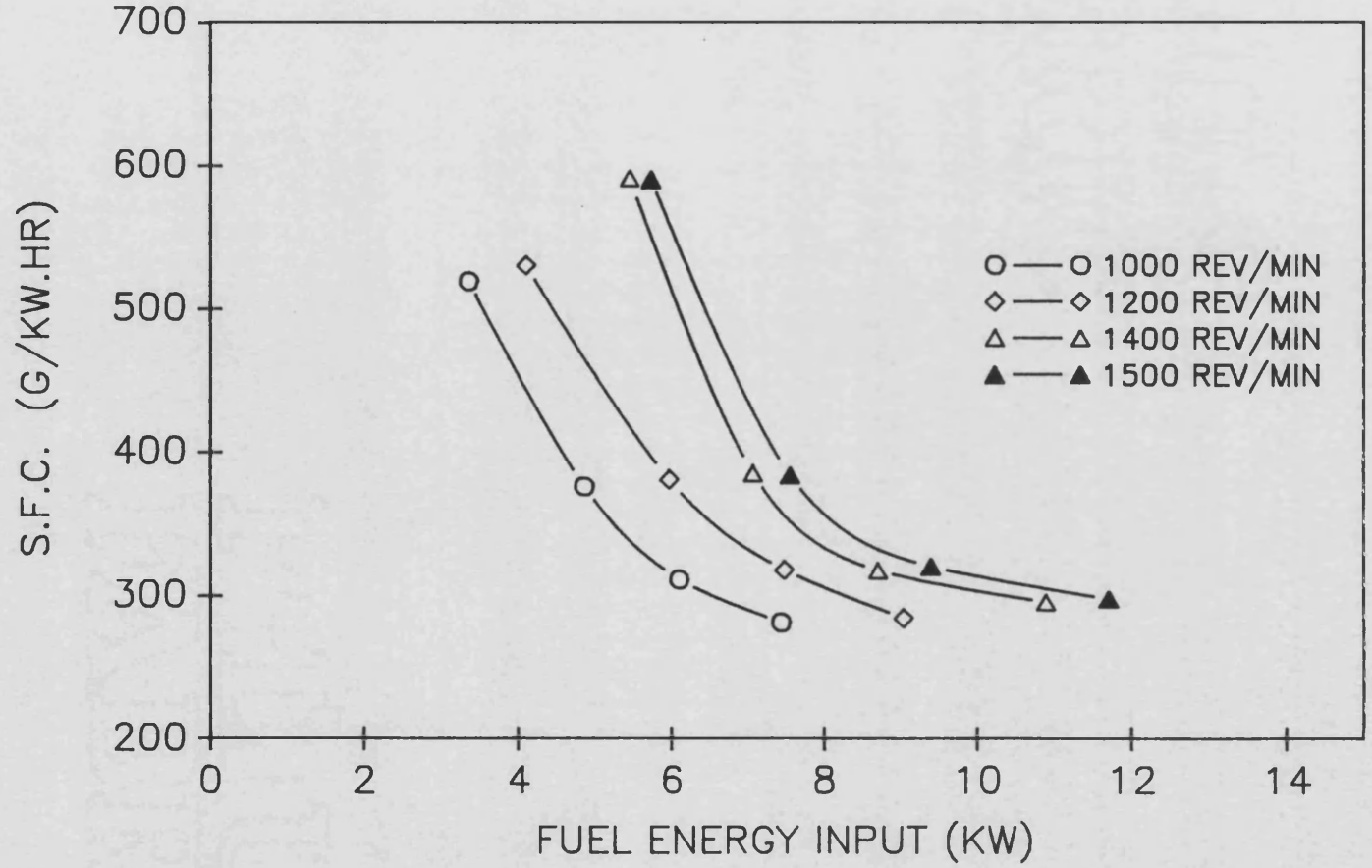

FIGURE 4.8 : AIR FLOW VS. FUEL ENERGY INPUT FOR STANDARD ENGINE CONFIGURATION.

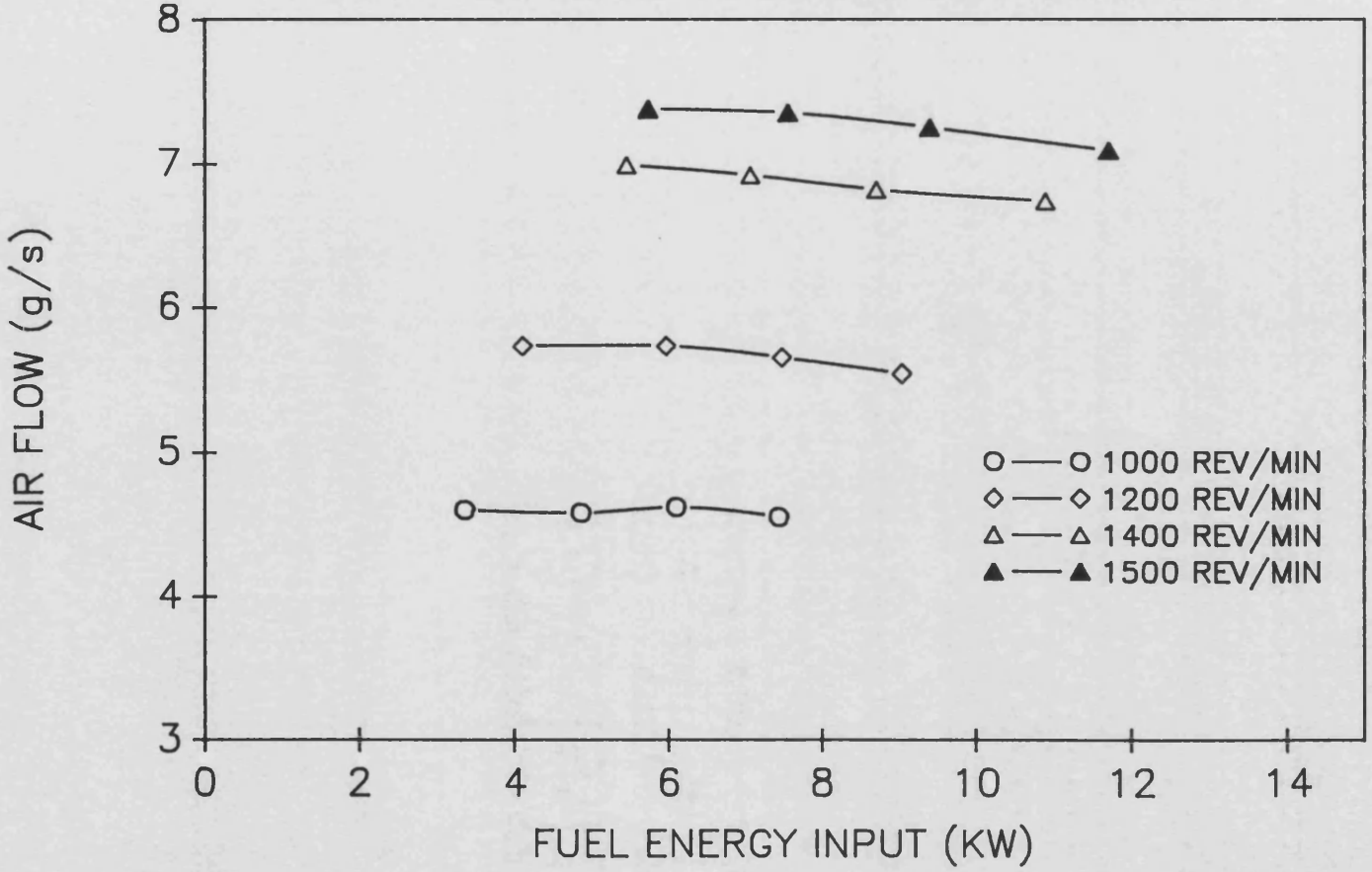

FIGURE 4.9 : VOLUMETRIC EFFICIENCY VS. FUEL ENERGY INPUT FOR STANDARD ENGINE CONFIGURATION.

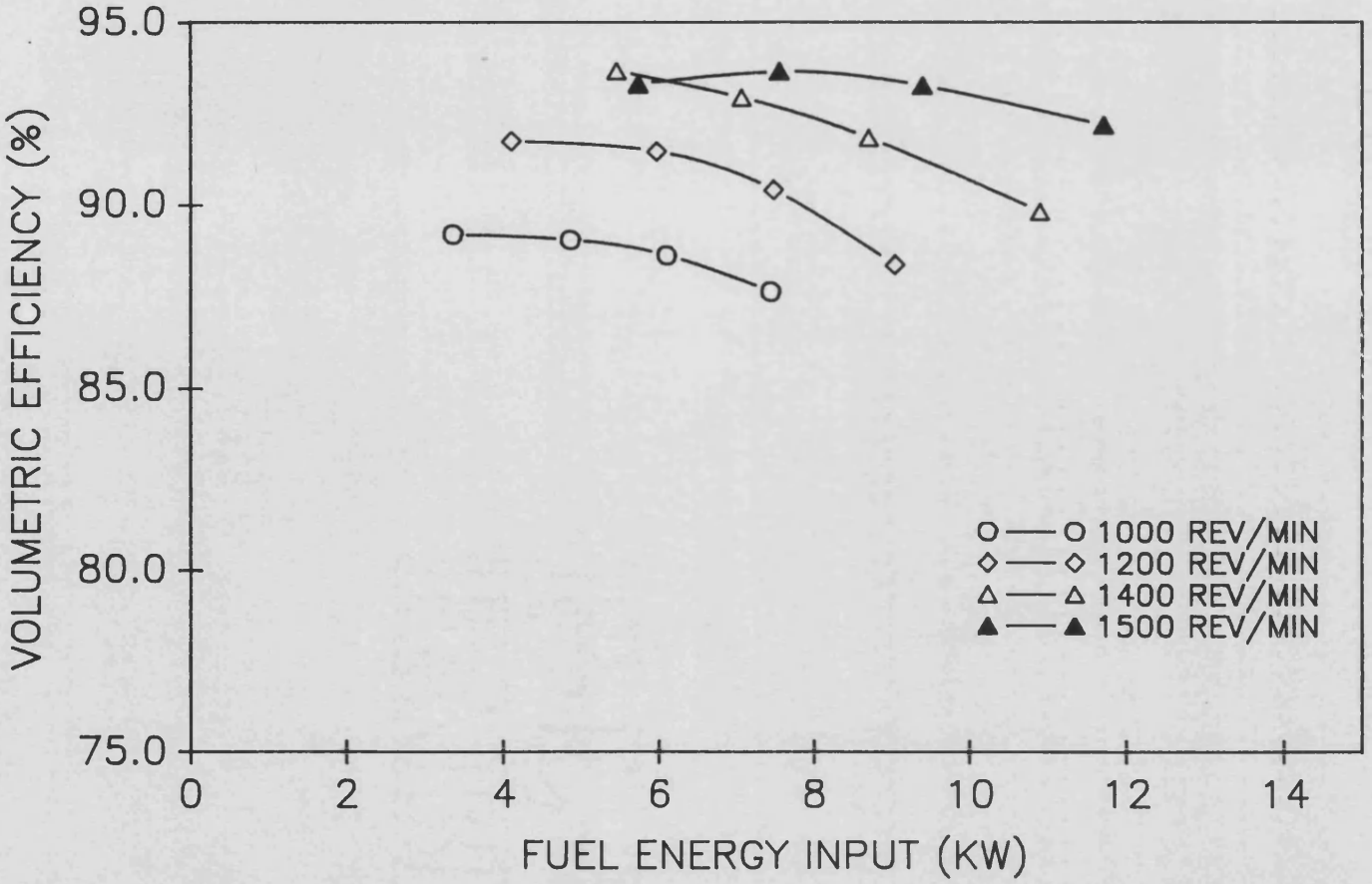

FIGURE 4.10 : AIR–FUEL RATIO VS. FUEL ENERGY INPUT FOR STANDARD ENGINE CONFIGURATION.

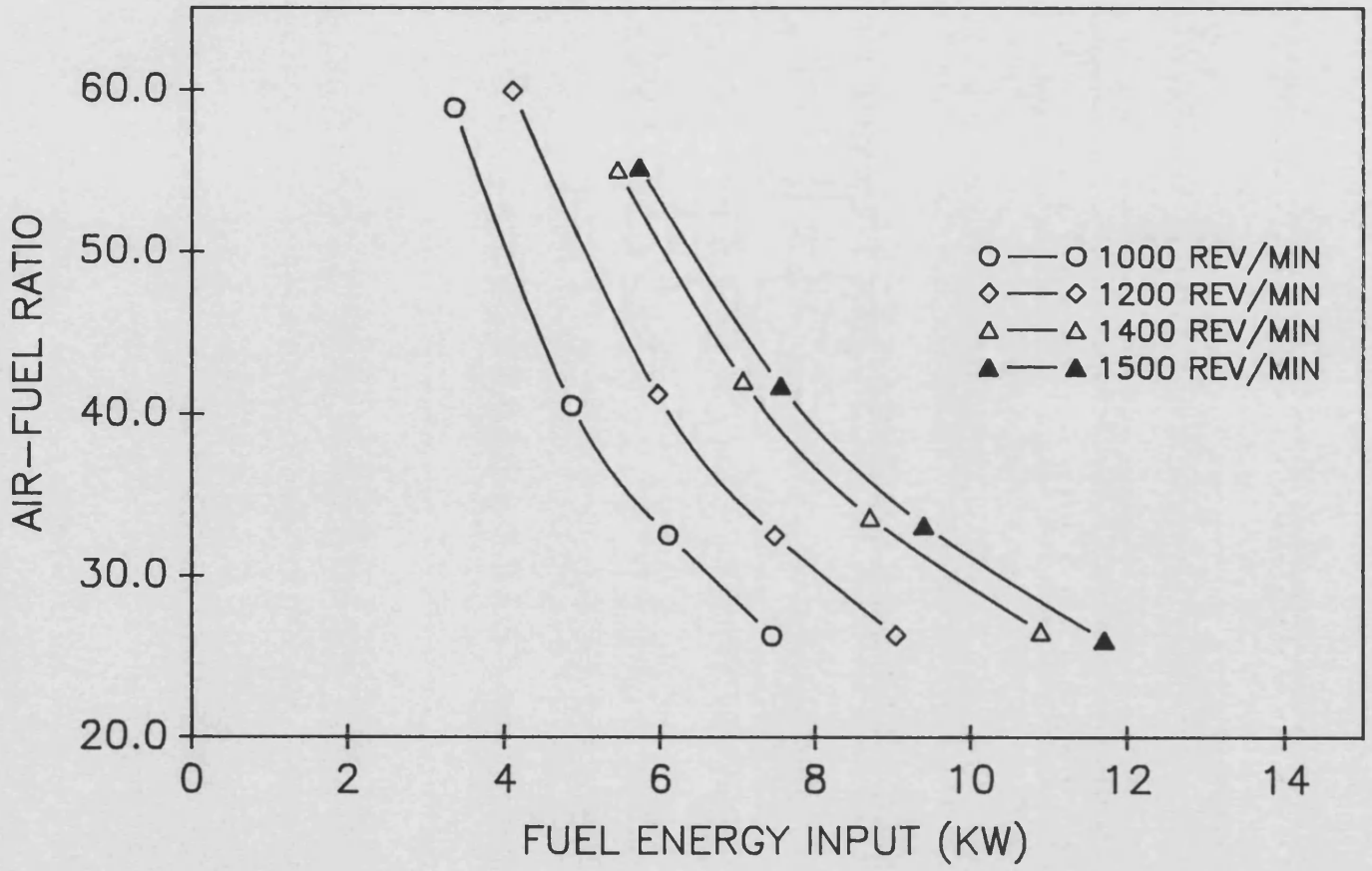

FIGURE 4.11 : SPECIFIC AIR CONSUMPTION VS. FUEL ENERGY INPUT FOR STANDARD ENGINE CONFIGURATION.

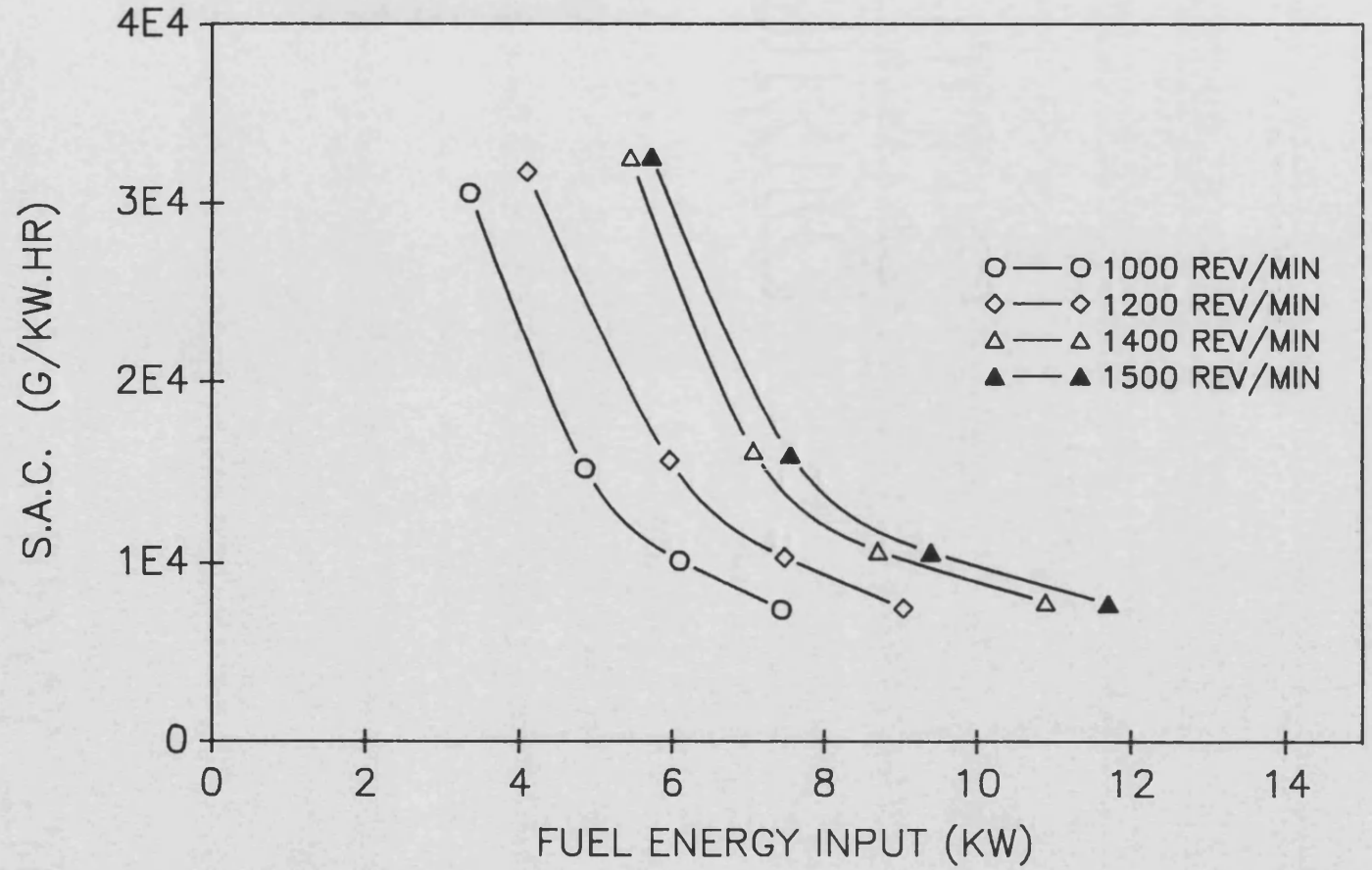

FIGURE 4.12 : HEAT REJECTION TO COOLANT VS. FUEL ENERGY INPUT FOR STANDARD ENGINE CONFIGURATION.

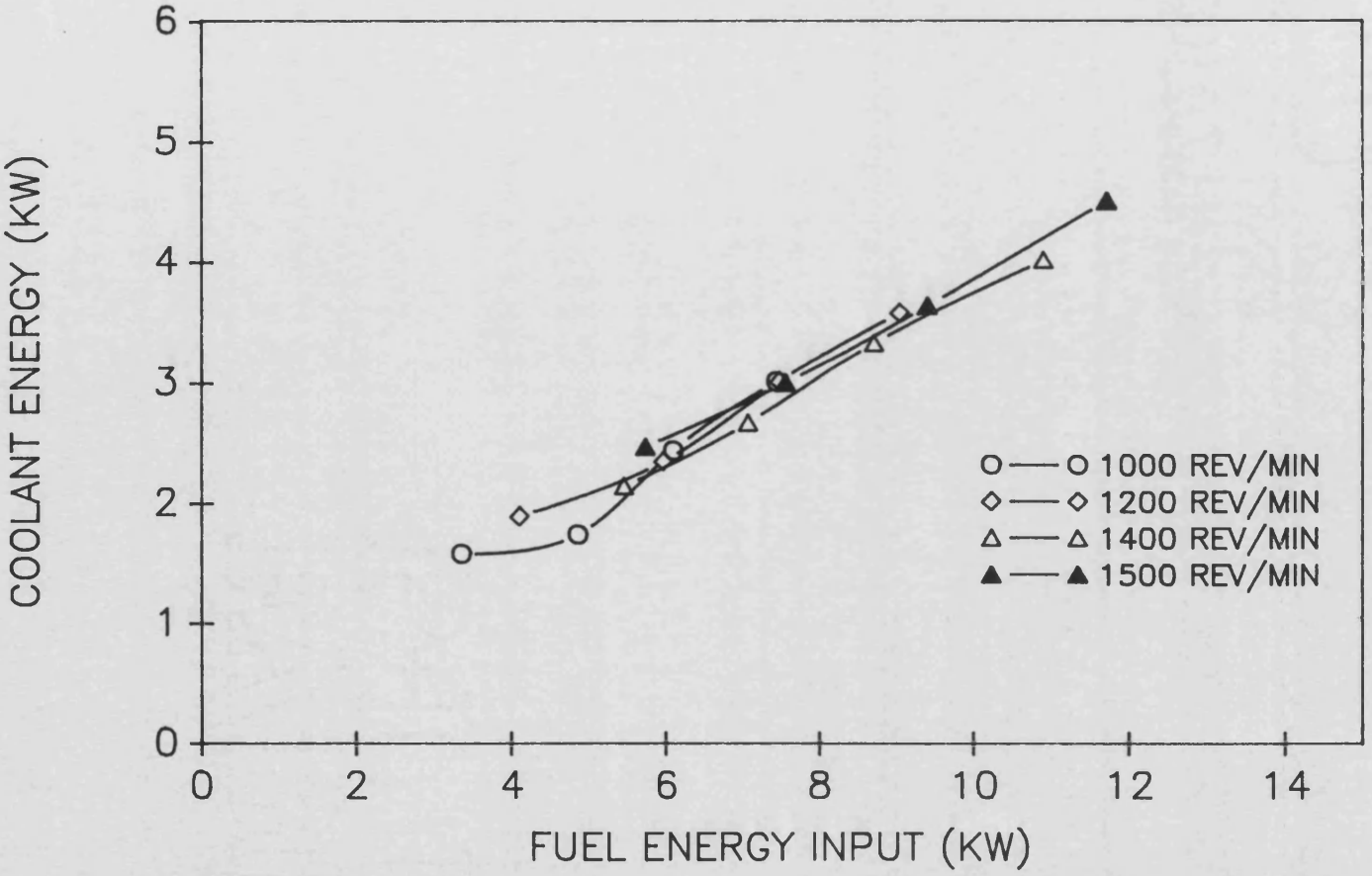

FIGURE 4.13 : PERCENTAGE HEAT REJECTION TO COOLANT VS. FUEL ENERGY INPUT FOR STANDARD ENGINE CONFIGURATION.

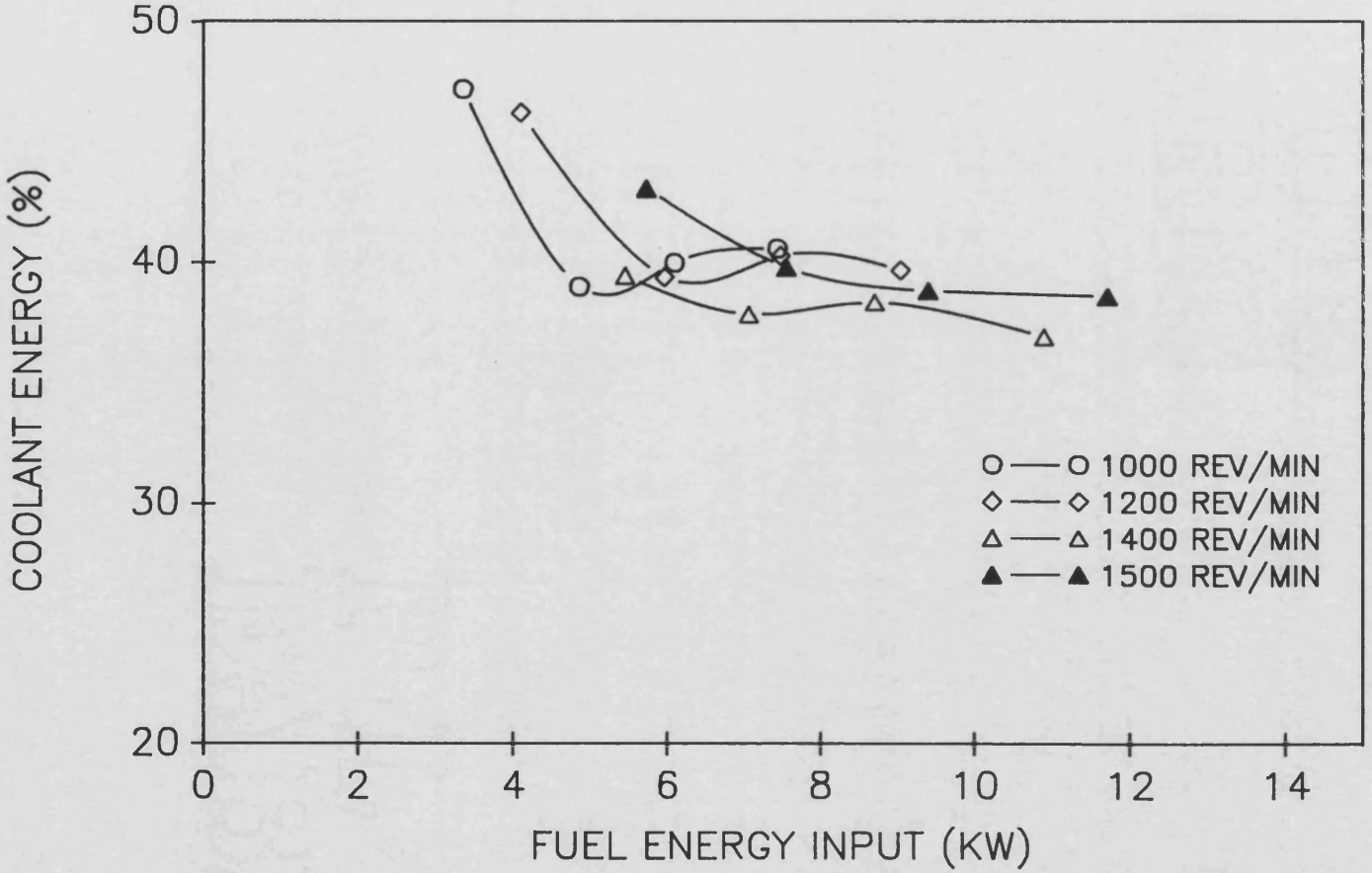

FIGURE 4.14 : EXHAUST ENERGY VS. FUEL ENERGY INPUT FOR STANDARD ENGINE CONFIGURATION.

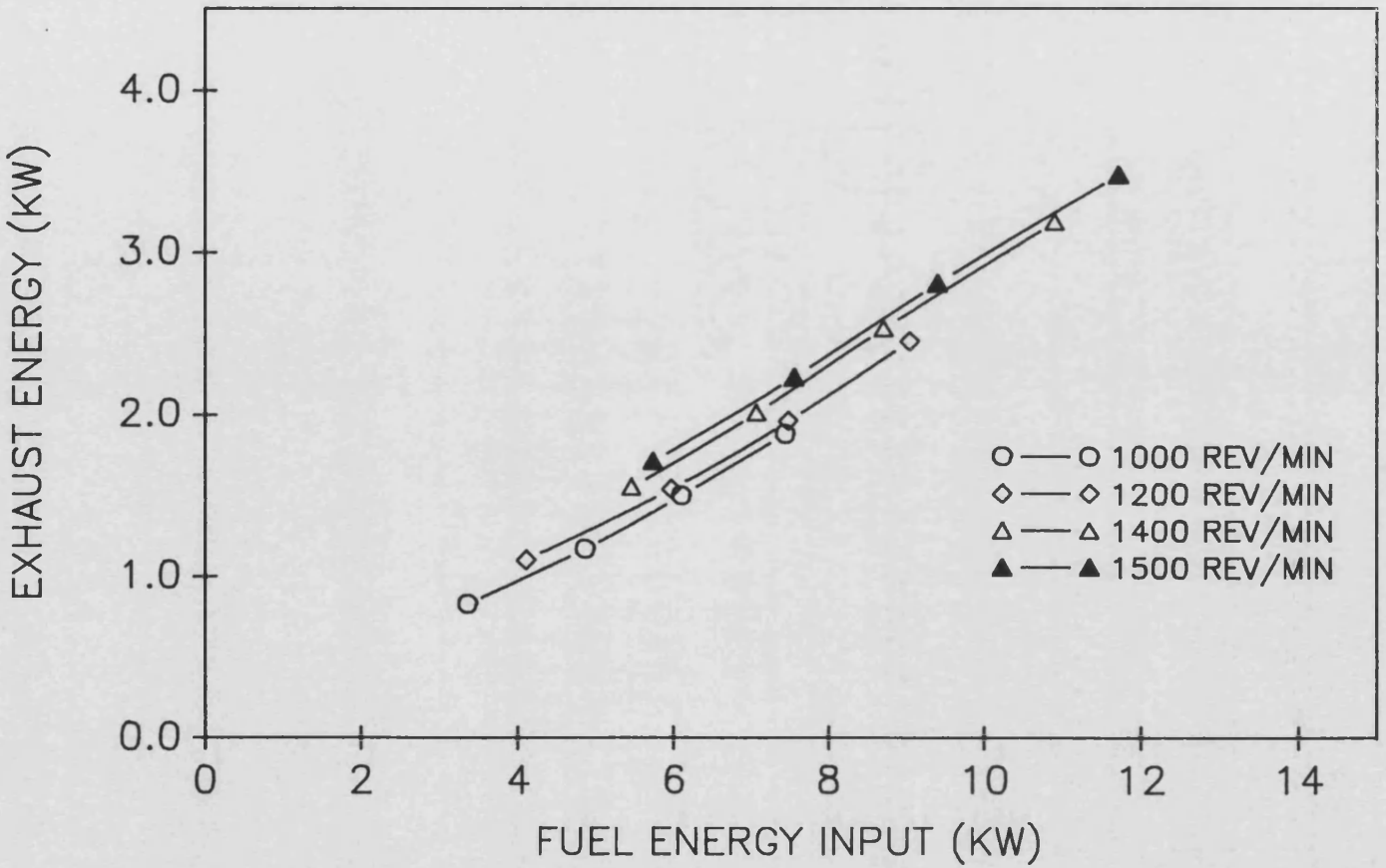

FIGURE 4.15 : PERCENTAGE EXHAUST ENERGY VS. FUEL ENRGY INPUT FOR STANDARD ENGINE CONFIGURATION.

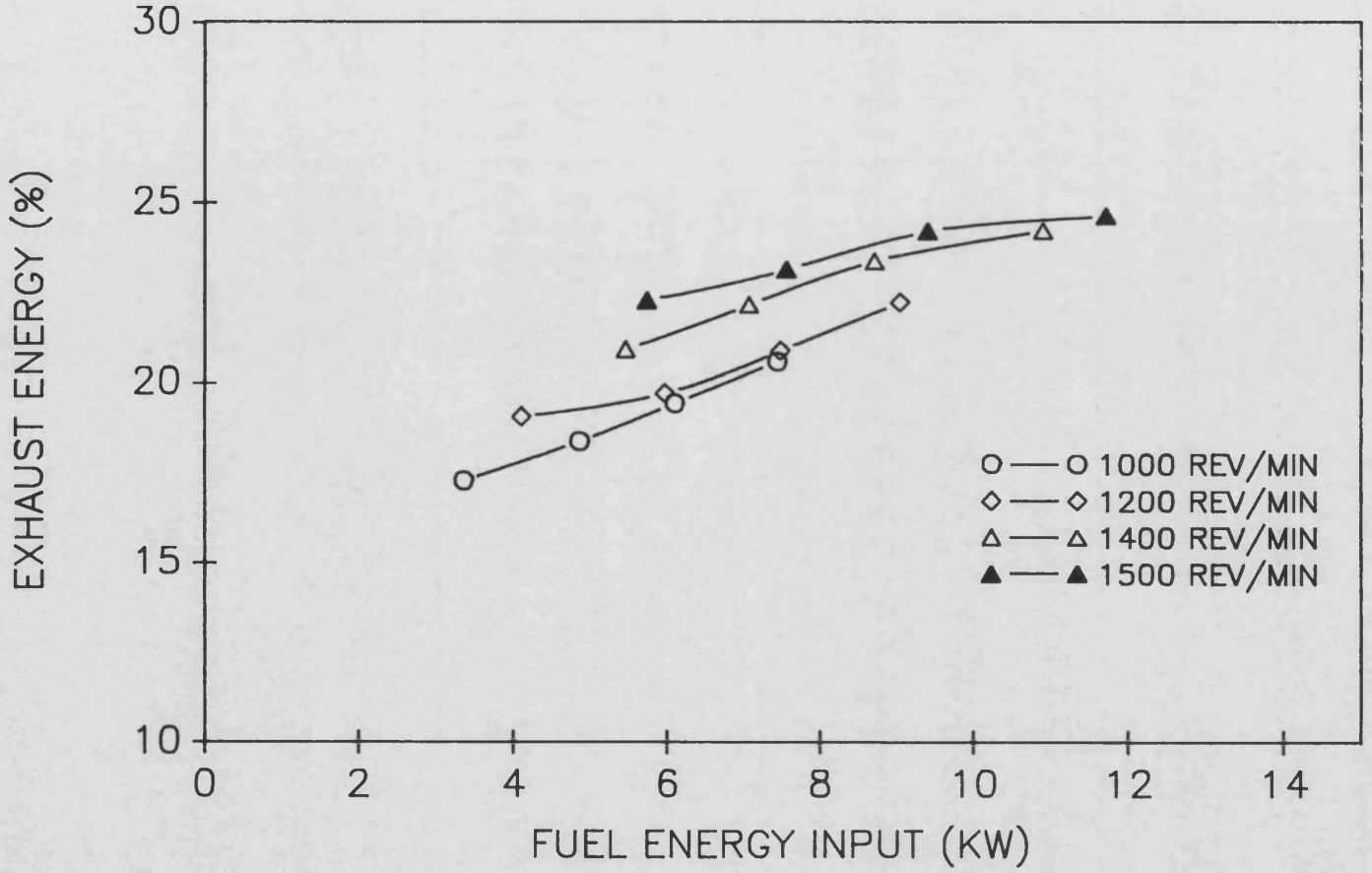

FIGURE 4.16 : EXHAUST TEMPERATURE VS. FUEL ENERGY INPUT FOR STANDARD ENGINE CONFIGURATION.

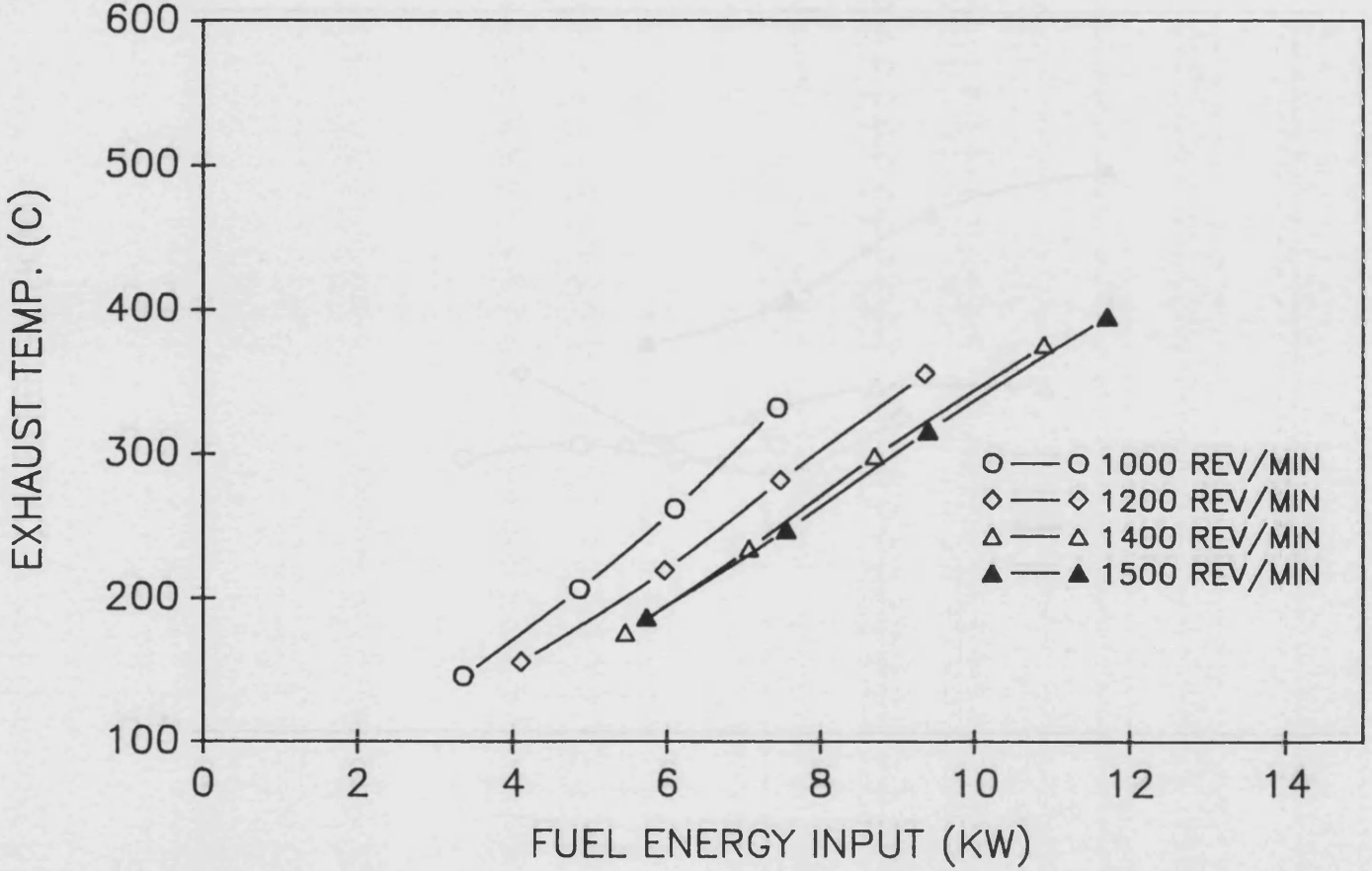

FIGURE 4.17 : HEAT REJECTION TO OIL VS. FUEL ENERGY INPUT FOR STANDARD ENGINE CONFIGURATION.

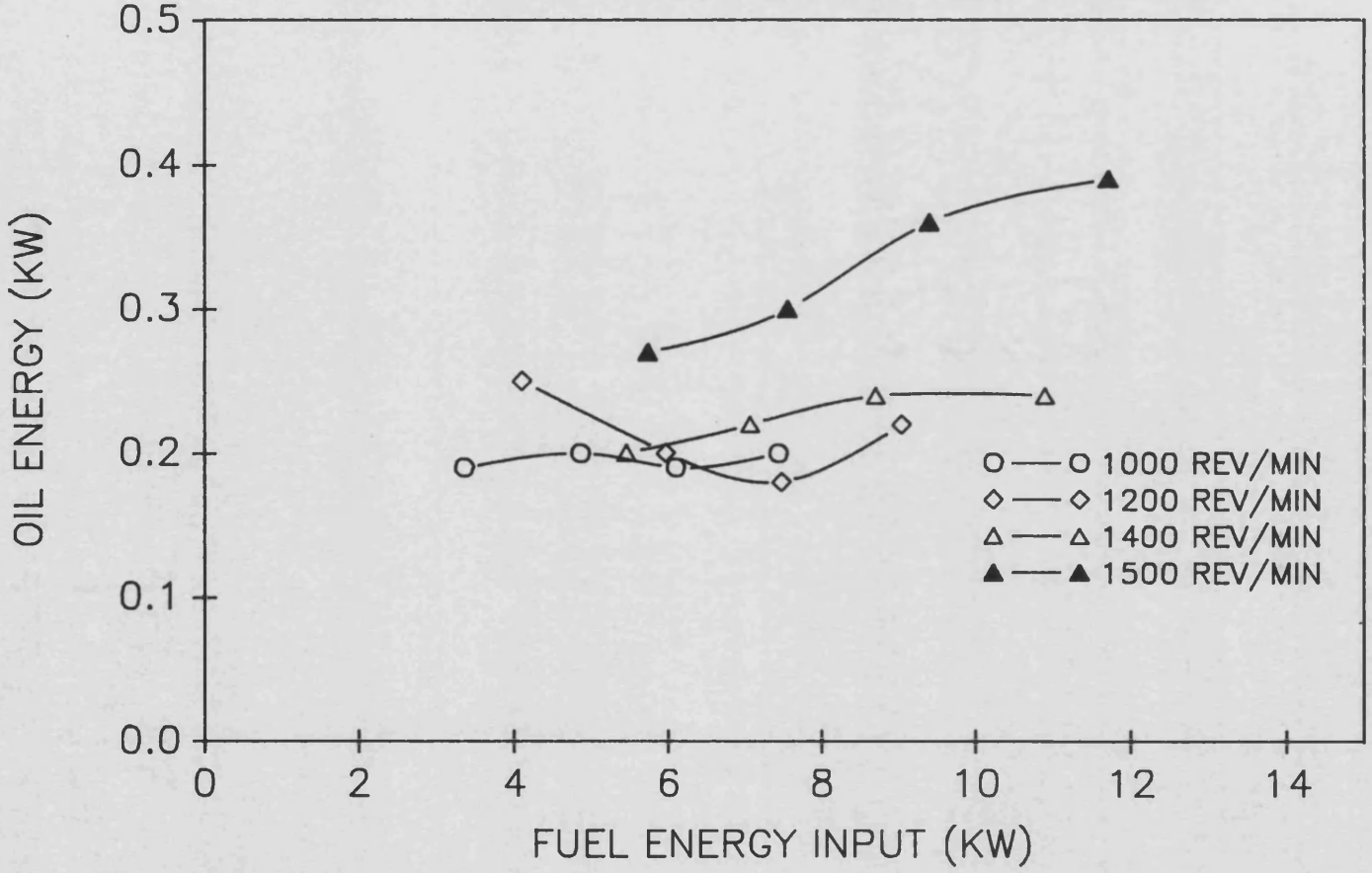

FIGURE 4.18 : HEAT BALANCE VS. FUEL ENERGY INPUT FOR STANDARD ENGINE CONFIGURATION.

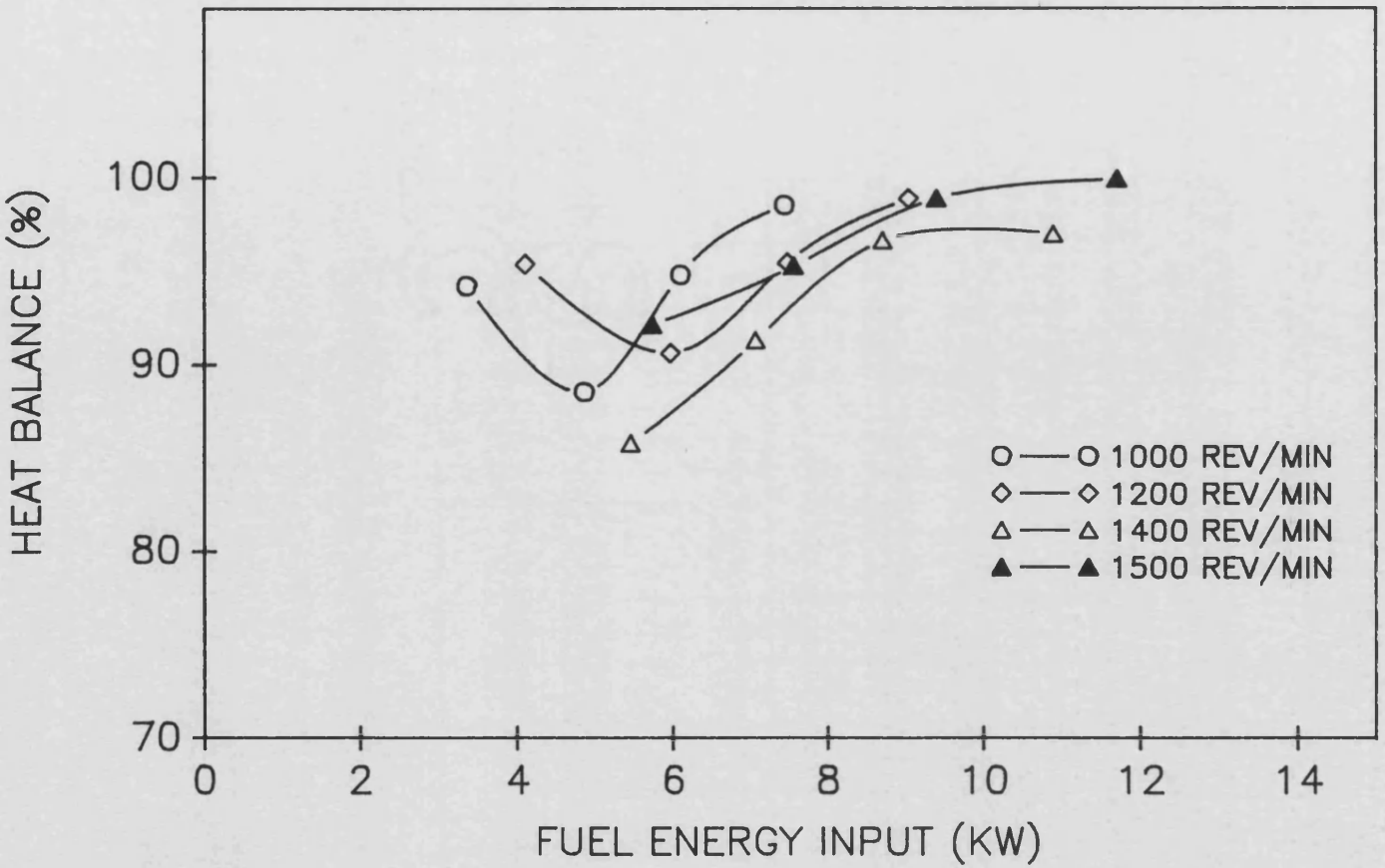

FIGURE 4.19: BRAKE POWER VS. FUEL ENERGY INPUT FOR INSULATED ENGINE.

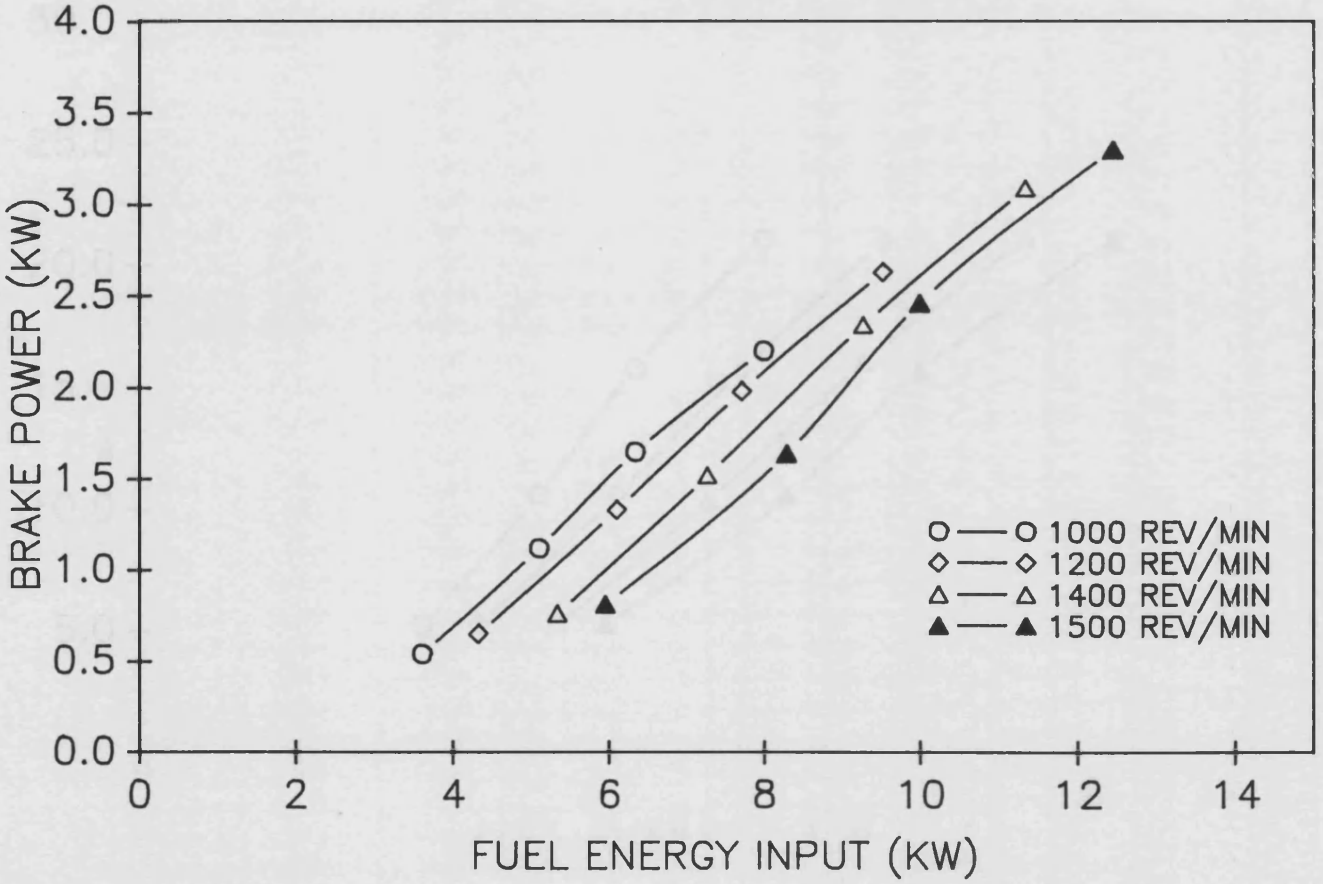

FIGURE 4.20 :ENGINE TORQUE VS. FUEL ENERGY INPUT FOR INSULATED ENGINE.

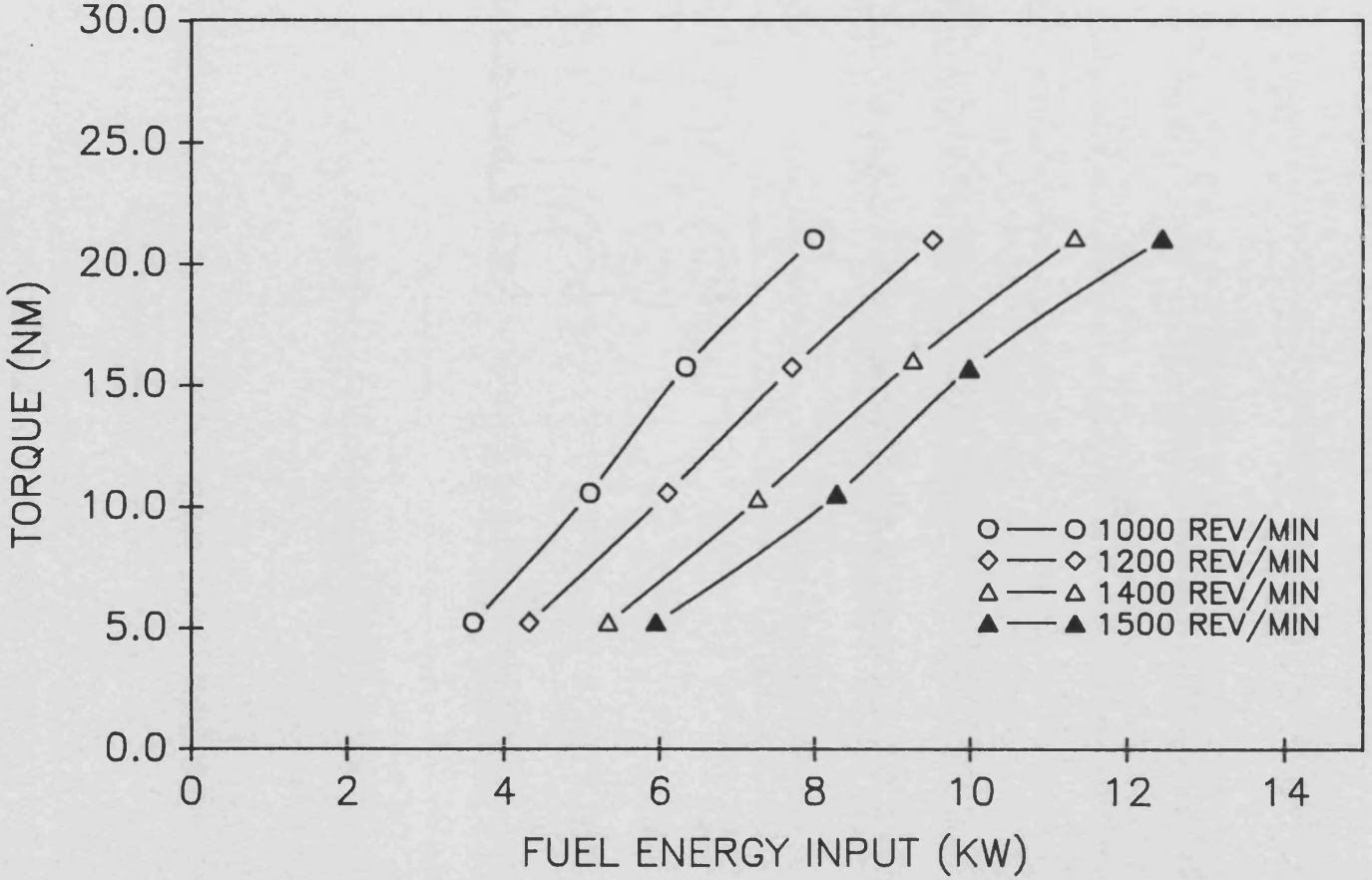

FIGURE 4.21 : BMEP VS. FUEL ENERGY INPUT
FOR INSULATED ENGINE.

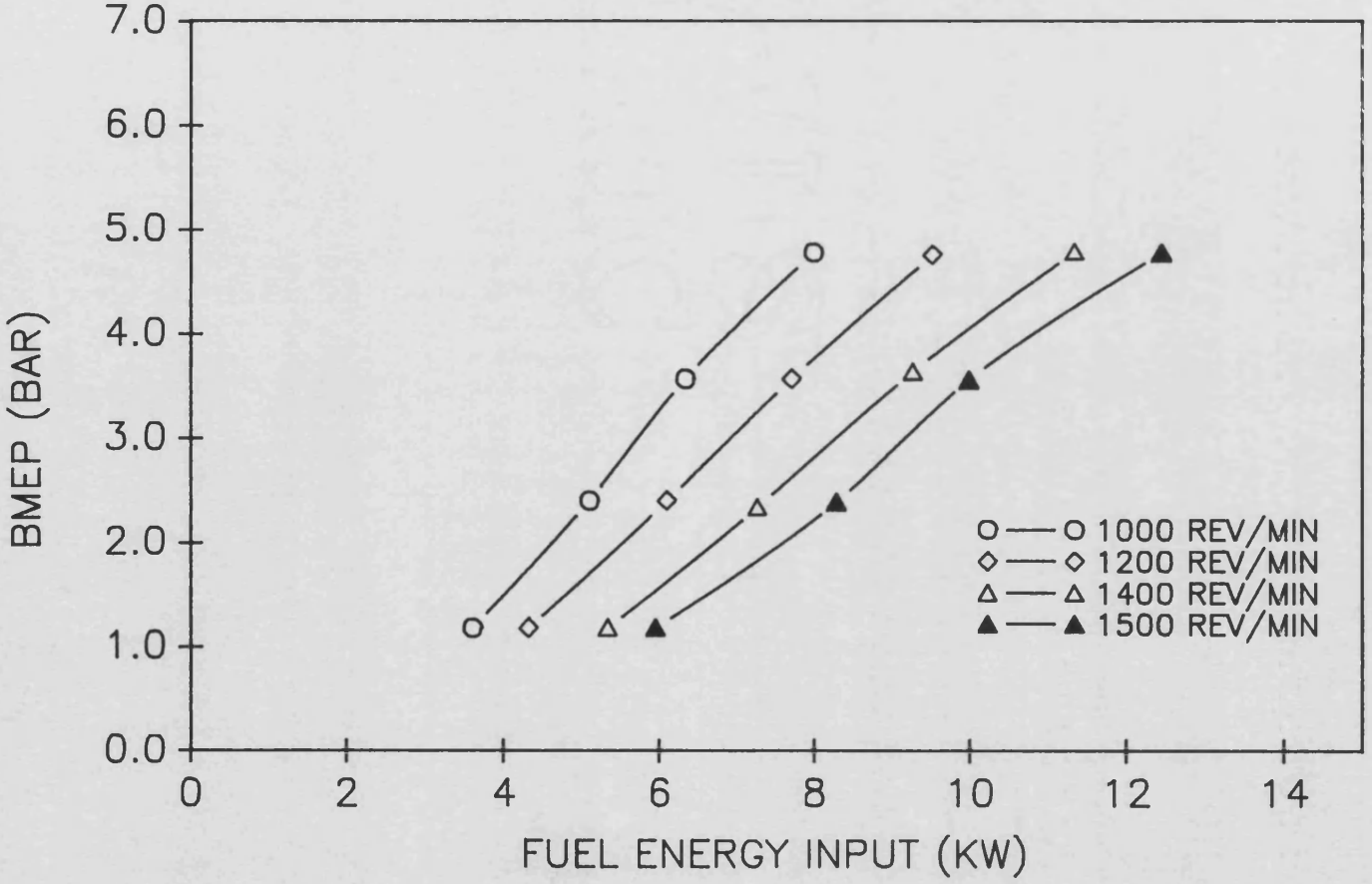

FIGURE 4.22 : THERMAL EFFICIENCY VS. FUEL ENERGY INPUT FOR INSULATED ENGINE

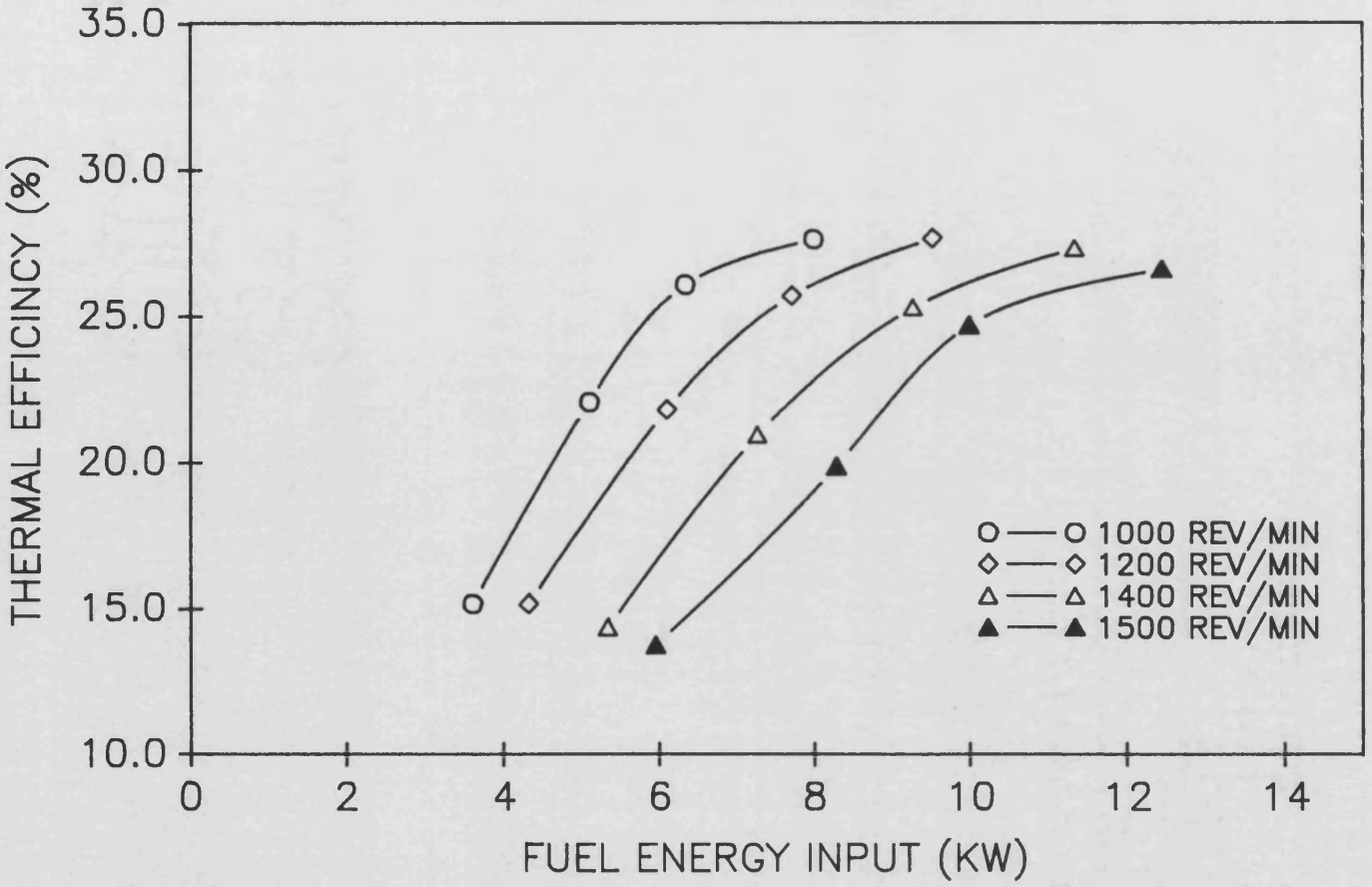

FIGURE 4.23 : SPECIFIC FUEL CONSUMPTION VS. FUEL ENERGY INPUT FOR INSULATED ENGINE.

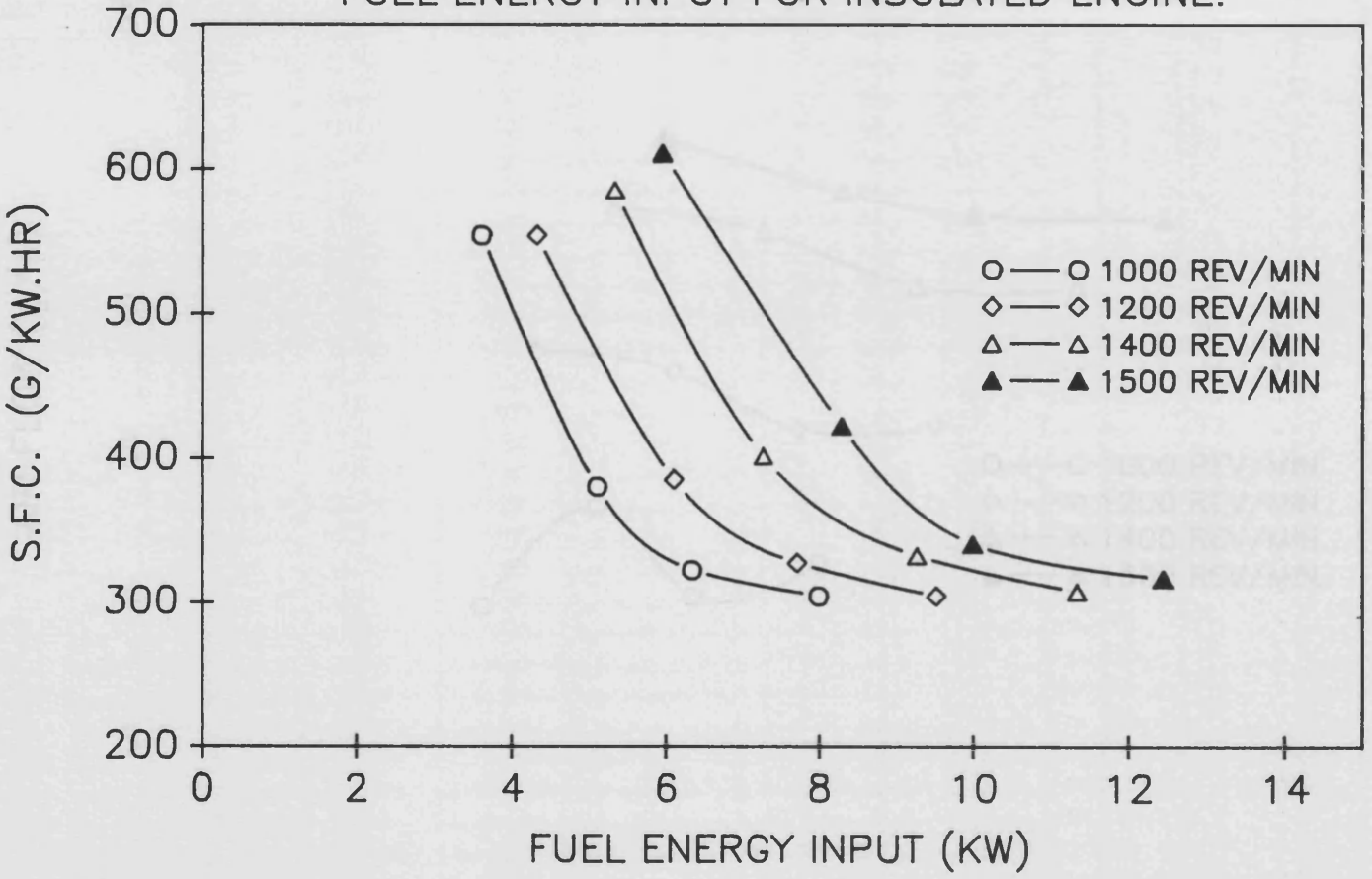

FIGURE 4.24 : AIR FLOW VS. FUEL ENERGY INPUT FOR INSULATED ENGINE.

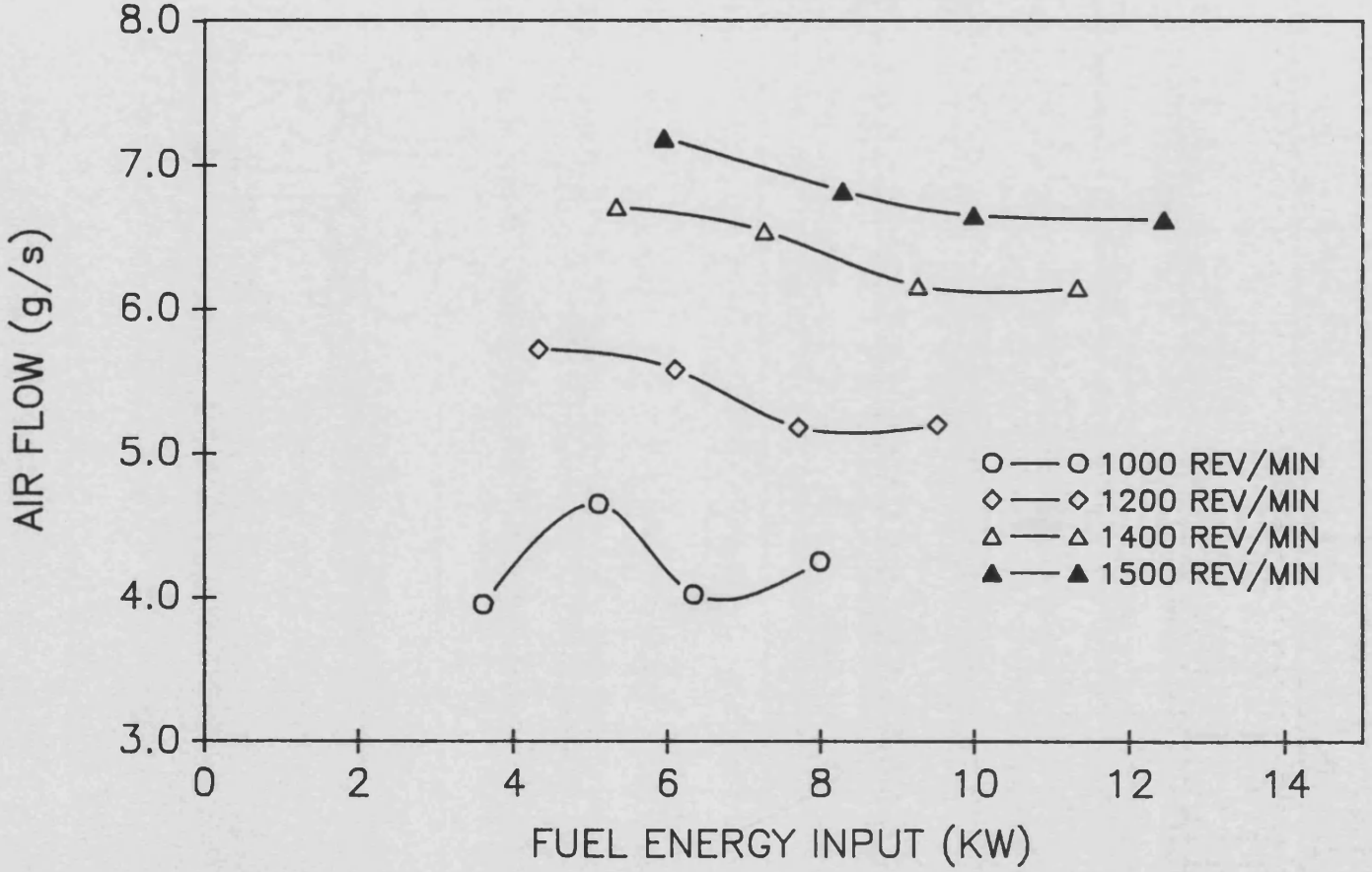

FIGURE 4.25 : VOLUMETRIC EFFICIENCY VS. FUEL ENERGY INPUT FOR INSULATED ENGINE.

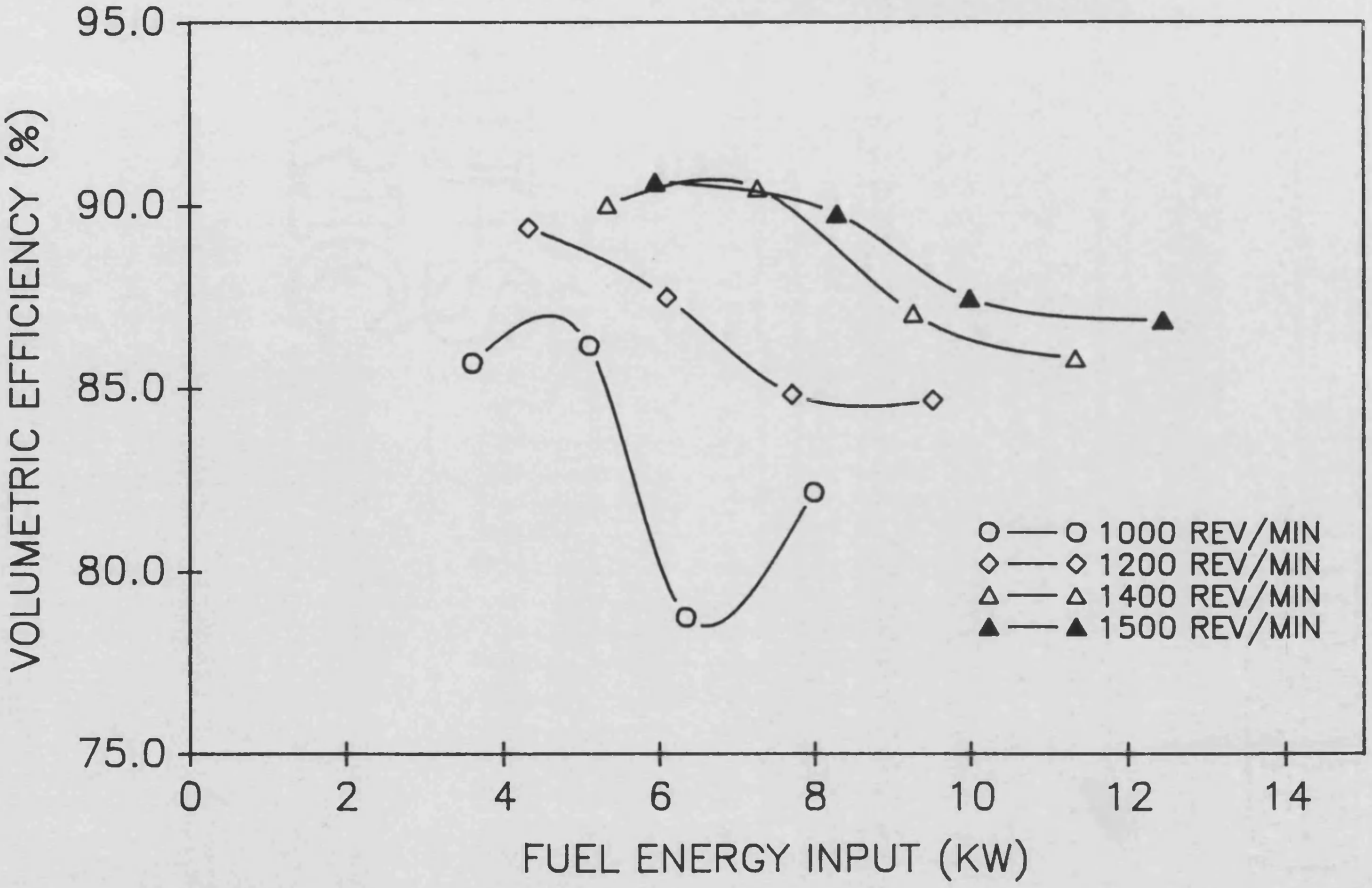

FIGURE 4.26 : AIR–FUEL RATIO VS. FUEL ENERGY INPUT FOR INSULATED ENGINE.

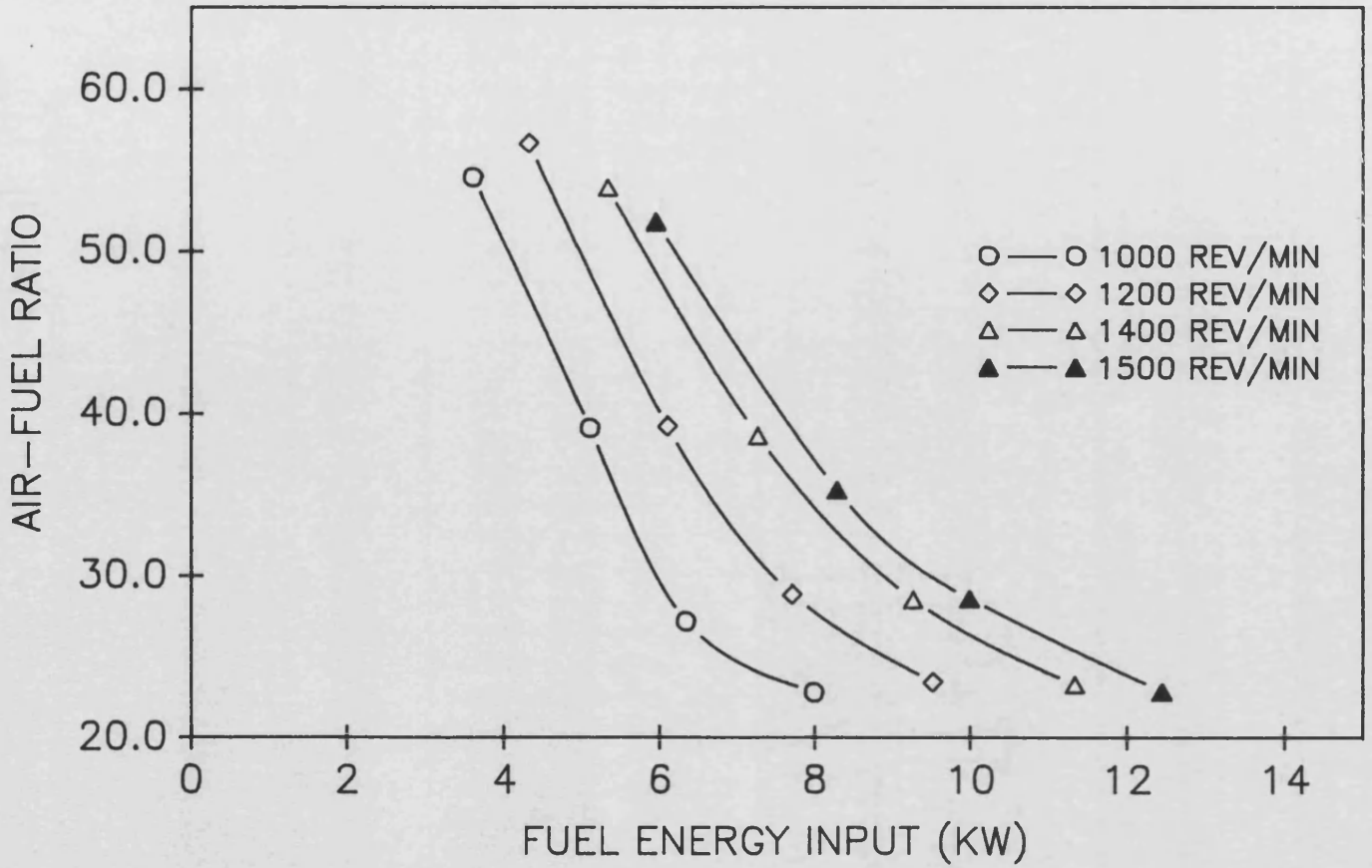

FIGURE 4.27 : SPECIFIC AIR CONSUMPTION VS.
FUEL ENERGY INPUT FOR INSULATED ENGINE.

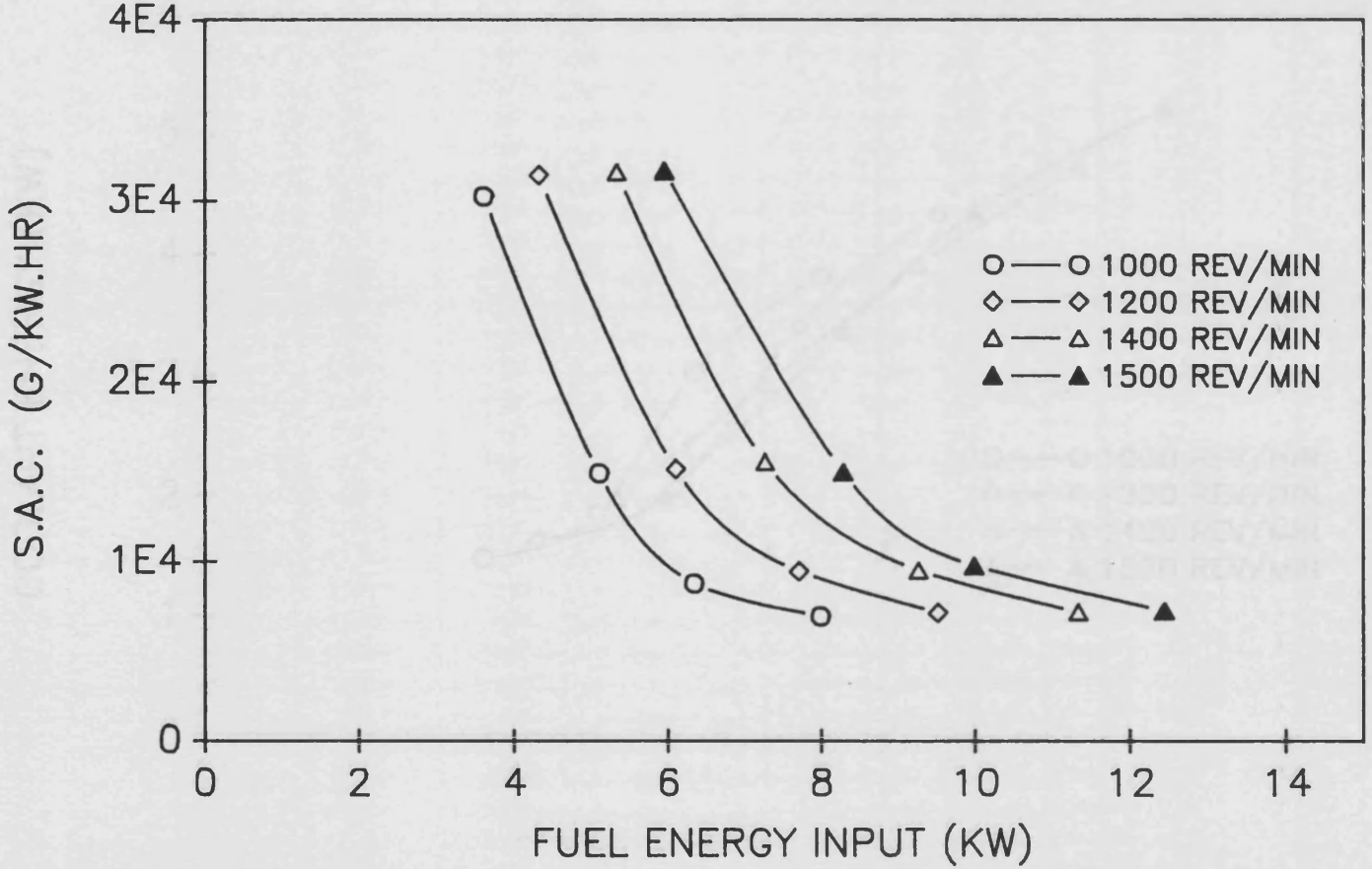

FIGURE 4.28 HEAT REJECTION TO COOLANT VS. FUEL ENERGY INPUT FOR INSULATED ENGINE.

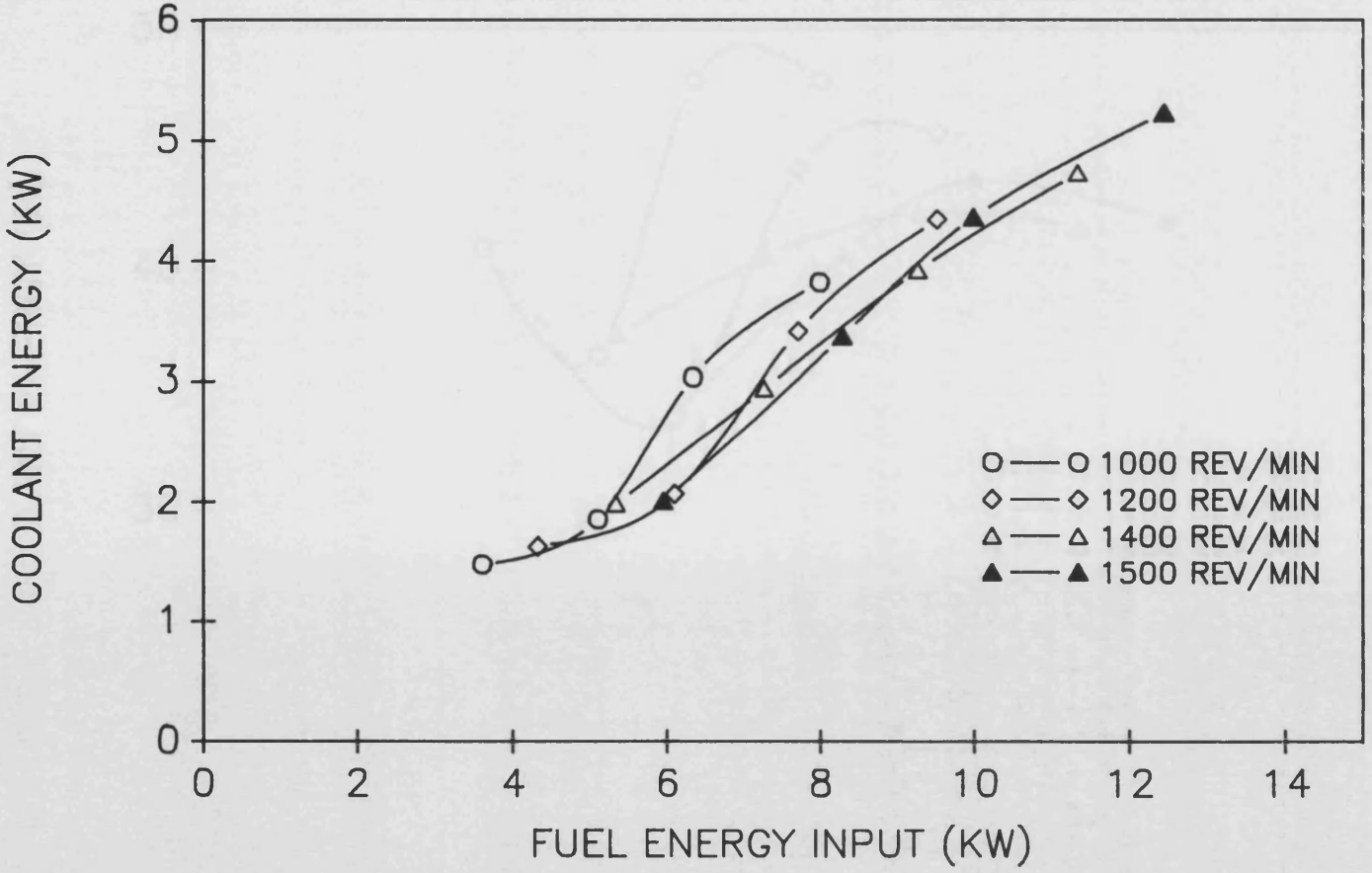

FIGURE 4.29 : PERCENTAGE HEAT LOST TO COOLANT VS. FUEL ENERGY INPUT FOR INSULATED ENGINE.

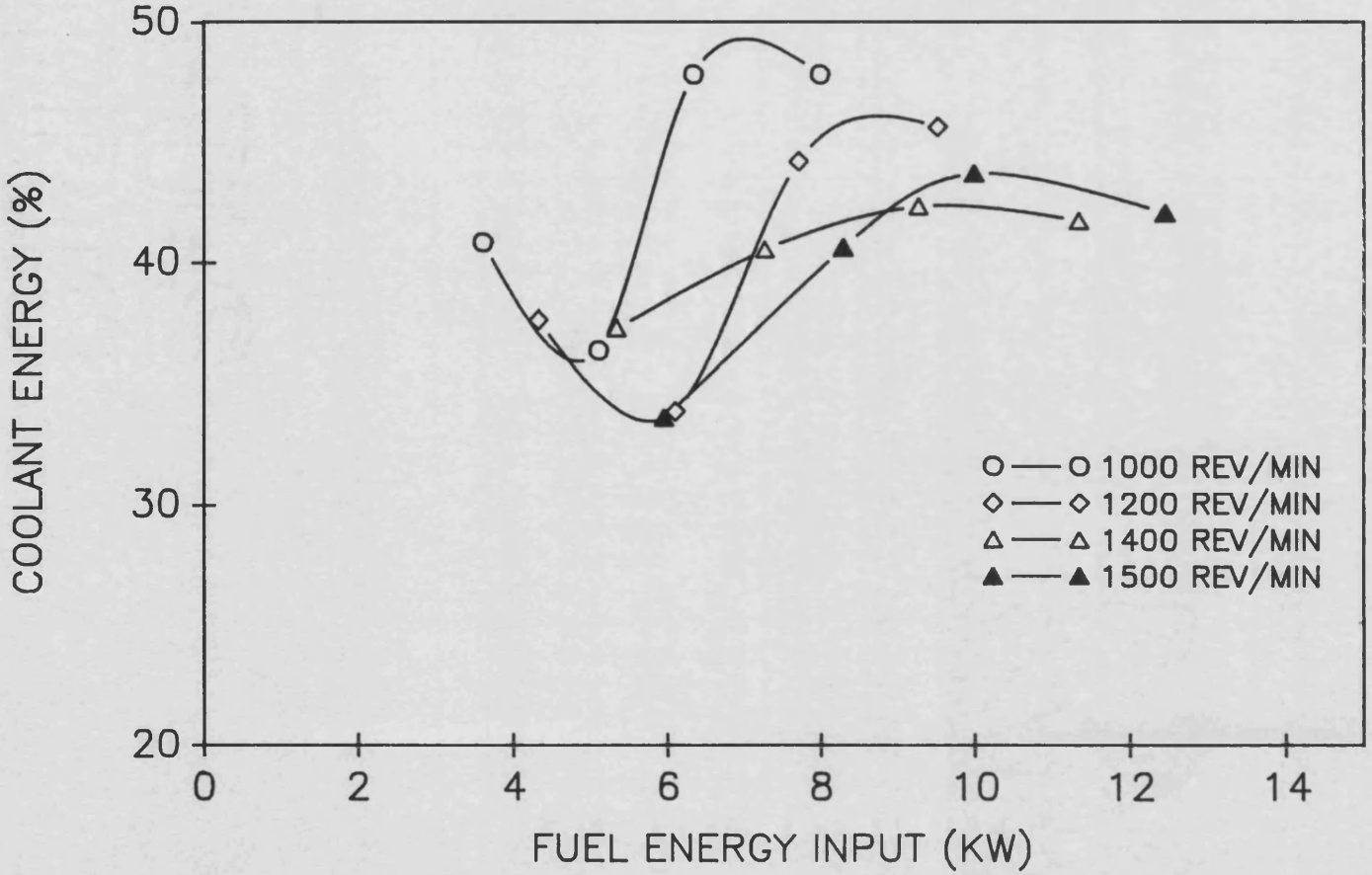

FIGURE 4.30: EXHAUST ENERGY VS. FUEL ENERGY INPUT FOR INSULATED ENGINE.

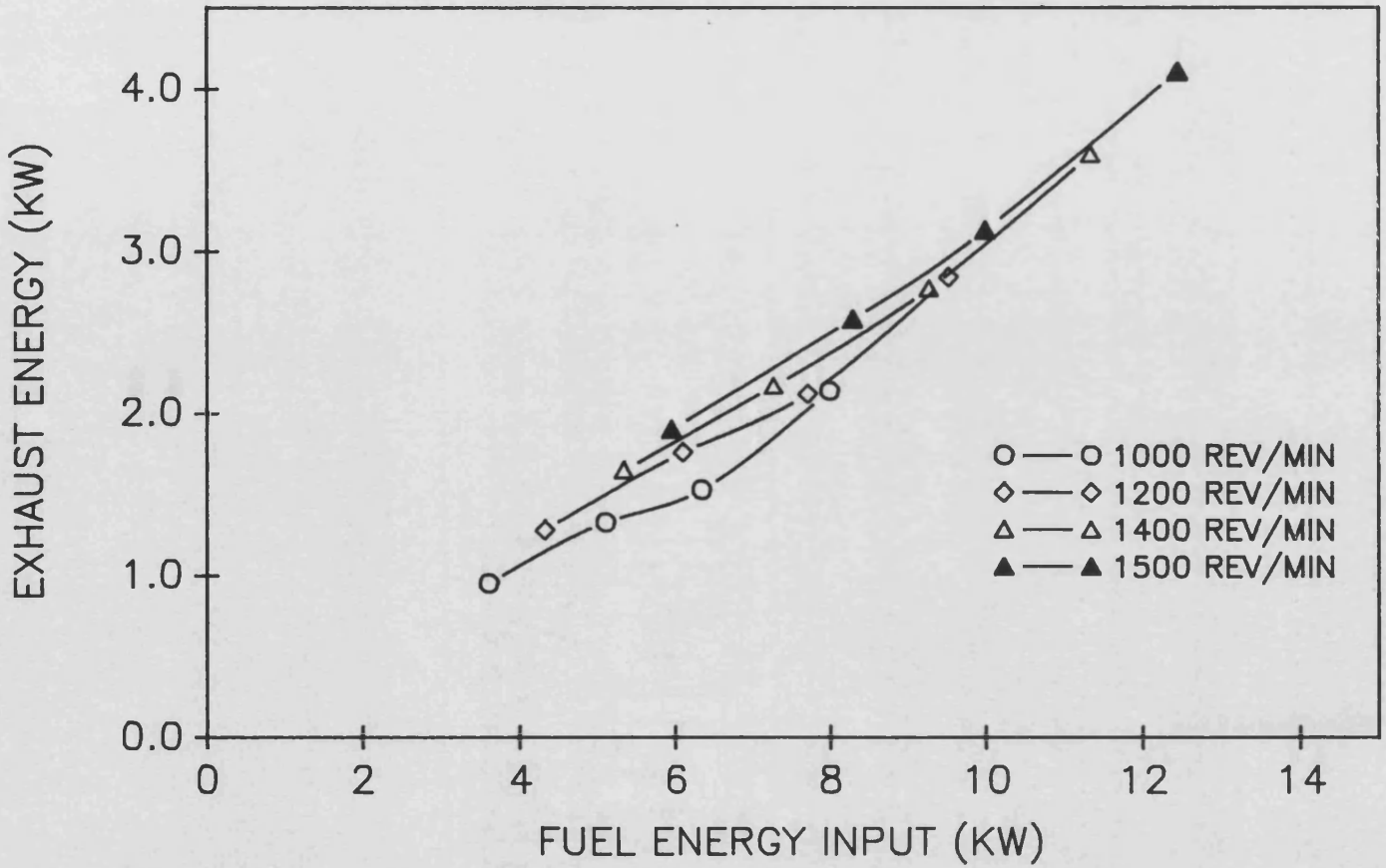

FIGURE 4.31 : PERCENTAGE EXHAUST ENERGY VS. FUEL ENERGY INPUT FOR INSULATED ENGINE.

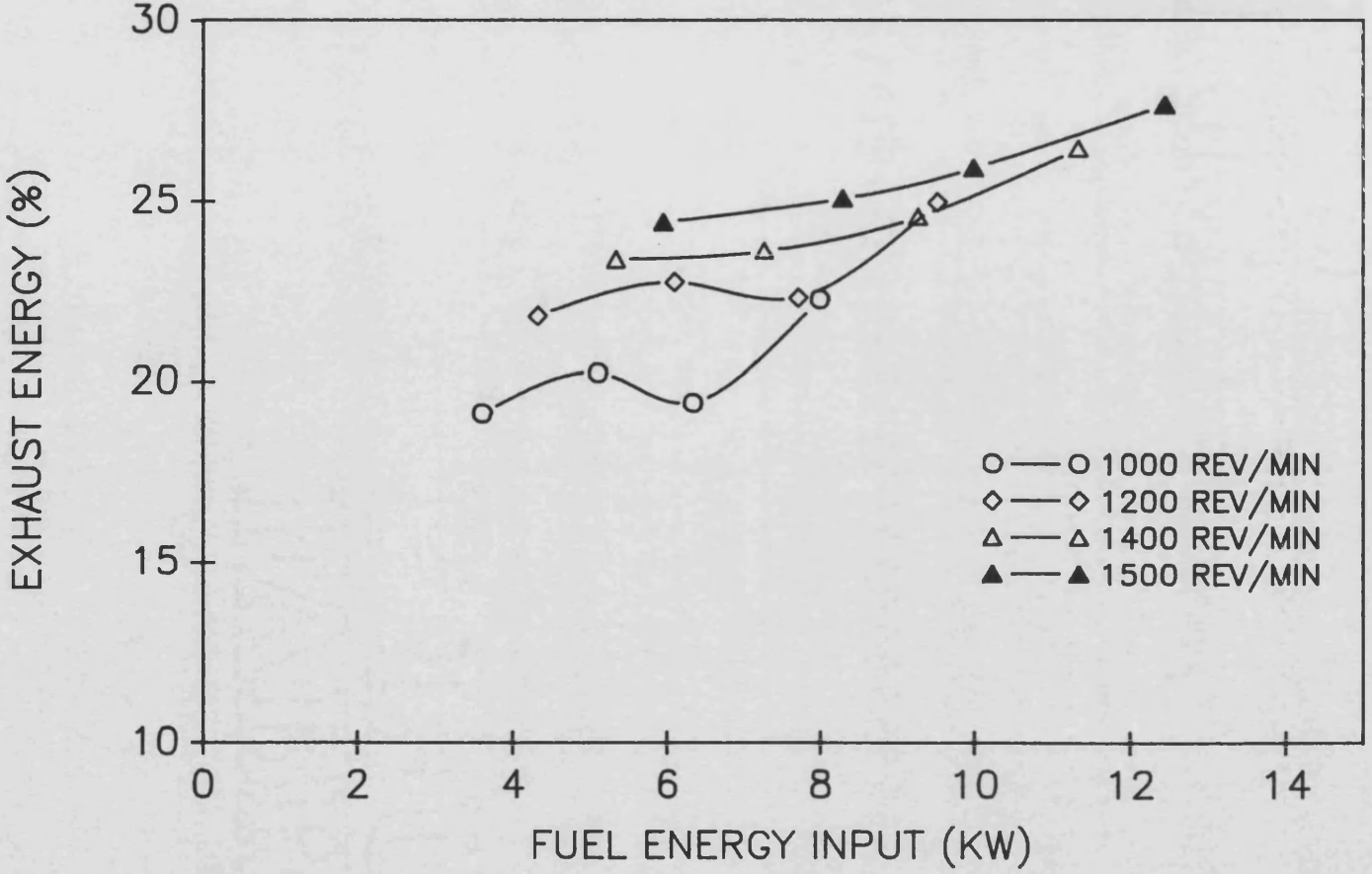

FIGURE 4.32 : EXHAUST TEMPERATURE VS. FUEL ENERGY INPUT FOR INSULATED ENGINE

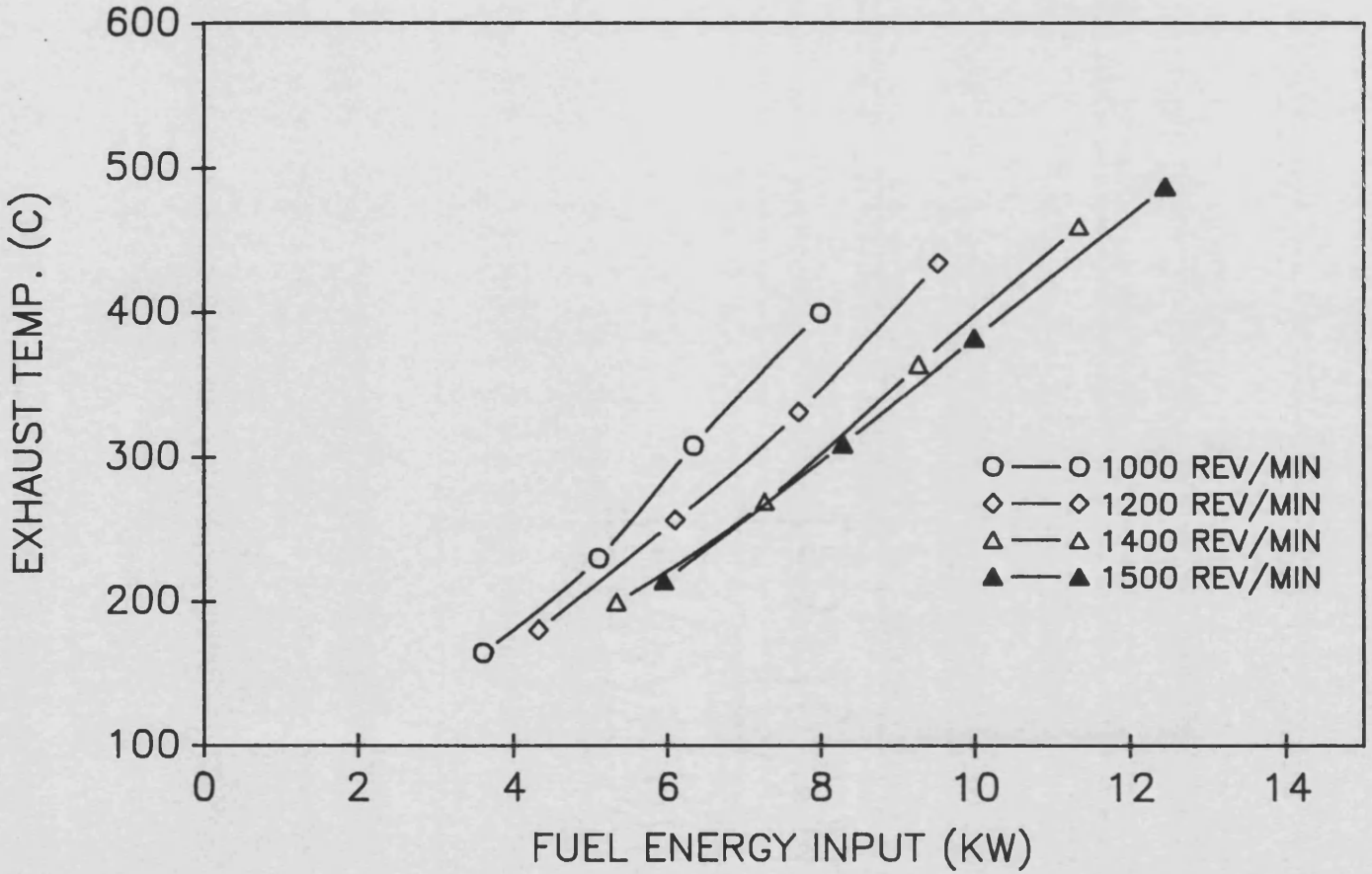

FIGURE 4.33 : HEAT LOSS TO OIL VS. FUEL ENERGY INPUT FOR INSULATED ENGINE.

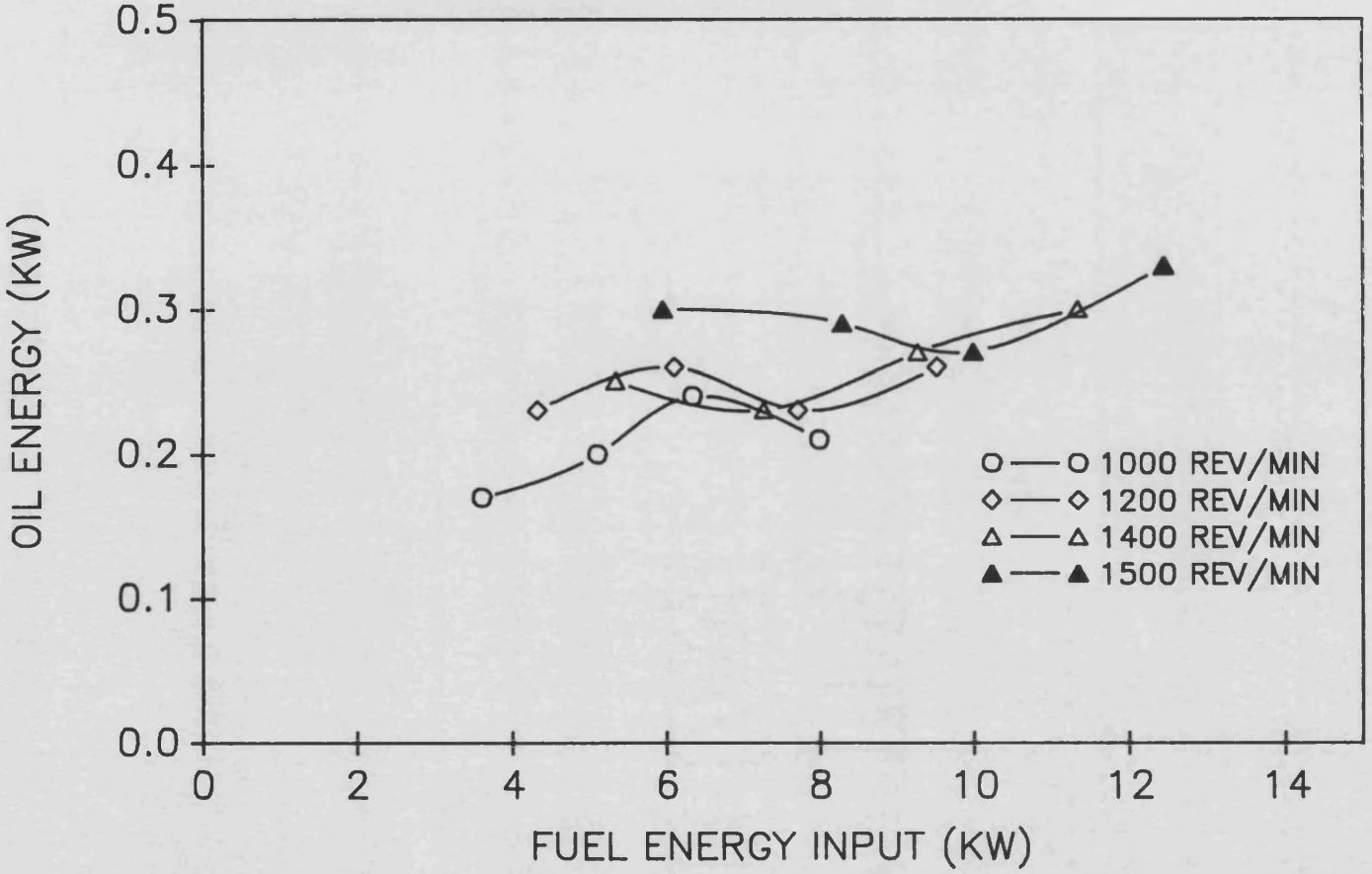

FIGURE 4.34 : HEAT BALANCE VS. FUEL ENERGY INPUT FOR INSULATED ENGINE.

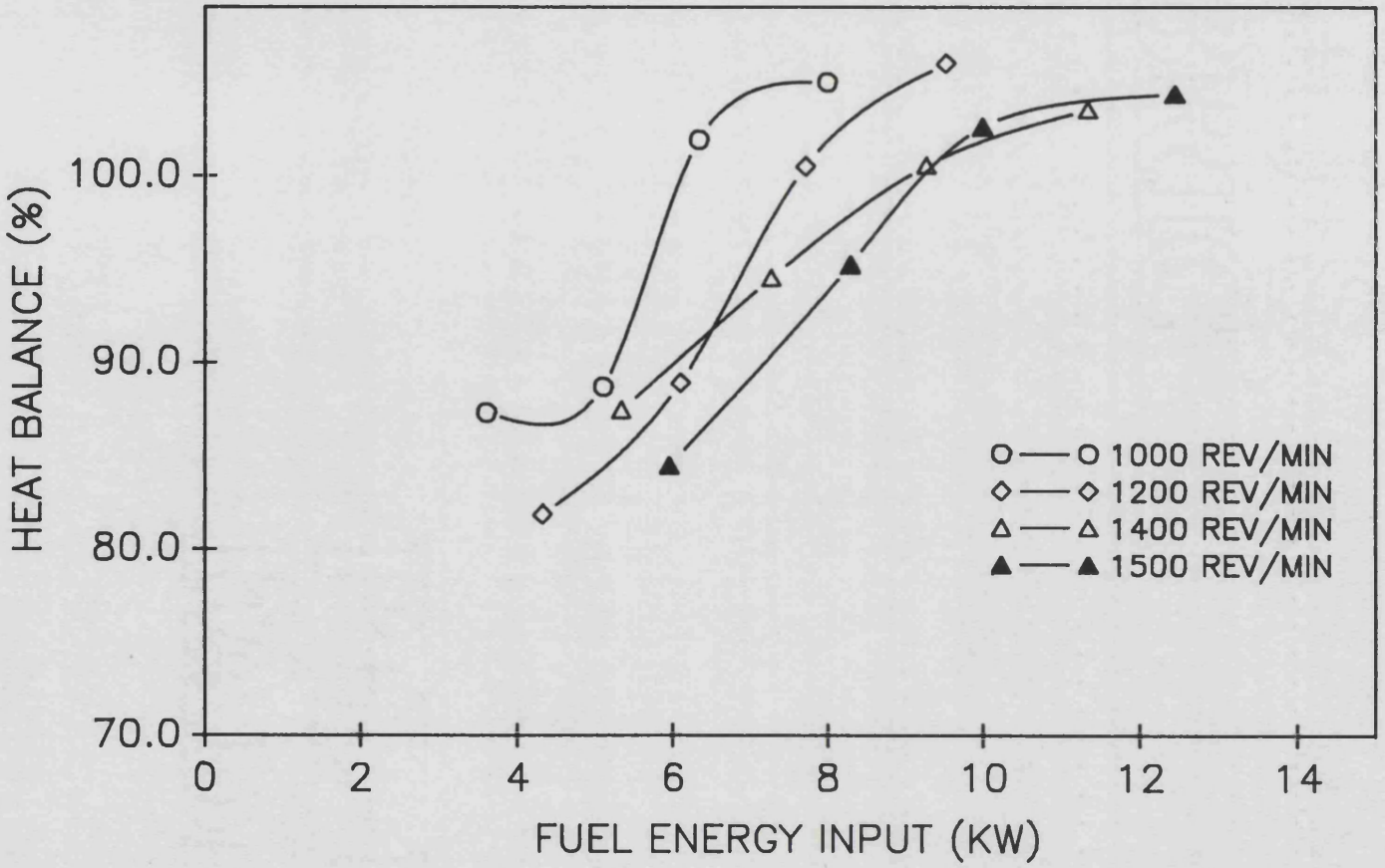

FIGURE 4.35 : BMEP VS. FUEL ENERGY INPUT
FOR EXPERIMENTAL AND MATCHED RESULTS
(STANDARD ENGINE CONFIGURATION.)

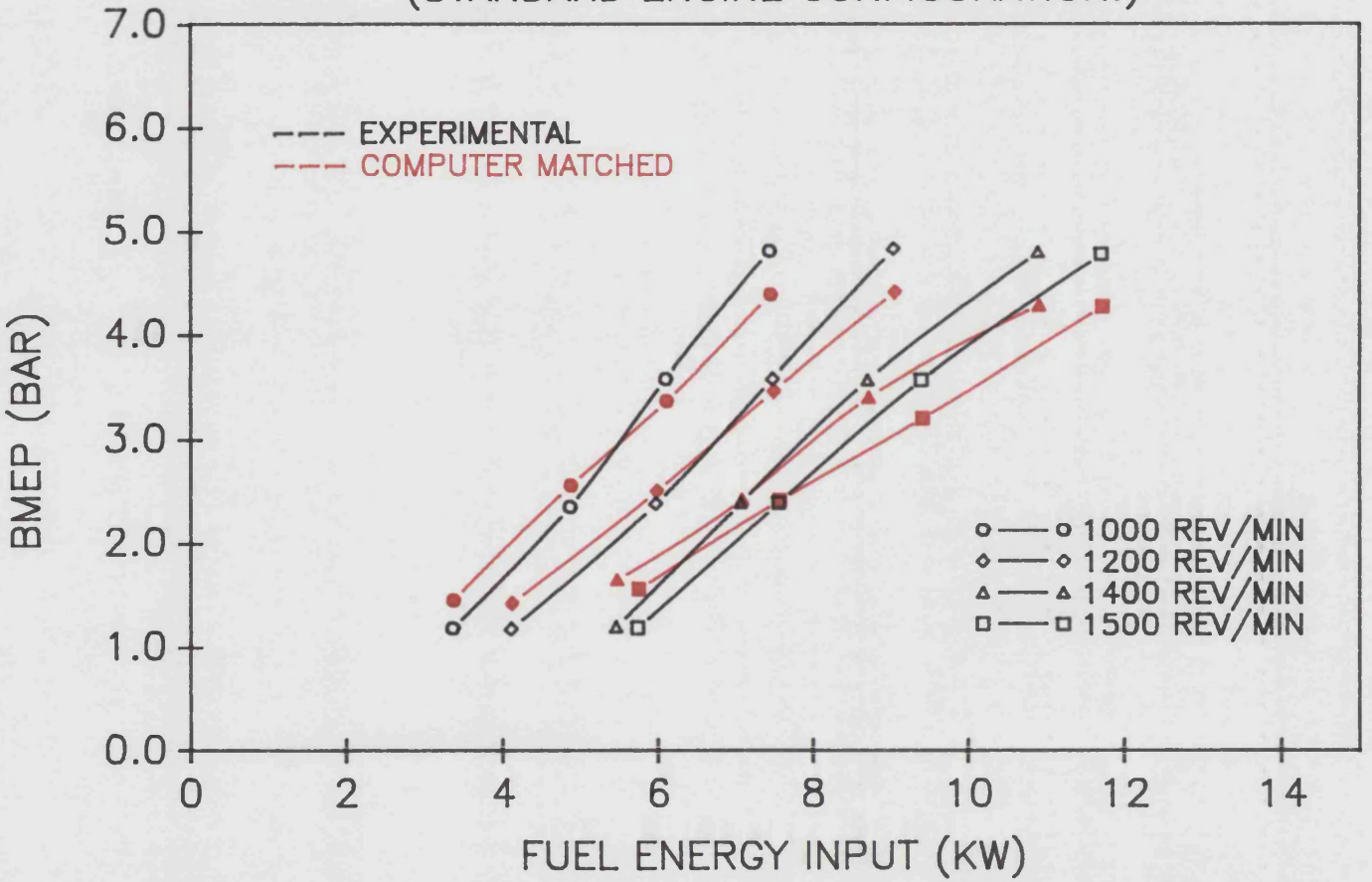

FIGURE 4.36 : THERMAL EFFICIENCY VS. FUEL ENERGY INPUT
FOR EXPERIMENTAL AND MATCHED RESULTS
(STANDARD ENGINE CONFIGURATION.)

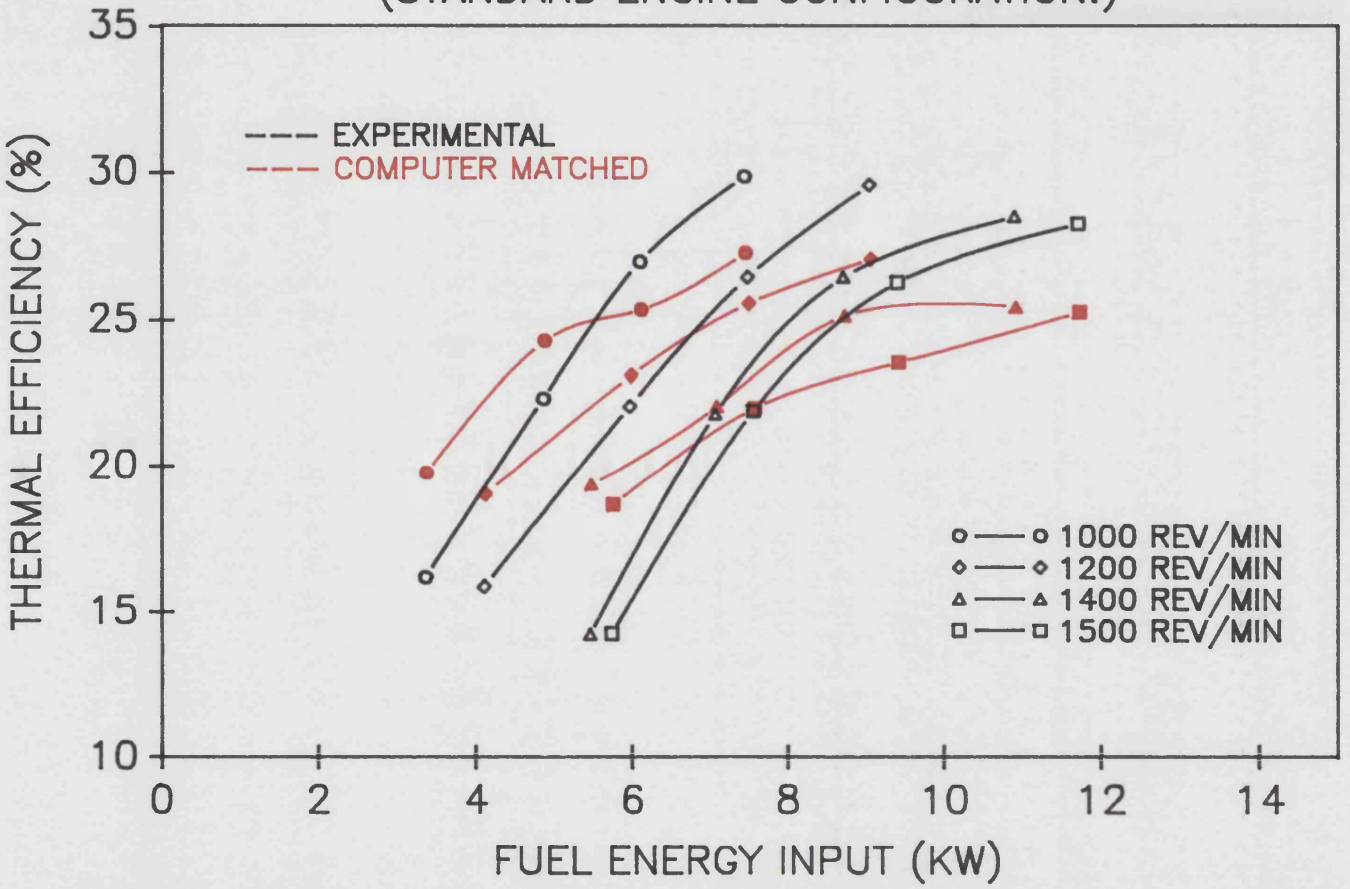

FIGURE 4.37 : AIR–FUEL RATIO VS. FUEL ENERGY INPUT
FOR EXPERIMENTAL AND MATCHED RESULTS
(STANDARD ENGINE CONFIGURATION.)

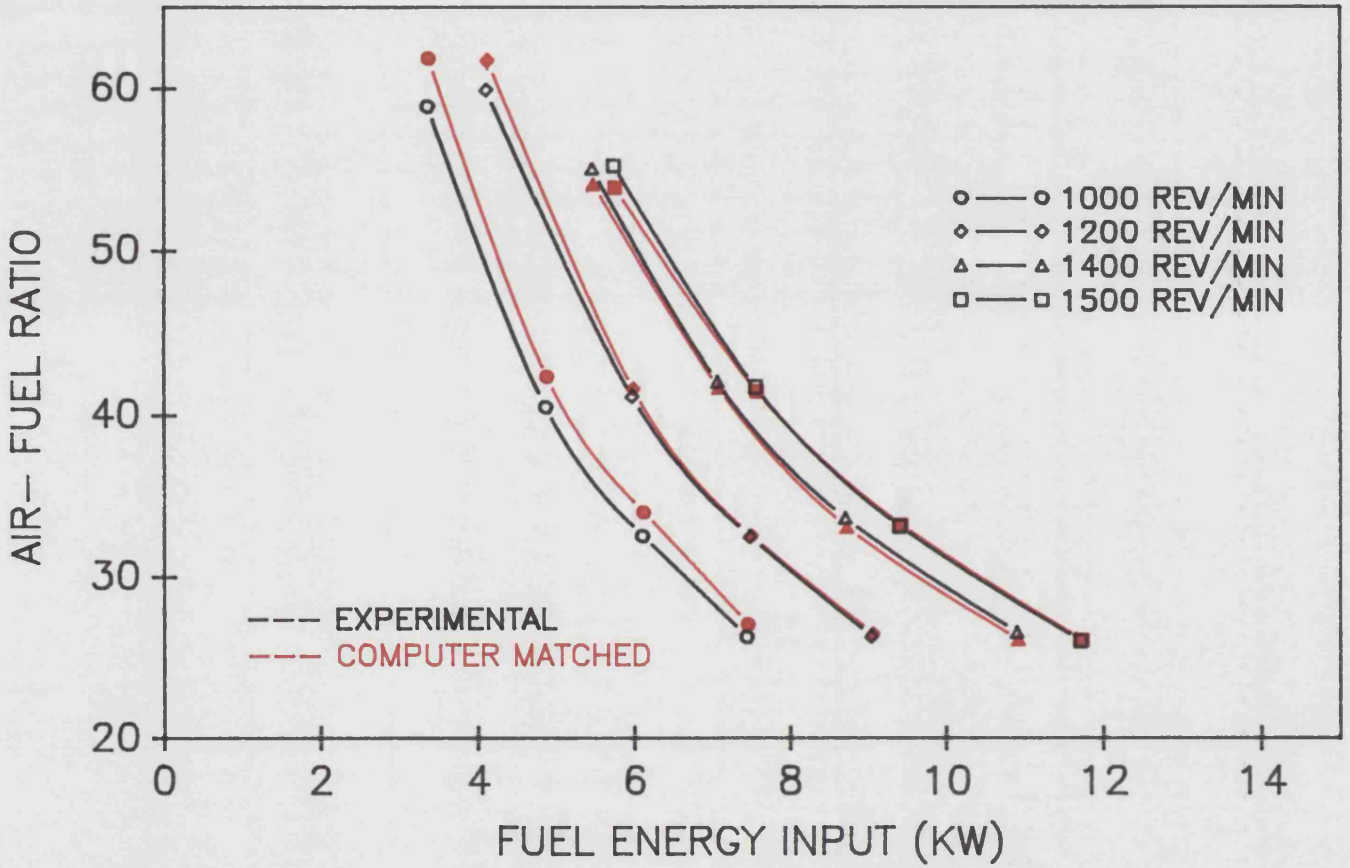

FIGURE 4.38 ABSOLUTE HEAT REJECTION TO COOLANT VS. FUEL ENERGY INPUT FOR EXPERIMENTAL AND MATCHED RESULTS (STANDARD ENGINE CONFIGURATION.)

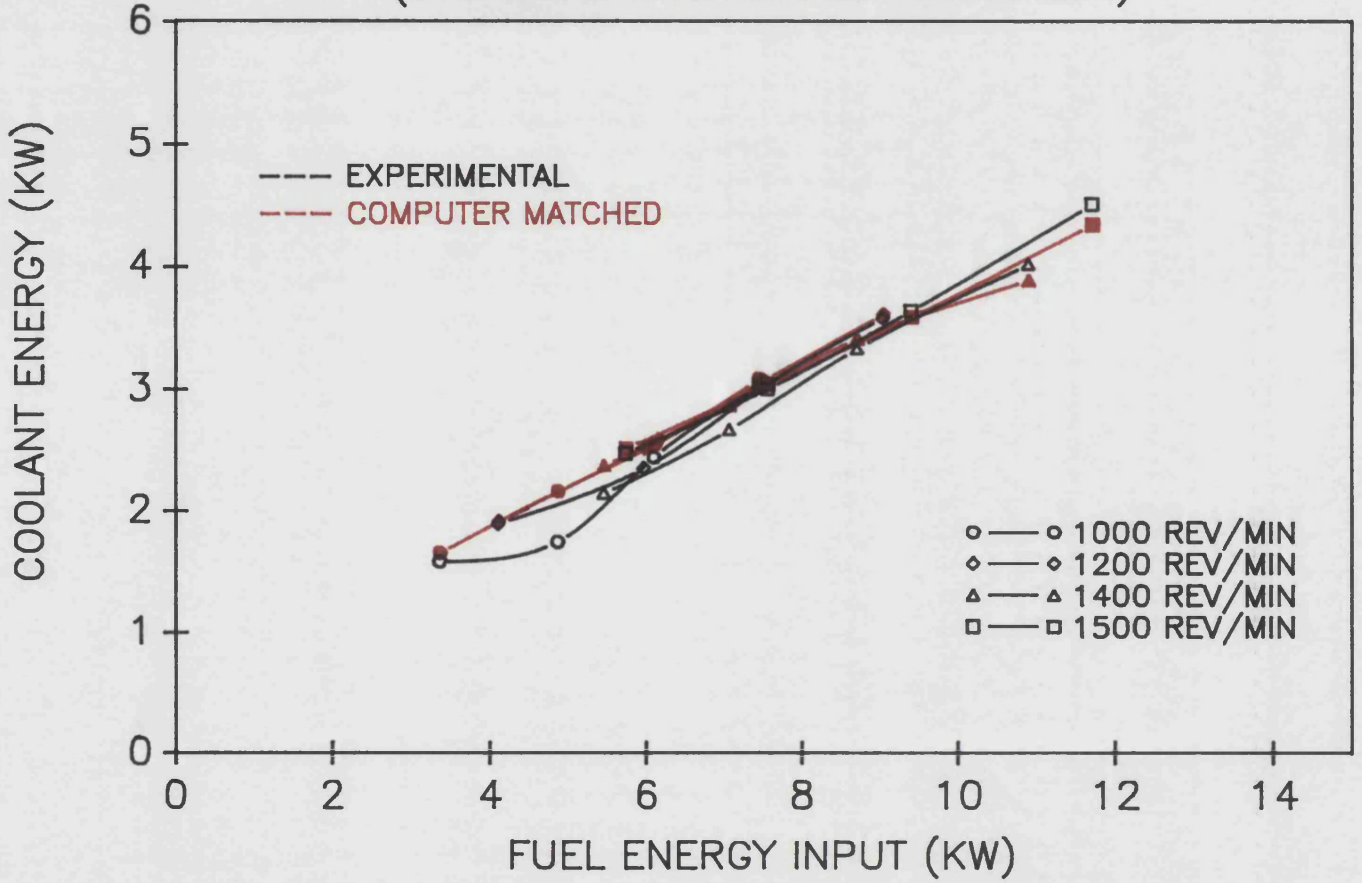

FIGURE 4.39 : PERCENTAGE HEAT REJECTION TO COOLANT VS. FUEL ENERGY INPUT FOR EXPERIMENTAL AND MATCHED RESULTS (STANDARD ENGINE CONFIGURATION.)

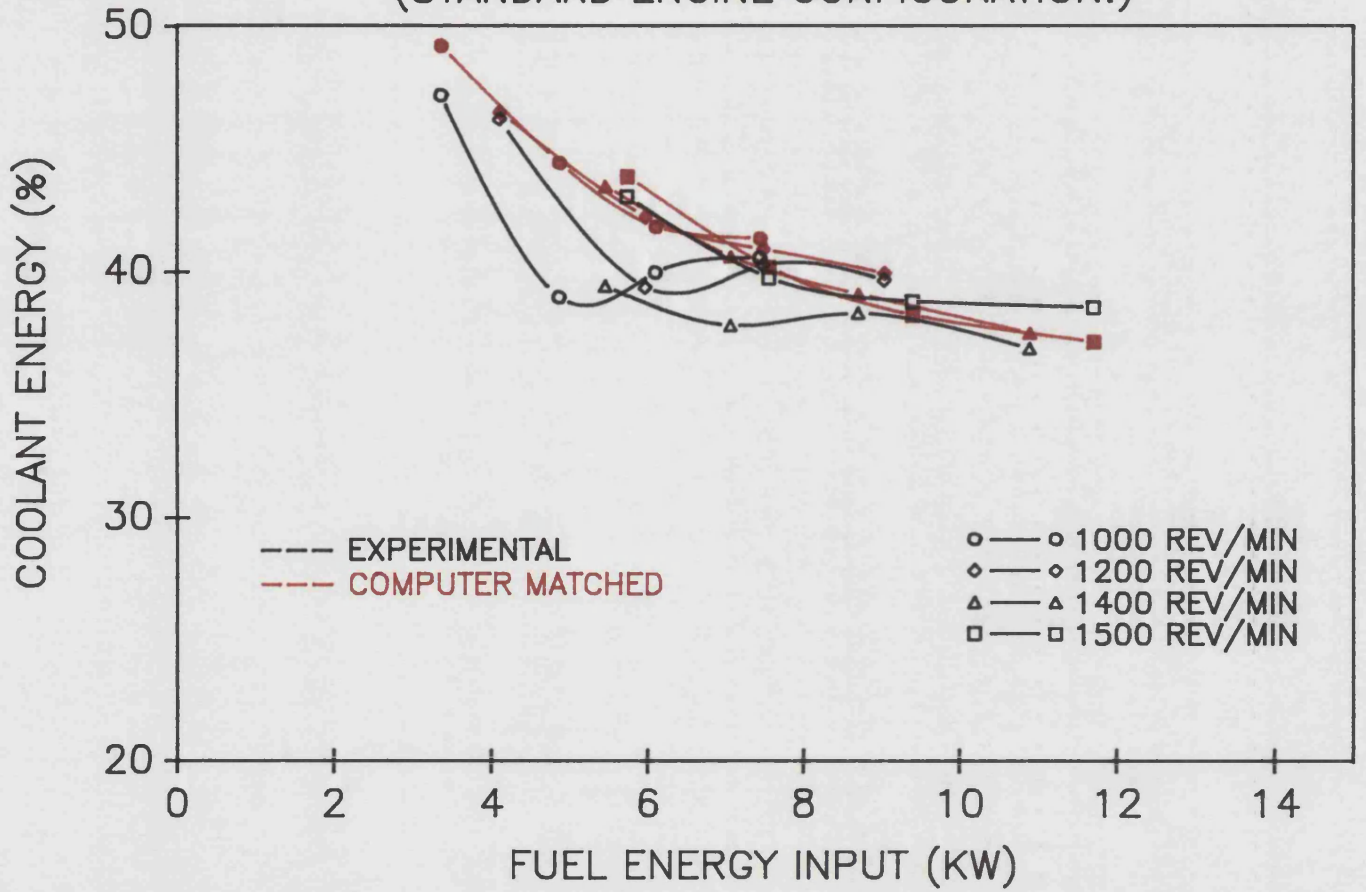

FIGURE 4.40 : EXHAUST TEMPERATURE VS. FUEL ENERGY INPUT FOR EXPERIMENTAL AND MATCHED RESULTS (STANDARD ENGINE CONFIGURATION)

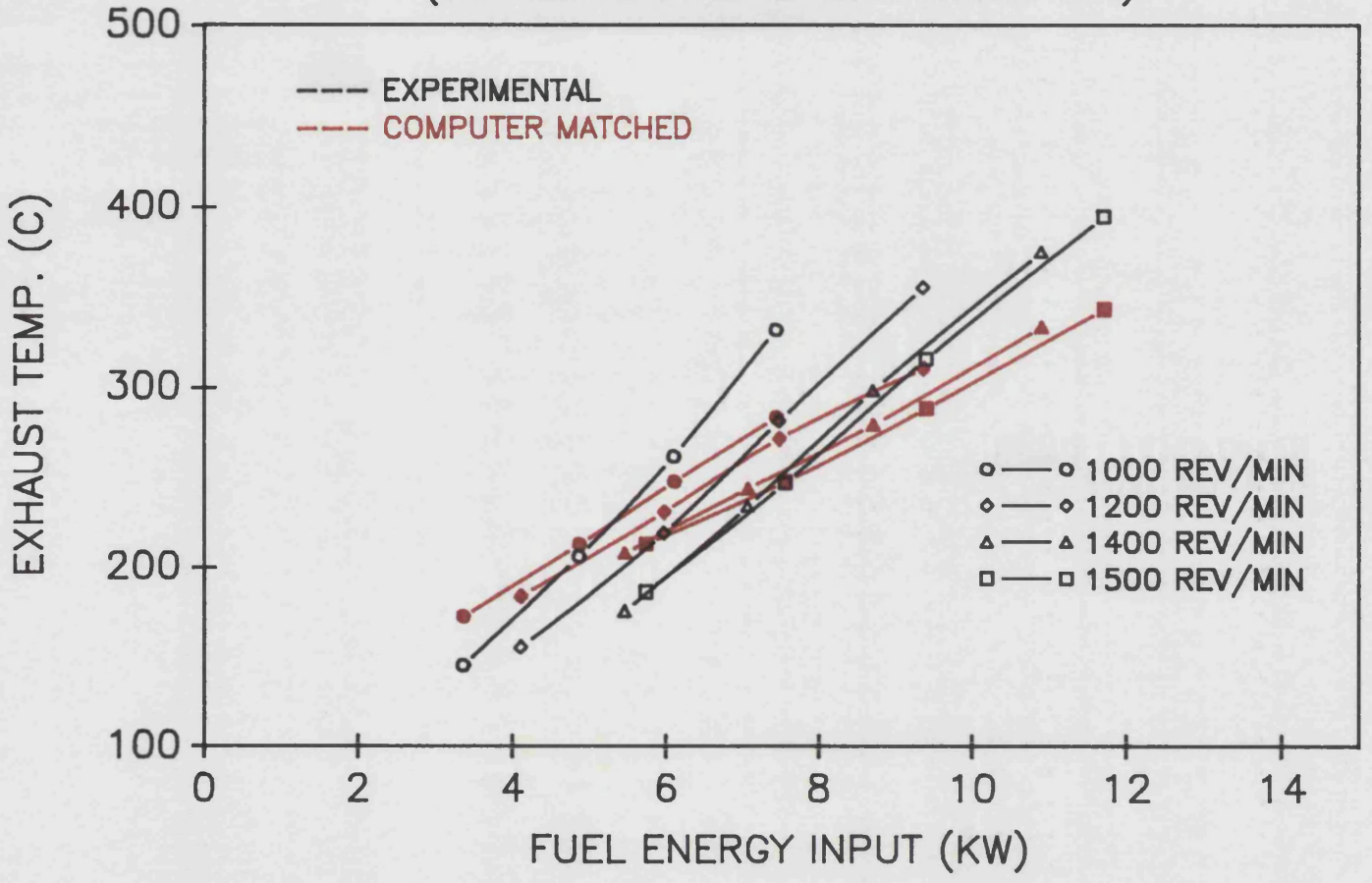

FIGURE 4.41 : BMEP VS. FUEL ENERGY INPUT
FOR EXPERIMENTAL AND MATCHED RESULTS
(INSULATED ENGINE CONFIGURATION.)

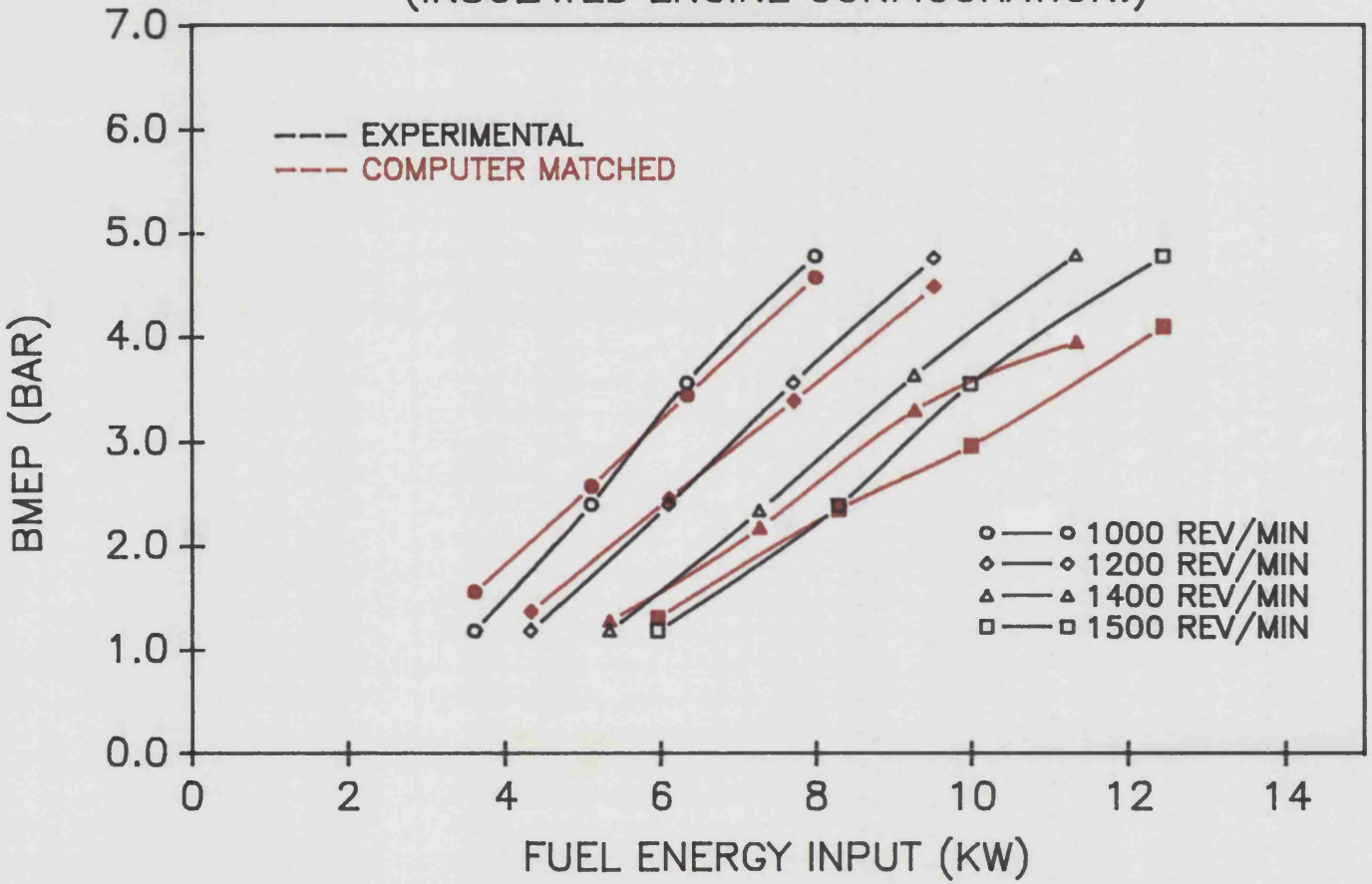

FIGURE 4.42 : THERMAL EFFICIENCY VS. FUEL ENERGY INPUT FOR EXPERIMENTAL AND MATCHED RESULTS (INSULATED ENGINE CONFIGURATION.)

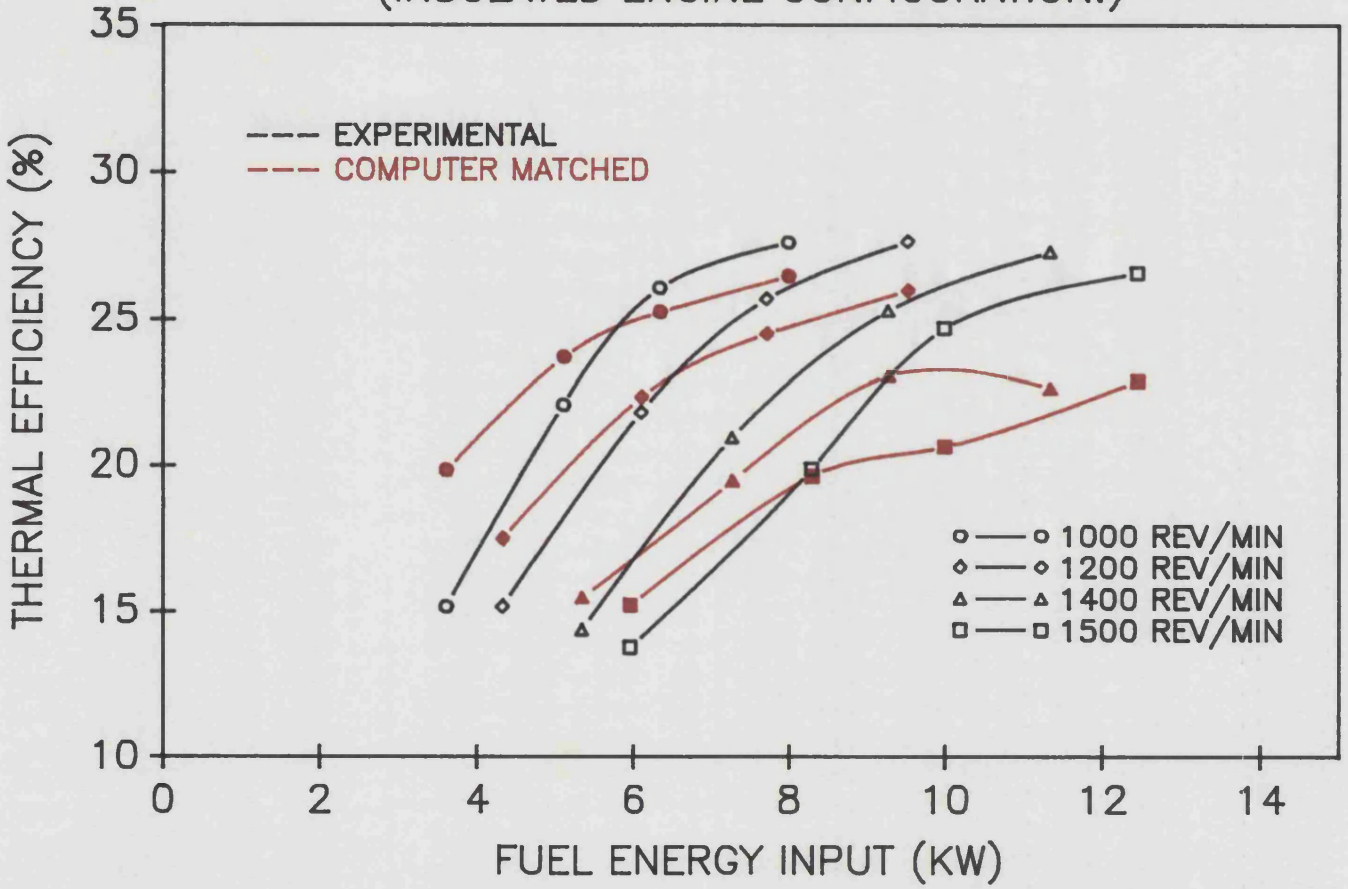

FIGURE 4.43 : AIR–FUEL RATIO VS. FUEL ENERGY INPUT
FOR EXPERIMENTAL AND MATCHED RESULTS
(INSULATED ENGINE CONFIGURATION.)

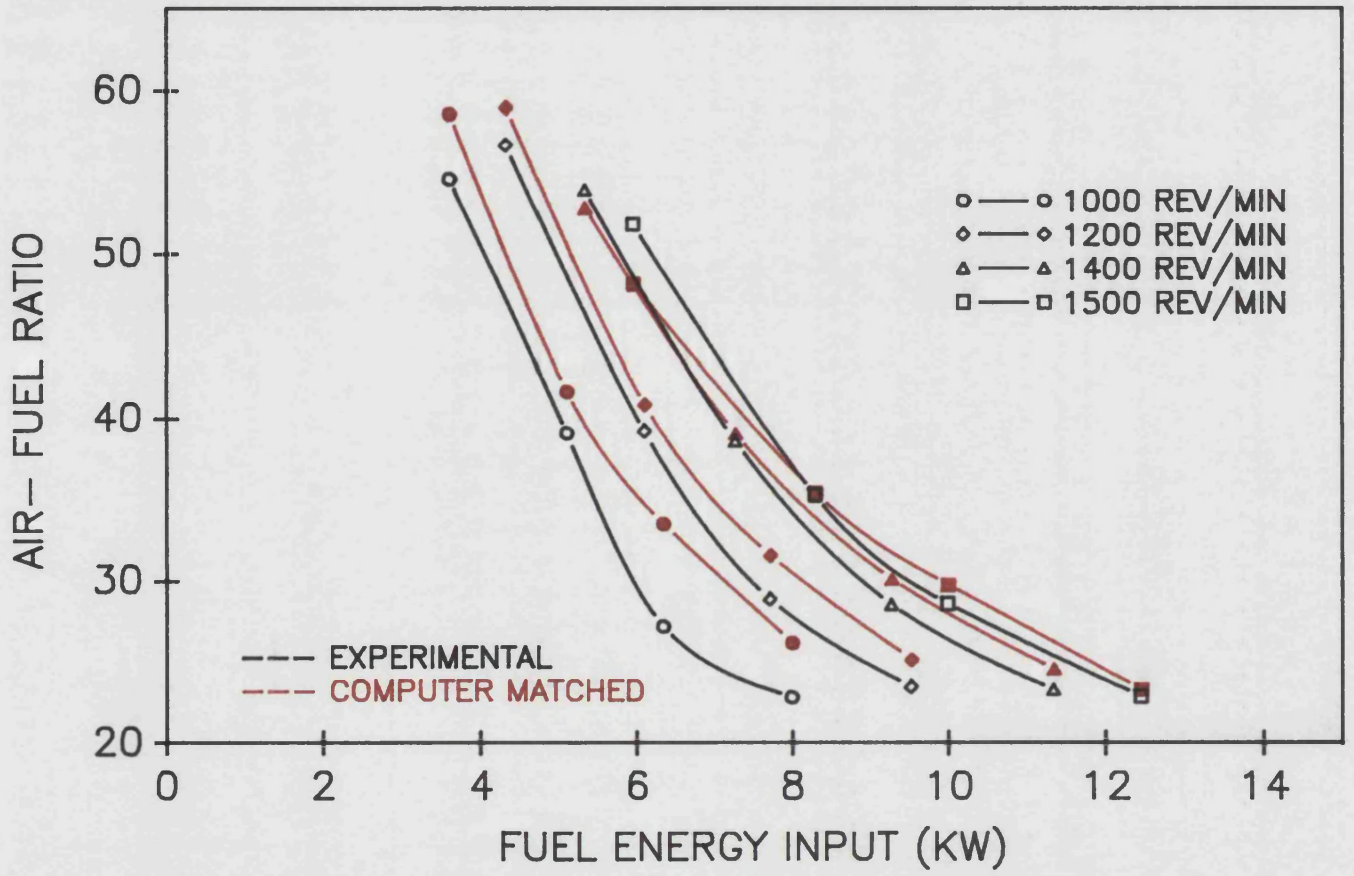

FIGURE 4.44 : ABSOLUTE HEAT REJECTION TO COOLANT VS. FUEL ENERGY INPUT FOR EXPERIMENTAL AND MATCHED RESULTS (INSULATED ENGINE CONFIGURATION.)

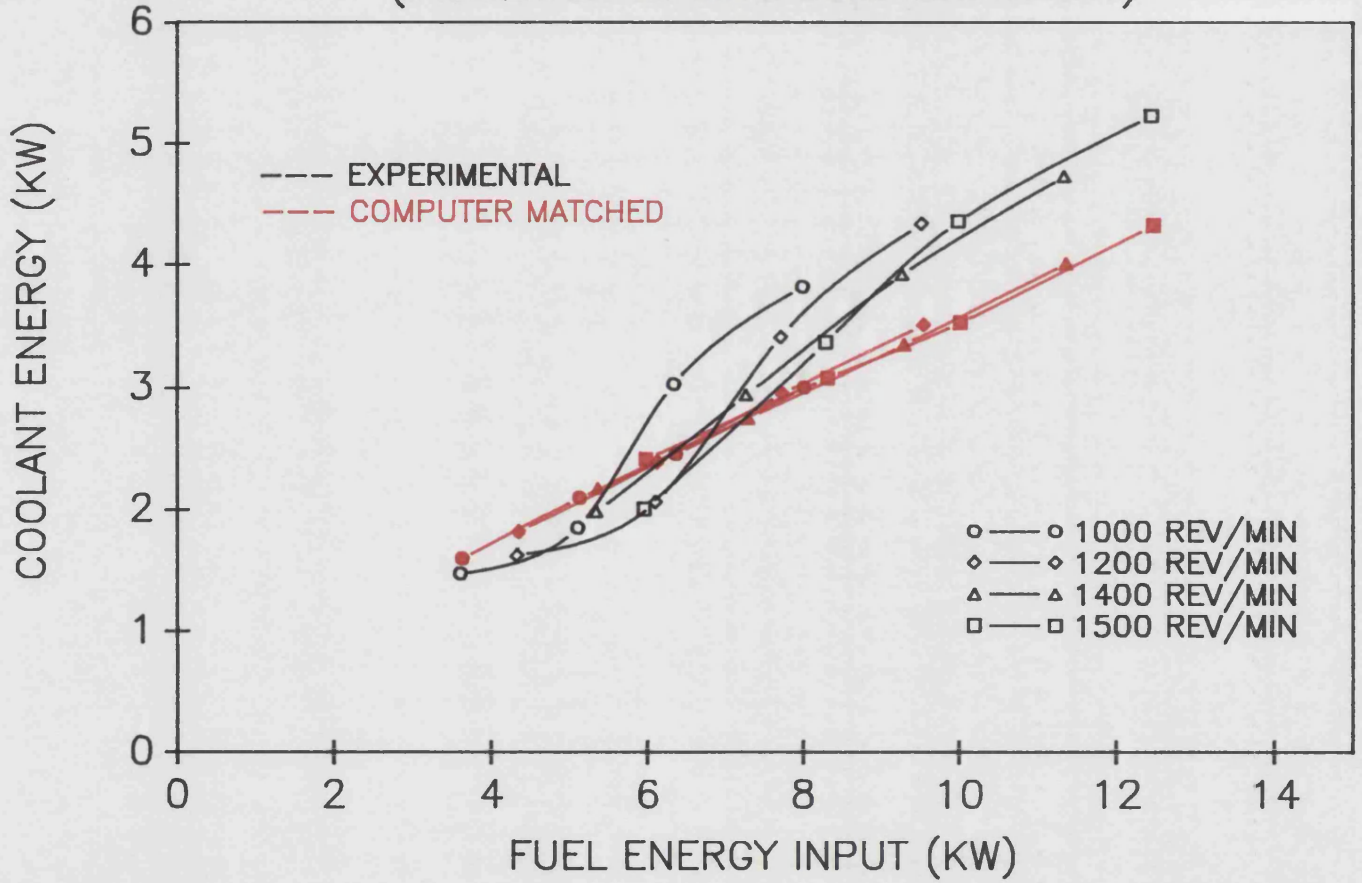

FIGURE 4.45 : PERCENTAGE HEAT REJECTION TO COOLANT VS. FUEL ENERGY INPUT FOR EXPERIMENTAL AND MATCHED RESULTS (INSULATED ENGINE CONFIGURATION.)

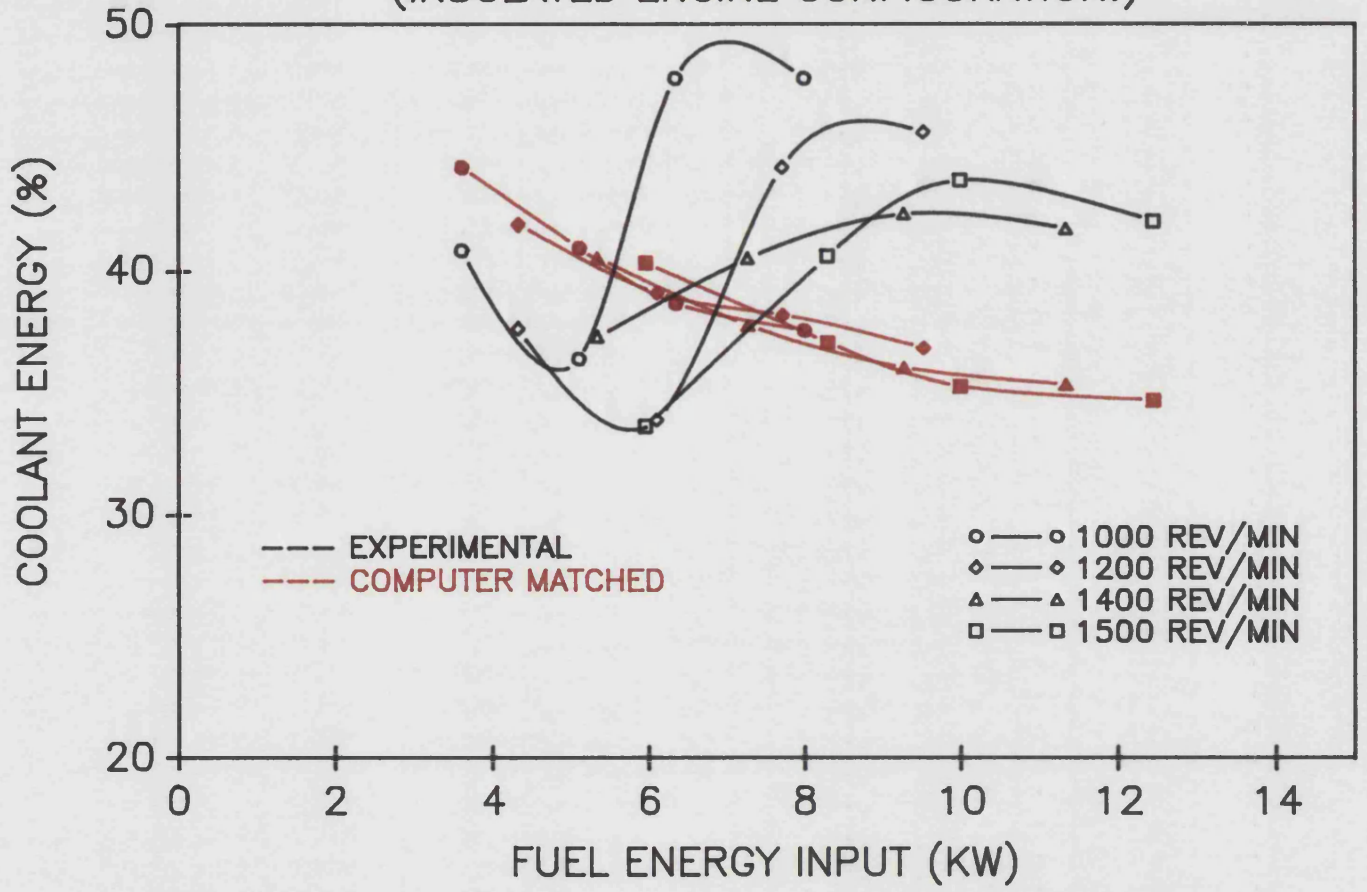

FIGURE 4.46 : ABSOLUTE HEAT REJECTION TO COOLANT VS. FUEL ENERGY INPUT FOR STANDARD AND INSULATED ENGINE BUILDS USING THE SIMULATION PROGRAM ODES.

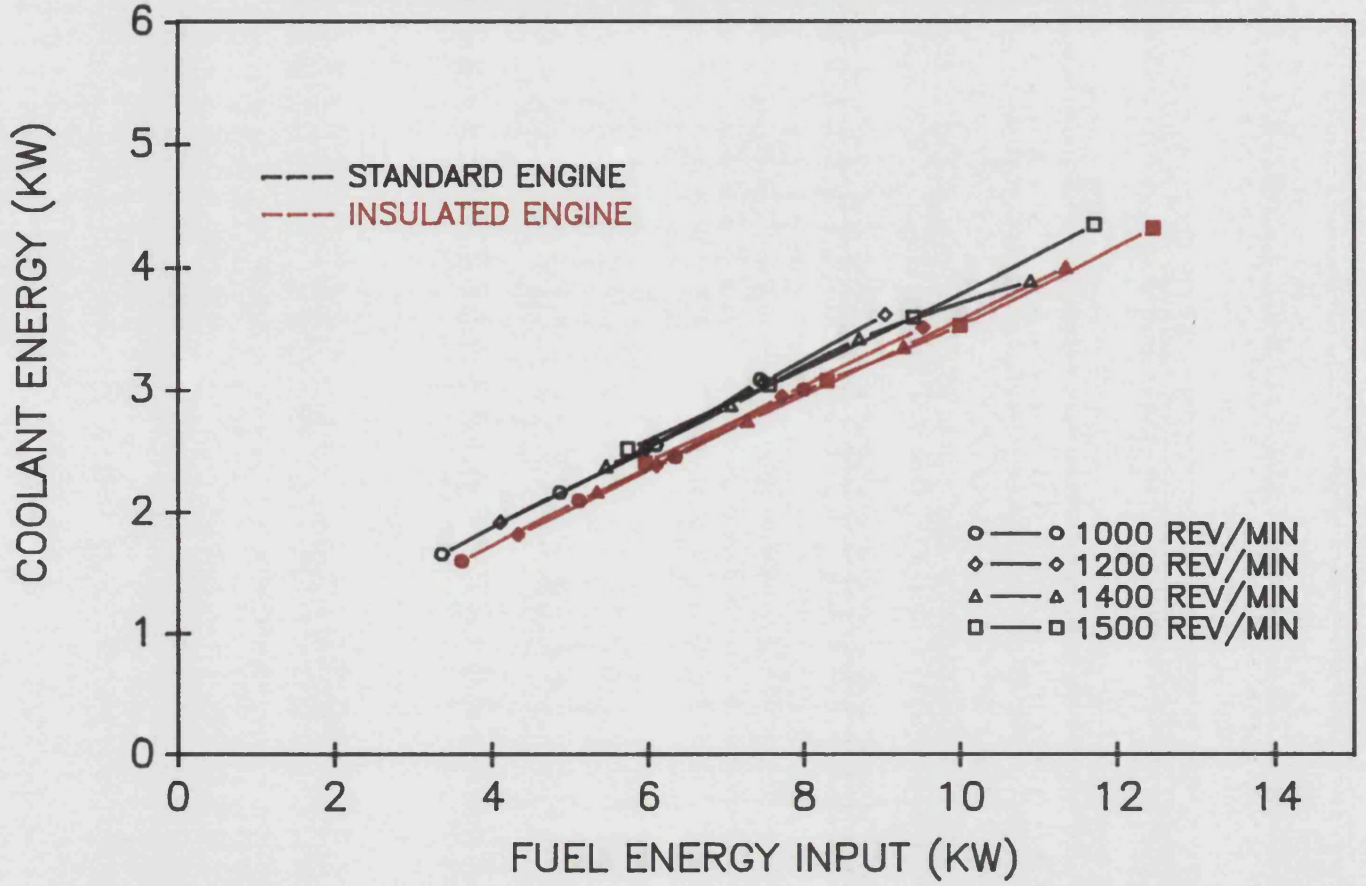

FIGURE 4.47 : EXHAUST TEMPERATURE VS. FUEL ENERGY INPUT FOR EXPERIMENTAL AND MATCHED RESULTS (INSULATED ENGINE CONFIGURATION.)

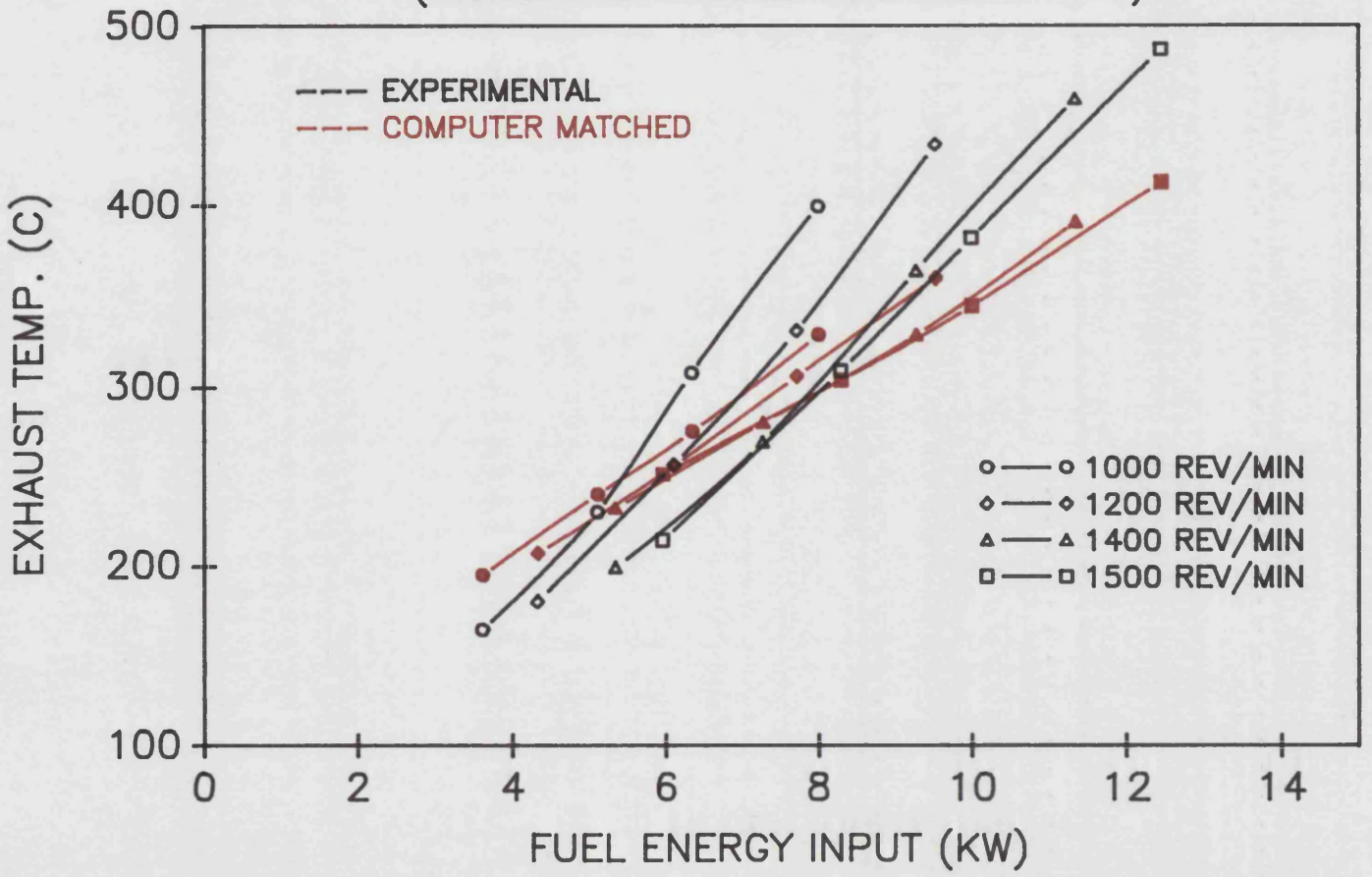

FIGURE 4.48 : EXHAUST TEMPERATURE VS. FUEL ENERGY INPUT FOR STANDARD AND INSULATED ENGINE BUILDS USING THE SIMULATION PROGRAM ODES.

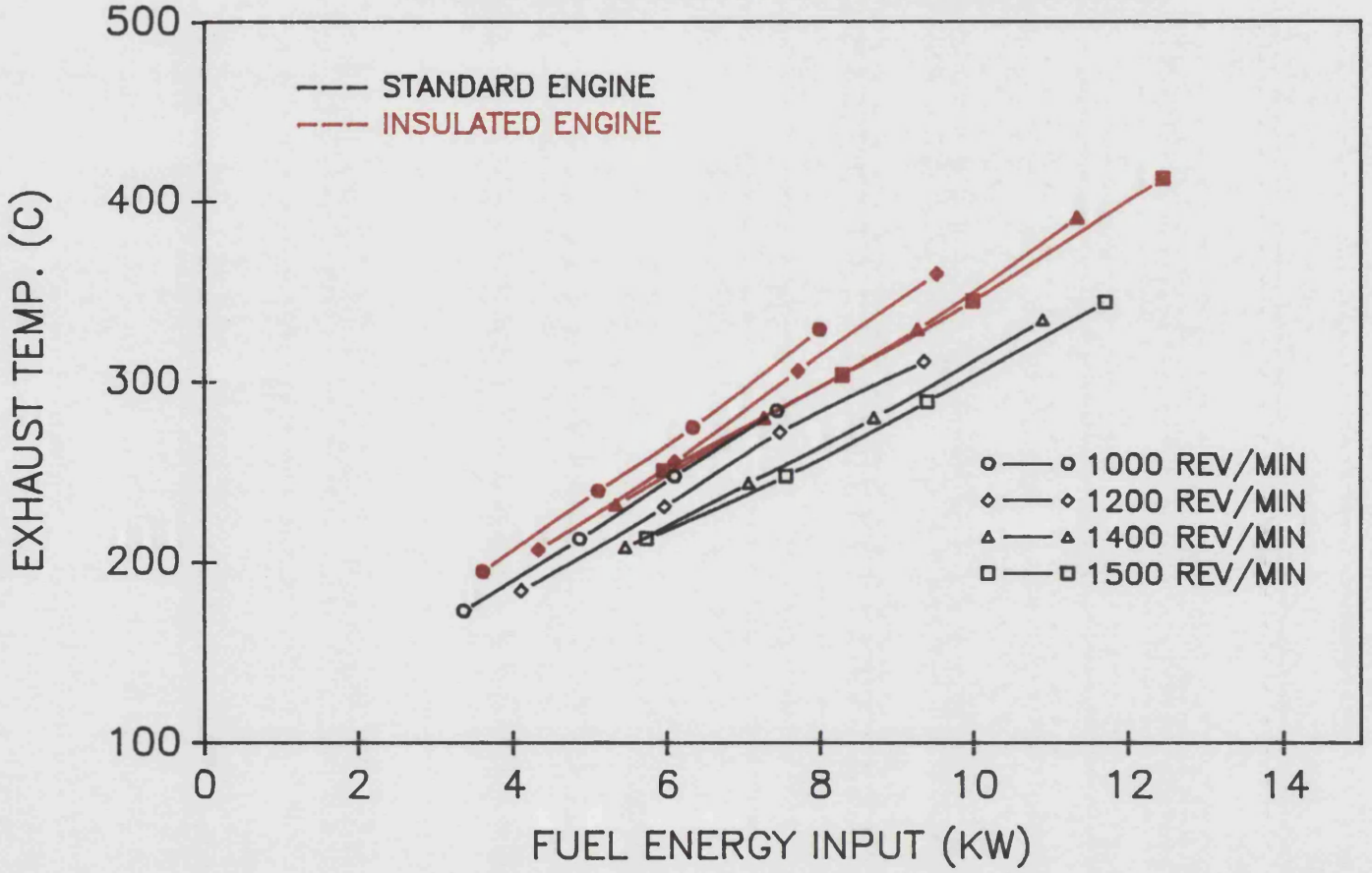

CHAPTER 5
HEAT RELEASE ANALYSIS

5.1 Introduction

One of the author's major tasks was to develop a heat release model for indirect injection (IDI) ie two chamber diesel engines, as opposed to the simpler single chamber direct injection (DI) engine.

Although there are references to this problem in the published literature (see references 40, 41 and 42) no program suitable for use in the present research was available at Bath. The writer therefore wrote a program ab initio incorporating all the necessary features, primarily separate inputs for prechamber and main chamber pressure, the use of a full gas property subroutine and allowance for heat losses to the walls of both chambers.

In the event it proved impossible to implement experimental measurement of both chamber pressures so that the program could not be applied directly to measured engine results.

A simpler version of this program was then derived which depended on only the prechamber pressure as the crucial input. The assumption made in the single pressure program (SPA) that both chambers of the IDI engine are treated as one.

5.2 Analysis Program Using Only Prechamber Pressure Data (SPA)

5.2.1 The use of perfect gas properties

As explained in Chapter 3, main and prechamber pressures are difficult to obtain simultaneously. Access to both chambers, is difficult and the potential unreliability

of the results obtained from using two transducers often results in only one transducer being used. Often the transducer is placed in the prechamber as has been the case in this research.

Heat release analysis relies heavily on accurate cylinder pressure data. With the aid of reliable pressure data, engine geometry and other simple information such as engine speed, fuel consumption etc, a full picture of the in-cylinder events can be obtained.

It is important to make certain assumptions in the process of this (or indeed any) analysis of this nature. In the present case the major assumption is to treat pre and main chambers as a single control volume and to adopt, in the first instance perfect gas properties. The analysis in this section will focus only on the closed period, that is the period after IVC and before EV0.

Figure 5.1 shows a schematic of the IDI engine where the main chamber is designated chamber 1 and the prechamber 2. By applying the first law of thermodynamics;

nett heat release = work + change of internal energy + nett outflow of enthalpy

which for the main chamber is;

$$\frac{dQ_1}{dt} = P_1\frac{dV_1}{dt} + \frac{du_1}{dt} - h_{2,1}\frac{dm}{dt} \qquad 1$$

and for the prechamber is;

$$\frac{dQ_2}{dt} = \frac{du_2}{dt} + h_{2,1}\frac{dm}{dt} \qquad 2$$

If flow from the prechamber to the main chamber is considered to be positive, the energy transfer term $h_{2,1}\frac{dm}{dt}$ can be defined as follows:-

if $\frac{dm}{dt} > 0$ (flow from prechamber to main chamber), $h_{2,1} = h_2$

if $\frac{dm}{dt} < 0$ (flow from main chamber to prechamber), $h_{2,1} = h_1$

From basic perfect gas thermodynamic relationships, the following equations can be stated:

$$PV = mRT \qquad 3$$

$$u = mC_vT \qquad 4$$

and $$\frac{du}{dt} = C_vT\frac{dm}{dt} + mC_v\frac{dT}{dt} \qquad 5$$

from the perfect gas equation 3,

$$T = \frac{PV}{mR}$$

and $$\frac{dT}{dt} = \frac{V}{mR}\frac{dP}{dt} + \frac{P}{mR}\frac{dV}{dt} - \frac{PV}{Rm^2}\frac{dm}{dt} \qquad 6$$

from equations 5 and 6,

$$\frac{du}{dt} = C_vT\frac{dm}{dt} + mC_v\left(\frac{V}{mR}\frac{dP}{dt} + \frac{P}{mR}\frac{dV}{dt} - \frac{PV}{Rm^2}\frac{dm}{dt}\right)$$

$$\frac{du}{dt} = C_vT\frac{dm}{dt} + \frac{C_v}{R}V\frac{dP}{dt} + \frac{C_v}{R}P\frac{dV}{dt} - C_vT\frac{dm}{dt}$$

$$\frac{du}{dt} = \frac{C_v}{R}\left(V\frac{dP}{dt} + P\frac{dV}{dt}\right) \qquad 7$$

since $$\gamma = \frac{C_p}{C_v} \text{ and } R = C_p - C_v \qquad 8$$

$$R = \gamma C_v - C_v$$

$$R = C_v(\gamma - 1) \qquad 9$$

substituting equation 9 into 7 yields

$$\frac{du}{dt} = \frac{V}{\gamma-1}\frac{dP}{dt} + \frac{P}{\gamma-1}\frac{dV}{dt} \qquad 10$$

and substituting equations 10 into 1 and 2 yields equations 11 and 12 respectively

$$\frac{dQ_1}{dt} = P_1\frac{dV_1}{dt} + \frac{V_1}{\gamma-1}\frac{dP_1}{dt} + \frac{P_1}{\gamma-1}\frac{dV_1}{dt} - h_{2,1}\frac{dm}{dt}$$

or

$$\frac{dQ_1}{dt} = \frac{\gamma}{\gamma-1}P_1\frac{dV_1}{dt} + \frac{V_1}{\gamma-1}\frac{dP_1}{dt} - C_p T_{2,1}\frac{dm}{dt} \qquad 11$$

$$\frac{dQ_2}{dt} = \frac{V_2}{\gamma-1}\frac{dP_2}{dt} + C_p T_{2,1}\frac{dm}{dt} \qquad 12$$

By adding equations 11 and 12, the total heat released in the cylinder can be expressed thus;

$$\frac{dQ_t}{dt} = \frac{\gamma}{\gamma-1}P_1\frac{dV_1}{dt} + \frac{1}{\gamma-1}\left(V_1\frac{dP_1}{dt} + V_2\frac{dP_2}{dt}\right) \qquad 13$$

If it is now assumed that

$$P_2 = P_1 + \Delta P$$

then

$$\frac{dP_2}{dt} = \frac{dP_1}{dt} + \frac{d\Delta P}{dt} \qquad 14$$

and by substituting equation 14 into 13,

$$\frac{dQ_t}{dt} = \frac{\gamma}{\gamma-1}P_1\frac{dV_1}{dt} + \frac{1}{\gamma-1}\left(V_1\frac{dP_1}{dt} + V_2\frac{dP_1}{dt} + V_2\frac{d\Delta P}{dt}\right) \qquad 15$$

In the case of only the prechamber pressure being recorded, the $d\Delta P/dt$ term cannot be found. As a compromise to the complexity of using a two chamber pressure monitoring system, accuracy has to be forfeited and thus the $d\Delta P/dt$ term is ignored. This loss in accuracy is large during the initial stages of combustion but later on (ie after approximately 20° ATDC) the errors become negligible (ref. 21). The final simple form of equation 15 becomes,

$$\frac{dQ_t}{dt} = \frac{\gamma}{\gamma-1} P \frac{dV}{dt} + \frac{V_t}{\gamma-1} \frac{dP}{dt} \qquad 16$$

where V_t is the instantaneous total volume of both chambers.

From equation 16, it can be seen that the total nett heat release can be calculated at any point in the cycle if cylinder pressure, engine geometry and gas properties are known. Cylinder pressure reveals the dp/dt term and the bore, stroke and clearance volume gives the instantaneous cylinder volume.

Two ways of solving equation 16 were employed, the first "simple" method by using fixed values of γ, C_p, C_v and R. The latter "comprehensive" method will be explained in the following subsection. A simple heat release program based on the equations developed was written using the following fixed property values for air treated as a perfect gas:

$\gamma = 1.35$
$R = 287$ J/kgK
$C_p = 1005$ J/KgK
$C_v = 718$ J/KgK

The assumptions used here were as follows:

1) The working fluid is pure air, treated as a perfect gas.
2) The effects of temperature and pressure on the working fluid are ignored.
3) Combustion and the input of fuel have no effects on the gas properties.

The main equation used for this analysis is equation 16.

5.2.2 The Use of Calculated Gas Properties

The first development of the rather crude program was to introduce "real" gas properties. This involved restructuring the equations used in section 5.2.1 to take into account the effects of variable gas properties. The difference starts at equation 4 where the internal energy term is now dependent on the effects of temperature, pressure and equivalence ratio viz:

$$u = \text{function}_1 (F,T,P) \qquad 17$$

and also $$R = \text{function}_2 (F,T,P) \qquad 18$$

from equation 17, it can be said that

$$\frac{du}{dt} = \frac{\partial u}{\partial F}\frac{dF}{dt} + \frac{\partial u}{\partial T}\frac{dT}{dt} + \frac{\partial u}{\partial P}\frac{dP}{dt} \qquad 19$$

recalling the equation of state

$$T = \frac{PV}{mR}$$

$$\frac{dT}{dt} = \frac{V}{mR}\frac{dP}{dt} + \frac{P}{mR}\frac{dV}{dt} - \frac{PV}{Rm^2}\frac{dm}{dt} - \frac{PV}{R^2m}\frac{dR}{dt} \qquad 20$$

from equation 18, it can be said that

$$\frac{dR}{dt} = \frac{\partial R}{\partial F}\frac{dF}{dt} + \frac{\partial R}{\partial T}\frac{dT}{dt} + \frac{\partial R}{\partial P}\frac{dP}{dt} \qquad 21$$

substituting equation 21 into 20,

$$\frac{dT}{dt} = \frac{\left(P\frac{dV}{dt} + V\frac{dP}{dt}\right) - mT\left(\frac{\partial R}{\partial P}\frac{dP}{dt} + \frac{\partial R}{\partial F}\frac{dF}{dt}\right) - RT\frac{dm}{dt}}{\left(mR + mT\frac{\partial R}{\partial T}\right)} \qquad 22$$

In order that equations 19 and 22 may be solved, an expression for dF/dt is needed. A gross simplification that was made during the course of this analysis was that there were no residuals at IVC and the compressed gas was pure air until the start of injection. The calculations for equivalence ratio and its rate of change with respect to time were carried out as follows:

$$F = \frac{\text{Fuel air ratio}}{\text{Stoichiometric fuel air ratio}} \qquad 23$$

$$F = \frac{m_f/m_a}{F_s} \qquad 24$$

The mass of air remains the same throughout the closed period and as such becomes a critical calculation heavily dependent on the trapped pressure and temperature. Since these values are of significant importance to the overall analysis, and their accurate measurement not possible, they were predicted using the simulation program ODES previously described in chapter 4 section 4.5. The simulation program was matched to the engine at 1500 rev/min and ½ load as accurately as possible, and from this condition, the fuelling and speed were varied for each case in order to predict the individual trapped conditions.

For the closed period, the mass of fuel is the only variable in equation 24 and is calculated as such,

$$m_f = \frac{Q_r}{LCV} \qquad 25$$

Where LCV is the fuel lower calorific value.

Since the only variable in equation 24 is the mass of fuel,

$$\frac{dF}{dt} = \frac{dm_f}{dt}\left(\frac{1}{m_a F_s}\right) \qquad 26$$

by substituting equations 26 and 22 into 19

$$\frac{du}{dt} = \frac{\partial u}{\partial F}\frac{dm_f}{dt}\left(\frac{1}{m_a F_s}\right) + \frac{\partial u}{\partial T}\left(\frac{P\frac{dV}{dt} + V\frac{dP}{dt} - mT\left(\frac{\partial R}{\partial P}\frac{dP}{dt} + \frac{\partial R}{\partial F}\frac{dm_f}{dt}\frac{1}{m_a F_s}\right) - RT\frac{dm}{dt}}{\left(mR + mT\frac{\partial R}{\partial T}\right)}\right) + \frac{\partial u}{\partial P}\frac{dP}{dt} \qquad 27$$

Having assumed that both pre and main chambers are treated as one control volume, the nett heat release is the sum of the work done and the change in internal energy, since there is no enthalpy outflow during the closed period. Equations 1 and 2 when added result in the nett heat release viz

$$\frac{dQ_t}{dt} = \frac{dQ_1}{dt} + \frac{dQ_2}{dt} = P_1\frac{dV_1}{dt} + \frac{du_t}{dt} \qquad 28$$

therefore nett heat release $\frac{dQ_t}{dt}$ is

$$\frac{dQ_t}{dt} = P\frac{dV}{dt} + A\frac{\partial u}{\partial F} + B\frac{\partial u}{\partial T} + \frac{\partial u}{\partial P}\frac{dP}{dt} \qquad 29$$

where $A = \frac{dm_f}{dt}\left(\frac{1}{m_a F_s}\right)$

$$B = \frac{\left(P\frac{dV}{dt} + V\frac{dP}{dt}\right) - mT\left(\frac{\partial R}{\partial P}\frac{dP}{dt} + \frac{\partial R}{\partial F}A\right) - RT\frac{dm}{dt}}{\left(mR + mT\frac{\partial R}{\partial T}\right)}$$

By using variable gas properties, a separate subroutine based on the work by Krieger & Borman (ref. 43) was used to evaluate instantaneous values of γ, C_p, C_v, and R from known temperatures, pressures and equivalence ratios. The behaviour of C_p and γ (and hence R and C_v) is shown in figure 5.2. The major problem of using this subroutine was the inaccuracy in the calculation of equivalence ratio due to the gross simplifications highlighted earlier.

The calculation for mass of fuel injected into the cylinder (equation 25) is directly dependent on the results of equation 29 which in turn relies heavily on both the pressure and the rate of change of pressure to be accurate. Due to signal distortions (mainly due to noise) the pressure signal can never be 100% accurate. The relatively small inconsistency in signal condition is grossly amplified when small changes in pressure are measured over a small time interval (1 degree crank angle). To overcome this problem, the signal is smoothed prior to its analysis and this smoothing has a marked effect on both pressure and dP/dt terms of equation 29.

The effect of this signal enhancement coupled with less than accurate values for C_v and R (which themselves depend on temperature, pressure and equivalence ratio for their calculation) results in errors in the values of heat release produced by equation 29. As a consequence the value for heat release can sometimes indicate that fuel is being injected into the cylinder well before the start of injection set by the fuel pump.

To overcome this problem, an additional condition is set in the analysis to limit the equivalence ratio artificially such that its calculation only starts nine degrees BTDC. In view of the highly retarded injection adopted for the engine tests, this is fully justified.

5.2.3 Assumptions Made in the Analysis Program SPA

To summarise the preceding sections with the assumptions made, the final form of the program assumed the following points:

1) Both prechamber and main chamber are treated as one volume
2) No heat is lost to friction
3) Heat transfer to walls is based on fixed wall temperatures for piston and cylinder head and an assumed variable temperature for the liner (see 5.4.1).
4) Equivalence ratio is zero until start of injection.
5) Residual gases are not accounted for at any point in the cycle.
6) Trapped temperature and pressure values are derived from the ODES simulation program.
7) Motored cylinder pressure follows a polytropic process as defined by equation 45 (see section 5.4.1).

5.3 Analysis Program Using Pre and Main Chamber Pressure Data (IDIPA)

5.3.1 The use of perfect gas properties

In the early stages of this research, before any decisions regarding cylinder pressure monitoring were taken, it was thought that a two chamber pressure measuring system may be employed. On the understanding that main and prechamber pressures were going to be measured, an analysis program was written based on these two measurements. The program was never used, as only one transducer was chosen to monitor the prechamber pressure alone.

The analysis of main and prechamber pressures relies on a high degree of accuracy in the recorded results. This is a problem in that the pressures in both chambers are only very slightly different. Any errors in these very small differences can lead to the analysis being wholly inaccurate as flow between the two chambers may be assumed to be in one direction when in fact it may be in the opposite direction altogether. Although transducers are relatively reliable, they are still insufficiently accurate for this particular application. For this reason the two pressure monitoring method was dropped in favour of the single pressure technique. Nevertheless, an analysis program using pre and main chamber pressure data was written and checked against synthesised

output from the ODES simulation program already referred to.

The analysis using two recorded pressures was conducted in a similar manner to that pertaining to the single pressure measurement method detailed in section 5.2. The only fundamental difference was the determination of flow between the two chambers. As with the single pressure analysis method, heat transfer calculations were carried out using the Woschni (ref. 22) correlation discussed in section 5.4.1.

Using the schematic of figure 5.1 and once again applying the energy equation to both main and prechambers, it is possible to recall equations 11, 12 and 13 viz

$$\frac{dQ_1}{dt} = \frac{\gamma}{\gamma-1} P_1 \frac{dV_1}{dt} + \frac{V_1}{\gamma-1}\frac{dP_1}{dt} - C_p T_{2,1} \frac{dm}{dt} \qquad 11$$

$$\frac{dQ_2}{dt} = \frac{V_2}{\gamma-1}\frac{dP_2}{dt} \; C_p T_{2,1} \frac{dm}{dt} \qquad 12$$

$$\frac{dQ_t}{dt} = \frac{\gamma}{\gamma-1} P_1 \frac{dV_1}{dt} + \frac{1}{\gamma-1}\left(V_1 \frac{dP_1}{dt} + V_2 \frac{dP_2}{dt}\right) \qquad 13$$

Having solved equation 13 it is necessary to solve either equations 11 or 12 in order that individual heat release patterns for each chamber can be calculated. This is not possible without first solving the flow equation viz

$$\frac{dm}{dt} = D\, C_d\, P_1 \sqrt{\frac{2\gamma}{(\gamma-1)RT_1}\left\{\left(\frac{P_2}{P_1}\right)^{2/\gamma} - \left(\frac{P_2}{P_1}\right)^{(\gamma+1)/\gamma}\right\}} \qquad 30$$

Where the flow is assumed to be subsonic and,

P_1 = Pressure upstream of flow restriction

P_2 = Pressure downstream of flow restriction

C_d = Discharge coefficient

D = Cross sectional area of orifice (throat)

In solving equations 11 and 12, it is important to adhere to a sign convention regarding flow. For the purpose of this study, flow was considered to be positive from prechamber to main chamber (see fig. 5.1). By using this convention the $T_{2,1}$ temperature can be defined as follows:

$$\text{if } \frac{dm}{dt} > 0 \text{ (flow from pre- to main chamber) } T_{2,1} = T_2$$

similarly $$\text{if } \frac{dm}{dt} < 0 \text{ (flow from main to pre-chamber) } T_{2,1} = T_1$$

5.3.2 The use of calculated gas properties

As in the previous section (5.2), this program also started off with constant gas property values. The obvious development was the introduction of calculated gas properties for each of the two chambers since both pressures and both temperatures were known. The same problems of equivalence ratio calculation were also encountered here and similar assumptions regarding the start of injection were also made (see section 5.2.2).

In obtaining expressions for the equivalence ratio, reference to figure 5.1 is made throughout this section. It is important at this stage to state clearly the following definitions:

$$F = \text{equivalence ratio} = \frac{\text{Fuel-air ratio}}{\text{stoichiometric fuel-air ratio}} \qquad 23$$

$$\text{fuel fraction} = \frac{\text{mass of fuel}}{\text{total mass}} \qquad 31$$

$$f = \frac{m_f}{m}$$

If flow from the prechamber to main chamber is considered (ie dm is positive)

$$dm = dm_2$$

$$\text{or} \quad m_2 = m_2' - dm_2 \qquad 32$$

where m_2' = previous mass in the prechamber

from equation 31,

$$m_f = fm$$

$$\therefore dm_f = mdf + fdm \qquad 33$$

$$\text{or} \quad mdf = dm_f - fdm \qquad 34$$

For the main chamber

$$f_1 = \frac{\text{mass of fuel in chamber 1}}{\text{total mass in chamber 1}} = \frac{m_{f1}}{m_1}$$

and for the pre-chamber

$$f_2 = \frac{\text{mass of fuel in chamber 2}}{\text{total mass in chamber 2}} = \frac{m_{f2}}{m_2}$$

By applying equation 34 to the main chamber

$$m_1 df_1 = dm_{f1} - f_1 dm \qquad 35$$

Where dm is positive when flow is into the main chamber (equation 30).

The proportion of fuel transfer from the prechamber as a fraction of dm is f_2dm which is also the quantity of fuel transferred into the main chamber thus:

$$f_2 dm = dm_{f1} \qquad 36$$

and by substituting equation 36 into 35,

$$m_1 df_1 = f_2 dm - f_1 dm$$

$$df_1 = \frac{dm(f_2-f_1)}{m_1} \qquad 37$$

Similarly if the flow direction is reversed such that the main chamber is feeding the prechamber and dm is negative, equation 34 becomes,

$$m_2\, df_2 = dm_{f2} - f_2\, dm \qquad 38$$

In this case, as the flow is reversed, the flow from the main chamber as a fraction of dm is $f_1 dm$ or dm_{f2} and equation 38 reduces to;

$$df_2 = \frac{dm(f_1-f_2)}{m_2} \qquad 39$$

From equations 37 and 39, the change in fuel fraction of each chamber can be calculated having obtained the value for mass flow between them. It is therefore possible to calculate the equivalence ratio in each chamber.

since $$F = \frac{f(m_f + m_a)}{F_s\, m_a}$$

$$\frac{dF_1}{dt} = \frac{df_1\,(m_{f1}+m_{a1})}{F_s\, m_{a1}} \qquad 40$$

and $$\frac{dF_2}{dt} = \frac{df_2(m_{f2} + m_{a2})}{F_s\, m_{a2}} \qquad 41$$

In order that the heat release in each chamber be calculated equations 1 and 2 are to be solved. Having obtained an expression for equivalence ratio in each chamber, an expression for the change in internal energy term for both equations 1 and 2 can be obtained in the same way as section 5.2.2 i.e.

$$\frac{du_1}{dt} = X_1 \frac{\partial u_1}{\partial F_1} + Y_1 \frac{\partial u_1}{\partial T_1}\left(\left(P_1 \frac{dV_1}{dt} + V_1 \frac{dP_1}{dt}\right) - m_1 T_1\left(\frac{\partial R_1}{\partial P_1}\frac{dP_1}{dt} + \frac{\partial R_1}{\partial F_1} X_1\right) - R_1 T_1 \frac{dm}{dt}\right) + \frac{\partial u_1}{\partial P_1}\frac{dP_1}{dt}$$

42

where $$X_1 = \frac{df_1(m_{f1} + m_{a1})}{F_s\, m_{a1}}$$

$$Y_1 = \frac{1}{m_1 R_1 + m_1 T_1 \frac{\partial R_1}{\partial T_1}}$$

and

$$\frac{du_2}{dt} = X_2 \frac{\partial u_2}{\partial F_2} + Y_2\left(V_2 \frac{dP_2}{dt} - m_2 T_2\left(\frac{\partial R_2}{\partial P_2}\frac{dP_2}{dt} + \frac{\partial R_2}{\partial F_2} X_2\right) - R_2 T_2 \frac{dm}{dt}\right) + \frac{\partial u_2}{\partial P_2}\frac{dP_2}{dt}$$

43

where $$X_2 = \frac{df_2(m_{f2} + m_{a2})}{F_s\, m_{a2}}$$

$$Y_2 = \frac{1}{m_2 R_2 + m_2 T_2 \frac{\partial R_2}{\partial T_2}}$$

Having obtained the expressions for the rate of change of internal energy (equations 42 and 43) the nett heat release for each chamber can be calculated using equations 1 and 2 where the flow enthalpy term is calculated using equation 30.

5.3.3 Assumptions made in the analysis program IDIPA

As in section 5.2.3 all the assumptions made are defined in points 2 to 7. The obvious assumption that does not apply here is the fact that both chambers are

considered separately. Further assumptions made here are:

1) Flow from prechamber to main chamber is considered positive
2) Isentropic flow occurs through the connecting passage
3) The coefficient of discharge is empirically obtained by comparing IDIPA output to a simulation program results and adjusting.

5.4 Further Correlations Used in Both Analysis Programs SPA and IDIPA

In the analysis of heat release, fundamental differences between the two methods used have previously been explained. Apart from these differences, the remaining considerations apply to both analyses. These universal relationships and conditions are discussed in the following subsections.

5.4.1 Heat transfer calculations

Prior to using any heat transfer correlations, it was assumed that the dQ_r/dt expression yielded the total heat released in the cylinder with no regard to losses through piston, liner or cylinder head. A heat transfer term clearly had to be introduced to produce valid results. The most commonly used heat transfer correlations are those due to Woschni (ref. 22) and Annand (ref. 38). The Woschni correlation was chosen in the light of its relative simplicity and effectiveness. The equation was used in conjunction with some assumptions;

$$h = Ab^{-0.2}\, T^{-0.53}\, P^{0.8} \left(Bcp + C \frac{V_s\, T_{ivc}}{P_{ivc}\, V_{ivc}} (P - P_m) \right)^{0.8} \qquad 44$$

Where A, B and C are constants

P_m = motored cylinder pressure

cp = mean piston speed

In calculating the motored cylinder pressure in equation 44, it is assumed that the motored pressure is related to the pressure at IVC (which itself is estimated) by a polytropic compression process.

$$PV^n = \text{constant} \qquad 45$$

or $$P_m V_m^n = P_{ivc} V_{ivc}^n$$

$$P_m = \frac{P_{ivc} V_{ivc}^n}{V_m^n} \qquad 46$$

Another assumption made in calculating the heat transfer is that wall temperatures are fixed. These values are obtained for a particular engine build by running the simulation program ODES.

A crude way of allowing for temperature changes in the liner is attempted. It is assumed that the cooler end of the liner (sump end as opposed to cylinder head end) is at an estimated temperature of say 80°C. If the hotter end is now assumed to be at a temperature of 300°C, the temperature difference from TDC to BDC is 220°C. The distance of the piston from TDC at any given crank angle interval can be deduced from the cylinder volume equation (equation 49) and thus the mean liner temperature at any point in the cycle can be calculated viz;

$$\bar{T}_{liner} = \frac{T_{max} + (T_{max} - T_\theta)}{2}$$

or $$\bar{T}_{liner} = 300 - \frac{T_\theta}{2} \qquad 47$$

Where T_θ is the temperature of the liner at a given crank angle θ.

and $$T_\theta = T_{max} - \left(\frac{4}{\pi b^2} (V_\theta - V_{TDC}) \right) \frac{T_{max} - T_{min}}{\text{Stroke}}$$

Given that the stroke of the Petter AV1 engine is 110mm eqn 47 can be rewritten thus

$$\bar{T}_{liner} = 300 - \left(\frac{300 - \left(\frac{4}{\pi b^2} (V_\theta - V_{TDC}) \right) \frac{220}{110}}{2} \right)$$

$$\bar{T}_{liner} = 150 - \frac{4}{\pi b^2} (V_\theta - V_{TDC}) \qquad 48$$

Having obtained an expression for the heat transfer term, the total heat release in the cylinder can be separated into its two components of heat release due to fuel burning and heat transfer to the cylinder walls.

5.4.2 Cylinder geometry

With reference to figure 5.1, the piston distance from the TDC position at a fixed value for crank angle θ can be calculated if the crank radius and connecting rod length are known thus;

$$V_\theta = \frac{\pi b^2}{4} (l + r - r\cos\theta - (l^2 - (r \sin\theta)^2)^{1/2}) + V_c \qquad 49$$

where V_c = prechamber volume + bumping clearance volume + throat volume

$$V_c = V_2 + \frac{\pi b^2 g}{4} + Dh \qquad 50$$

From equation 49, the rate of change of volume with respect to crank angle can be obtained.

$$\frac{dV}{d\theta} = \frac{\pi^2 b^2}{4(180)} \left(r \sin\theta + r \sin\theta.\cos\theta \left(l^2 - (r \sin\theta)^2 \right)^{-\frac{1}{2}} \right) \quad 51$$

and naturally mean piston speed,

$$cp = \frac{2 N_e r}{30} \quad 52$$

5.4.3 Initial conditions

At the start of any analysis program, a set of assumed data has to be fed as a means of starting the calculations with the closed period, the calculations are started at the time both valves close (i.e. at IVC).

The trapped mass is the first important calculation and as the rest of the calculations depend on this crucial quantity, errors in the value of trapped mass can have a large impact on the accuracy of the results. Recalling the equation of state (equation 3), the trapped mass can be expressed thus;

$$m_{tr} = \frac{P_{tr} V_{tr}}{R T_{tr}}$$

The values for V_{tr} and R can be taken as accurate but slight errors in assuming the trapped temperature and pressure are obviously detrimental. The simulation program previously mentioned (ODES) is used to obtain as accurate a match to the real engine as possible in order that realistic P_{tr} and T_{tr} values can be used.

Values for gas properties are entered as those for pure air at atmospheric temperature and pressure for the first calculation, and as soon as in-cylinder conditions at the end of this step are evaluated, the gas property subroutine is used to obtain corrected end of step values.

The rate of change of pressure dP/dt is assumed to be zero for the first calculation. Subsequent values for dP/dt are calculated by subtracting the pressure at the crank angle for which the calculations are being conducted from the pressure, one incremental step previously (in this case one degree crank angle).

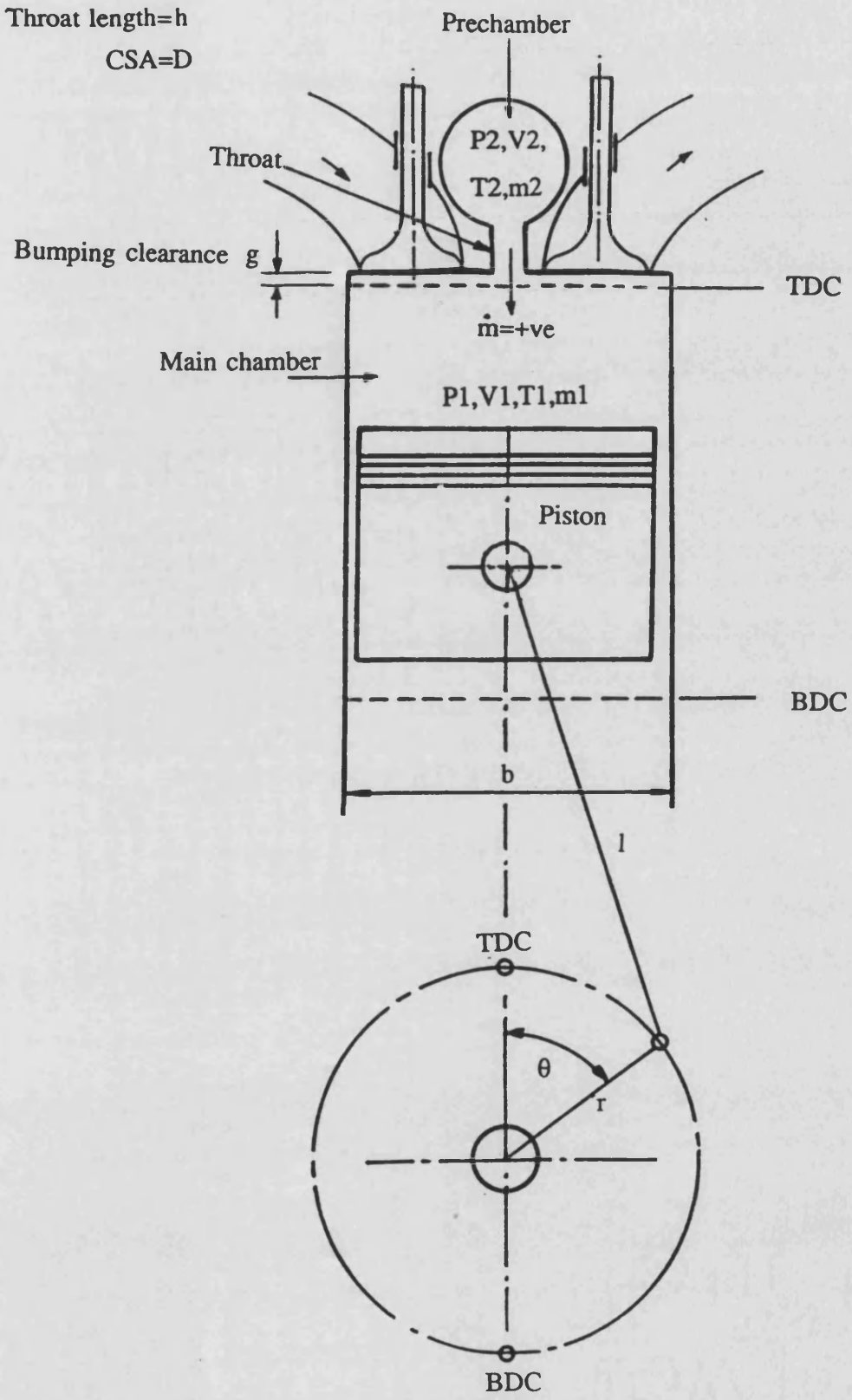

Figure 5.1 : IDI engine cylinder schematic.

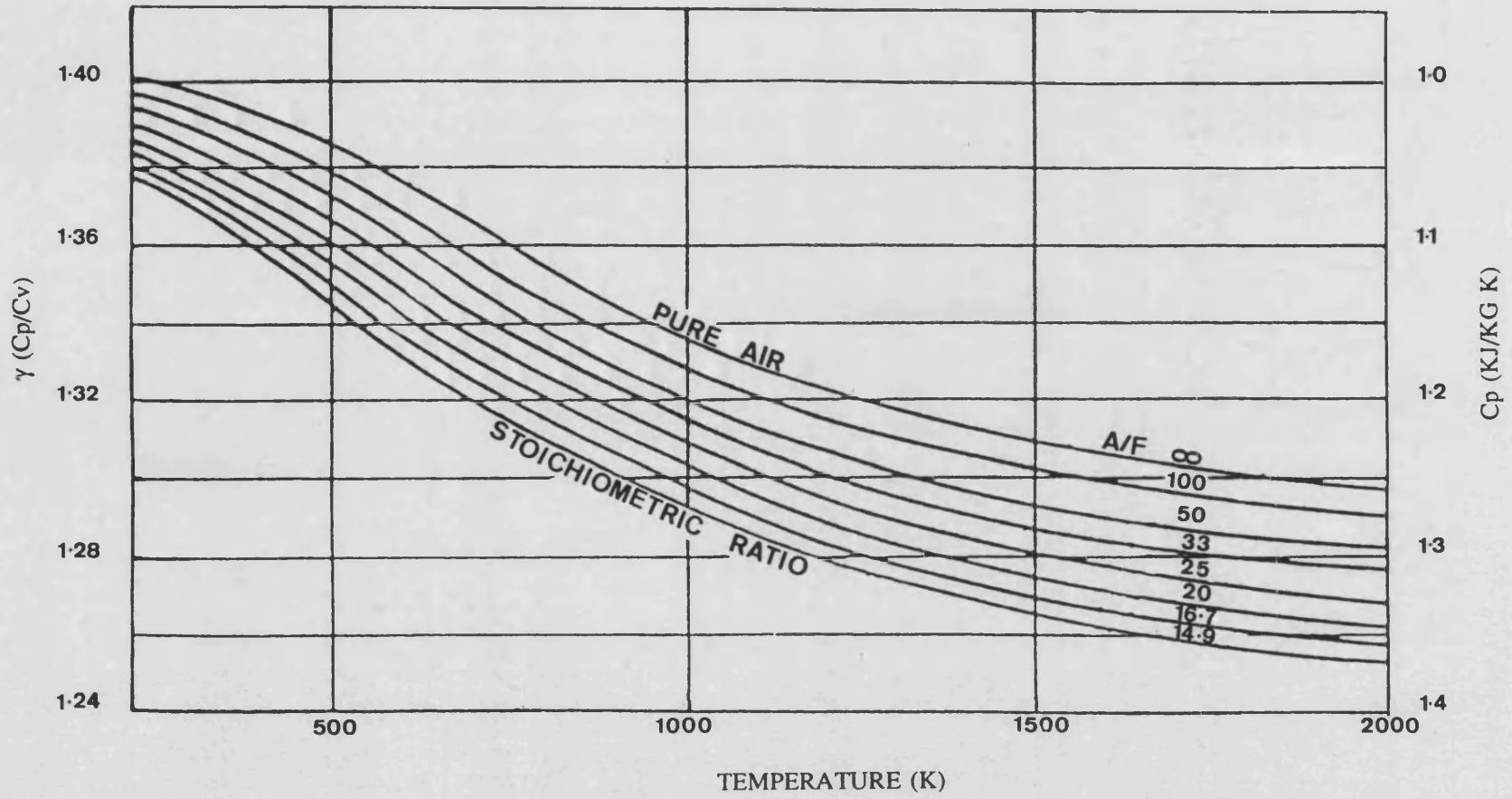

Figure 5.2 : Ratio of specific heats γ and specific heat Cp as a function of temperature and fuel/air ratio

CHAPTER 6
HEAT RELEASE RESULTS

6.1 Introduction

This chapter aims to present the large volume of available heat release results in a concise yet comprehensive manner. The engine was run at 16 different conditions (four loads and four speeds) for both engine builds. This meant that the recorded pressure data alone would have required 32 plots if they were to be individually represented. Each of the 32 cases was analysed and the results from the analysis had to be limited to avoid confusion and excessive bulk. Unfortunately it was not possible to produce tabulated results for close inspection in this chapter as each plot was made up of individual points per degree of crank angle over the closed period of 290 degrees.

Two separate analyses have been detailed in chapter 5, these rely on cylinder pressure as the only input to the calculations but differ slightly in their method of analysis. The difference lies in the fact that the former treats the trapped charge as pure air with fixed gas properties throughout the cycle whereas the latter takes into account the effects of temperature, pressure and equivalence ratio on gas properties and their derivatives. The following section of this chapter outlines the difference in results using these two methods.

The second half of this chapter details all the remaining results obtained for the standard engine and those for the engine with the Cordierite piston cap.

In obtaining these results, the analysis programs detailed in chapter 5 were run with cylinder pressure as the only input. The trapped conditions, as well as wall temperature for piston, head and liner were obtained from the simulation program ODES (see chapter 4 section 4.5). For the reasons highlighted in chapter 4, the

simulation program was matched to the engine at 1500 rev/min and 50% load. Having obtained the closest possible match, the only variables were speed and fuel input per condition.

6.2 Comparison of Analyses Using the Comprehensive and Simplified Computations of Heat Release

The two methods of analysis that are compared in this section are those detailed in chapter 5 sections 2.1 and 2.2 where the principal equations are 16 and 29 respectively. Apart from the difference in the calculation of heat release, the former analysis (to be referred to as the "simple" method) assumes constant values for the gas constants R and γ of 287 J/KgK and 1.35 respectively. The second method detailed in chapter 5 section 2.2 calculates instantaneous values for the gas properties and uses those along with the partial derivatives to evaluate equation 29. This method will be referred to as the "comprehensive" method.

6.2.1 Standard Engine

Figure 6.1 for the standard engine at 1500 rev/min, 50% load shows the pressure data (in its smoothed form) which both types of analysis are based on. At a glance it is evident that this is not a normal pressure curve. The double hump near TDC is very abnormal and is the direct result of a severely retarded engine. The first hump is due to the compression of air (and residuals), and under optimised conditions the curve would then increase in gradient rather than decrease. What is clear from fig. 6.1 is that the piston starts to travel downwards (away from TDC) for a significant period of approximately 6 degrees before the pressure increases due to combustion. The fuel injection timing of 7.5 degrees before TDC is clearly far too late for the engine to have only one hump and run efficiently. This injection timing setting results in an ignition delay of approximately 15 degrees, much needed to keep the peak cylinder pressure (and hence temperature) down, in order that the ceramic monoliths have a

chance of survival. It is clear that the pressure resulting from combustion is only just greater than that due to compression but since the piston is no longer at TDC, the maximum firing pressure is "spread out" over a larger volume resulting in the "softer" conditions discussed previously in this thesis.

It must be stated that the pressure signal shown in figure 6.1 (and indeed all pressure signals in this chapter) have been smoothed and are therefore free of noise and other disturbances. In the unsmoothed condition the signals would have minor distortions that only confuse the analysis (see figures 4.1 and 4.2 of chapter 4).

The rate of change of pressure relative to crank angle ($dP/d\theta$) is shown in fig. 6.2 for the test case in question. The striking features of this plot are the jagged edges and the non conventional shape especially around TDC. The shape is easily explained by the fact that the pressure signal of fig. 6.1 is itself unconventional, so it is only expected for the derivative to follow suit.

The jagged edges are the result of the way in which this parameter is calculated. The pressure signal of fig. 6.1 is made up of one point per crank angle degree and the logical way of arriving at $dP/d\theta$ for such a set of data points is to subtract a data point from that of the previous crank angle value. Since these values are considerably smaller than those of the original pressure points, the $dP/d\theta$ values produce a less smooth curve.

The two plots shown in figures 6.1 and 6.2 are the basis of all analysis in any set of results. It is therefore here that distinctions between the "comprehensive" and "simple" methods start.

Figure 6.3 is the first sign that the two methods of analysis show some slight differences. Although there is a very small difference around 175° AIVC it is insignificant. The only difference in calculating cylinder temperature is in the value of the gas constant R which is almost constant anyway.

The temperature graph of fig. 6.3 shows that combustion starts approximately 6° ATDC and rises to a peak of approximately 1150°C then declines gradually to approximately 500°C at EVO. The shape of these superimposed plots are as expected and appear to be healthy.

The first sign of any visible difference in results from the two methods of analysis is reflected in fig 6.4 for the nett heat release. The definition of "nett" heat release for the simple method is the result of applying equation 16 of chapter 5 (section 5.2.1). The same parameter for the comprehensive method is defined by equation 29 of chapter 5 (section 5.2.2). In both methods the nett heat release is defined as the heat released by the fuel in the cylinder less the heat transfer to (or plus the heat transfer from) the walls to gas.

The marginal difference between the two methods is such as not to cause concern but it is clear that the biggest discrepancies occur during the hottest period of the cycle. At this point in the cycle, the high temperatures have a marked effect on the gas constant γ. The simple method takes γ to be 1.35 whereas at a temperature of approximately 1400 K the γ value is nearer 1.3 (see fig 5.2 of chapter 5). The difference in results given by the two methods can be attributed to two possible factors. The first being the values of the gas properties and the second being the effects of the partial derivatives of equation 29. Judging by how close the two methods are to each other everywhere in the cycle apart from when the cylinder is hottest indicates that for rapid calculations, the simple method gives adequate accuracy.

The rate of fuel heat release of figure 6.5 is defined as the nett heat release previously explained plus the heat transfer components from gas to cylinder head, piston and liner. The heat transfer components are calculated using the Woschni (ref. 22) correlations detailed in chapter 5 section 4.1.

The differences in the curves produced by the two methods again follow the same pattern as that for the previous figure. The shape of the heat release curves are not

conventional but that was only to be expected given the unconventional injection timing of the engine and the resultant shape of the pressure curve. A "normal" heat release curve would have a sharp premix spike followed by a diffusion curve. As established previously from figure 6.3, burning occurs approximately 6° ATDC, which means that the first spike at TDC of fig. 6.5 is not a premix spike, but a discrepancy, probably caused by the less than smooth $dP/d\theta$ curve of fig. 6.2. Apart from this minor blip, the rest of the curve shows an apparent absence of the premix spike, indicating the predominance of diffusion burning.

This lack of premix burning was purposely sought in order to lessen the temperature and pressure swings this creates in the cylinder. The elimination of the premix spike was instrumental in the survival of the ceramic piston caps.

Irregularities in the $dP/d\theta$ plot of figure 6.2 are responsible for the "unsmooth" tail end of the heat release curve (fig. 6.5).

The cumulative heat release curves of fig. 6.6 are quite simply the integration with respect to crank angle of the rate of heat release from IVC to EVO. Hence the difference between the two methods is clearly visible both before and after TDC with the simple method showing reduced maximum and minimum values. The shapes of both the curves are considered generally to be good with the first 80 or so degrees of crank angle AIVC dominated by heat transfer from walls to gas. This is where the fresh charge is cooler than the walls and heat transfer is obviously from walls to gas. The following 70 degrees shows heat given off by the compressed hot gas to the walls until combustion starts some 6° ATDC. At this point, heat is rapidly given off by the burning fuel, until approximately 230° AIVC, where there is no more fuel to burn and the curve levels off.

Figures 6.7 and 6.8 depicting equivalence ratio and mass of fuel burnt in the cylinder are again of good general shape but compared to the experimentally obtained results are considerably higher than expected. However, much closer agreement between experimental and calculated values is obtained at 1500 rev/min, full load (see fig.

6.73) which is discussed in the final summing up of this chapter. The experimentally obtained values for these parameters can be inferred from table 4.5 in chapter 4 and are 0.35 and 1.411×10^{-5} Kg respectively. It would appear that the simple method comes closer to the above results than the comprehensive method, but that is not proof enough to favour the former. Possible explanations for the large discrepancy are as follows:

a) The analysis assumes the engine to be a DI engine when in fact the IDI combustion mechanism is substantially different. No consideration is given to swirl, flow between chambers or fuel mixing rates.

b) The pressure trace of fig. 6.1 used to arrive at equivalence ratio and mass of fuel burnt covers only one cycle with no regard to cyclic fluctuations. It is possible that the particular trace used for this test was a non representative or "rogue" signal. If an average of 100 or 50 cycles were sampled and averaged, this problem would have been less severe.

c) Trapped conditions play a major role in the calculation of all the parameters of both methods of analysis and as such are critical to the sensitivity of the results. The trapped conditions arrived at by ODES could be slightly inappropriate given that the conditions of matching were not exactly the same conditions under which the pressure signal was recorded (see chapter 4 section 4.3).

d) The results tabulated in chapter 4 (tables 4.4 to 4.6) were taken over a period of approximately 10 minutes per condition (due to the physical time needed in accumulating all the data). At an engine speed of 1500 rev/min, 10 minutes represents 7,500 cycles which means that tables 4.4 to 4.6 are <u>average</u> values which due to the nature of experimental work are themselves subject to errors. In contrast the graphs of figures 6.7 and 6.8 are taken over only <u>one</u> cycle.

6.2.2 Insulated engine

Figures 6.9 to 6.16 are the equivalent insulated engine results to those of figures 6.1 to 6.8 which have already been discussed. The discussions for the insulated engine are in many ways similar to those of the standard engine. Wherever a significant difference arises, that difference will be highlighted to avoid tedious repetition. When analysing the pressure data with respect to heat release, the only difference between the analyses for the two engine builds is the different pressure data and the corresponding trapped conditions. As far as the analysis itself is concerned, no differentiation between the two engine builds is made.

Figure 6.9 shows a completely different pressure trace than the equivalent standard engine plot of figure 6.1. The highest pressure is approximately 10 bar higher in the insulated engine with a more rapid pressure rise associated with the second hump. the second hump starts approximately at TDC suggesting combustion commencing at TDC. The ignition delay of 15° associated with fig. 6.1 is reduced significantly to approximately 8°. Although this reduction in ignition delay produces a more efficient combustion and hence higher peak temperatures and pressures these effects were deliberately minimised by the use of retarded injection. Looking at figures 6.9 and 6.1 it can be seen that piston insulation nevertheless, increased cylinder pressure (and looking at figs. 6.11 and 6.3, also temperature).

Figures 6.10 and 6.2 are only as different to each other as their corresponding pressure plots. The higher second hump of fig. 6.9 is reflected in fig 6.10 where if a comparison between the two $dP/d\theta$ plots were to be made, the effects of the relative second hump size are clear.

Figure 6.11 is very interesting especially when compared to fig. 6.3. Here the start of rapid temperature rise clearly starts at TDC for reasons explained above. The peak temperature of approximately 1700 K corresponds to an increase of 300 k for a pressure increase of 10 bar. Up to TDC, the temperature (and indeed pressure) traces

follow a similar pattern, but after the peak temperature is reached, the temperature history during the subsequent expansion indicates a much steeper drop for the insulated than for the standard engine, such that the EVO temperature is less for the former than for the latter.

An explanation is required for the unexpected EVO temperatures in the light of exhaust temperature trends discussed in chapter 4. The temperature at EVO obviously dictates the exhaust temperature and if the results of fig. 6.3 and 6.11 were taken as concrete, then the exhaust temperature of the insulated engine would have to be lower than the standard engine. This is obviously not the case as it has already been explained that the results of chapter 4 span several hundred cycles whereas the results in this chapter cover only one cycle. Since temperature is derived from pressure, a small discrepancy in the pressure signal at the low values around 250° AIVC will result in marked differences in the equivalent temperature calculations. From fig. 6.9, the pressure at 250° AIVC is approximately 5 bar and from fig. 6.11 the temperature is approximately 750 K. Using the equation of state,

$$PV = mRT$$

$$\frac{T_1}{P_1} = \frac{V_1}{m_1 R_1} = \frac{T_2}{P_2}$$

$$\frac{750}{5\times10^5} = \frac{T_2}{P_2} = 0.0015 \qquad 53$$

If the pressure signal was considered slightly inaccurate and an error of 1 bar was considered likely, the resulting temperature could according to equation 53 range from 600 K to 900 K. In practice the signal could easily be within the error margin indicated above, and for this reason the EVO temperatures should not really be considered for comparison. The problem of possible pressure transducer errors is discussed in section 4 of this chapter.

The nett rate of heat release plot of figure 6.12 shows a more significant difference between the two methods than for the standard engine (figure 6.4). The difference in the two methods is however restricted to the peak values corresponding to the larger hump of fig. 6.9. As in the standard engine result, the difference is attributed to the fixed values for the gas constants γ and R, but due to the higher magnitude of pressure (and hence temperature) the effect of gas properties is relatively bigger since both γ and R are functions of temperature and pressure.

The fuel heat release of figure 6.13 follows a more normal pattern than the corresponding standard build curves of figure 6.5. The fluctuations caused by noise are still evident but the spurious blip of figure 6.5 at TDC is not apparent. It can be seen that the peak rate of fuel heat release is larger, and burning duration is less than that for the standard build case. This is due to the fact that a similar quantity of fuel is injected in both cases which can either be burnt slowly over a long period or quickly over a short period.

The discussion of cumulative heat release shown in figure 6.14 is based on similar arguments to those in section 6.2.1, except for the rate of increase in heat release after TDC. The increased pressure (and temperature) results in a much faster rate of burning, as already stated.

The equivalence ratio and mass of fuel burnt shown in figures 6.15 and 6.16 are similar to those of figures 6.7 and 6.8, and as in the cumulative heat release discussion, the rate of increase is pressure related. The difference between the two methods of analysis is due to the calculated difference in heat release around the second pressure peak being carried over in both mass of fuel and equivalence ratio calculations.

6.3 Summary of Heat Release Results for All Operating Conditions for the Standard Engine

In order to discuss the heat release results, it is important also to study the source of these results. The pressure plots are the most important feature of the analysis and as such will be discussed first followed by the derived temperatures. Having discussed the pressure and temperature plots, the heat release results can be analysed for each condition. The derived fuel mass and equivalence ratios will then be presented and discussed.

6.3.1. Cylinder Pressure Results

The cylinder pressure results for the standard engine are shown in figures 6.17 to 6.20 where each figure represents all four load conditions at a particular speed. The same colour convention will be adhered to throughout this chapter.

Figure 6.17 for the 1000 rev/min speed, shows a continuous rise in recorded pressure with respect to load where the pressure curve appears to be almost scaled up with increasing load. Both compression and combustion pressure values appear to increase by similar amounts, but the combustion peak appears to occur progressively later with respect to TDC with increased load. Since the process is largely one of diffusion burning, i.e., no premixed burning, combustion is mixing controlled. It can be shown that with diffusion burning, the peak of heat release generally occurs towards the end of injection, which obviously occurs progressively later as the fuel quantity increases. This is then reflected in peak pressures similarly occurring progressively later. As discussed in the previous section, the pressure signals become less reliable after 200° AIVC and this is confirmed very clearly in figure 6.17 where the sequence becomes confused.

Relative to the 1000 rev/min case, figures 6.18, 6.19 and 6.20 show all the same features including the loss in confidence at the end of the closed period. The one

striking feature of the four figures (6.17 to 6.20) is the effect of speed on the combustion hump.

It is clear that as the engine speed increases, so does the time taken for the combustion to begin. The start of the combustion hump becomes later with respect to speed and as a consequence, the peak of the hump is decreased with speed.

6.3.2. Cylinder Temperature Results

The temperature plots of figures 6.21 to 6.24 should be considered collectively for analysis since any peculiarity which is apparent applies to all four plots. Looking at all four figures it can be seen that the compression and combustion temperatures are ordered for each of the loads, with the 100% load showing the highest temperatures and the 25% load showing the lowest. The peculiarities arise both before 100° AIVC and after 220° AIVC. Within these boundaries the temperature plots appear to be physically meaningful. To explain the unreliable portion of the curves, reference to the pressure curves of figures 6.17 to 6.20 has to be made. It is clear that up to 100° AIVC and again between 220° AIVC and EVO, the pressure curves lack precision. Having considered the analysis in 6.2.2 it becomes evident that small errors at these points in the cycle are reflected with high amplification with respect to temperature. The obvious response in the light of this argument is only to consider the region between 100° AIVC and 220° AIVC. It would be fair to say that there really is no significant difference in temperature relative to speed, and that load is the only contributing factor to temperature.

6.3.3. Analysis of Cumulative Heat Release and Rate of Heat Release

In order to represent the heat release results of the 16 cases covered in this section as clearly as possible, it was decided to represent the three parameters of nett, fuel and cumulative heat release on one plot for each case. Consequently figures 6.25 to 6.40

will be discussed in this section, where each figure is produced in identical format and scale.

It has already been stated in section 6.3.2 that the results up to 100° AIVC are not very reliable due to the errors in the pressure signal at low values. In the analysis of the following figures attention will be drawn to the more reliable areas of the curves namely those between 100° AIVC and 220° AIVC.

a) 1000 rev/min (Figures 6.25 to 6.28)

Figure 6.25 for the lowest load and speed condition, shows slow diffusion burning, as seen clearly in the cumulative heat release curve. In direct comparison, figure 6.26 where the load is doubled shows a significantly higher rate of heat release as well as a steeper cumulative heat release curve and a shorter burning duration. When comparing the cumulative heat release for all four loads, it is the 25% condition which shows the strikingly slow rate of combustion. It will also be seen later in this section that the 25% load condition exhibits consistently slow rates of combustion throughout the speed range.

One possible theory put forward to explain this slow rate of combustion could be prolonged injection due to inadequate needle lift caused by low fuel line pressures when the injection quantity is small. It would appear that the quantity of fuel needed to sustain a more efficient rate of combustion starts at the ½ load condition. The 50%, 75% and full load cases show a more efficient rate of combustion suggesting that the ¼ load case is a condition to be avoided if economic running of the engine was an important criterion.

The burning duration for the four load conditions in figures 6.25 to 6.28 appears to decrease with increasing load up to a point where the limiting factor (quantity of available fuel) is exceeded. This point is the ¾ load case beyond which the burning duration once again increases slightly. This limiting condition is further illustrated by the fact that the peak rate of heat release has also reached a limiting value.

As the maximum rate of heat release increases, so does the slope of the cumulative heat release curve of figures 6.25 to 6.27. However the full load condition (see figure 6.28) indicates that the slope of the cumulative heat release curve is not significantly increased from the ¾ load condition, possibly due to the mixture being too rich with insufficient air to ensure efficient combustion.

The cumulative heat release seems to go from 600J to 800J to 900J to 1000J for the four load conditions (see table 6.1), which compares reasonably with the corresponding 400J, 580J, 730J and 890J obtained during performance tests described in chapter 4. The comparison is considered "reasonable" in view of the fact that the performance results were average values taken over thousands of cycles, as opposed to one, and the fact that the tests were conducted at different times resulting in slightly different running conditions.

Another observation to be made with respect to figures 6.25 to 6.28 is the fact that heat transfer increases such that at full load, a significant quantity of heat is lost to the walls whereas the 25% load condition shows negligible heat transfer effects.

b) 1200 rev/min (Figures 6.29 to 6.32)

Figure 6.29 for the ¼ load, to figure 6.32 for full load, indicate broadly similar trends to the previous set (figures 6.25 to 6.28) for the 1000 rev/min case. The peak heat release increases progressively without any obvious "limiting condition" at ¾ load. The result is a progressively shortening burning duration and increasing slope of the cumulative heat release curves, these effects diminishing as full load is approached. The absolute values of the maximum cumulative heat release curves for the 1200 rev/min are similar to the 1000 rev/min case throughout the load range. Compared to the results from the performance studies, the 1200 rev/min case is not very different from the 1000 rev/min case already discussed previously (see table 6.1).

c) 1400 rev/min (figures 6.33 to 6.36)

Having observed the insignificant effect of speed on heat release for 1000 rev/min and, 1200 rev/min, the 1400 rev/min speed results show much the same patterns with almost identical cumulative heat release trends. The ¼ load result of figure 6.33 is slightly suspect in that it shows a very high negative heat transfer effect from gas to wall before combustion. Otherwise, diffusion burning is evident throughout the operating range with the full load case (figure 6.36) showing an absolute peak value in both the fuel and nett heat release thus far. For the three speeds analysed thus far, the engine is obviously most efficient running at 1400 rev/min full load. As in the previous speeds, table 6.1 shows a relatively good comparison between the analysis heat release results and those calculated on an actual fuel input basis.

d) 1500 rev/min (Figures 6.37 to 6.40)

As the rated speed of this engine is 1500 rev/min, a more detailed analysis of the results at this speed is necessary. Figures 6.37 to 6.40 however show very little difference in any pattern to those already discussed for the other three speeds. Once again the ¼ load case (figure 6.37) shows slow combustion but in contrast to previous speeds, the ¾ and full load cases show little difference. The peak of fuel and nett heat release is slightly earlier for the ¾ load case, which could explain the similarity in heat release for the two cases. Effectively, the ¾ load case has a more advanced fuel injection than the equivalent full load condition. Although the timing was never altered, the shift in the heat release peak nearer TDC would have resulted if the fuel injection timing was advanced. The reason for this is immediately apparent when figure 6.20 is studied. The second (or combustion) humps of the ¾ and full load cases although correct in amplitude, are clearly "out of phase". This unfortunately is a limitation of single cycle analysis in that a "rogue" pressure signal of 1500 rev/min full load was captured. Had a healthy signal been captured, the combustion humps of figure 6.20 would have all been in line with each other resulting in the peak heat release of figure 6.40 being both closer to TDC and higher (due to the similar volume closer to TDC).

6.3.4. Computed Equivalence Ratio and Mass of Fuel

Since the calculations of both fuel mass and equivalence ratio are conducted in a similar manner to that of cumulative heat release, it is obvious that they will all follow the same trends. The absolute values are obviously different, but both equivalence ratio and mass of injected (or burnt) fuel are derived from calculated values of cumulative heat release. Details of the calculations for equivalence ratio and mass of fuel are laid out in chapter 5 section 2.2.

In the previous section it was shown that there was little difference in the heat release for any one load, regardless of engine speed. Figures 6.41 to 6.44 reinforce this. It becomes clear on closer inspection that the plots range from an equivalence ratio of approximately 0.4 to 0.6 for all four load conditions corresponding to 15 to 25 mg of injected fuel. The small discrepancies within the load range due to the limitations of single cycle raw data availability make it difficult to see the emergence of any pattern.

When considering the mass of fuel injected into the cylinder, table 6.1 and figure 6.73 serve as good tools in analysing the results. whilst figure 6.73 will be discussed at a later stage in section 6.5, its relevance here must also be acknowledged. It shows comparisons of the ratio of mass of fuel calculated in the performance studies, (tables 4.4 and 4.5), to the mass of fuel calculated in the heat release analysis. This ratio should equal unity, but for obvious reasons this is not the case. Figure 6.73 shows a consistently higher prediction from the pressure data throughout the speed and load range, however the full load conditions appear to be predicted much more accurately every time. This is mirrored by the reduced differences in the full load heat release comparisons of table 6.1.

6.4 Summary of Heat Release Results for all Operating Conditions for the Insulated Engine. **

Much has already been written in section 6.3 regarding common features to both engine builds which will not be repeated here. These include the problems associated with single cycle pressure measurement, the errors associated with low cylinder pressures and general loss in confidence in results pertaining to suspect pressure data. To this extent, only striking differences or peculiarities will be detailed in this section.

A very important point to consider throughout this section, is that the insulated engine was tested before the standard engine. This was the sequence chosen in order that the "standard" engine could be built around the state of tune of the insulated engine for comparison purposes. Having established a set of "tuned" conditions (largely by trial and error) whereby an insulated engine could run without failure, the "standard" engine was then run to obtain the corresponding "standard" engine results.

During rebuilding of the standard engine, the pressure transducer housing was assembled slightly out of true (see figure 3.17 of chapter 3) resulting in the inner sections of the housing compressing the transducer axially, with probable damage. After calibrating the transducer, it was very clear that the damage was irreversible. Another transducer of very similar calibration was obtained, and it was this unit that produced the results that have been discussed in the previous section.

In a way it was fortunate rather than unfortunate that the transducer became the victim of a catastrophic accident. Although the original transducer showed a good calibration characteristic over its range (see figure 3.18 of chapter 3), the results it produced have cast some doubt over its integrity. This statement will become clearer in the following sections.

** Footnote

Figures 6.45 to 6.72 referring exclusively to the insulated engine will be found in appendix 2. Figures 6.73 and 6.74 referred to in the discussion (section 6.5) are likewise found in appendix 2.

6.4.1 Cylinder Pressure Results

As mentioned previously, the format of the plots used is uniform throughout this chapter. The cylinder pressure plots of figure 6.45 draw the eye immediately to the apparent randomness of the pressure signals. It has already been mentioned in section 6.4 above, that the transducer which produced these results was a different unit to that which produced the equivalent standard build plots of figure 6.17. It must also be stated that the transducer responsible for the results of figure 6.45 did show good linearity during calibration (see figure 3.18 of chapter 3). The pressure plots of figure 6.45 show a reasonable sequence of the peak pressures of the compression hump, but not of those of the combustion hump. Until TDC, the pressure plots are very plausible indeed, and the slightly high ¼ load pressure could be explained as a "rogue" or slightly abnormal signal. After compression however, the sequence becomes confused suggesting random combustion or irregular engine performance. The apparently irregular engine performance implied by the pressure records can be attributed to transducer malfunction, or any of the following; fuel quality, injector condition, improperly sealed combustion chamber (cylinder head gasket, injector or prechamber seals), poor adjustments (valve clearances, injection timing etc) or poorly sealed valves and piston rings.

Due to the number of variables, it is difficult to pinpoint the source of this erratic behaviour with any degree of confidence. It is worth mentioning that the recommended running in period was almost dispensed with in the case of the newly assembled insulated engine due to fears of possible catastrophic failure of the Cordierite cap. In sharp contrast, the standard engine had the benefit of being fully run in according to the Hepworth and Grandage schedule of table 4.1.

For the slightly faster speed of 1200 rev/min, (see figure 6.46), the combustion pressures are still as random as those for the 1000 rev/min case of figure 6.45. This unfortunate randomness continues throughout this exercise as can be seen in figures 6.45 to 6.48.

In an attempt to find a consistent explanation for these results, it is possible to link the randomness of the pressure records to anything from a damaged transducer to worn injector, or the erosion on the cordierite cap shown in figure 2.35 of chapter 2. However, the former is much more likely.

Armed with this knowledge, any further analysis can be deemed superfluous, but for the sake of completeness, the results are included, with brief comments on the anomalies.

6.4.2 Cylinder Temperature Results

This subsection deals with the results of figures 6.49 to 6.52 which have obviously been derived from the pressure traces of figures 6.45 to 6.48. The 1000 rev/min and 1200 rev/min speeds of figures 6.49 and 6.50 are as expected more random in their order than those for the 1400 and 1500 rev/min of figures 6.51 and 6.52. Although the peak temperatures show little numerical order, it can be said that the maximum cylinder temperatures do increase with speed for the insulated engine. In section 6.3.2, it was found that the standard engine showed temperature to be related to load and not speed.

Looking at each of figures 6.49 to 6.52, it is clear that the faster engine speeds produce larger temperature increases from the start of compression to maximum cylinder temperature. These larger temperature increases in all cases take place over the same period of approximately 30 degrees crank angle, suggesting larger $dT/d\theta$ for the higher speeds. These results are also in line with predictions from the simulation program ODES.

Another interesting feature of the insulated engine compared to the standard build is the relatively higher compression temperatures of the insulated engine at all speeds (see figures 6.49 to 6.52 and 6.21 to 6.24). The reason for this is attributed to the hotter cylinder walls and the greater resistance to heat transfer through the piston cap.

The arguments advanced in section 6.4.1 for the poor transducer performance also apply here.

6.4.3 Analysis of Cumulative Heat Release and Rate of Heat Release

Unfortunately it will not be possible to discuss figures 6.53 to 6.68 separately since they represent calculated heat release derived from pressure data which has already been shown to lack consistency.

It is noted that the maximum cumulative heat release values are surprisingly similar, with a very small deviation around the 0.6 KJ mark for all loads up to 1400 rev/min (see figures 6.53 to 6.64). The 1500 rev/min case however, shows a marked rise to between 0.9 KJ and 1 KJ (see figures 6.65 to 6.68).

Although the transducer has been identified as the root of the anomalies, an explanation of the procedure used in obtaining these results may shed more light on the matter. Almost immediately after starting up the insulated engine, it was considered good practice to start accumulating performance data. After only 25 hours of running time, the Cordierite piston assembly was extracted in order that a LAS assembly could be tried. The LAS piston assembly survived only several minutes running time before failing (see figure 2.33). The engine was then stripped and rebuilt using the original Cordierite piston assembly. As soon as the "old" Cordierite piston assembly was refitted into the engine, pressure data started to be accumulated for the insulated engine. Although the Cordierite assembly retained its set of rings and therefore need not have been "run in" again, the cylinder had had a different set of rings scouring it for several thousand strokes, as well as highly abrasive particles shed by the failed LAS monolith. Initially, the low speed and low load pressures were recorded and by the time the 1500 rev/min readings were taken, the engine had had the benefit of an extra 5 hours running time (equivalent to the modified running in schedule of table 4.2).

One possible explanation for the higher heat releases at 1500 rev/min could be the fact that the small voids between the piston rings and liner had been "machined out" by the action of the engine running an extra 5 hours. The small voids would have caused a path for a small loss in cylinder pressure.

It is not possible to establish any pattern of higher or lower heat release between the standard and insulated engine, regardless of whether the basis is load or speed. Even when comparing individual cases from figures 6.53 to 6.68 and their equivalent standard build results, no pattern emerges, other than the fact that in certain cases, fuel and nett heat release curves are further apart for the insulated engine than the standard equivalent. In an attempt to relate these differences for the two engine builds, to the differences in heat loss to coolant, as discussed in chapter 4, one would expect the gap between these parameters to be at its widest in the case of the insulated engine at high loads and speeds, where heat loss to coolant is at its highest. In fact no such clear trend is observed.

6.4.4 Computed Equivalence Ratio and Mass of Fuel

From what has already been said, it must be expected that the equivalence ratio and mass of fuel injected into the cylinder (figures 6.69 to 6.72) ought to show inexplicable discrepancies. Figures 6.69 and 6.70 show an inconsistent sequence of curves, where the suggestion is that the ¾ load condition has the least overall equivalence ratio and hence mass of fuel. This is clearly wrong and it will have to be assumed that figures 6.69 and 6.70 are not worthy of further discussion.

Figure 6.71 shows the correct sequence, but with insufficient differences. However, figure 6.72 is the only set of curves that show both an orderly sequence and significant differences. Looking at figure 6.74, the random distribution of points is as expected, but interestingly the 1500 rev/min case is similar both in order and magnitude to the standard engine case.

It is not possible to establish whether the insulated engine is less fuel conscious than its standard counterpart from the results of the analysis, but the results previously discussed in chapter 4 show a lower economy trend for the insulated engine.

6.5 Discussion

This chapter was based on analysing pressure data obtained from two engine configurations using a specially written heat release program. Whereas the program was considered reliable, the raw data has often been the focus of much doubt, particularly with respect to the insulated engine build.

The root cause of inconsistencies encountered in the analysis of the results has been attributed to poor transducer performance. It has to be noted however, that the capture of one pressure trace at random is simply not good enough when comparisons of small differences are being considered. In the case of the standard engine, which is accepted as being more stable, the differences between individual cycles were obviously less severe than in the insulated engine. The introduction of a multi-component piston must have also introduced instability from one cycle to the next, which can either be attributed to the construction of the piston assembly or the Cordierite itself.

There is a possibility that the interaction of glue, stainless steel, aluminium and Cordierite result in a composite with a certain degree of elasticity in the vertical plane. The instantaneous pressure fluctuations in the cylinder could have been "cushioned" by this possible elasticity.

Another consideration could be the possibility of a limited degree of porosity within the Cordierite allowing some fuel to pass through it rather than completely burn in the cylinder.

An overlooked factor could also be the tolerances of build of the piston assembly. A detailed look at figure 2.34 of chapter 2 shows the piston assembly in its "as extracted

from cylinder" state revealing an interesting assembly inconsistency. The liner side of the Cordierite is not uniform in appearance, with certain patches showing no discolorations whatsoever. Sooty deposits, in theory, cover all exposed surfaces within the combustion chamber, and any component shielded from combustion will remain free of deposits. The small unexposed area on the side of the Cordierite cap is proof that the surface in question could under no circumstances have been parallel to the liner wall since only half the thickness is free from soot. This is one positive indication that the piston assembly was not entirely perfect.

As an ultimate test of the overall exercise, it was considered useful to compare results obtained from the performance studies to those obtained from the heat release study. The two studies are completely different since they took place at different times, and whereas the performance studies were conducted over several thousand cycles, the heat release studies apply to only one cycle. The one parameter that could be directly compared was mass of fuel. The comparison was made on a relative basis i.e. as the ratio of mass of fuel in the performance studies (tables 4.4 and 4.5), to mass of fuel in the heat release analysis, which should equal unity. Figures 6.73** and 6.74** show the above ratios for the two engine configurations. As expected, the standard engine results compare much better than the insulated equivalents with the full load case showing the highest fit. The standard build results of figure 6.73** shows a consistently higher prediction from the pressure data throughout the speed and load range. The insulated build results however show a relatively random distribution with no pattern as expected.

Throughout this research, maximum care had been taken in ensuring the highest level of accuracy of experimental results. It would be true to say that the level of accuracy could not have been exceeded in order to achieve better results. With this in mind, it becomes easier to comprehend the inconsistency in the findings of leading researchers in the field of engine insulation such as Woschni (ref. 12 and 13) and Alkidas (ref. 35).

** See appendix 2

Engine Speed (rev/min)	Load	Heat Release / Cycle (J)	
		Performance Studies Results	Analysis Results
1000	25%	403	600
1000	50%	582	800
1000	75%	733	900
1000	100%	889	1000
1200	25%	410	600
1200	50%	596	750
1200	75%	748	850
1200	100%	902	950
1400	25%	466	600
1400	50%	606	800
1400	75%	746	900
1400	100%	930	1050
1500	25%	459	600
1500	50%	604	850
1500	75%	750	950
1500	100%	935	1000

Table 6.1 : Comparison of heat release between computed and measured results for the standard engine

FIGURE 6.1
MEASURED PRECHAMBER PRESSURE
VS. CRANK ANGLE FOR A STANDARD ENGINE OPERATING
AT 1500 REV/MIN 50% LOAD.

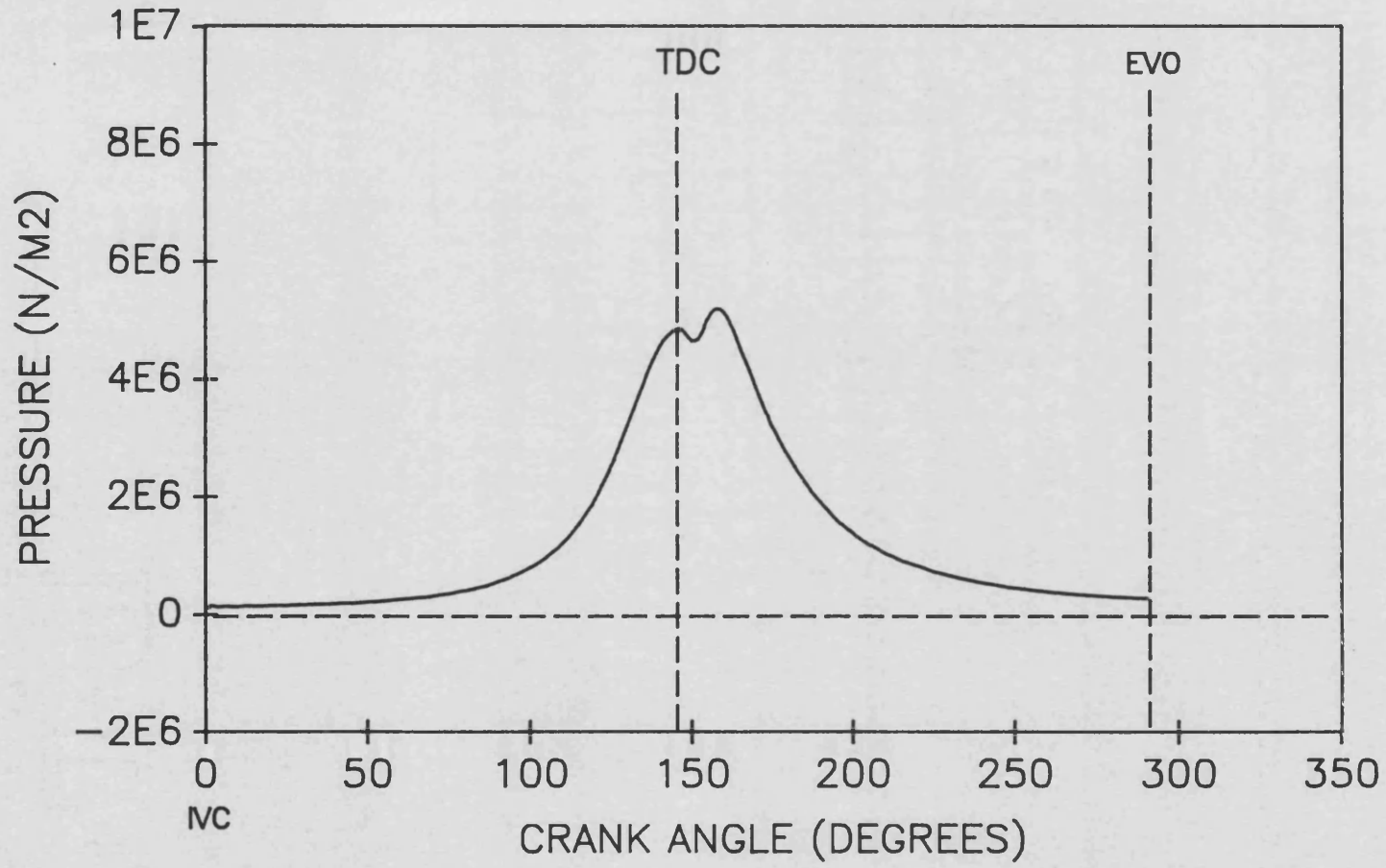

FIGURE 6.2
RATE OF CHANGE OF PRESSURE
VS. CRANK ANGLE FOR A STANDARD ENGINE OPERATING
AT 1500 REV/MIN 50% LOAD.

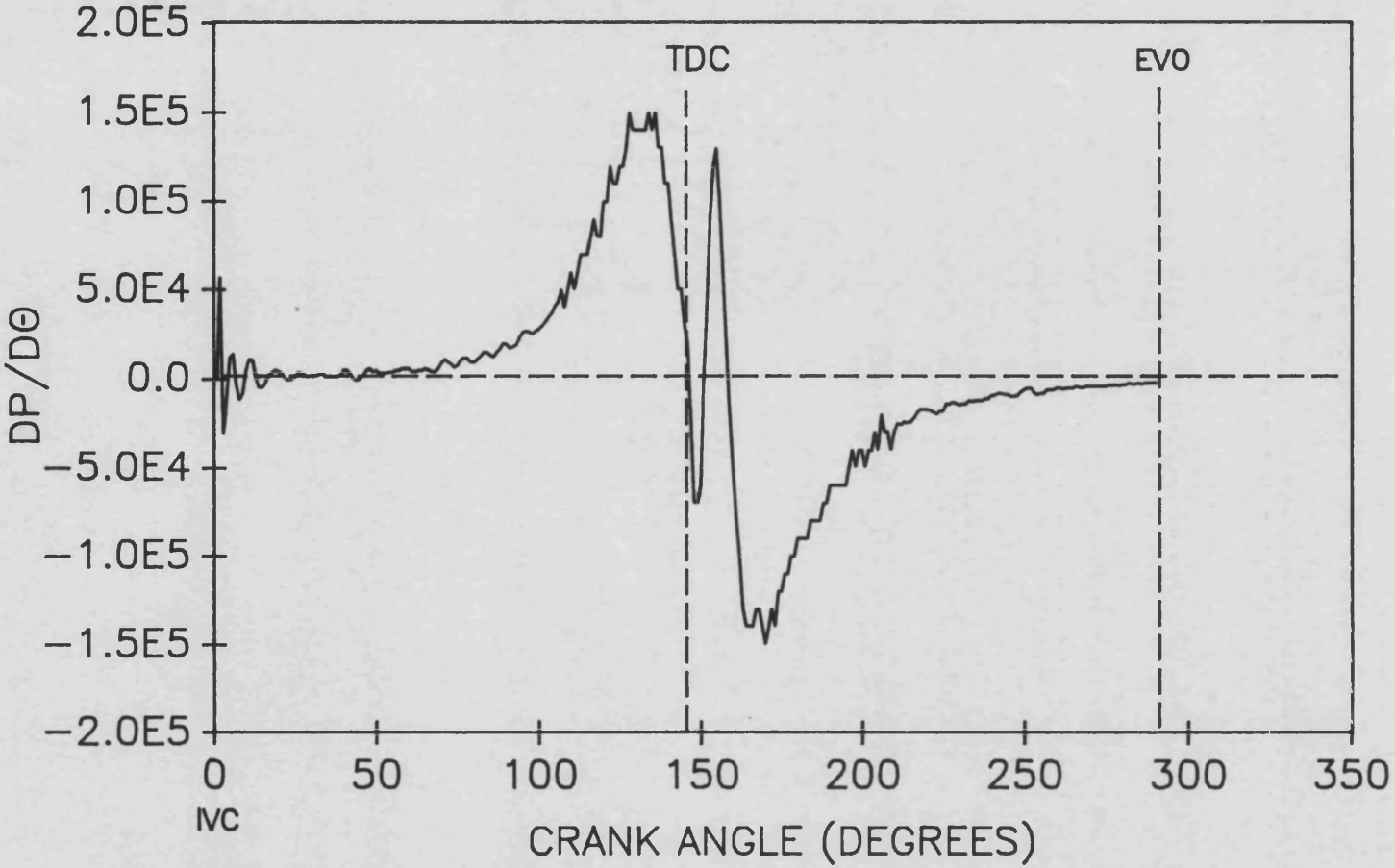

FIGURE 6.3
CYLINDER TEMPERATURE USING TWO SEPARATE ANALSES
VS. CRANK ANGLE FOR A STANDARD ENGINE OPERATING
AT 1500 REV/MIN 50% LOAD.

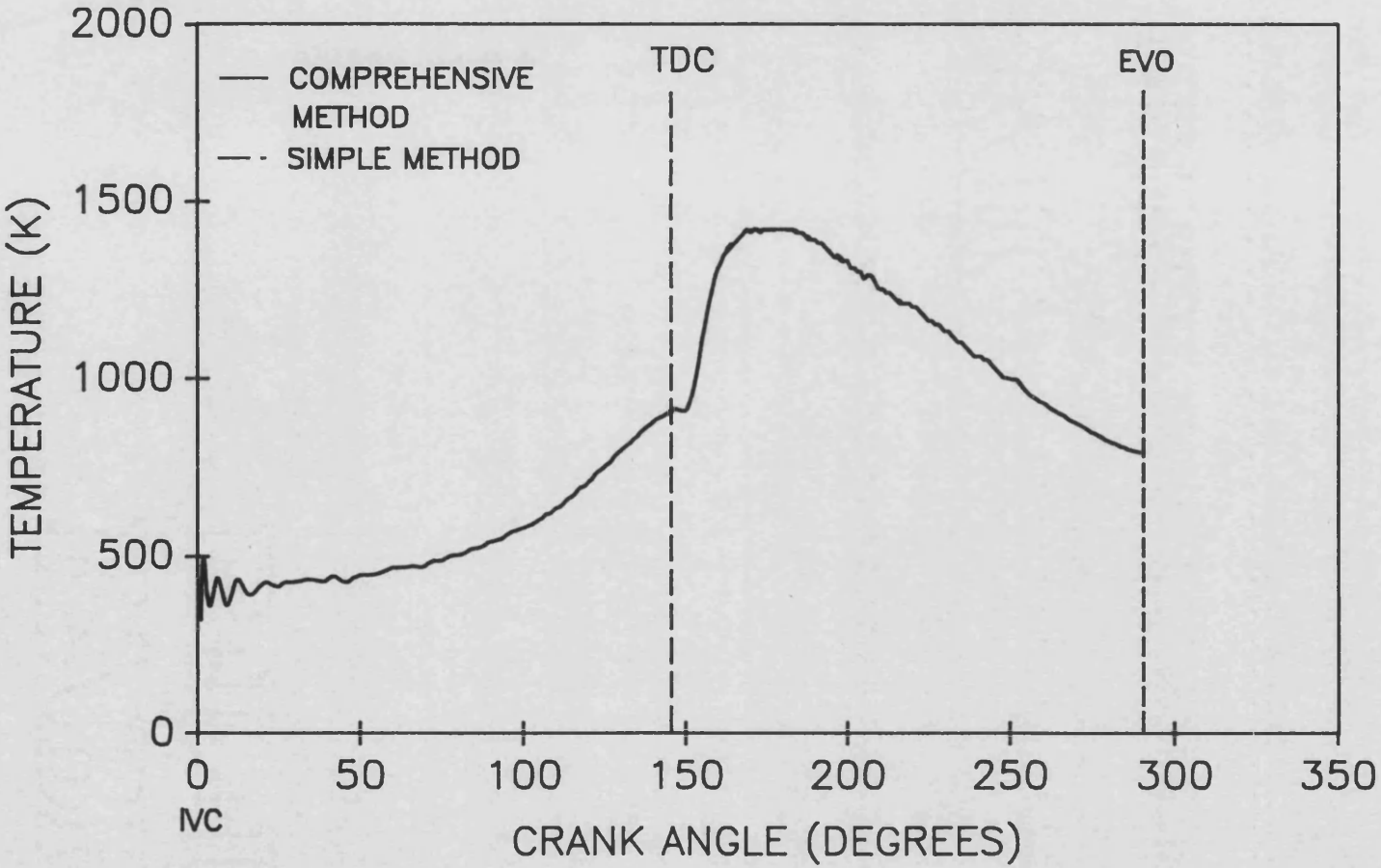

FIGURE 6.4
NETT RATE OF HEAT RELEASE USING TWO SEPARATE ANALYSES VS. CRANK ANGLE FOR A STANDARD ENGINE OPERATING AT 1500 REV/MIN 50% LOAD.

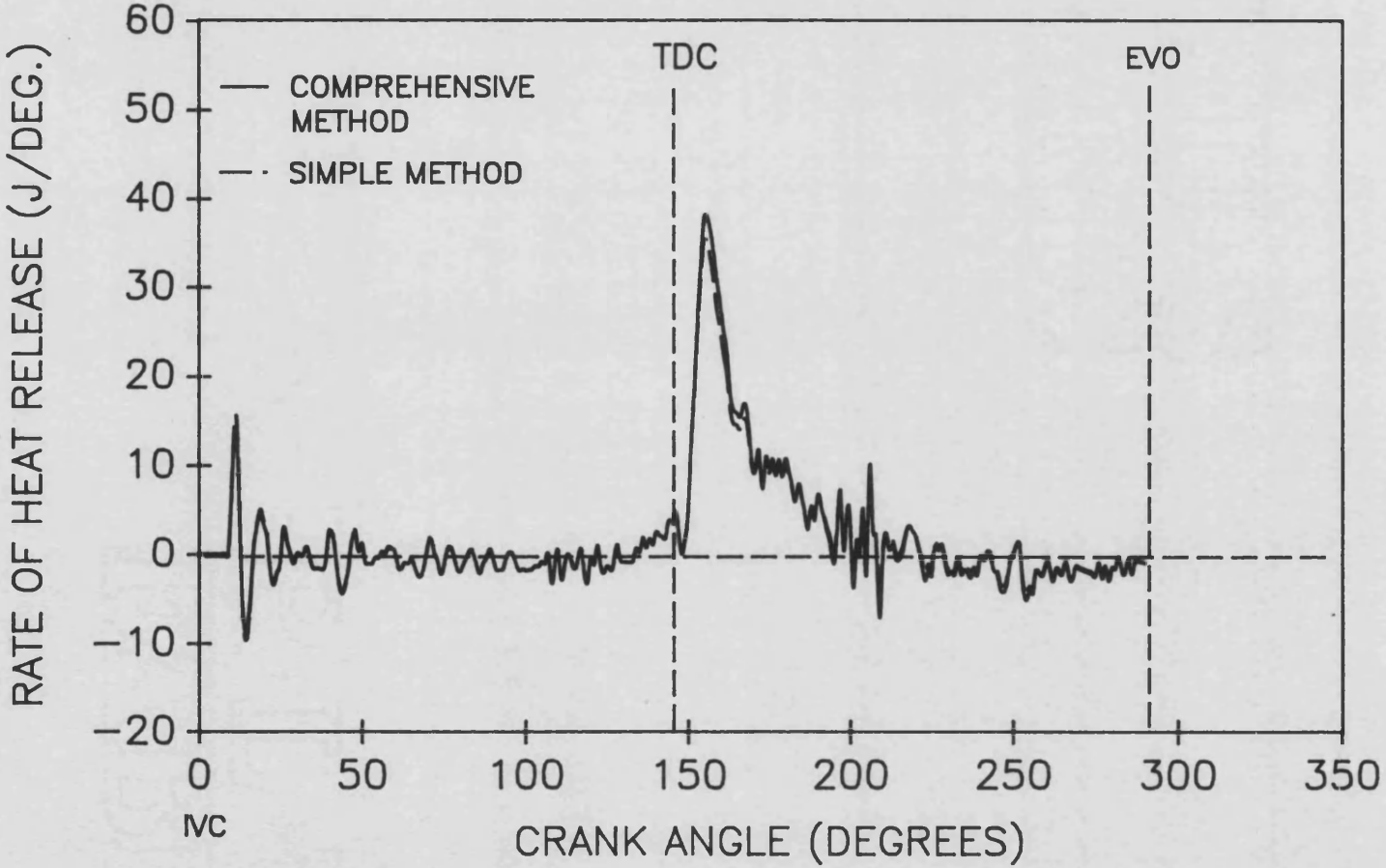

FIGURE 6.5
RATE OF FUEL HEAT RELEASE USING TWO SEPARATE ANALYSES VS. CRANK ANGLE FOR A STANDARD ENGINE OPERATING AT 1500 REV/MIN 50% LOAD.

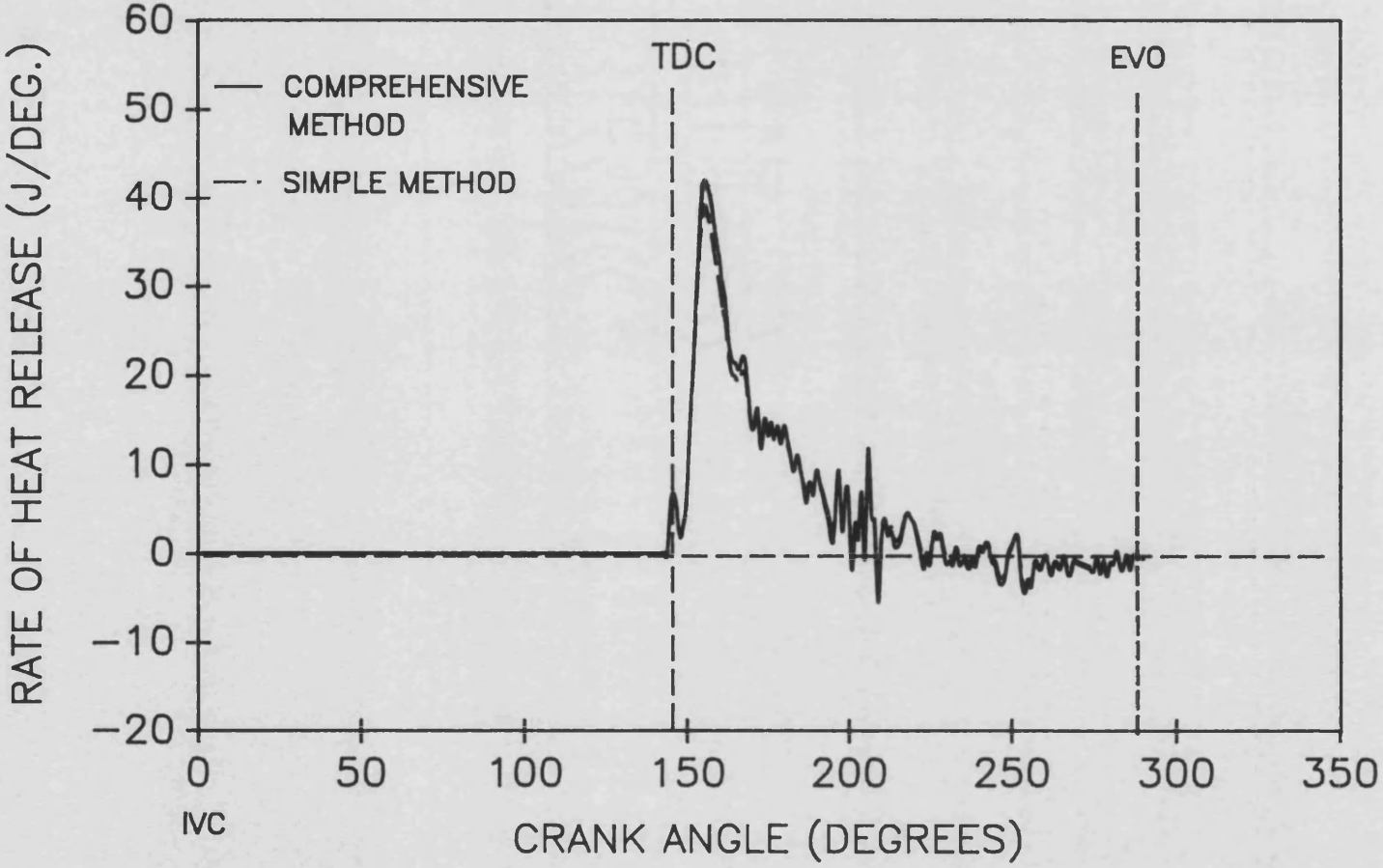

FIGURE 6.6
CUMULATIVE HEAT RELEASE USING TWO SEPARATE ANALYSES
VS. CRANK ANGLE FOR A STANDARD ENGINE OPERATING
AT 1500 REV/MIN 50% LOAD

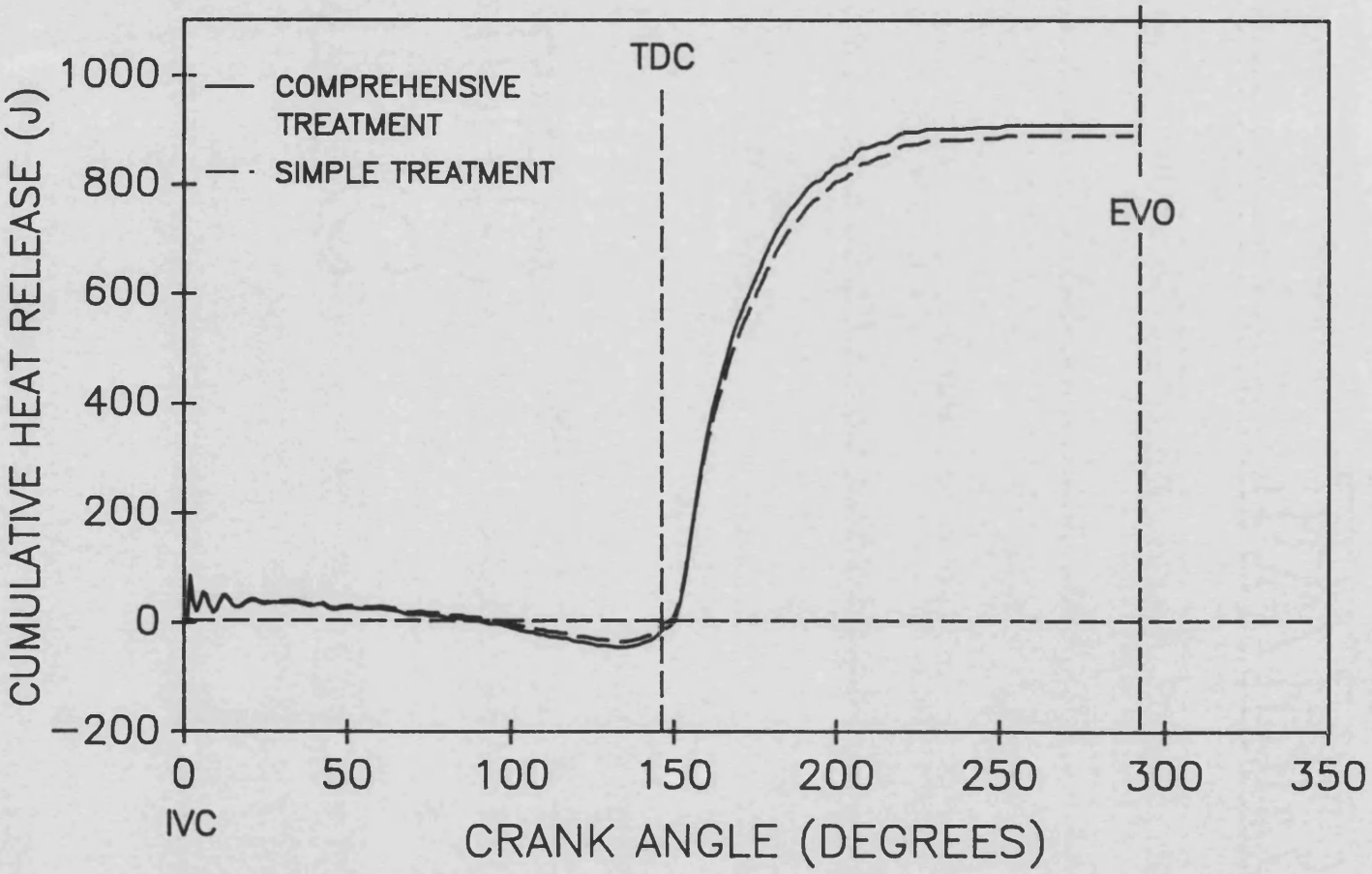

FIGURE 6.7
EQUIVALENCE RATIO USING TWO SEPARATE ANALYSES
VS. CRANK ANGLE FOR A STANDARD ENGINE OPERATING
AT 1500 REV/MIN 50% LOAD.

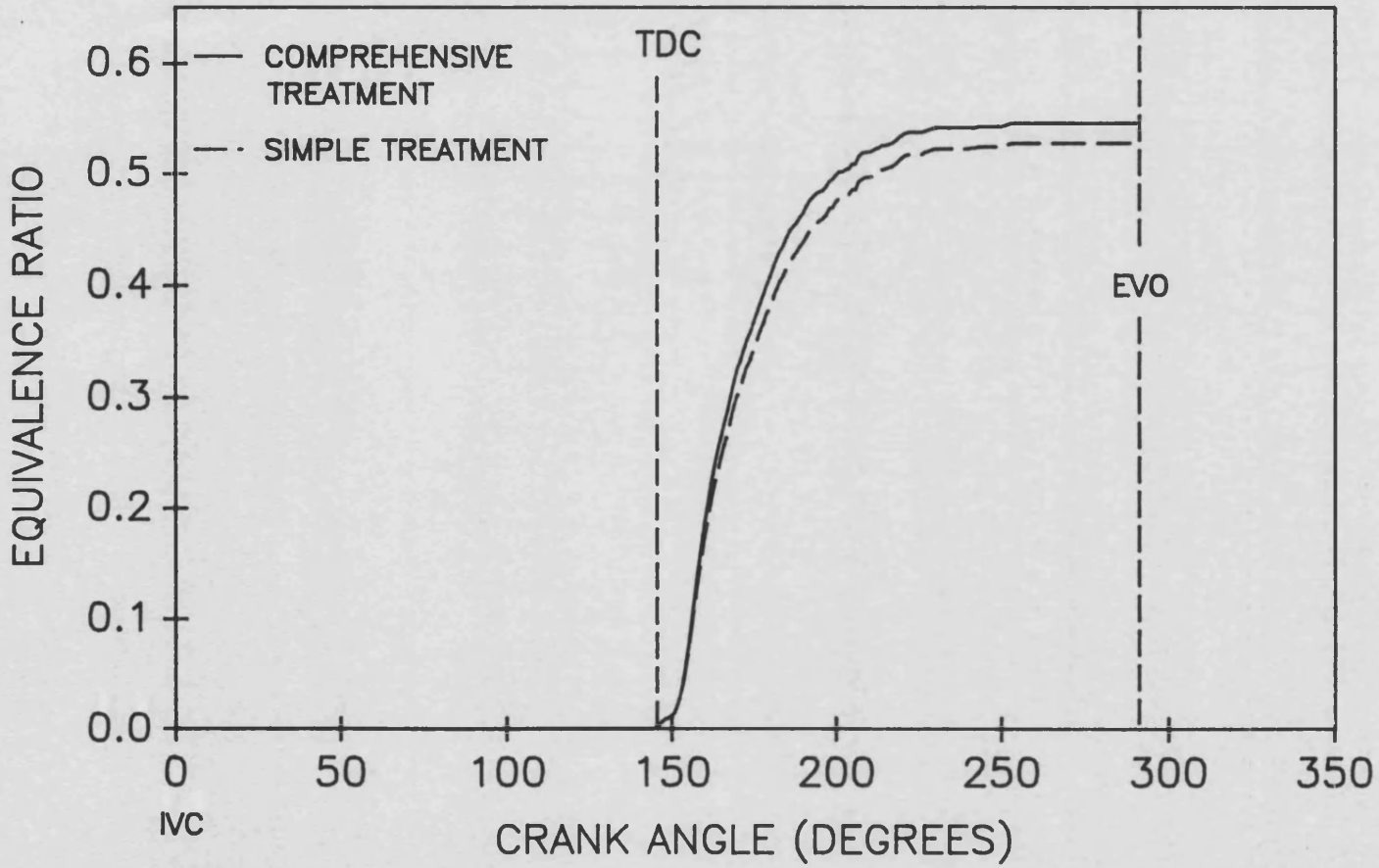

FIGURE 6.8
MASS OF FUEL USING TWO SEPARATE ANALYSES
VS. CRANK ANGLE FOR A STANDARD ENGINE OPERATING
AT 1500 REV/MIN 50% LOAD.

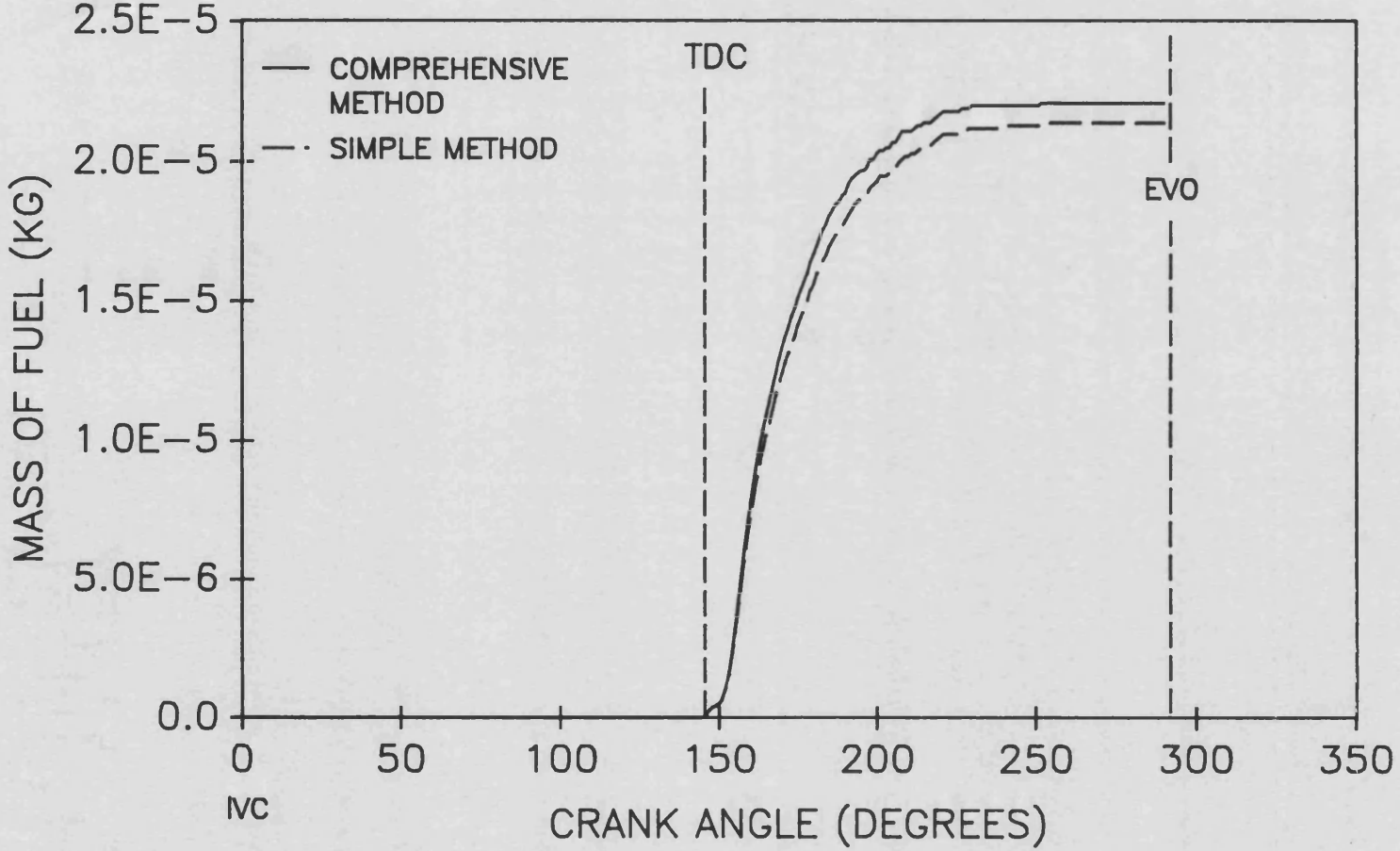

FIGURE 6.9
MEASURED PRECHAMBER PRESSURE
VS. CRANK ANGLE FOR AN INSULATED ENGINE OPERATING
AT 1500 REV/MIN 50% LOAD.

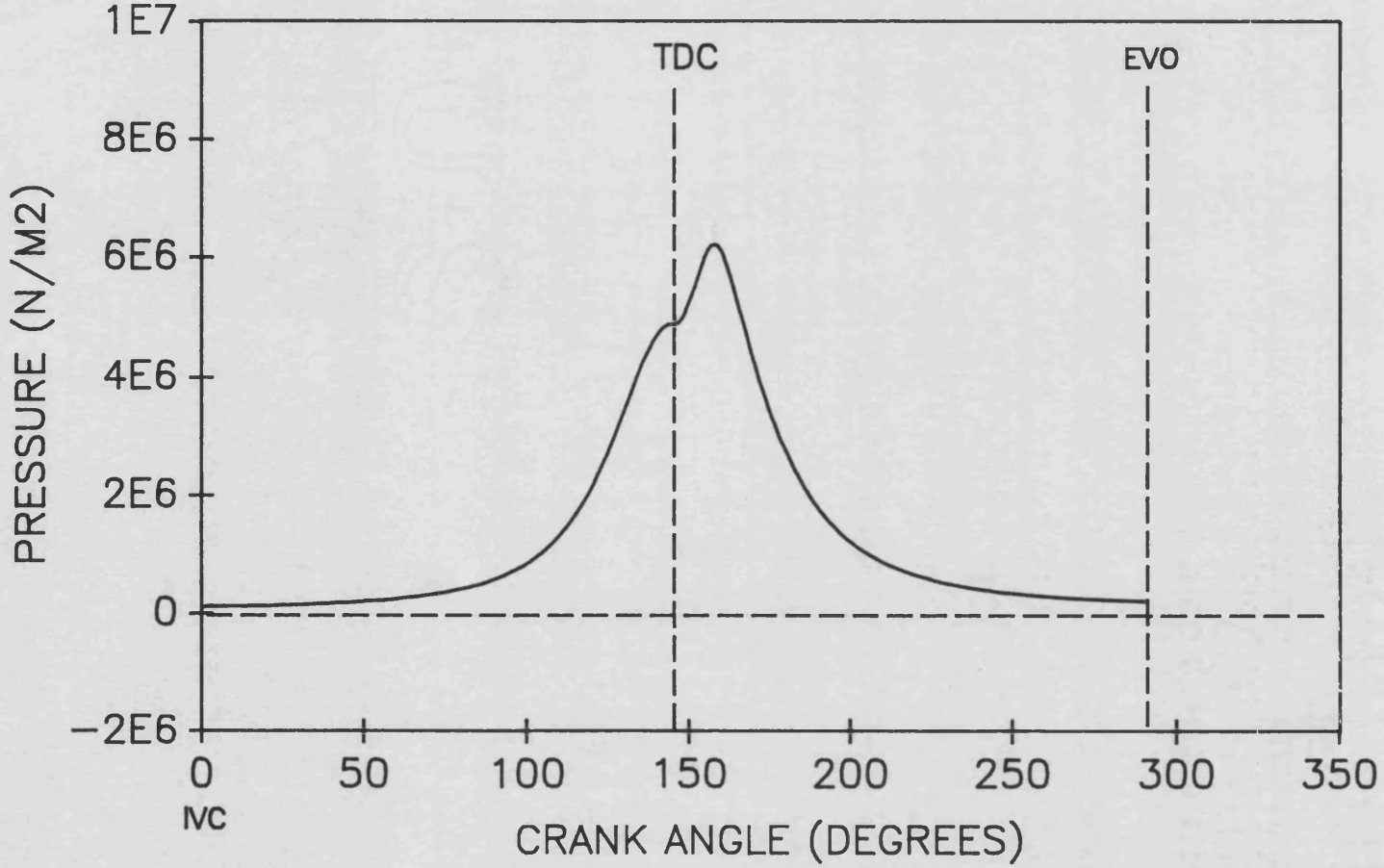

FIGURE 6.10
RATE OF CHANGE OF PRESSURE
VS. CRANK ANGLE FOR AN INSULATED ENGINE OPERATING
AT 1500 REV/MIN 50% LOAD.

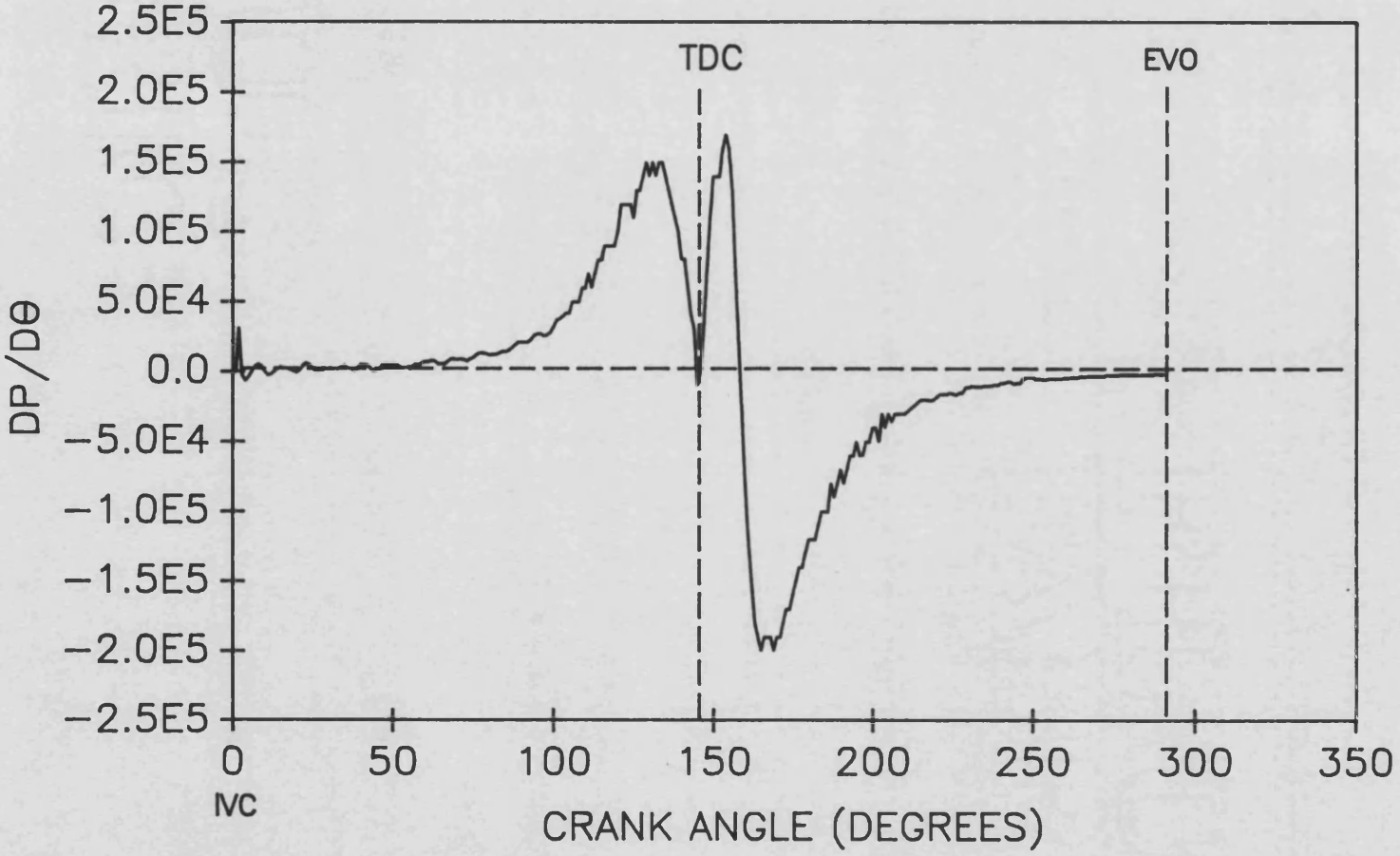

FIGURE 6.11
CYLINDER TEMPERATURE USING TWO SEPARATE ANALSES
VS. CRANK ANGLE FOR AN INSULATED ENGINE OPERATING
AT 1500 REV/MIN 50% LOAD.

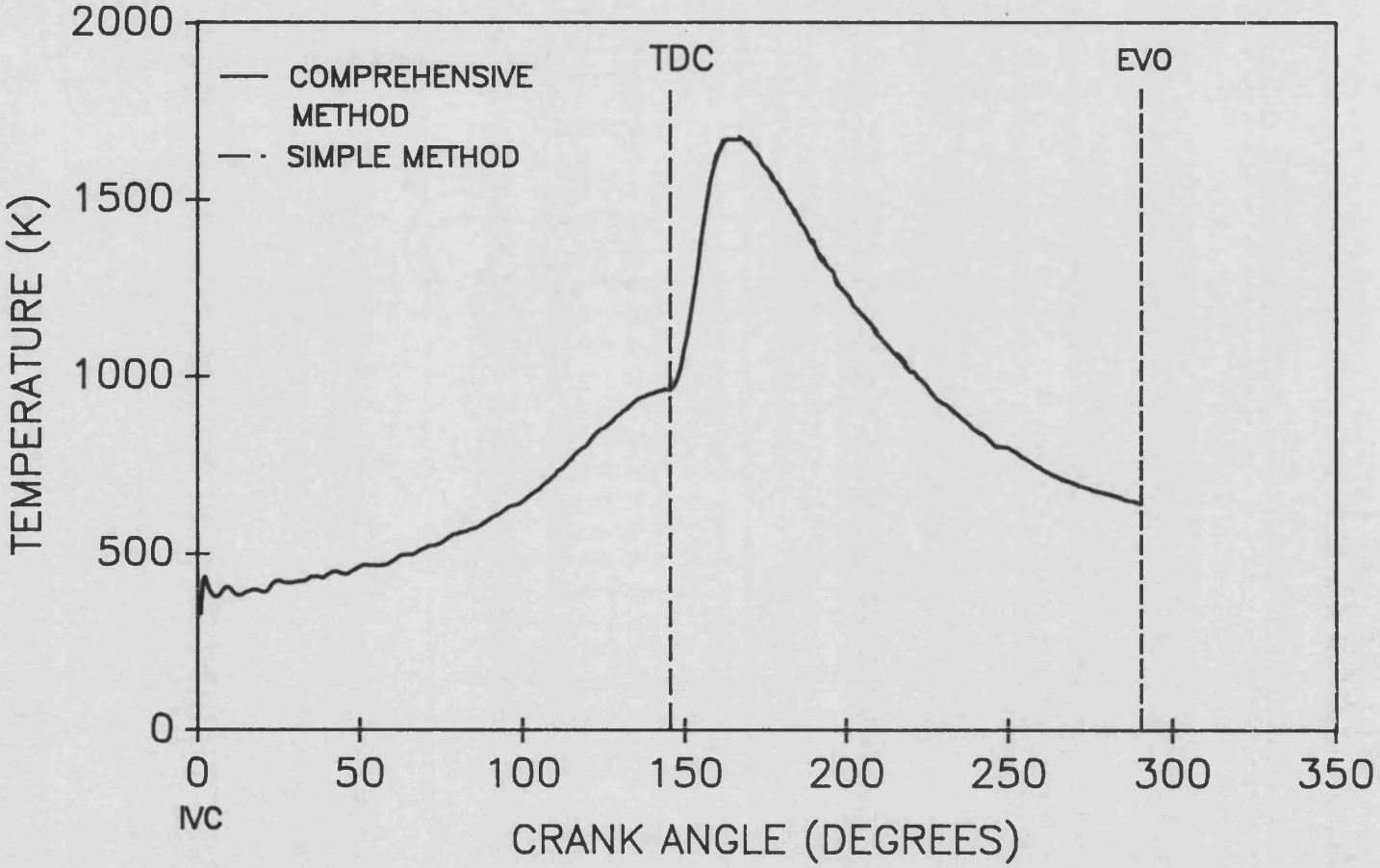

FIGURE 6.12
NETT RATE OF HEAT RELEASE USING TWO SEPARATE ANALYSES VS. CRANK ANGLE FOR AN INSULATED ENGINE OPERATING AT 1500 REV/MIN 50% LOAD.

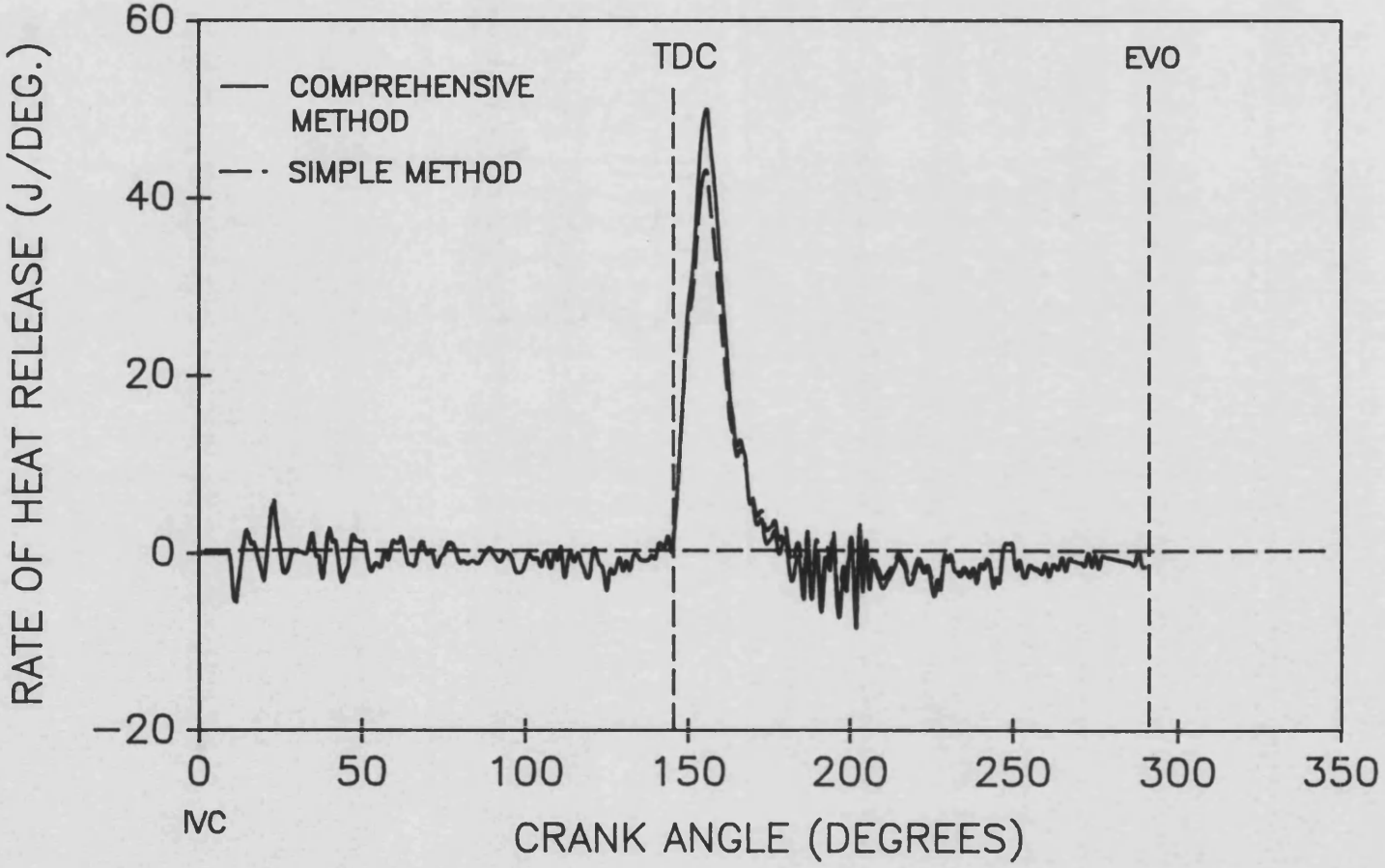

FIGURE 6.13
RATE OF FUEL HEAT RELEASE USING TWO SEPARATE ANALYSES
VS. CRANK ANGLE FOR AN INSULATED ENGINE
AT 1500 REV/MIN 50% LOAD.

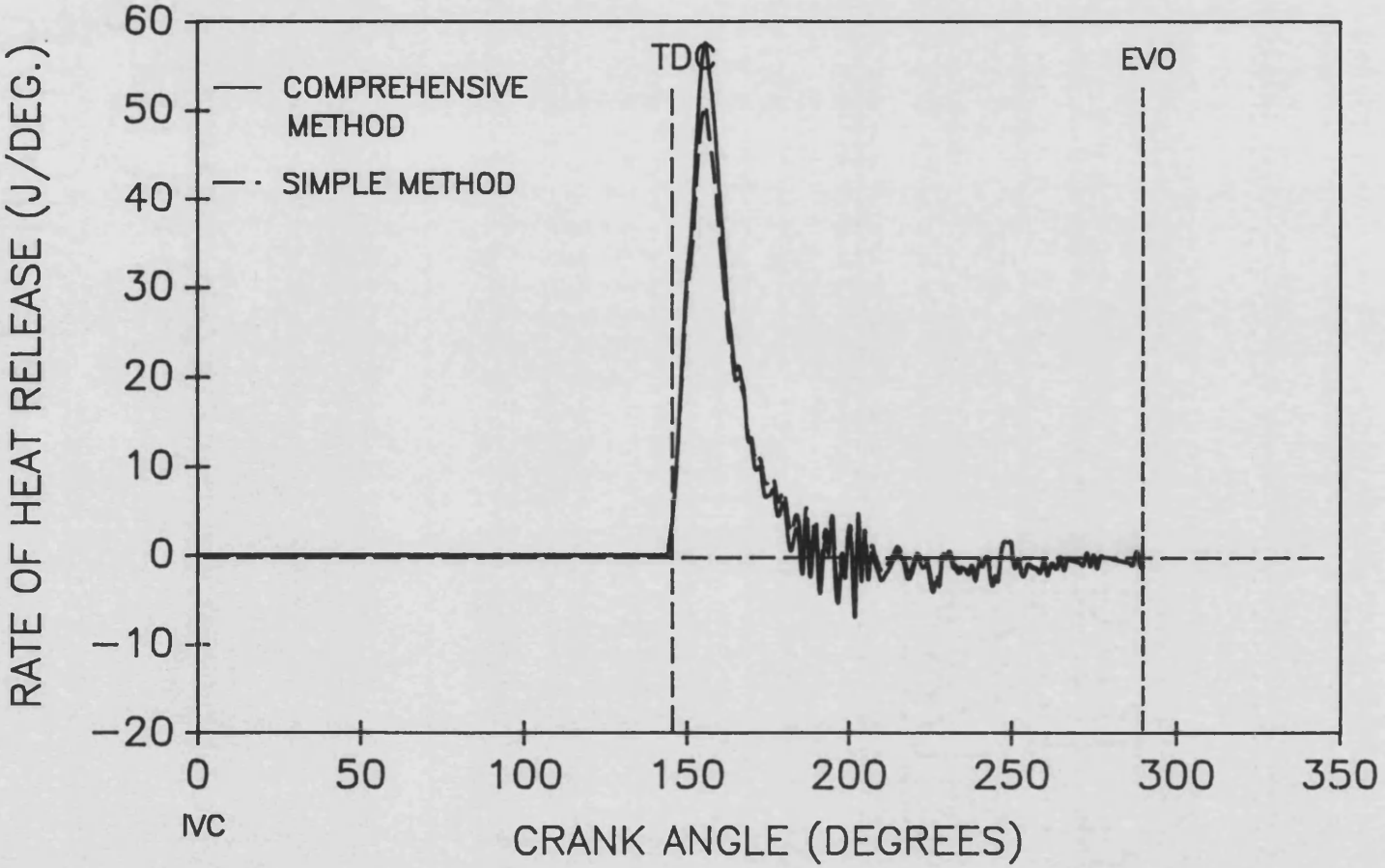

FIGURE 6.14
CUMULATIVE HEAT RELEASE USING TWO SEPARATE ANALYSES VS. CRANK ANGLE FOR AN INSULATED ENGINE OPERATING AT 1500 REV/MIN 50% LOAD

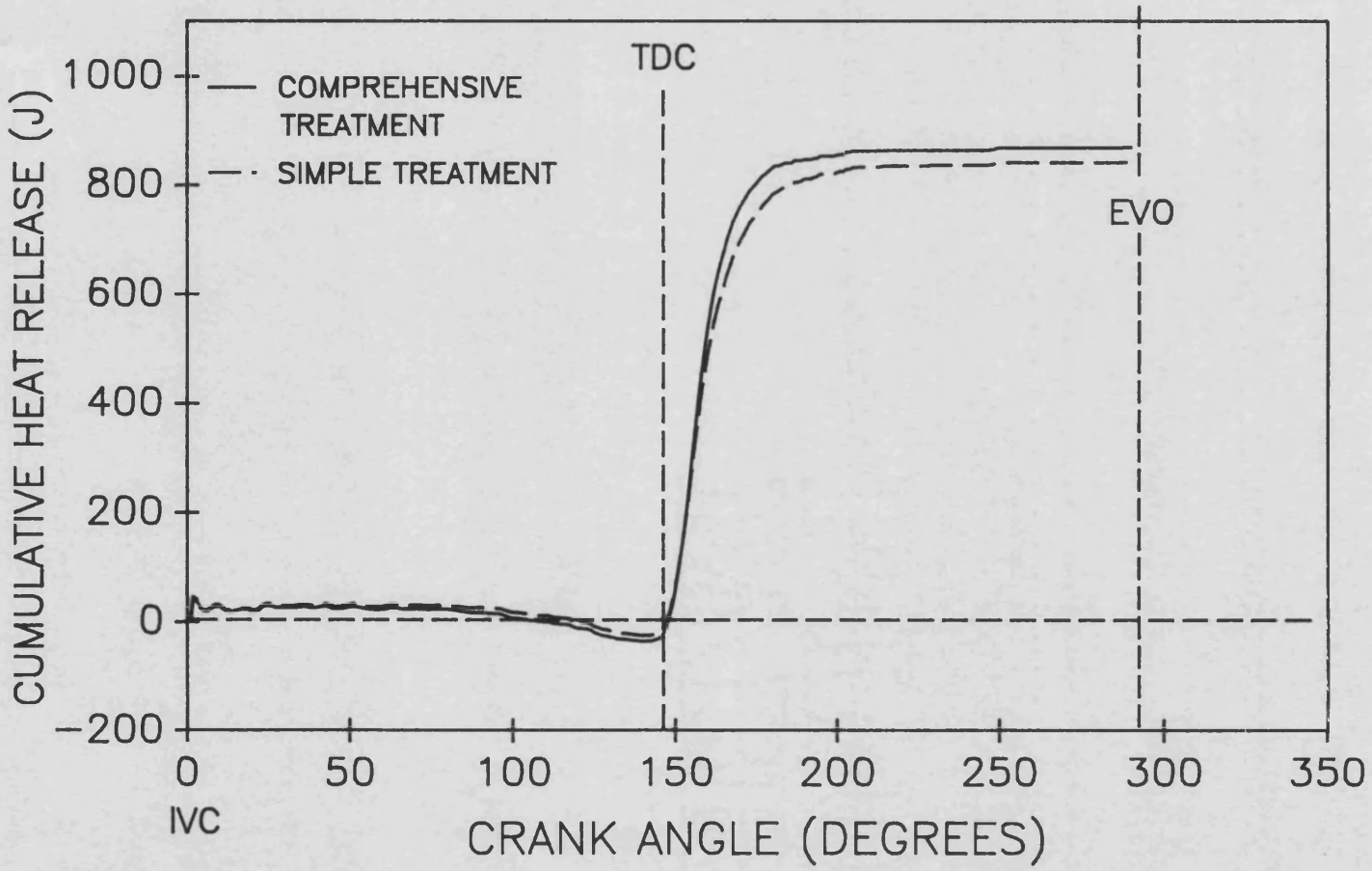

FIGURE 6.15
EQUIVALENCE RATIO USING TWO SEPARATE ANALYSES
VS. CRANK ANGLE FOR AN INSULATED ENGINE OPERATING
AT 1500 REV/MIN 50% LOAD.

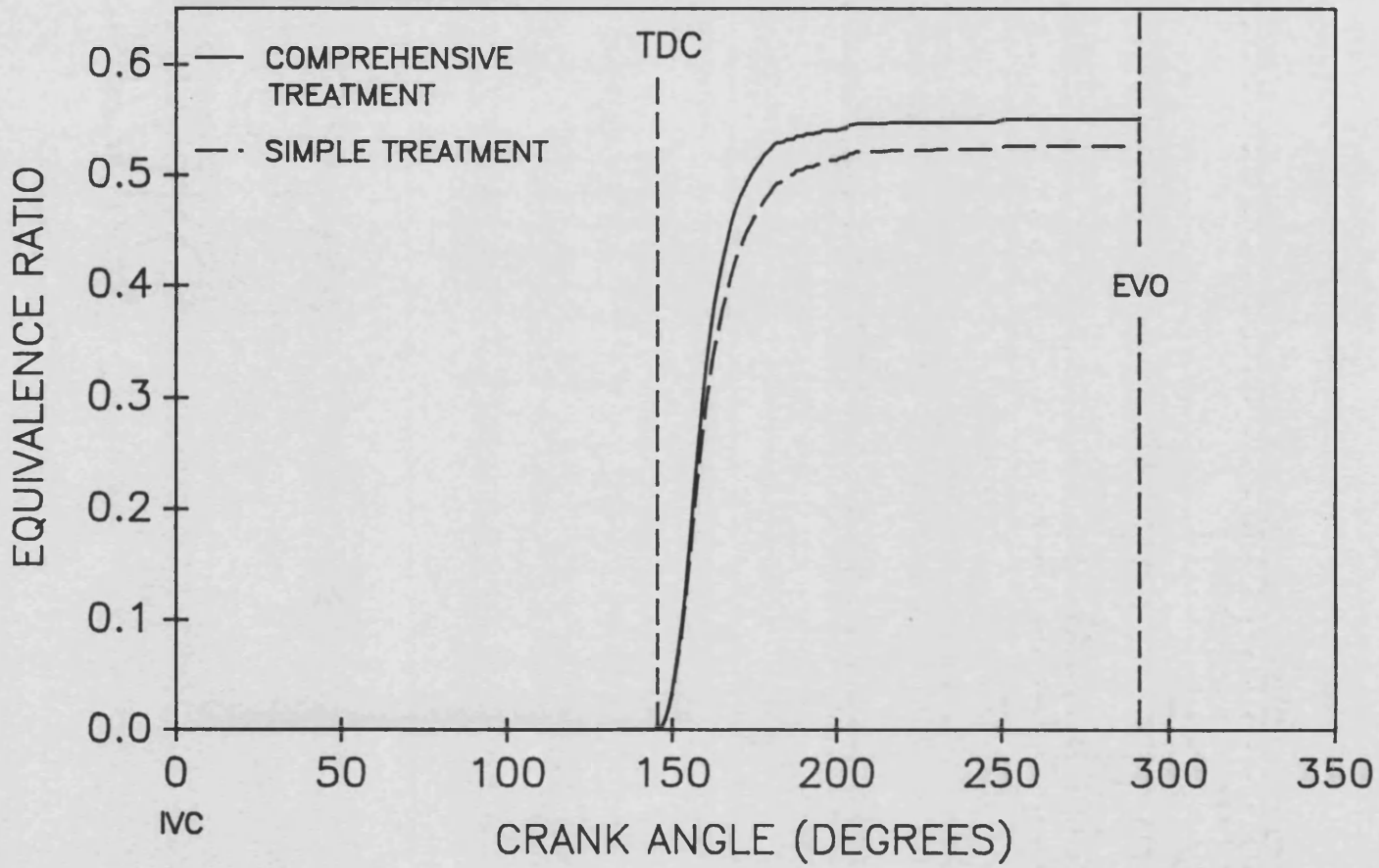

FIGURE 6.16
MASS OF FUEL USING TWO SEPARATE ANALYSES
VS. CRANK ANGLE FOR AN INSULATED ENGINE OPERATING
AT 1500 REV/MIN 50% LOAD.

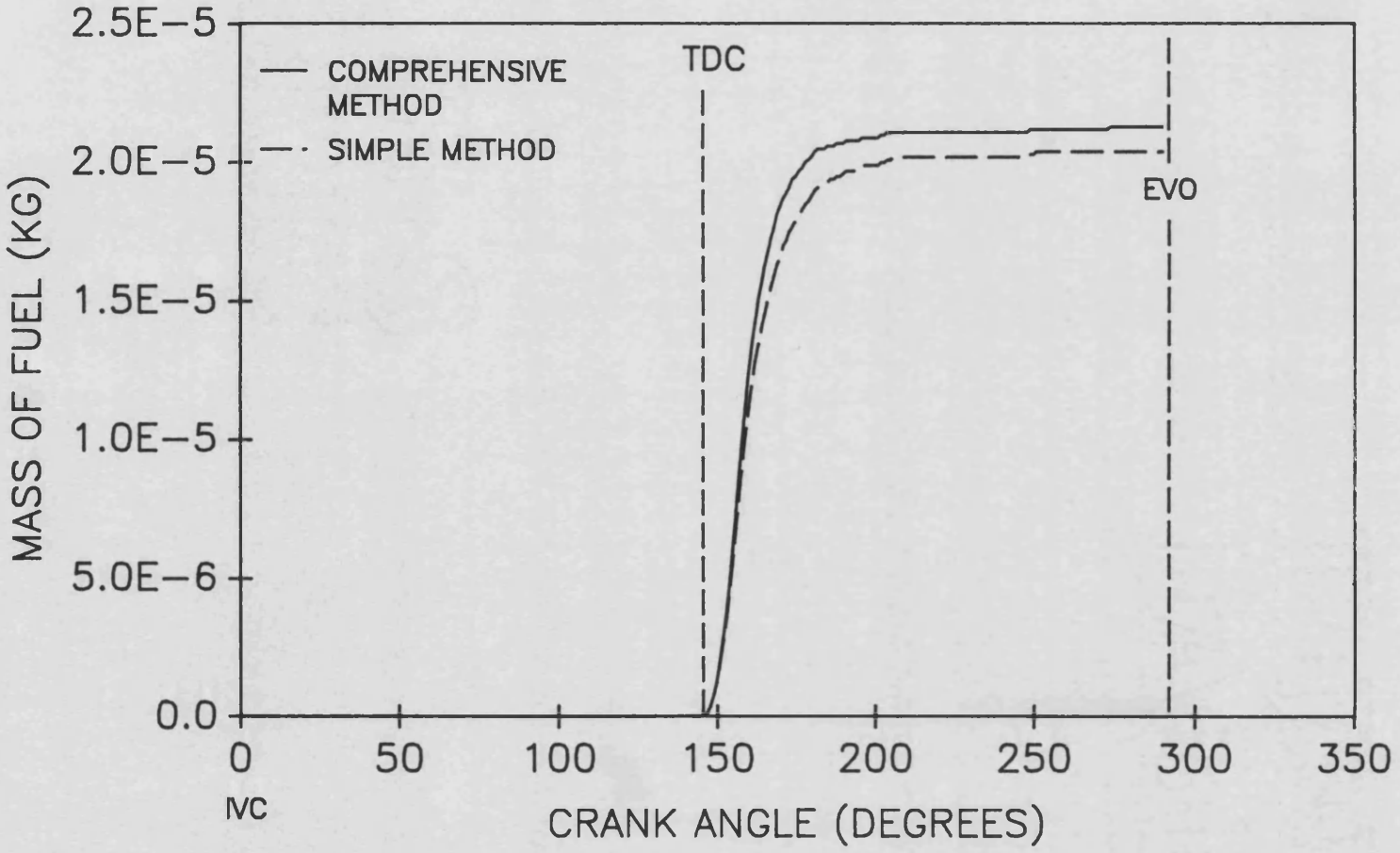

FIGURE 6.17
MEASURED PRECHAMBER PRESSURE
VS. CRANK ANGLE FOR A STANDARD ENGINE OPERATING
AT 1000 REV/MIN.

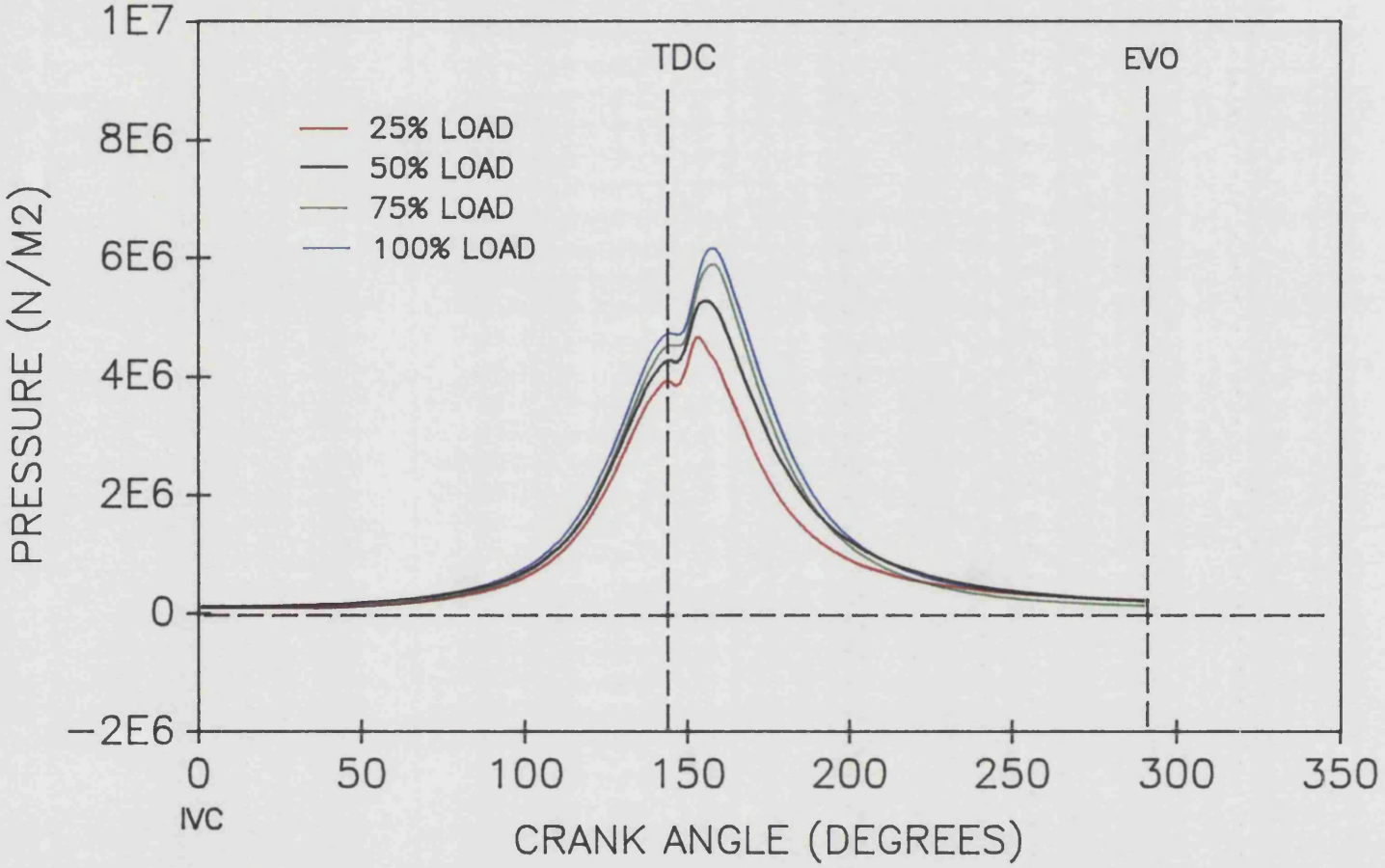

FIGURE 6.18
MEASURED PRECHAMBER PRESSURE
VS. CRANK ANGLE FOR A STANDARD ENGINE OPERATING
AT 1200 REV/MIN.

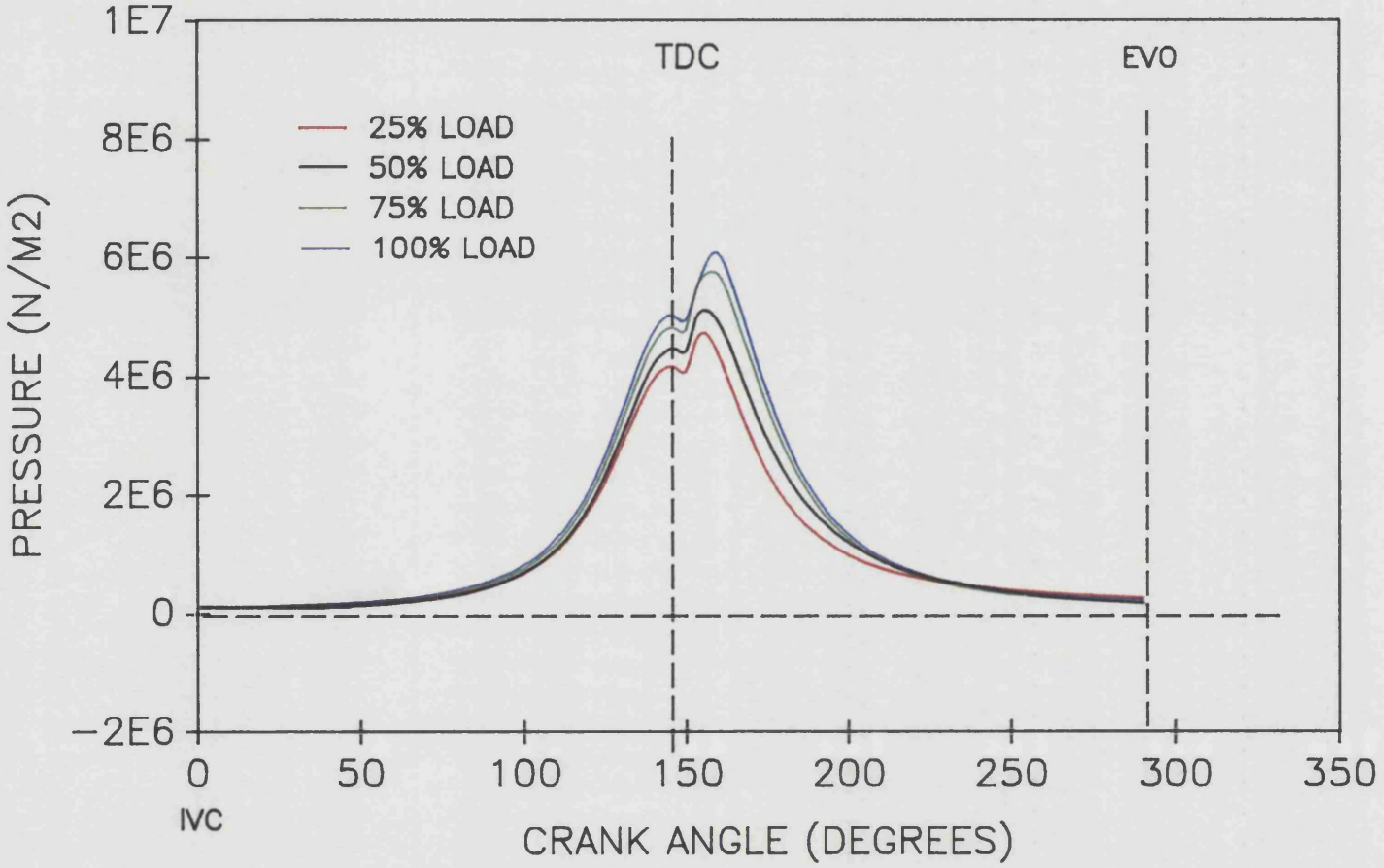

FIGURE 6.19
MEASURED PRECHAMBER PRESSURE
VS. CRANK ANGLE FOR A STANDARD ENGINE OPERATING
AT 1400 REV/MIN.

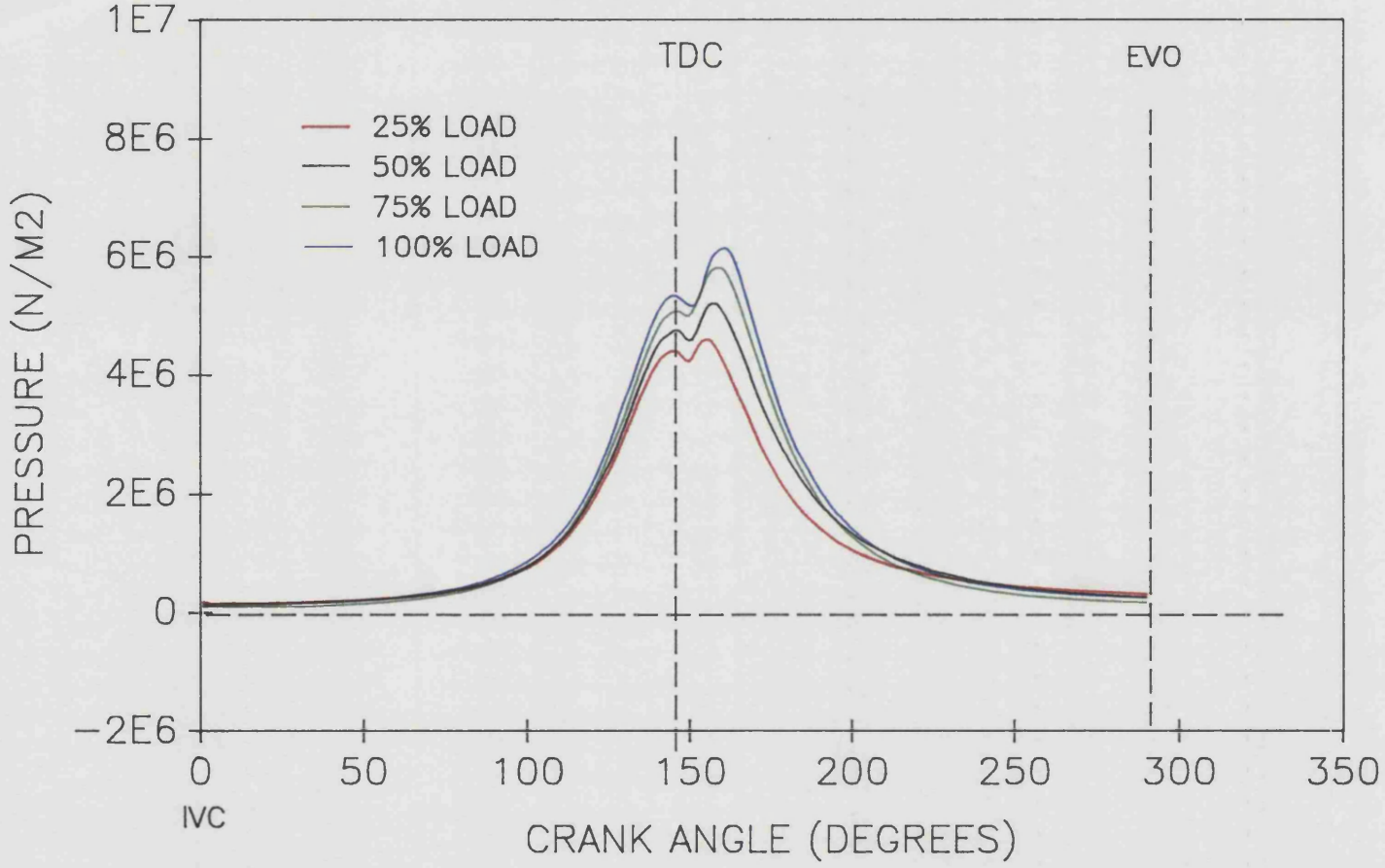

FIGURE 6.20
MEASURED PRECHAMBER PRESSURE
VS. CRANK ANGLE FOR A STANDARD ENGINE OPERATING
AT 1500 REV/MIN.

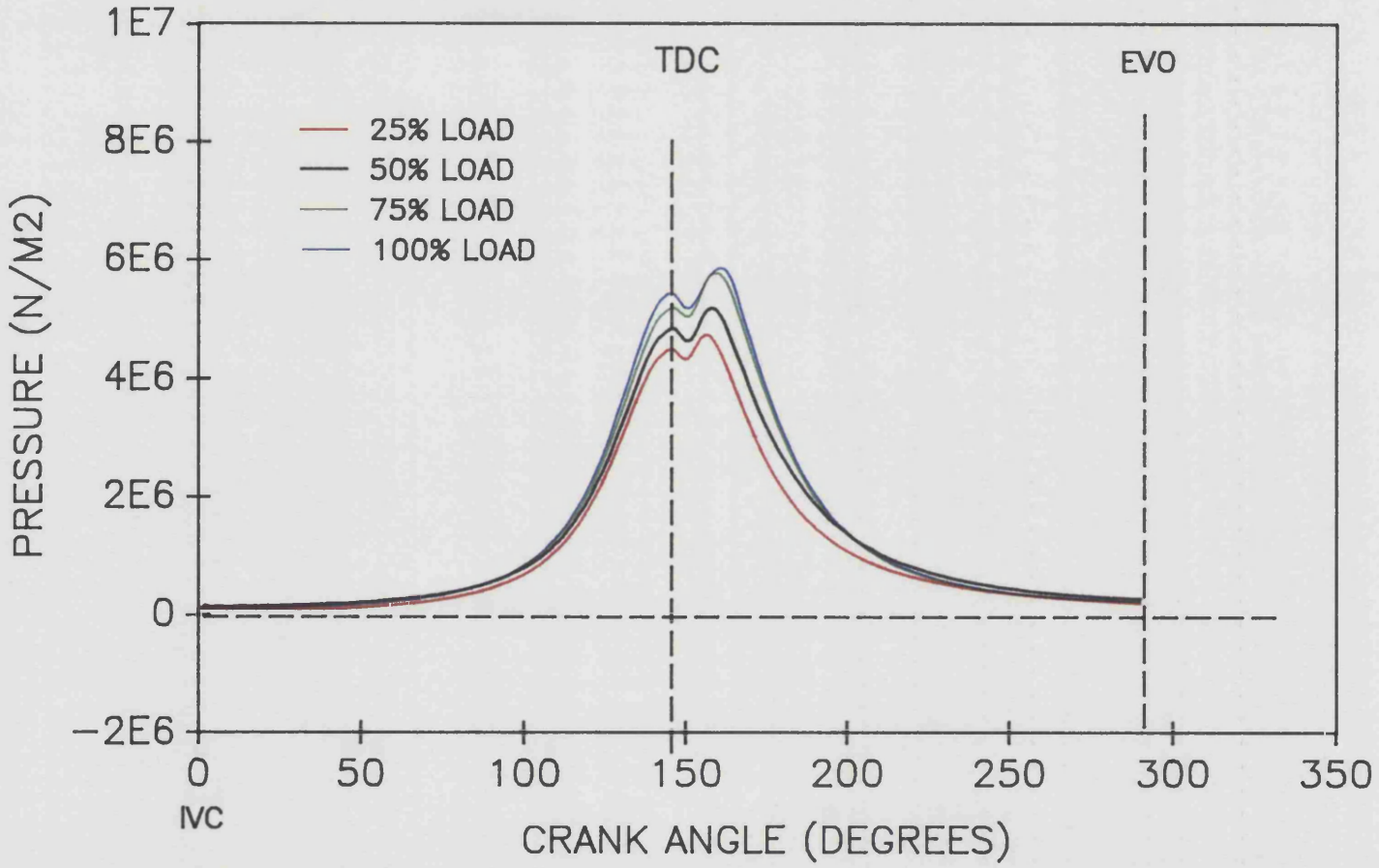

FIGURE 6.21
CALCULATED CYLINDER TEMPERATURE
VS. CRANK ANGLE FOR A STANDARD ENGINE OPERATING
AT 1000 REV/MIN.

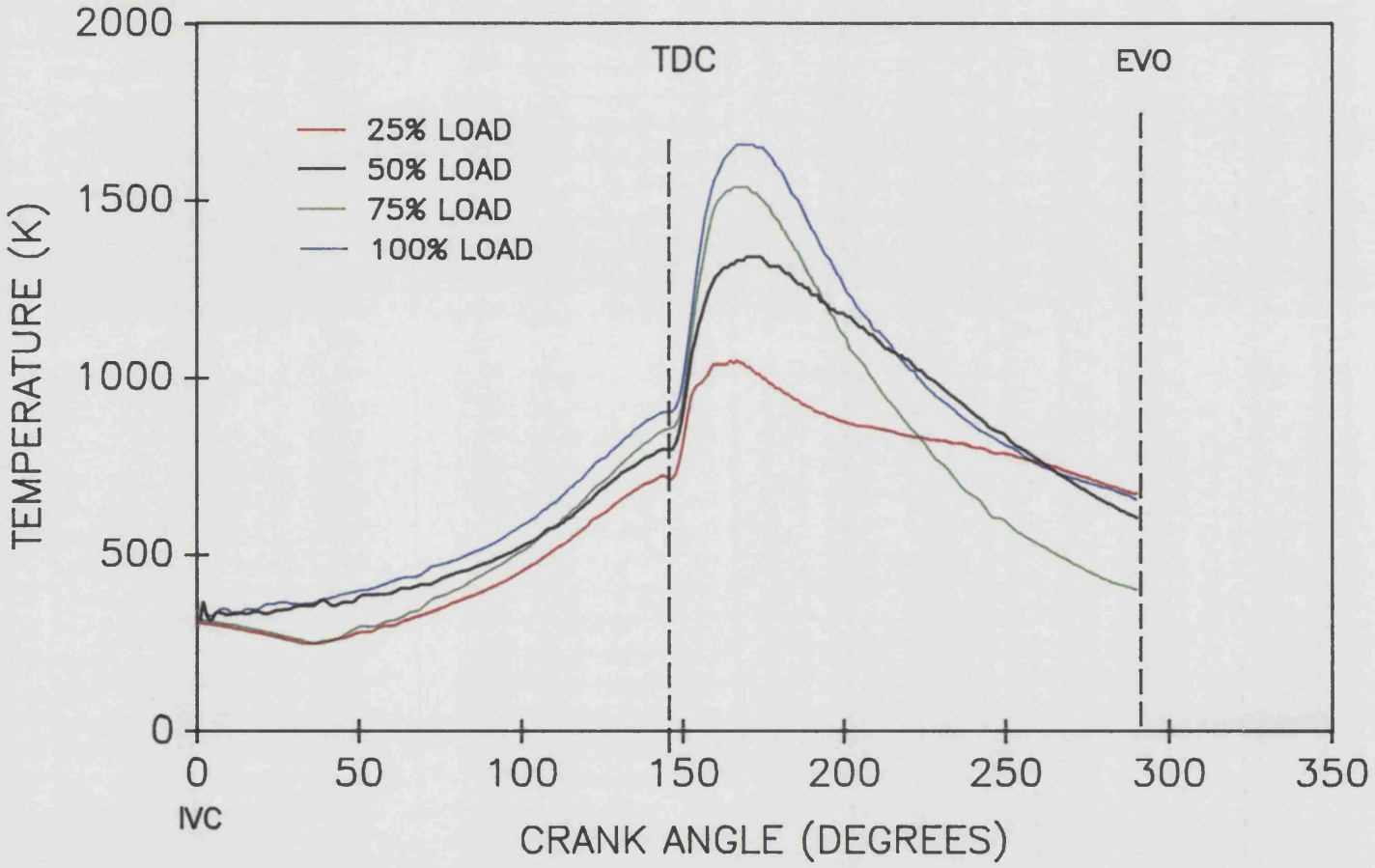

FIGURE 6.22
CALCULATED CYLINDER TEMPERATURE
VS. CRANK ANGLE FOR A STANDARD ENGINE OPERATING
AT 1200 REV/MIN.

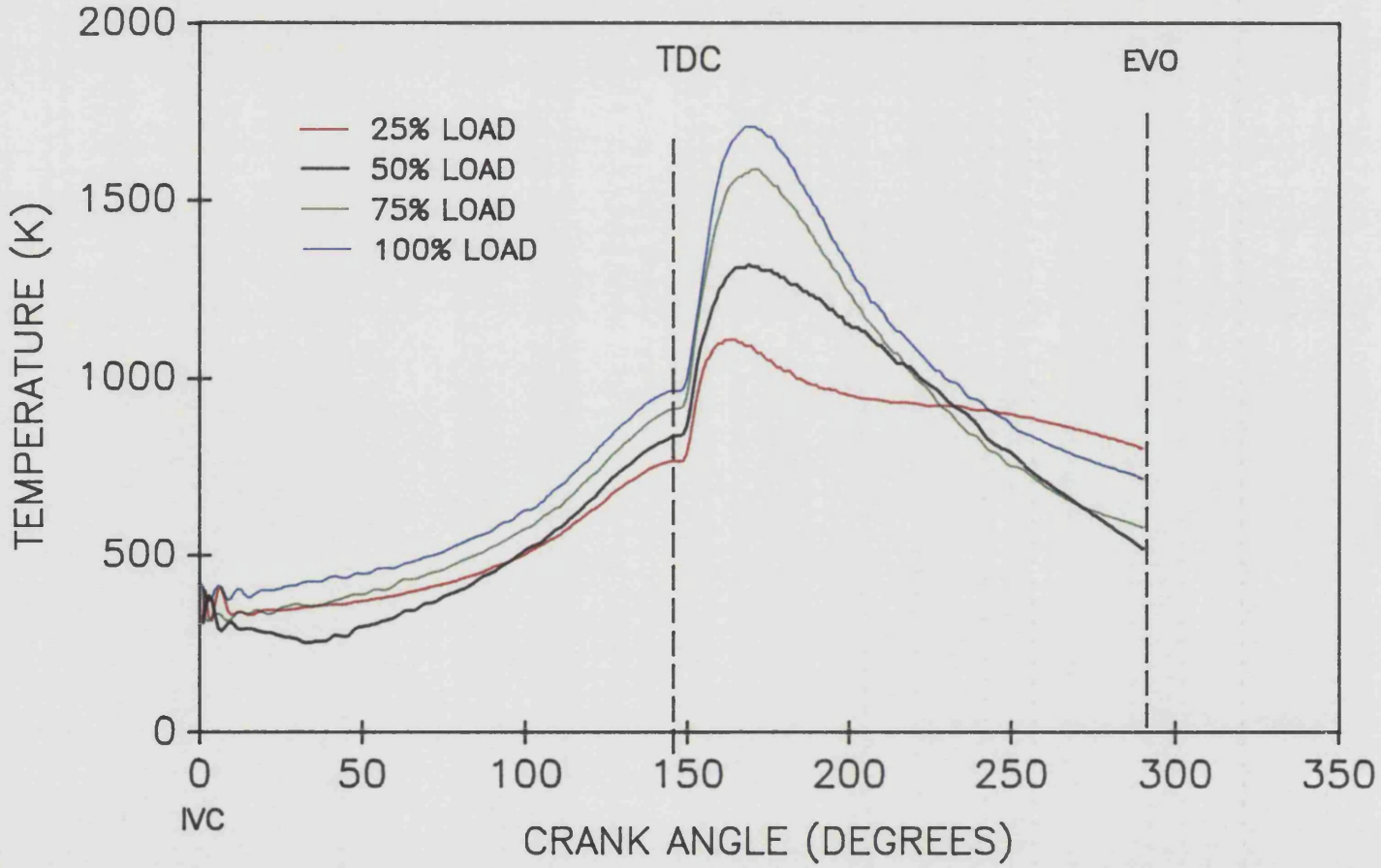

FIGURE 6.23
CALCULATED CYLINDER TEMPERATURE
VS. CRANK ANGLE FOR A STANDARD ENGINE OPERATING
AT 1400 REV/MIN.

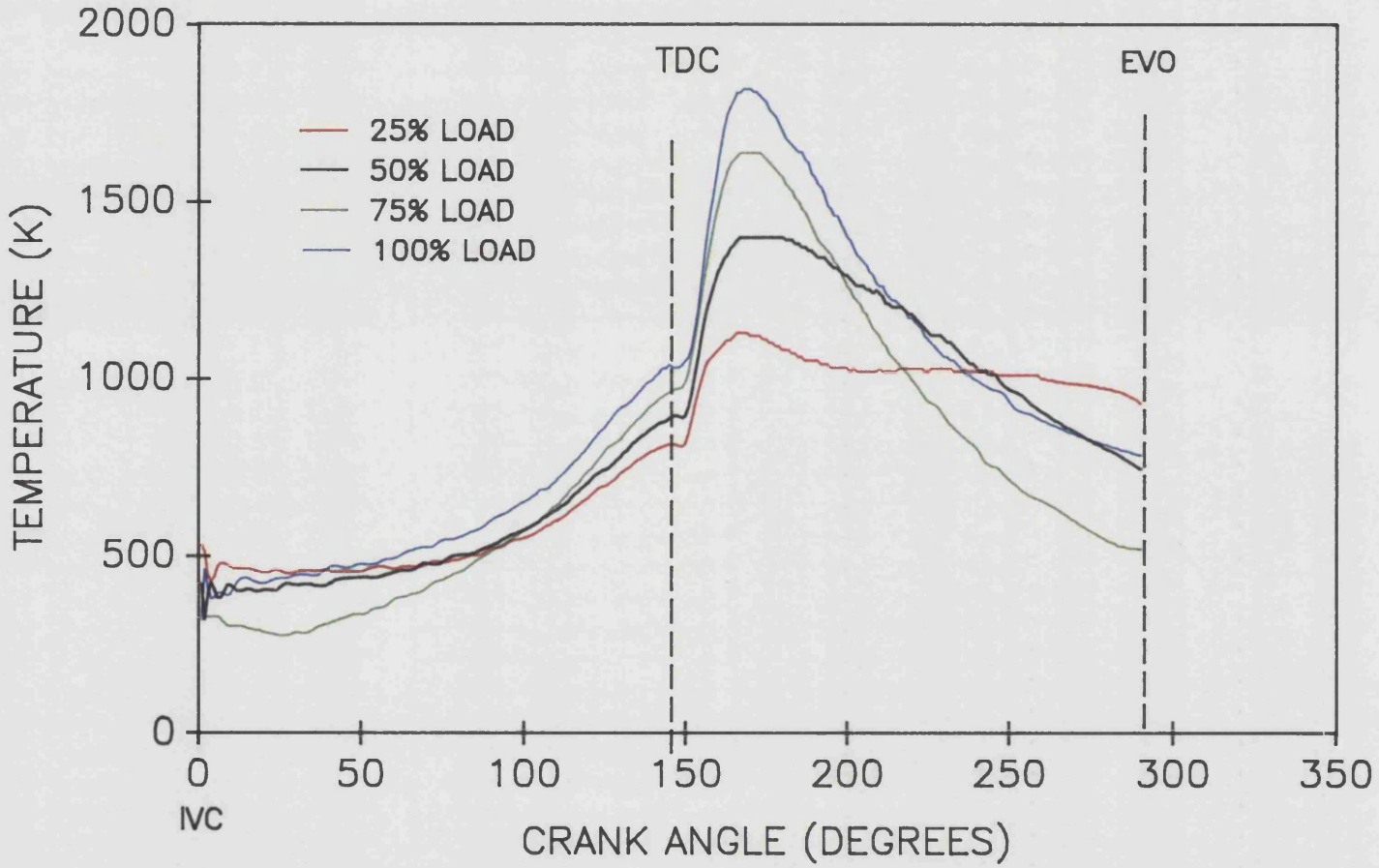

FIGURE 6.24
CALCULATED CYLINDER TEMPERATURE
VS. CRANK ANGLE FOR A STANDARD ENGINE OPERATING
AT 1500 REV/MIN.

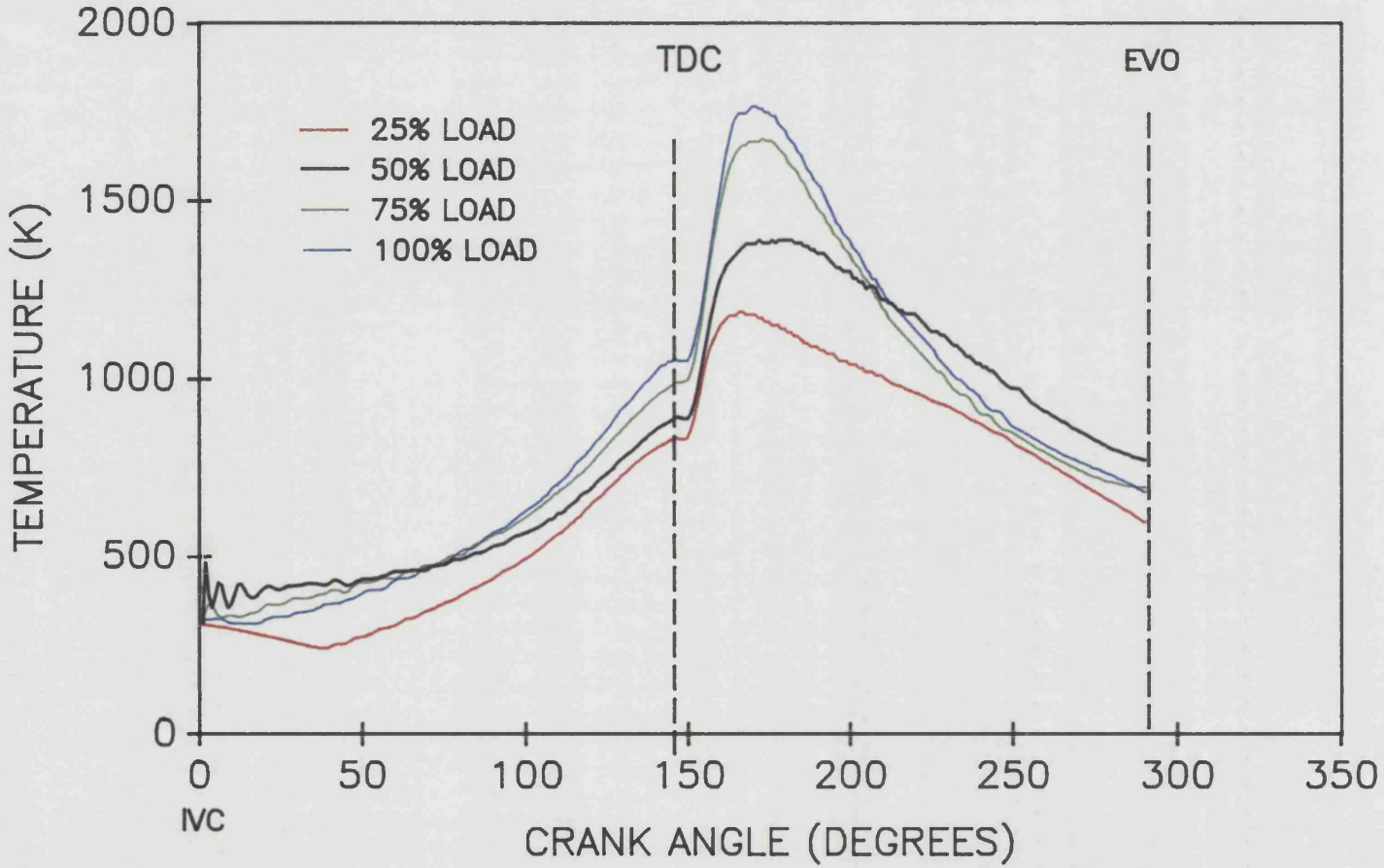

FIGURE 6.25
CUMULATIVE & RATE OF HEAT RELEASE (NETT & FUEL)
VS. CRANK ANGLE FOR A STANDARD ENGINE OPERATING
AT 1000 REV/MIN 25% LOAD.

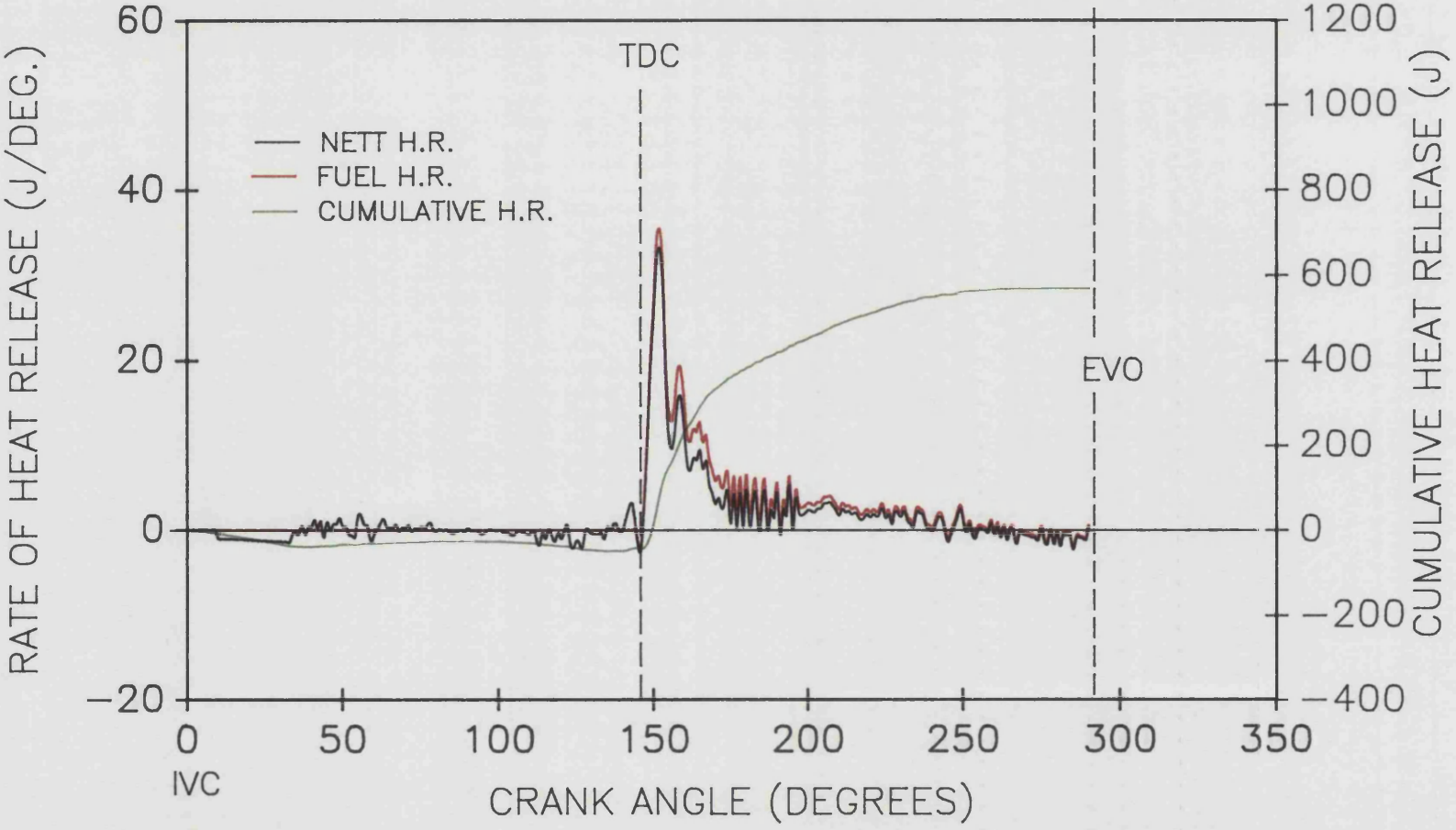

FIGURE 6.26
CUMULATIVE & RATE OF HEAT RELEASE (NETT & FUEL)
VS. CRANK ANGLE FOR A STANDARD ENGINE OPERATING
AT 1000 REV/MIN 50% LOAD.

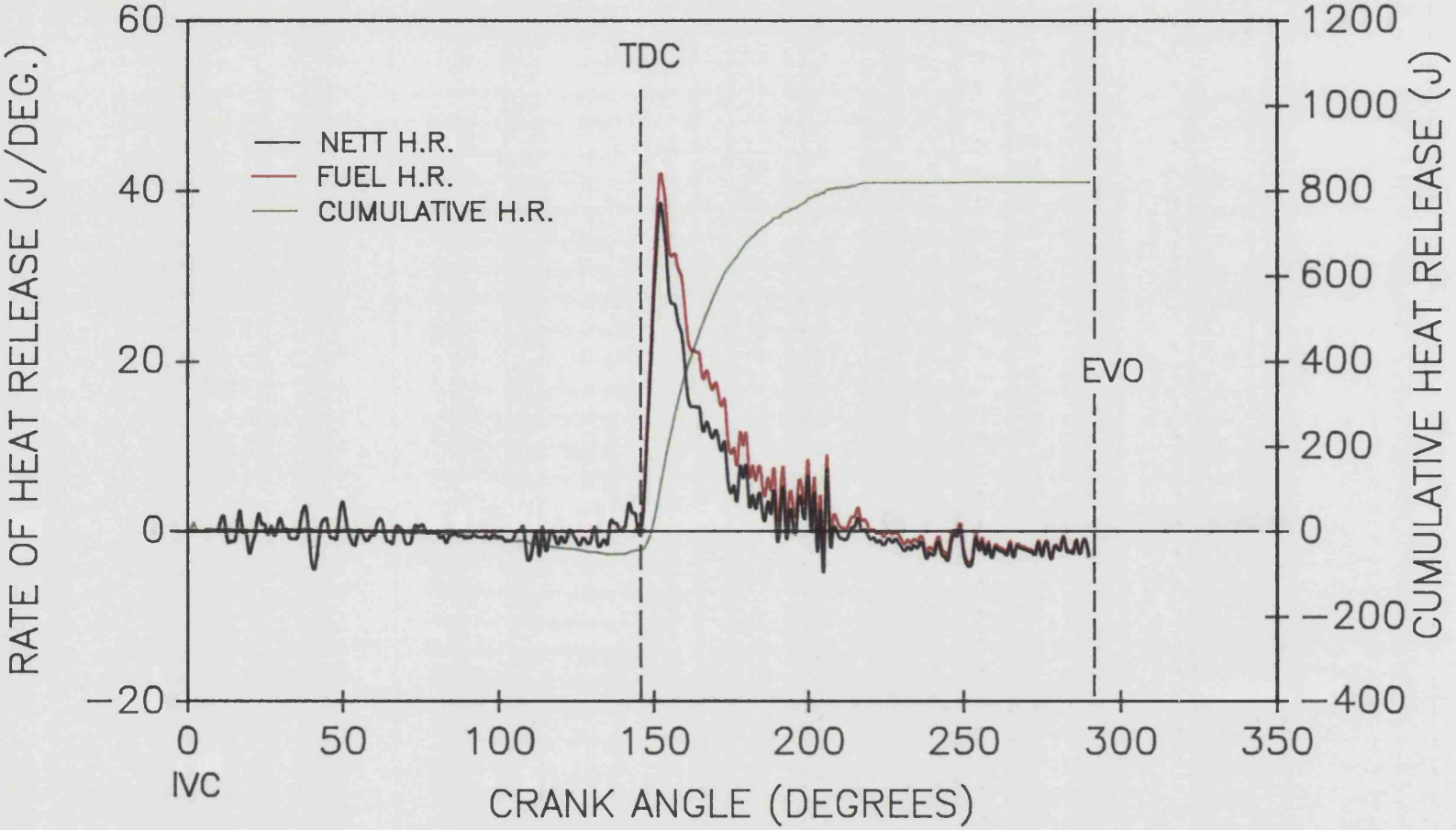

FIGURE 6.27
CUMULATIVE & RATE OF HEAT RELEASE (NETT & FUEL)
VS. CRANK ANGLE FOR A STANDARD ENGINE OPERATING
AT 1000 REV/MIN 75% LOAD

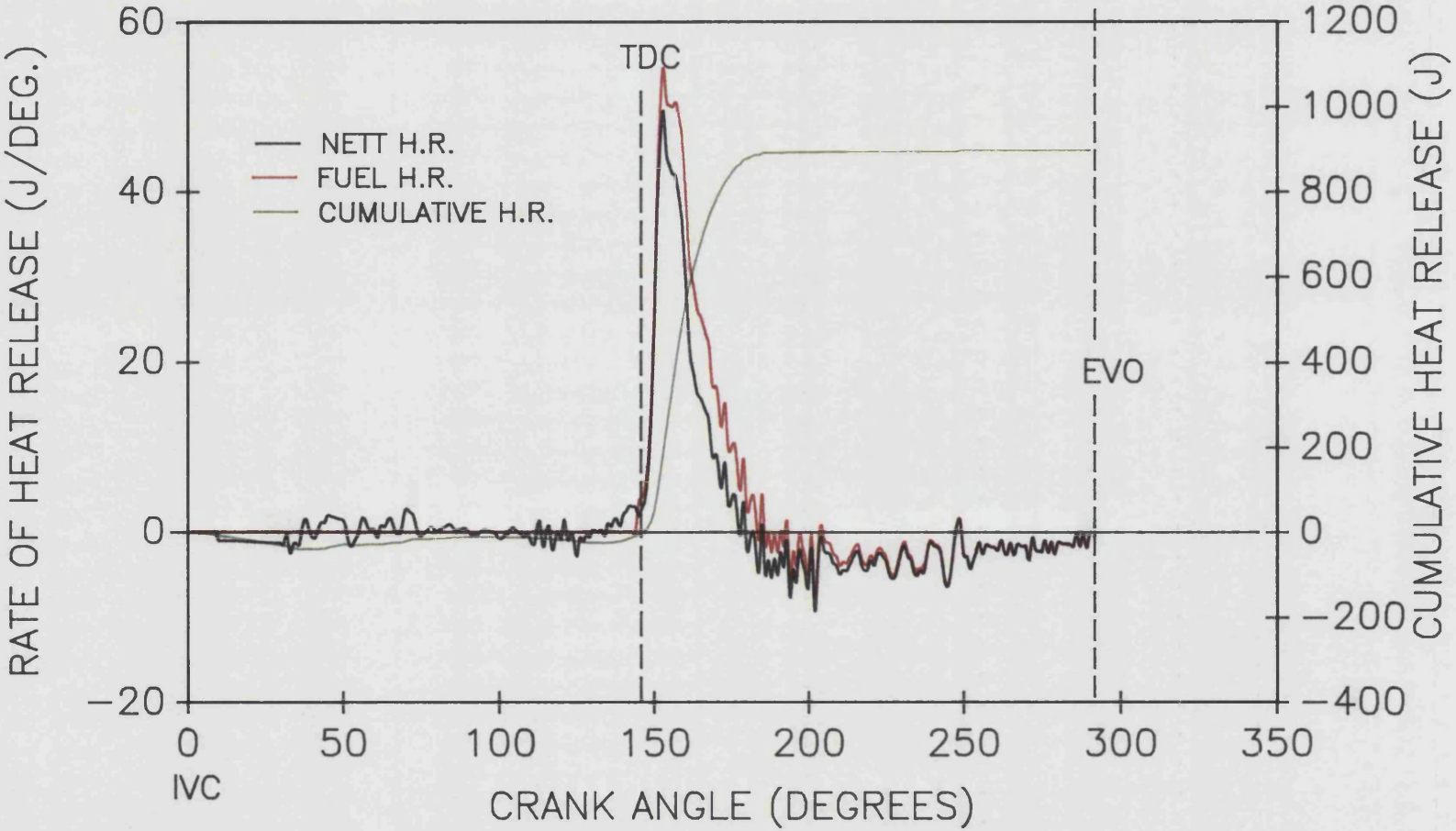

FIGURE 6.28
CUMULATIVE & RATE OF HEAT RELEASE (NETT & FUEL)
VS. CRANK ANGLE FOR A STANDARD ENGINE OPERATING
AT 1000 REV/MIN FULL LOAD.

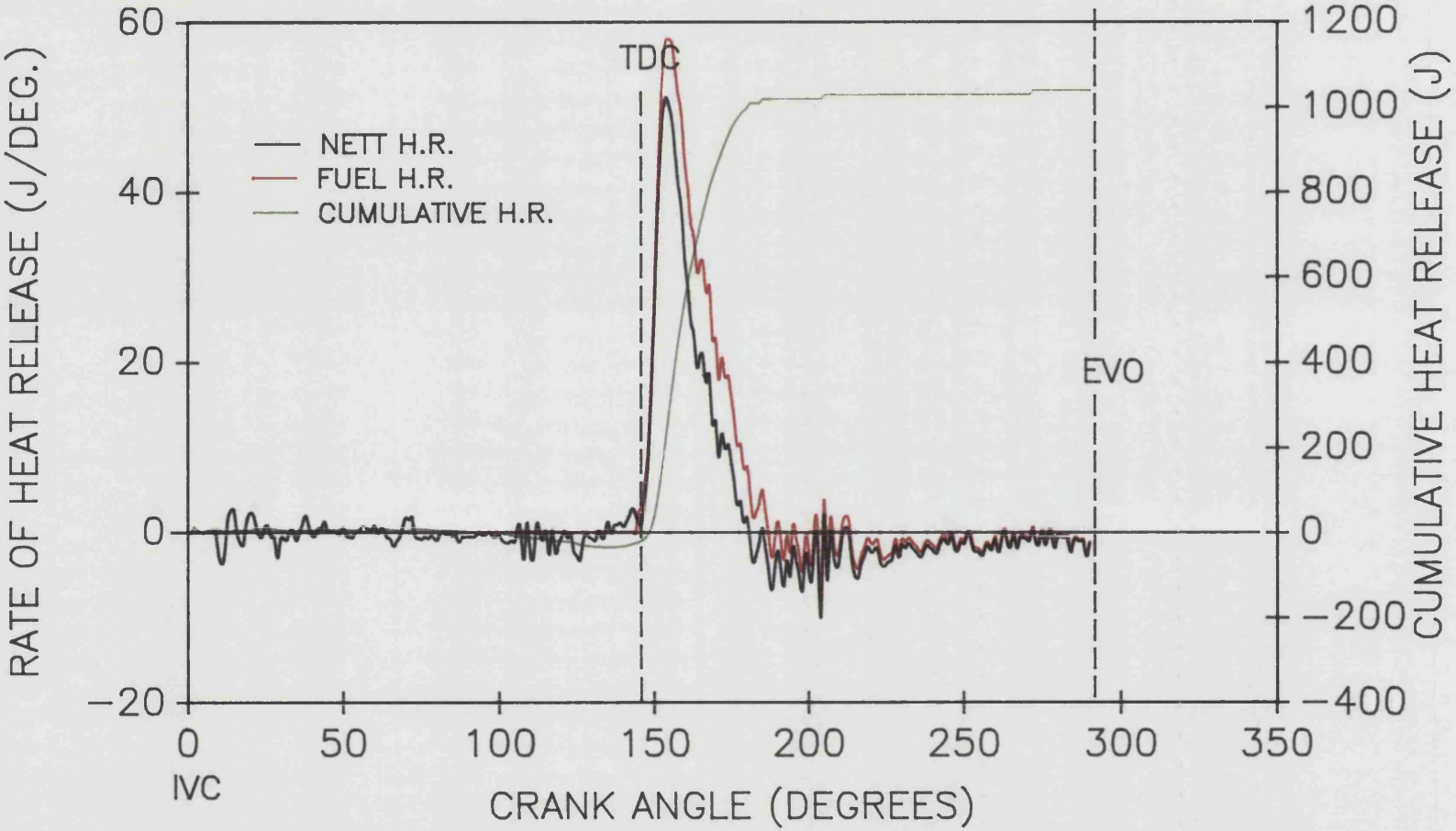

FIGURE 6.29
CUMULATIVE & RATE OF HEAT RELEASE (NETT & FUEL)
VS. CRANK ANGLE FOR A STANDARD ENGINE OPERATING
AT 1200 REV/MIN 25% LOAD.

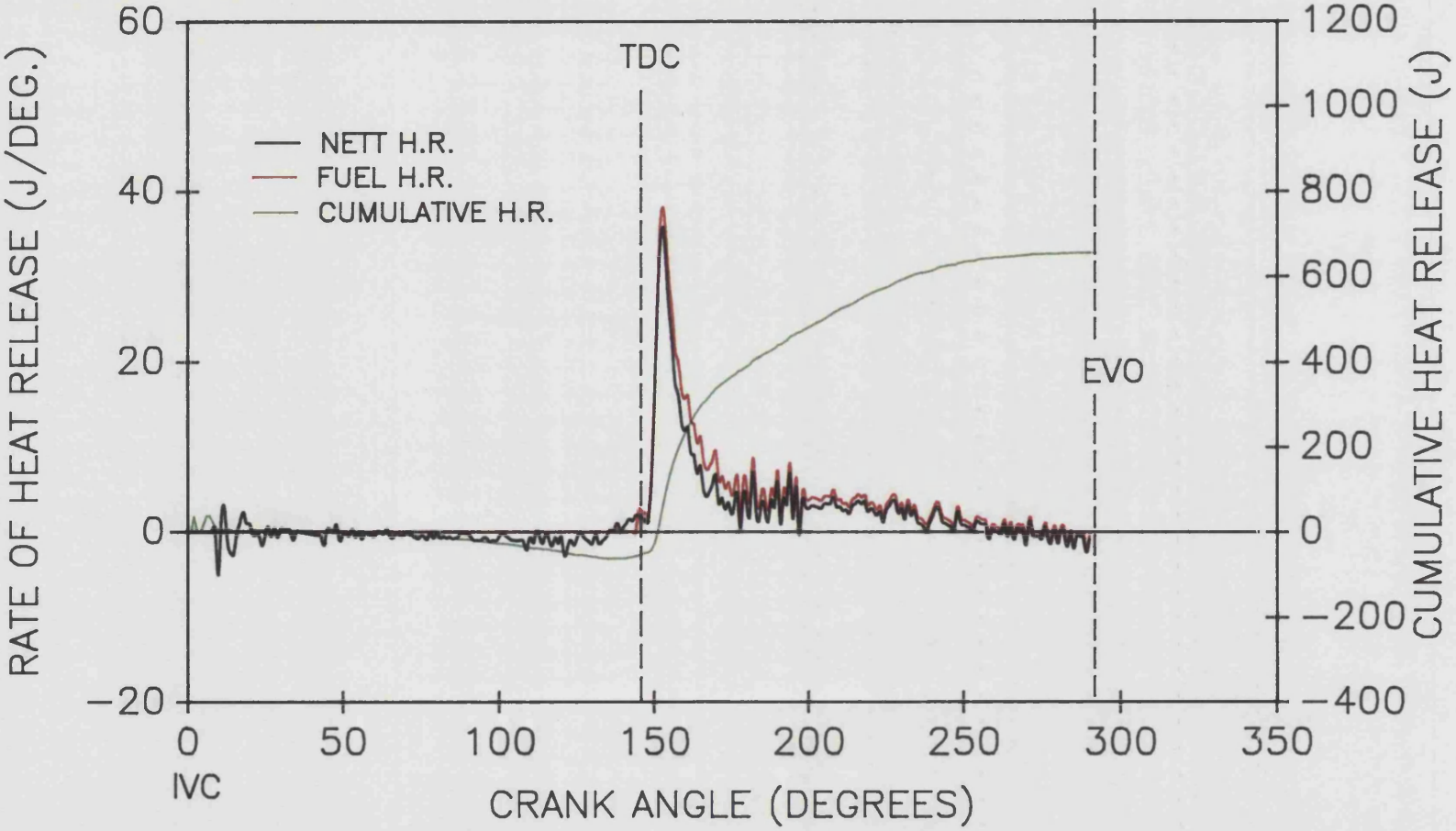

FIGURE 6.30
CUMULATIVE & RATE OF HEAT RELEASE (NETT & FUEL)
VS. CRANK ANGLE FOR A STANDARD ENGINE OPERATING
AT 1200 REV/MIN 50% LOAD.

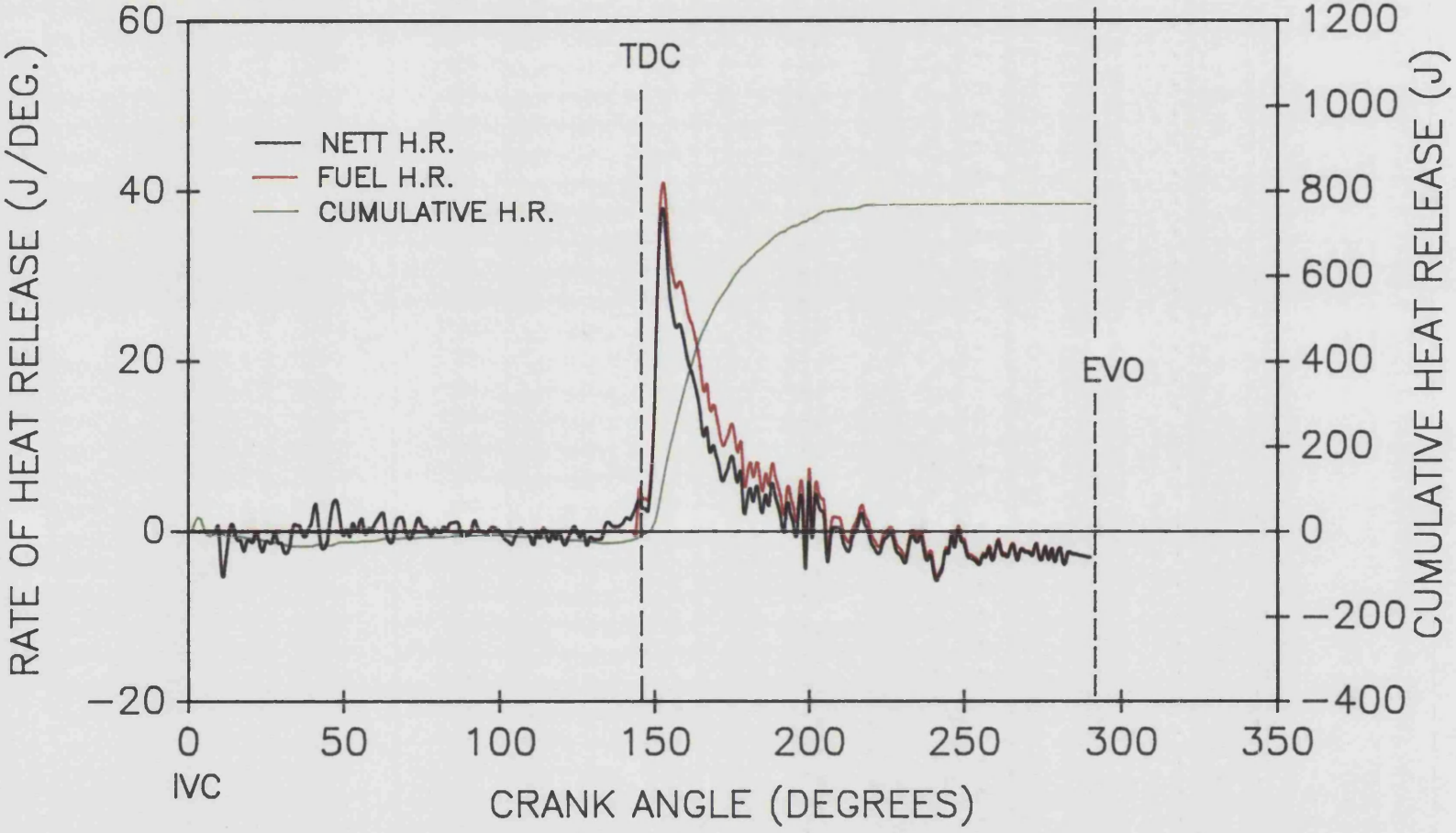

FIGURE 6.31
CUMULATIVE & RATE OF HEAT RELEASE (NETT & FUEL)
VS. CRANK ANGLE FOR A STANDARD ENGINE OPERATING
AT 1200 REV/MIN 75% LOAD.

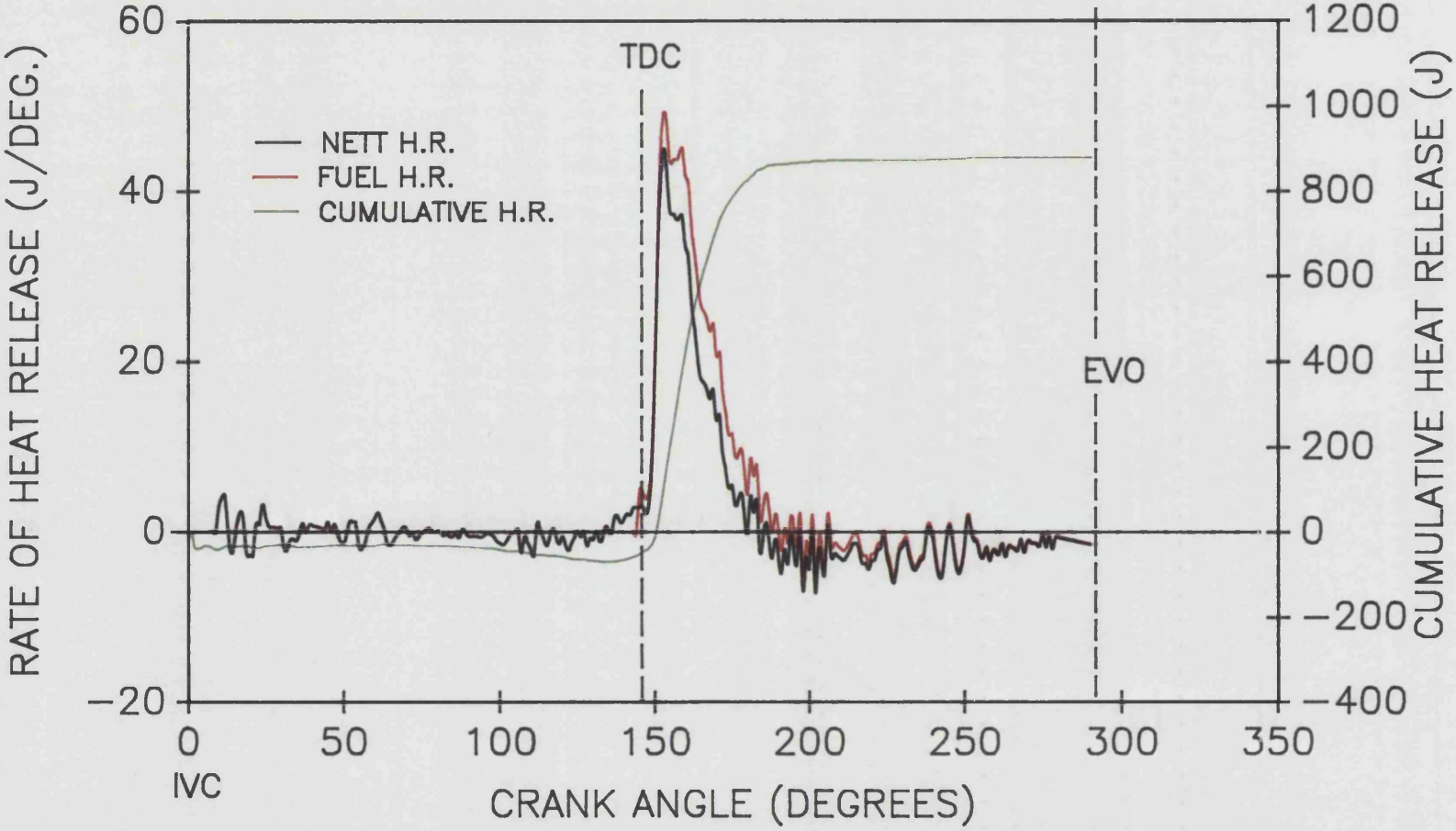

FIGURE 6.32
CUMULATIVE & RATE OF HEAT RELEASE (NETT & FUEL)
VS. CRANK ANGLE FOR A STANDARD ENGINE OPERATING
AT 1200 REV/MIN FULL LOAD.

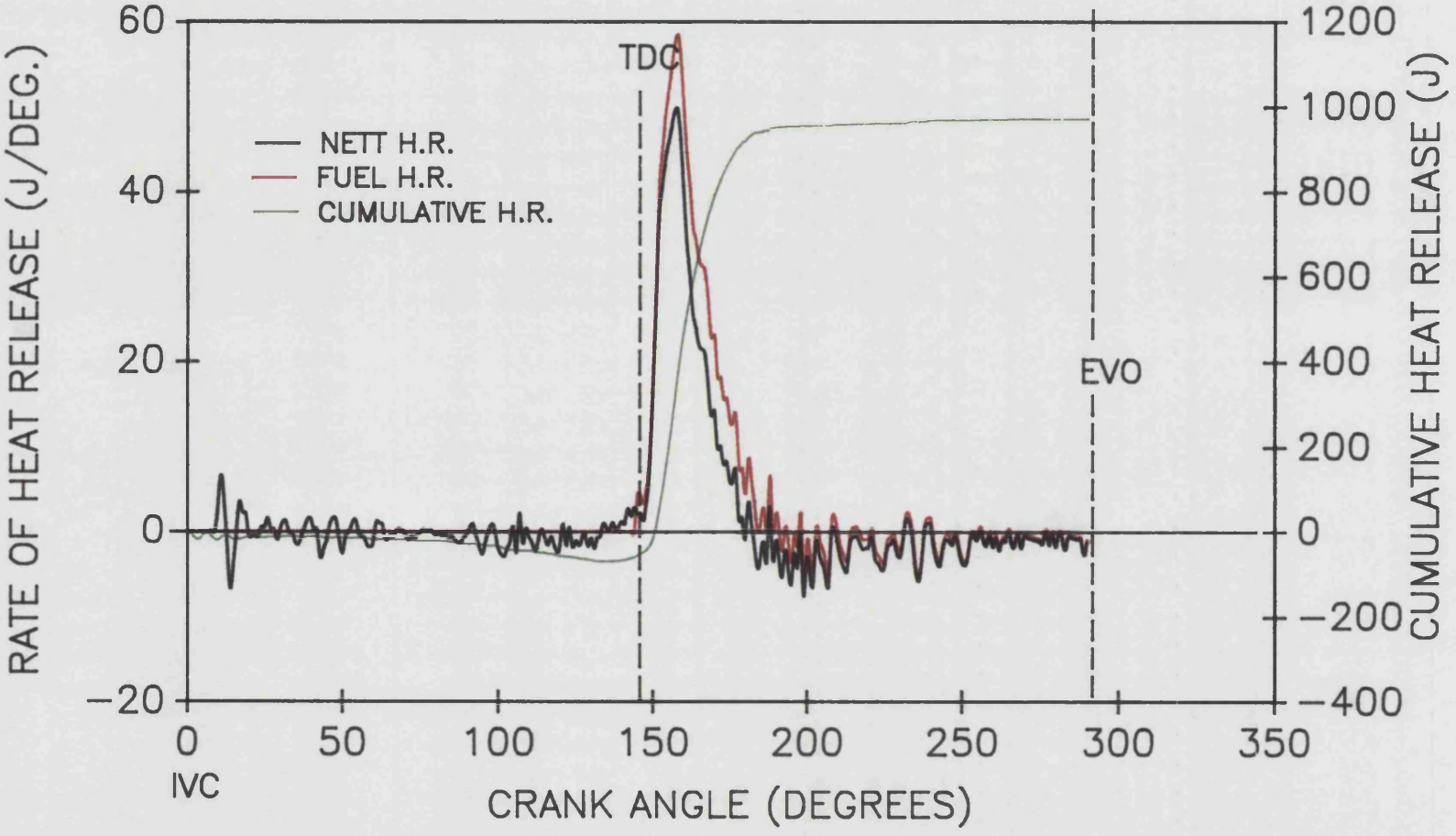

FIGURE 6.33
CUMULATIVE & RATE OF HEAT RELEASE (NETT & FUEL)
VS. CRANK ANGLE FOR A STANDARD ENGINE OPERATING
AT 1400 REV/MIN 25% LOAD

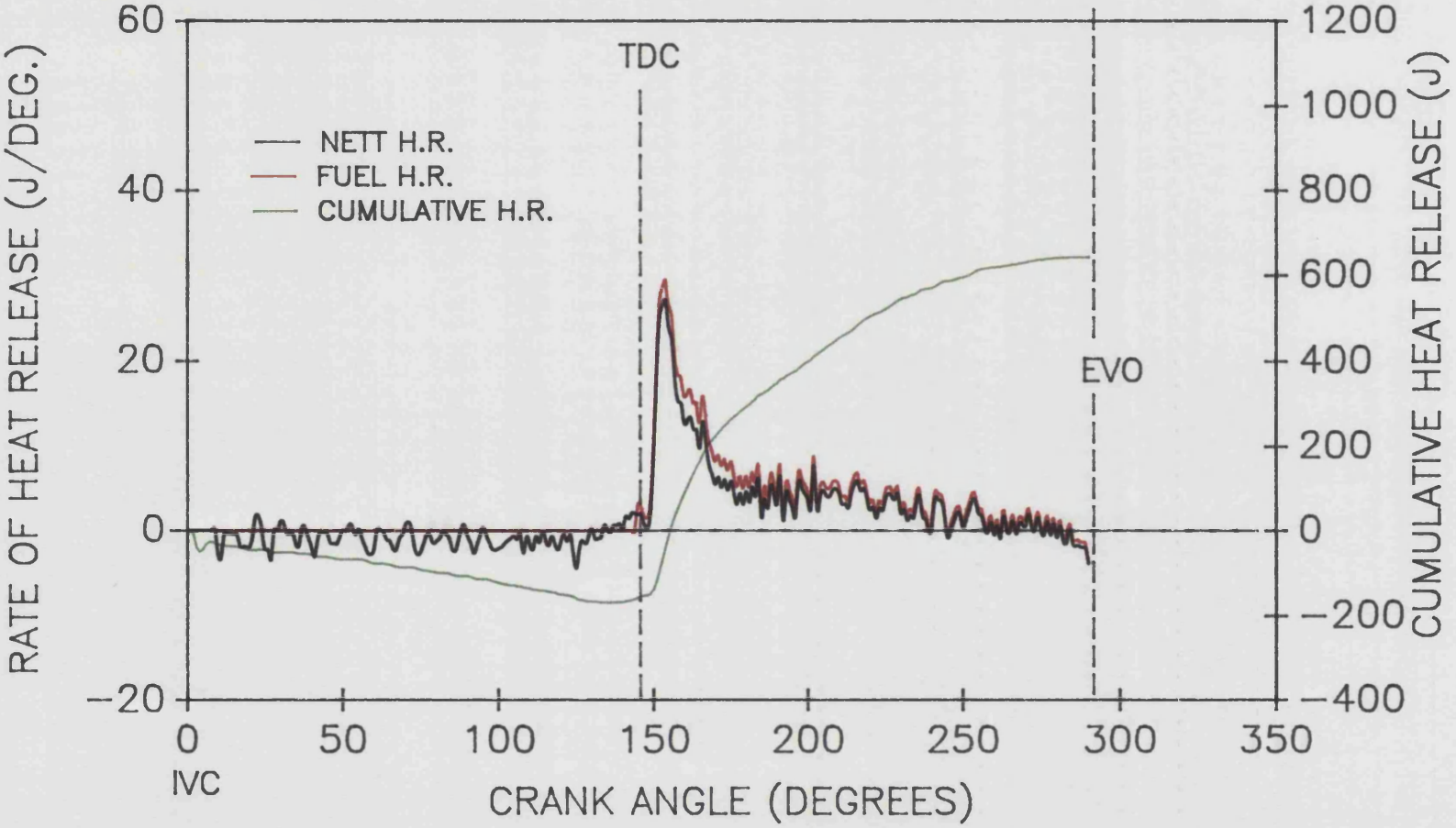

FIGURE 6.34
CUMULATIVE & RATE OF HEAT RELEASE (NETT & FUEL)
VS. CRANK ANGLE FOR A STANDARD ENGINE OPERATING
AT 1400 REV/MIN 50% LOAD.

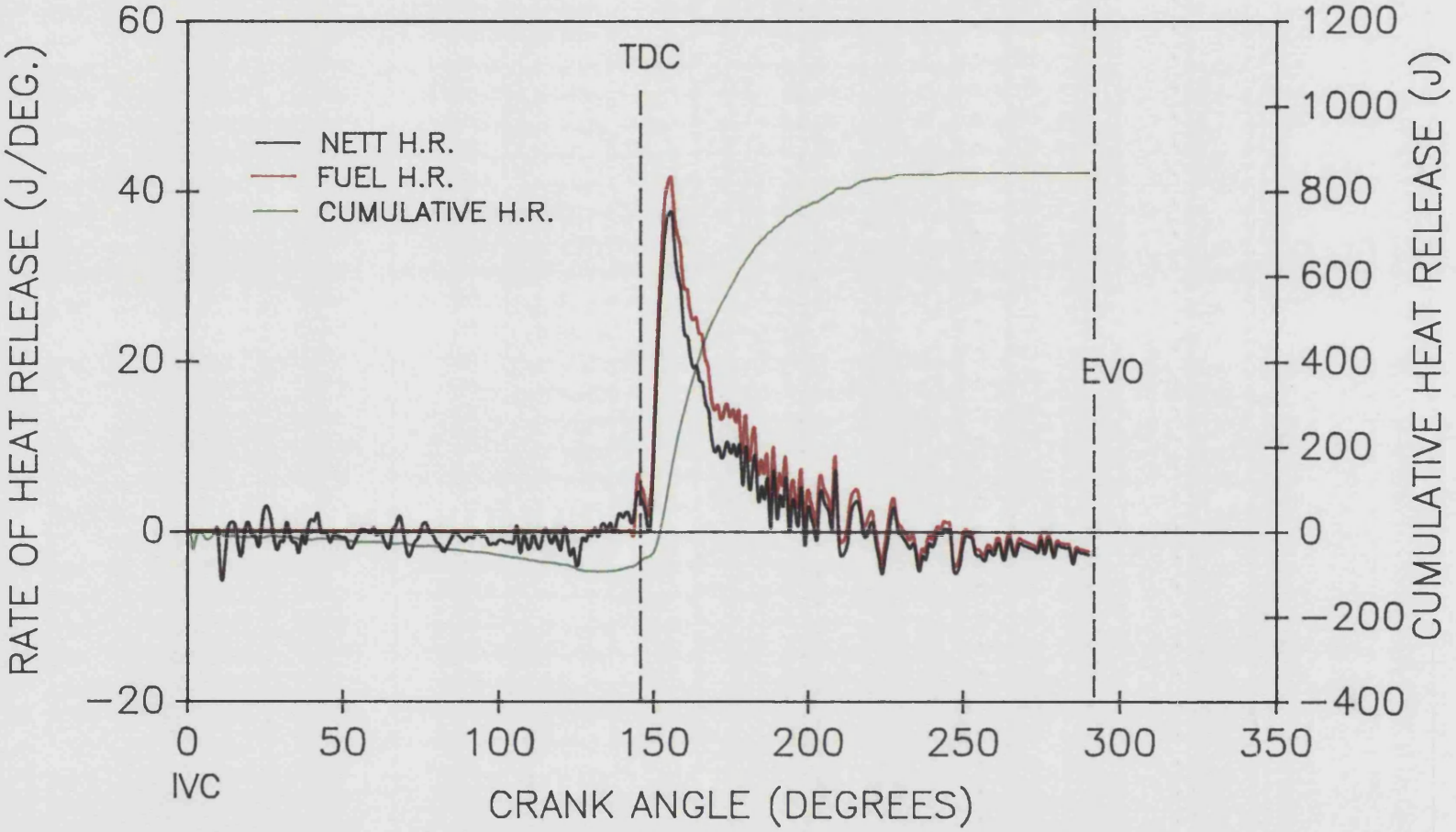

FIGURE 6.35
CUMULATIVE & RATE OF HEAT RELEASE (NETT & FUEL)
VS. CRANK ANGLE FOR A STANDARD ENGINE OPERATING
AT 1400 REV/MIN 75% LOAD.

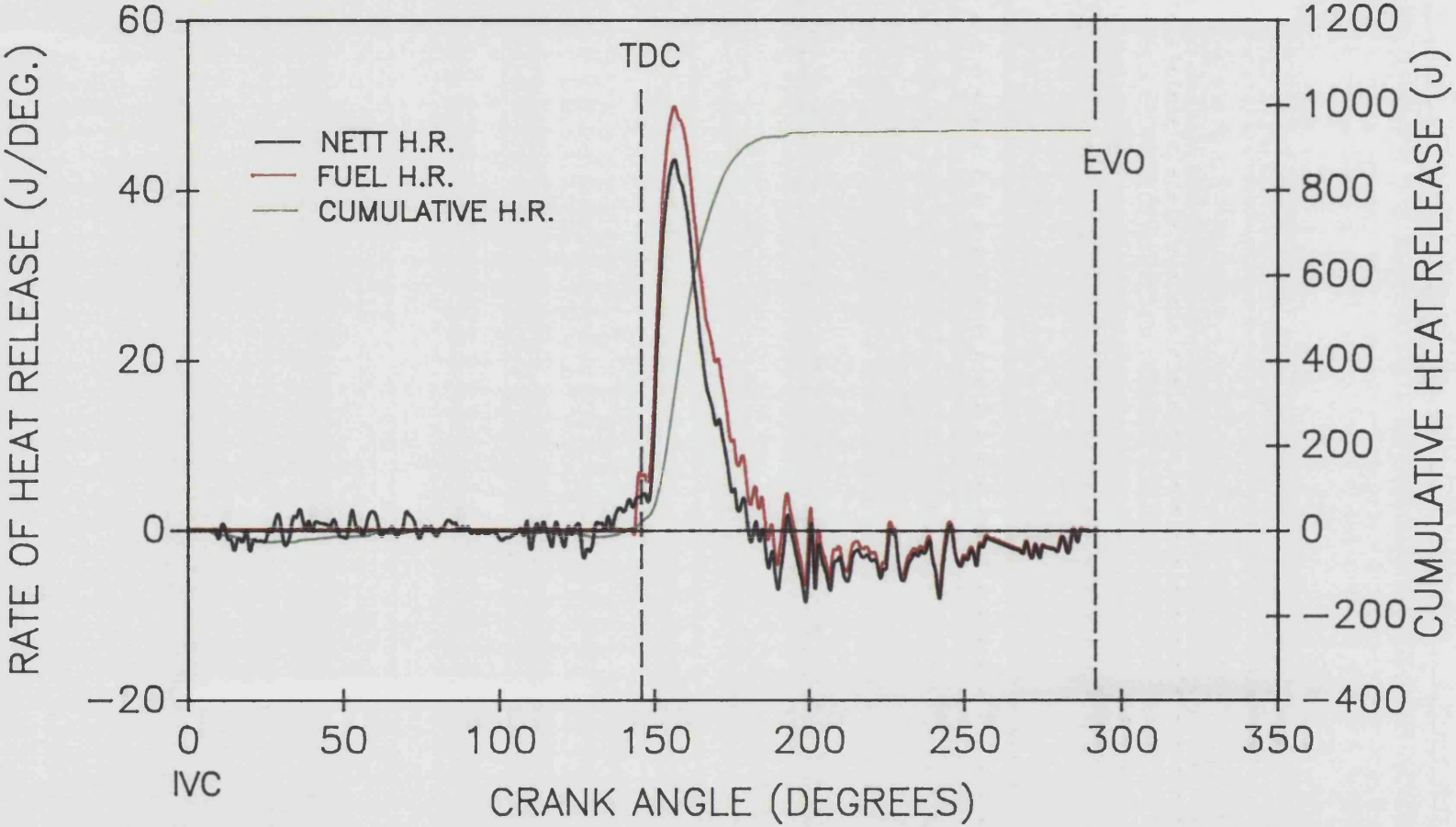

FIGURE 6.36
CUMULATIVE & RATE OF HEAT RELEASE (NETT & FUEL)
VS. CRANK ANGLE FOR A STANDARD ENGINE OPERATING
AT 1400 REV/MIN FULL LOAD.

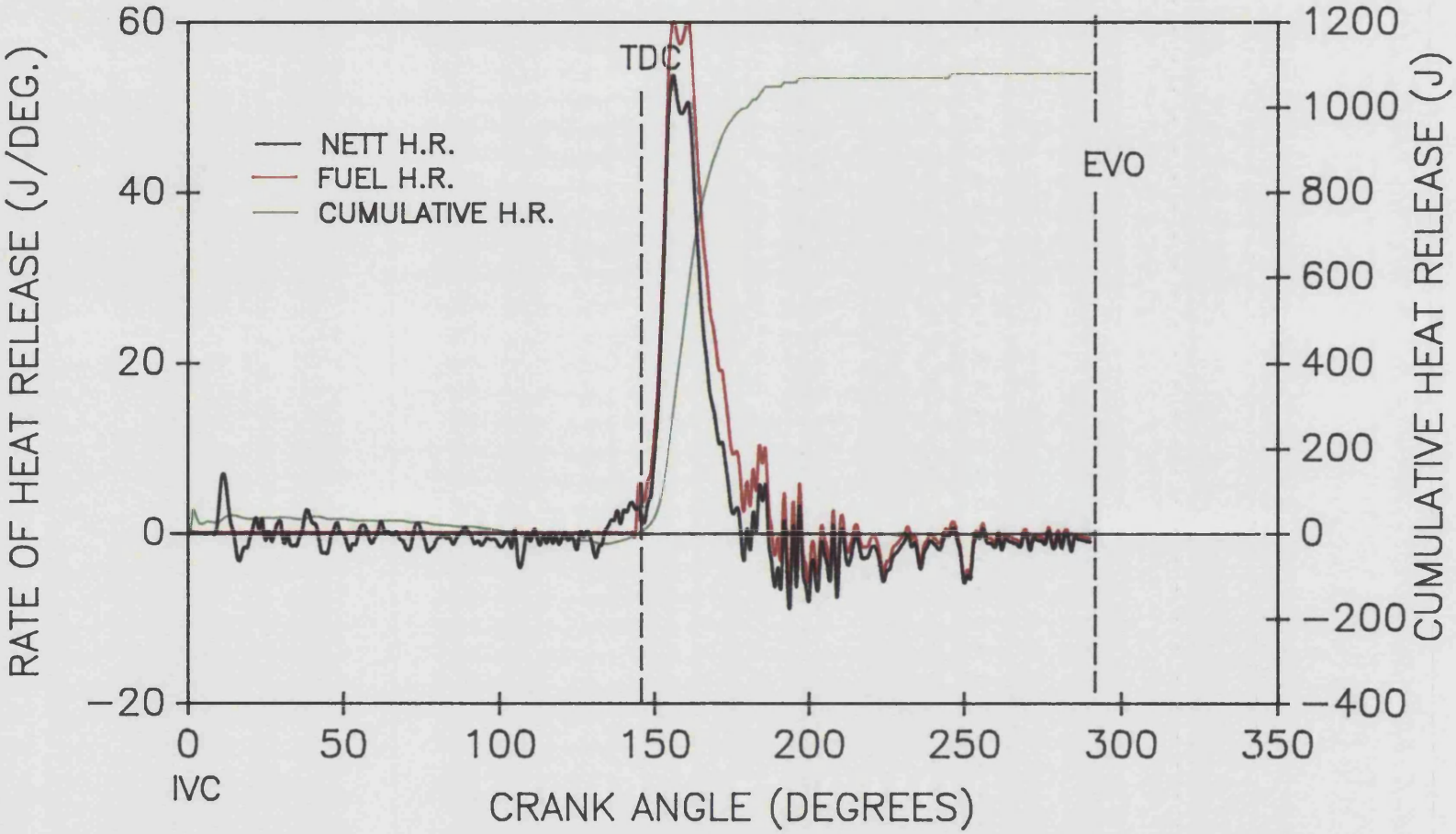

FIGURE 6.37
CUMULATIVE & RATE OF HEAT RELEASE (NETT & FUEL)
VS. CRANK ANGLE FOR A STANDARD ENGINE OPERATING
AT 1500 REV/MIN 25% LOAD.

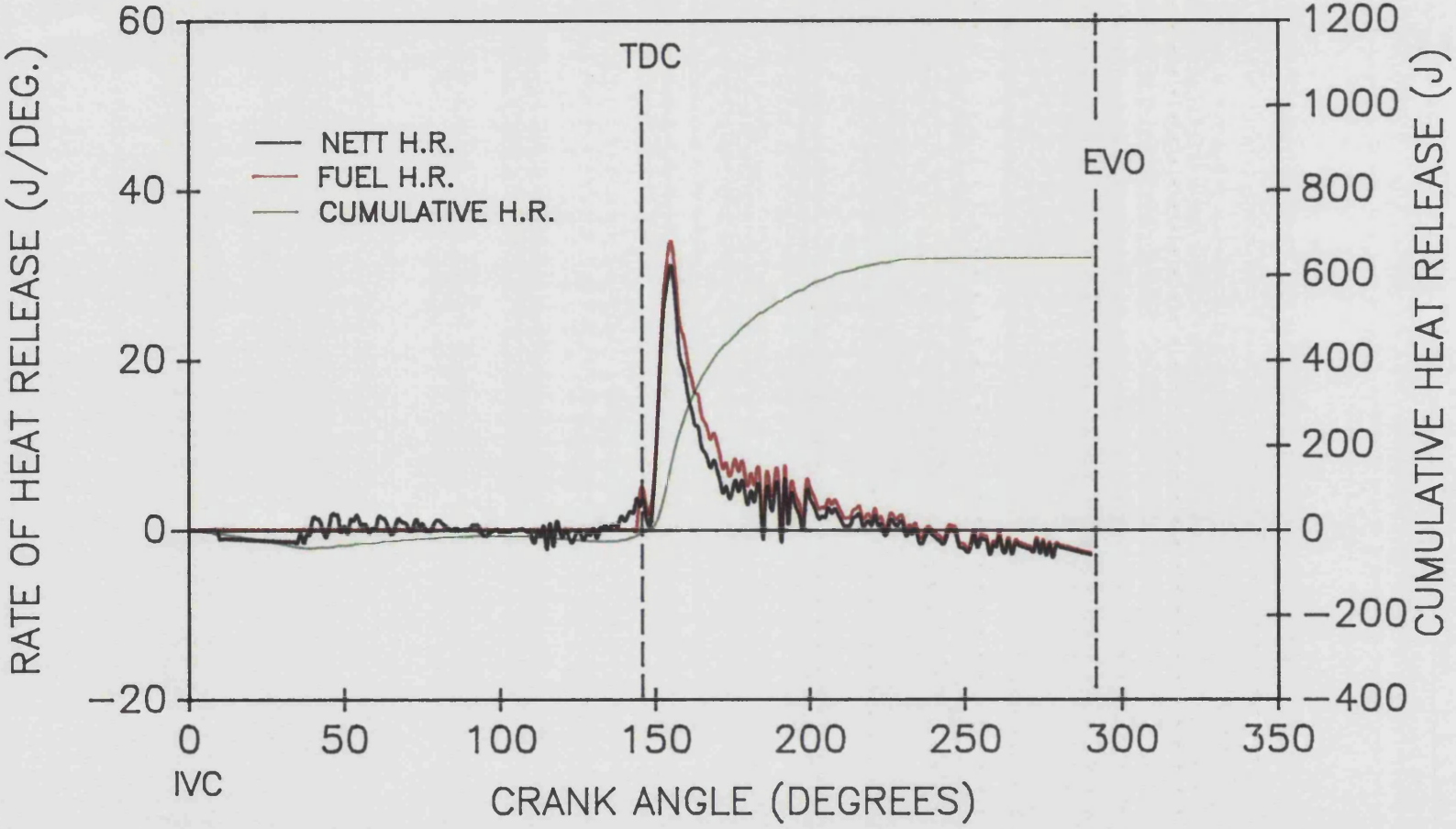

FIGURE 6.38
CUMULATIVE & RATE OF HEAT RELEASE (NETT & FUEL)
VS. CRANK ANGLE FOR A STANDARD ENGINE OPERATING
AT 1500 REV/MIN 50% LOAD.

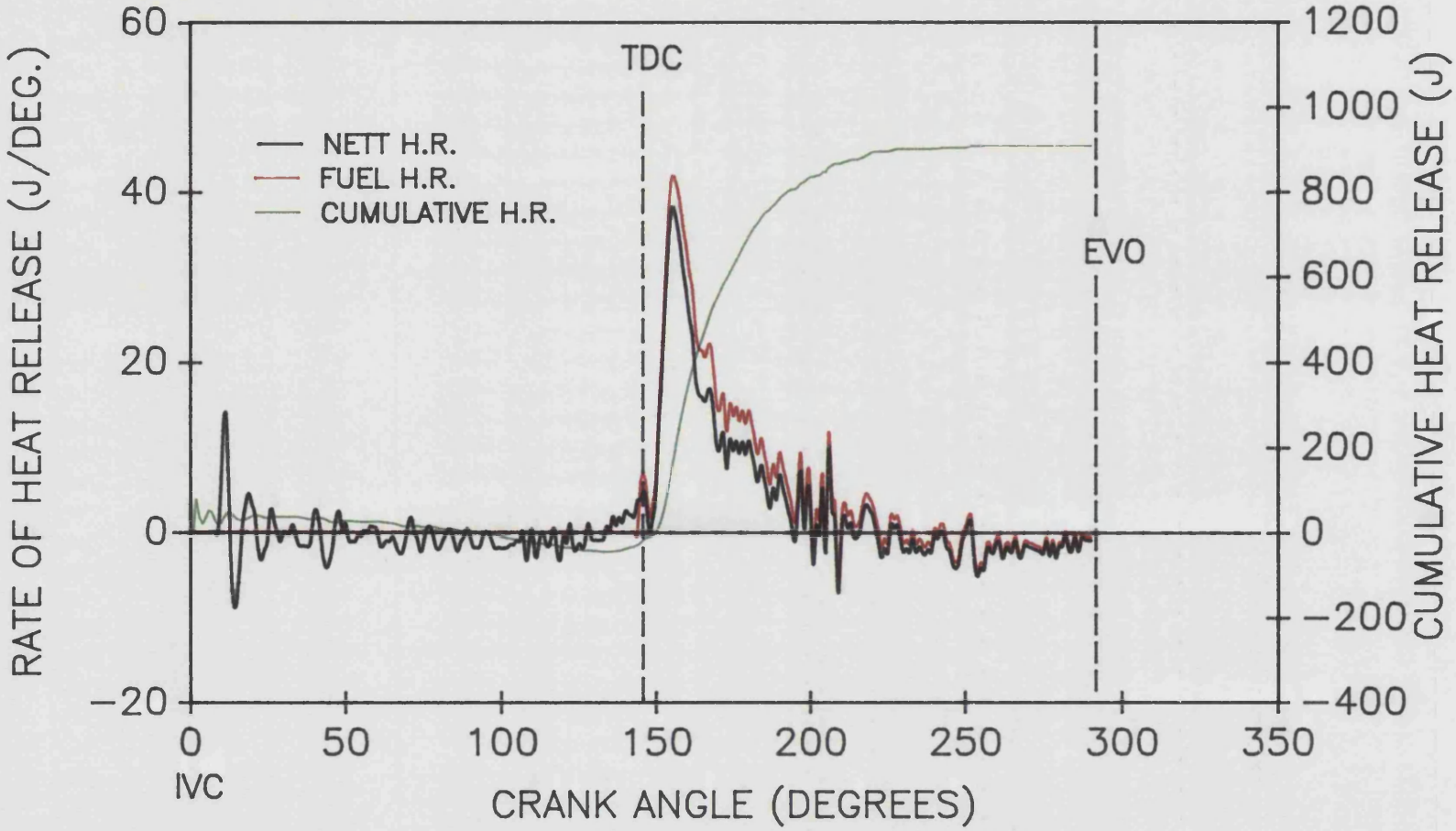

FIGURE 6.39
CUMULATIVE & RATE OF HEAT RELEASE (NETT & FUEL)
VS. CRANK ANGLE FOR A STANDARD ENGINE OPERATING
AT 1500 REV/MIN 75% LOAD.

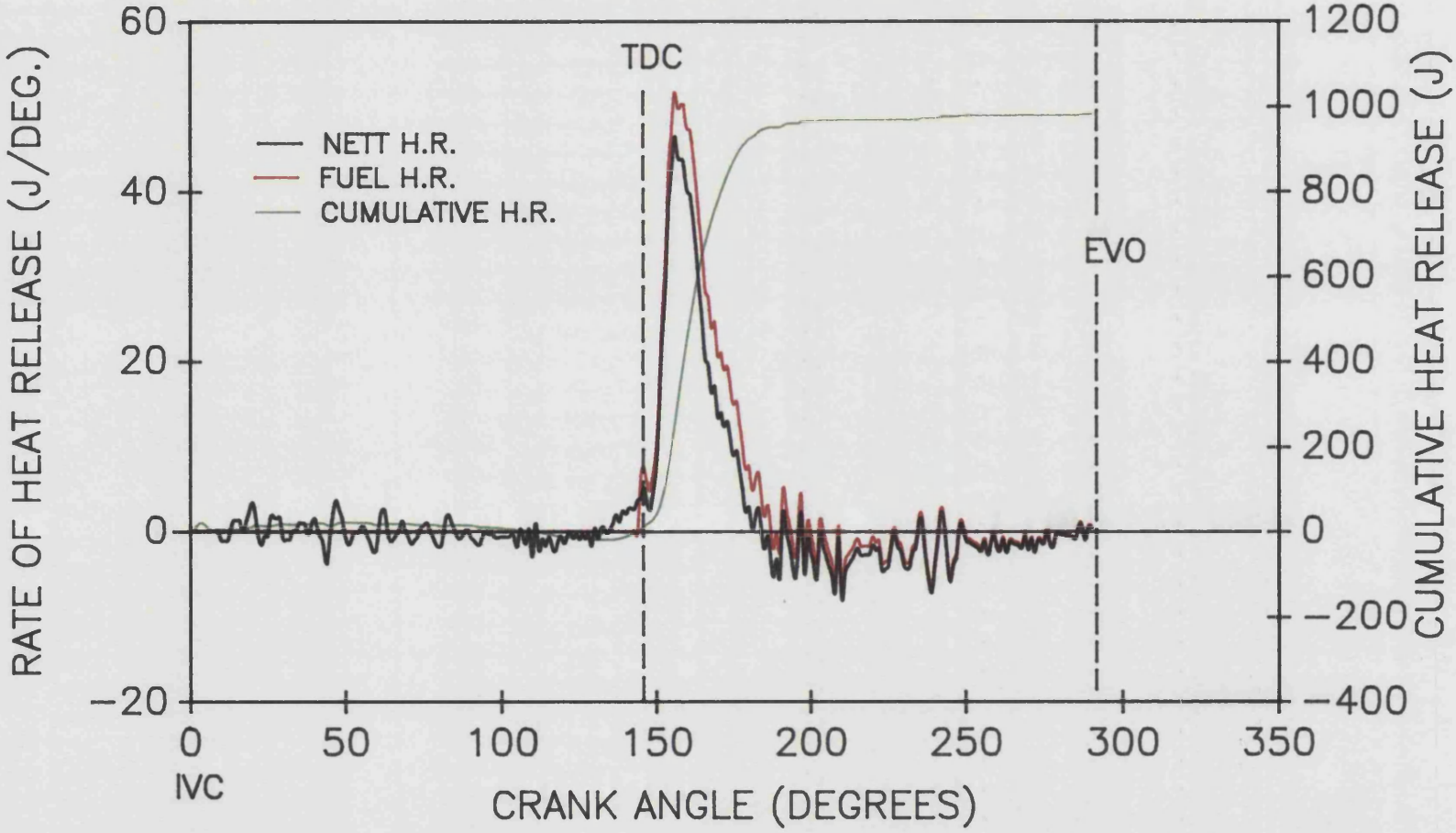

FIGURE 6.40
CUMULATIVE & RATE OF HEAT RELEASE (NETT & FUEL)
VS. CRANK ANGLE FOR A STANDARD ENGINE OPERATING
AT 1500 REV/MIN FULL LOAD.

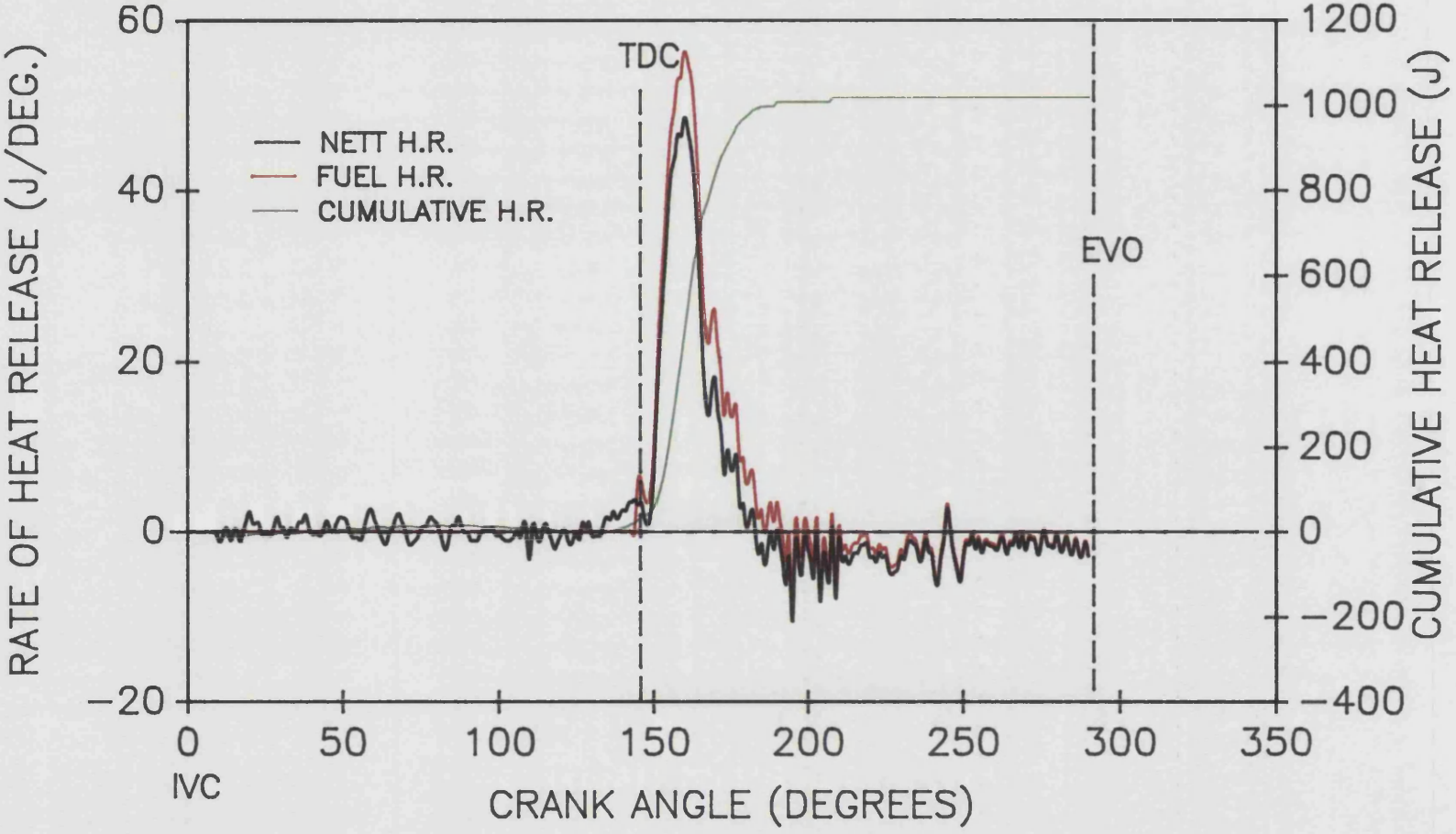

FIGURE 6.41
COMPUTED EQUIVALENCE RATIO & MASS OF FUEL
VS. CRANK ANGLE FOR A STANDARD ENGINE OPERATING
AT 1000 REV/MIN.

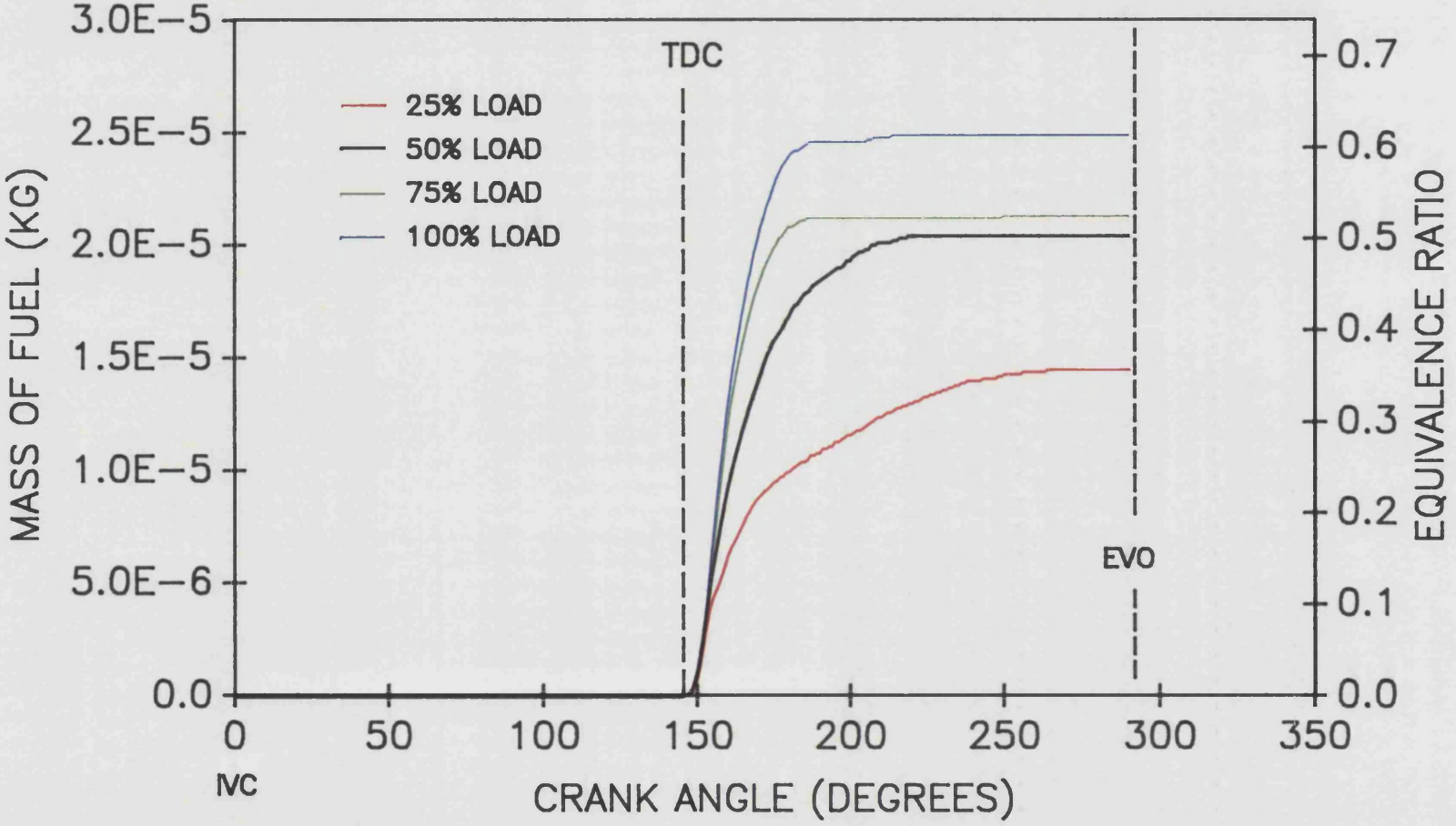

FIGURE 6.42
COMPUTED EQUIVALENCE RATIO & MASS OF FUEL
VS. CRANK ANGLE FOR A STANDARD ENGINE OPERATING
AT 1200 REV/MIN.

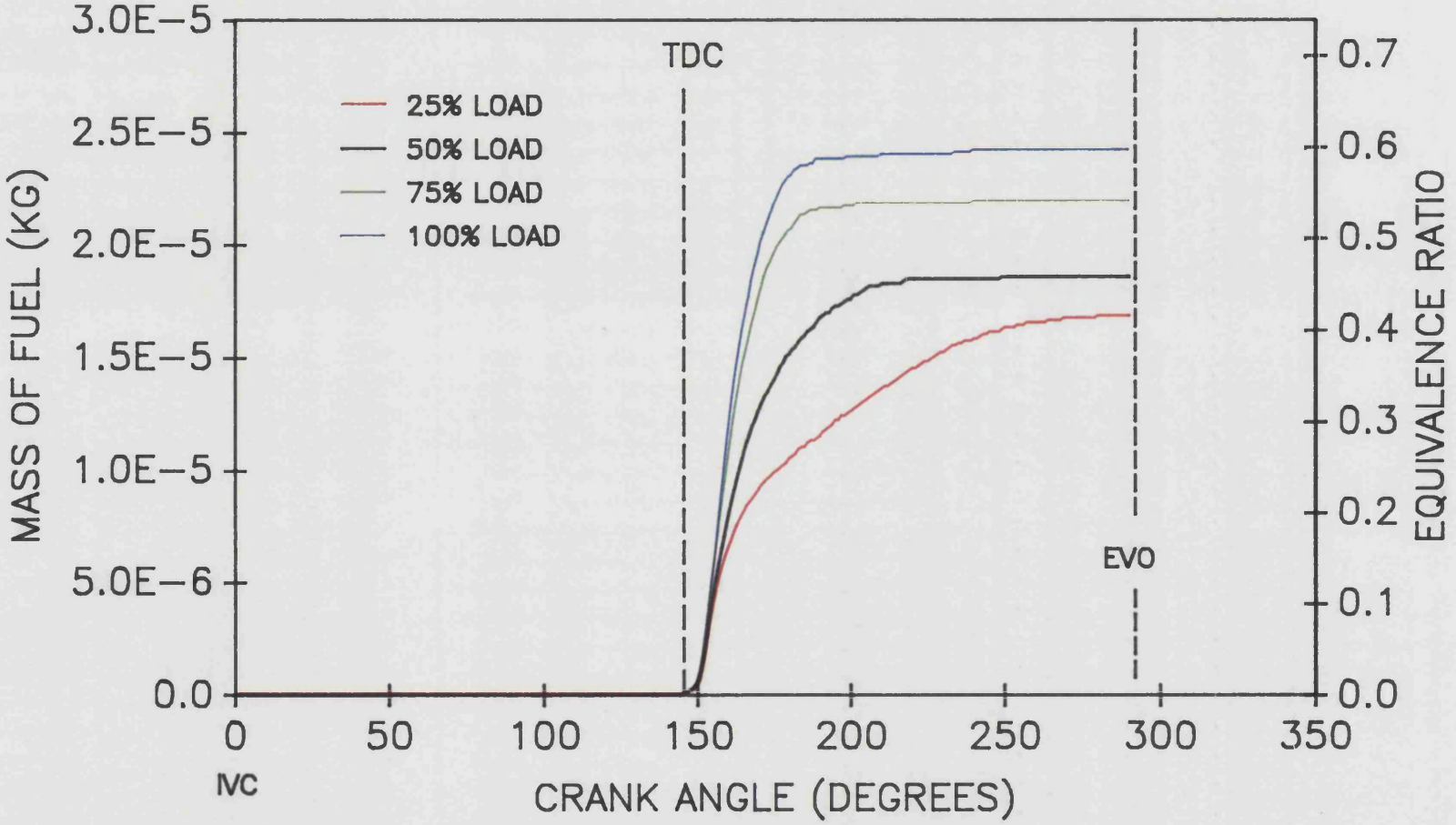

FIGURE 6.43
COMPUTED EQUIVALENCE RATIO & MASS OF FUEL
VS. CRANK ANGLE FOR A STANDARD ENGINE OPERATING
AT 1400 REV/MIN.

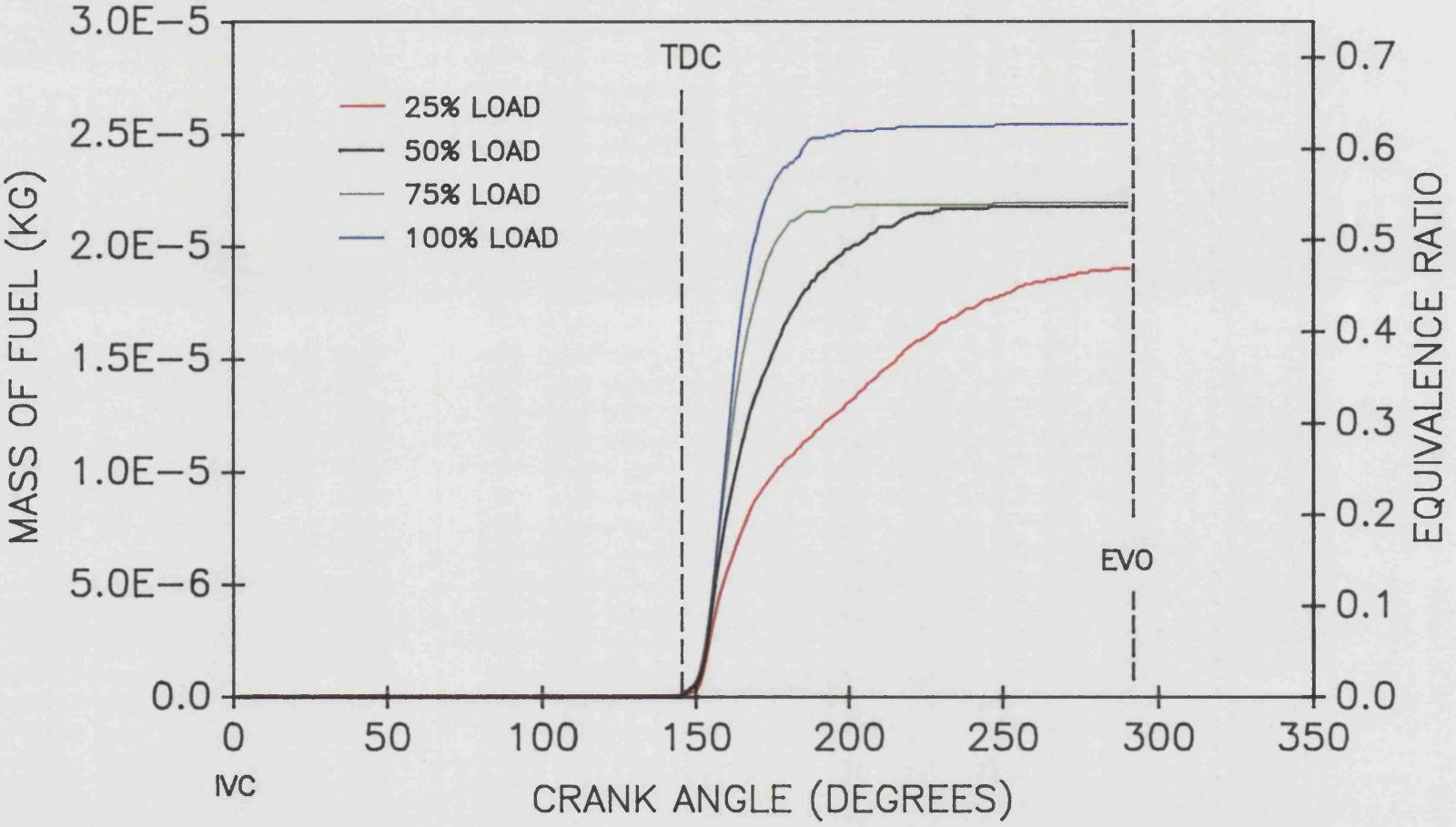

FIGURE 6.44
COMPUTED EQUIVALENCE RATIO & MASS OF FUEL
VS. CRANK ANGLE FOR A STANDARD ENGINE OPERATING
AT 1500 REV/MIN .

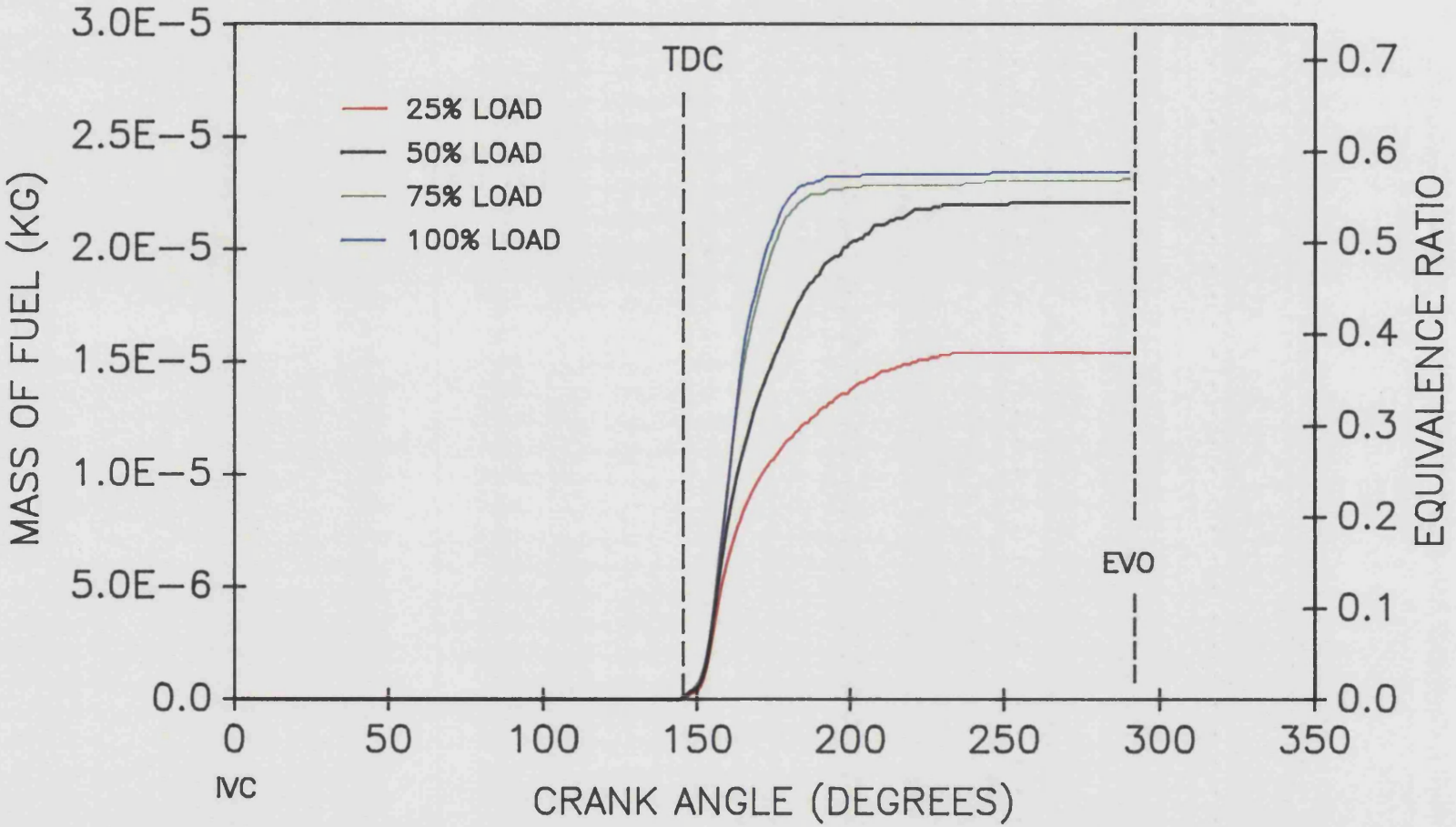

CHAPTER 7
CONCLUSIONS

7.1 General Conclusions

The overall result of this research was that both candidate materials, namely Cordierite and LAS, proved unsatisfactory for their intended application. The two materials were originally chosen for their reasonable strength, and their low densities, conductivities and expansion coefficients. However, cracking caused by either surface damage or internal flaws resulted in these materials exhibiting considerably lower failure strengths than expected. For either LAS or Cordierite to be successful as future engine component materials, the process by which they are formed has to be developed to a level where their full strength can be realised without impurities or imperfect machining having a detrimental effect on their physical properties.

The optimum method of attaching the ceramic monoliths to the aluminium piston bodies, was found to be the "glueline" method, described in section 2.4.4 of chapter 2. The adhesive used was "Aremco-Bond 568" which was made by Aremco U.S.A.

The contribution of the simulation rig to the research was considered not to have been as beneficial as initially expected. It was originally thought that a ceramic piston assembly surviving sixty hours at every possible load condition in this rig would run satisfactorily in the firing engine. This theory was proved wrong when the very first unit failed catastrophically in the firing rig after only 30 minutes running time.

At this stage it became clear that ceramic failures were occurring because of thermal rather than mechanical loading. To overcome this problem, the engine injection timing was severely retarded from an original 18° BTDC to only 7.5° BTDC, and cracking pressure reduced from 3000 psi to 1800 psi.

Although the Petter engine ran with a Cordierite cap, there was much doubt about the

insulated Ford four cylinder unit running at all. The four fold increase in the number of caps, coupled with the much faster engine speed and the possibility of high stress concentration points around the "cloverleaf cut-outs" on the Cordierite caps (see figure 2.37 of chapter 2) increased the chance of catastrophic failure enormously.

7.2 The Effect of Selective Insulation on Performance

The expected result of engine insulation is an increase in exhaust temperature and enthalpy. This is confirmed by exhaust temperature increases of up to 100°C for a given fuelling. The corresponding energy increases of the order of 0.5KW are, nethertheless, over 15% of the maximum useful power this low BMEP engine can produce.

The difference in power output between the standard and insulated engines is not immediately obvious. Closer inspection, of the results, however, revealed that more fuel was needed by the latter to produce the same power output. This extra quantity of fuel was found to increase with increasing load. At these high output conditions, the loss in thermal efficiency was found to be of the order of two percentage points.

The loss in performance for the insulated engine was attributed to the higher heat loss to coolant at the higher loads and speeds, and to higher exhaust heat rejection at every condition. The loss in volumetric efficiency due to charge heating was also evident.

For the insulated engine, coolant heat loss was found to be greater at high loads and speeds but slightly lower at the other end of the scale. The "break-even" point was found to be at the ½ load condition. This trend, however, was not mirrored by the results obtained from the simulation program ODES.

Although ODES was a useful tool throughout this research, the need to empirically modify the friction and thermal network models led to predictions being less than precise. The program underpredicts friction at the lower fuelling levels and

overpredicts it at the higher fuellings. The results obtained through using ODES, however, were considered to be useful to the overall research.

7.3 The Effect of Selective Insulation on Heat Release

It was unfortunate that recorded pressure data for the insulated engine was substandard. This meant that any information derived from these suspect records could itself be inaccurate. In general, it was noted that heat release for both engine builds followed a diffusion burning characteristic with no premix burning whatsoever.

In the case of the standard engine, it was observed that the ¼ load condition displayed very slow burning throughout the speed range. This was not evident in the insulated engine, but that was attributed to the poor pressure records, rather than to behavioural differences between the two engine builds.

Peak cylinder temperatures for the standard engine were found to increase with increasing load. A different pattern emerged for the insulated engine as speed rather than load was observed to be the determining parameter.

7.4 Recommendations for Further Work

a) As material technology becomes more advanced, the time will come when it will be possible to produce both Cordierite and LAS with consistent mechanical properties. When this happens, their use in monolithic form in diesel engines will be worth pursuing.

b) A useful feature of any future engine test bed would be a dynamically variable fuel injection timing device. It would be advantageous were this device to be controlled by the output of a cylinder pressure transducer, in order that optimum engine running could be achieved to whatever pressure

or temperature limit the ceramic was capable of withstanding.

c) It has been observed that an improvised data acquisition system has its shortcomings. Any new research therefore would require an up to date proprietary system capable of averaging, sampling and storing at least three separate signals.

d) Future work would also have to consider environmental effects much more seriously. Public awareness of global environmental issues and efforts to prevent damaging pollution has led to a plethora of tight emissions legislation worldwide. From the start of this research programme to date, emissions control has progressed from being considered a secondary aspect of diesel engine behaviour to being a major factor in design and development.

References

1) Jackson N.S. and Wotton C.R.N.
"The effects of ceramic thermal insulation on D.I. diesel engine combustion, emissions and heat transfer." Proceedings of the CARE consortium conference; June 1990.

2) Shephard W.J.J. Charlton S.J. Cook G. and Watts M.J.
"The effect on performance of thermal insulation of IDI diesel pre-combustion chamber". Proceedings of the CARE consortium conference; June 1990.

3) Godfrey D.J. and May E.R.W.
"The resistance of silicon nitride ceramics to thermal shock and other hostile environments"; Ceramics in Severe Environments, Ed. Kriegel, W.W. and Palmour III, Hayne; Plenum Press, New York; 1971; p.149.

4) Gibson B.D. and Stone R.B.
"The design and performance of a ceramic piston"; Proc. Conference on non-metallic materials for the Royal Navy, Plymouth; 1975; paper 2.

5) Kamo R. and Bryzik W.
"Adiabatic turbocompound engine performance prediction"; SAE 7800068; 1978.

6) Kamo R. and Bryzik W.
"Ceramics in heat engines"; SAE 790645; 1979.

7) Wallace F.J. Way R.J.B. and Vollmert H.
"Effect of Partial suppression of heat loss to coolant on the high output diesel engine cycle"; SAE 790823; 1979.

8) Wallace F.J. and Way R.J.B.
"Results of matching calculations for turbocharged and compound engines with reduced heat loss"; SAE 790824; 1979.

9) Yoshimitsu T. Toyama K. Sato F. and Yamaguchi H.
"Capabilities of heat insulated diesel engine"; SAE 820431; 1982.

10) Toyama K. Yoshimitsu T. Nishiyama T. Shimauchi T. and Nakagaki T.
"Heat insulated turbocompound engine"; SAE 831345; 1983.

11) Wallace F.J. Kao T.K. Tarabad M. Alexander W.D. and Cole A.C.
"Thermally insulated diesel engines"; Proc. I.MECH.E Vol. 198A No.5; PP.97-105 ; 1984.

12) Woschni G. Spindler W. and Kolesa K.
"Heat insulation of combustion chamber walls. A measure to decrease the fuel consumption of I.C. Engines ?"; SAE 870339; 1987.

13) Woschni G. and Spindler W.
"Heat transfer with insulated combustion chamber walls and its influence on the performance of diesel engines"; ASME Journal of Engineering for gas turbines and power; Vol.110; p.482-502 ; July 1988.

14) Morel T. Wahiduzzaman S. and Fort F.
"Heat transfer experiments in an insulated diesel"; SAE 880186; 1988.

15) Churchill R.A. Smith J.E. Clark N.N. and Turton R.A.
"Low heat rejection engines - A concept review"; SAE 880014; 1988.

16) Wilson M.
"Finite element analysis of a ceramic piston cap" ; University of Bath; 1988.

17) Wilson M.
"Finite element analysis of piston shrink-fit attachment to a ceramic piston cap."; University of Bath; 1989.

18) Alexander W.D.
"The design and evaluation of components for low heat loss diesel engines."; PhD. Thesis, University of Bath; 1989.

19) Cole A.C.
"Diesel engine thermal insulation"; PhD. Thesis, University of Bath; 1986.

20) Barker D.J.
"Nicol 46 - A package designed to interface the Nicolet 3091 digital storage scope to the BBC computer"; Bath University; 1983.

21) Heywood J.B.
"Internal combustion engine fundamentals"; McGraw-Hill book company ISBN 0-07-028637x ; 1988.

22) Woschni G.
"A universally applicable equation for the instantaneous heat transfer coefficient in the internal combustion engine."; SAE 670931; 1967.

23) Chen C.
"Otto diesel engine simulation (ODES) comprehensive general purpose program"; Bath University ; 1987.

24) Kao T.K.
"Prediction of heat flow,temperature and stress in diesel engine pistons incorporating thermal barrier pistons"; PhD. Thesis University of Bath ; 1983.

25) Kao T.K.
"Prediction of heat flow and temperature distribution in adiabatic engine components"; MSc. Thesis University of Bath ; 1981.

26) Rentsch R.
"Kleine studienarbeit"; University of Bath ; 1987.

27) Kassens I.
"Design of a glass-ceramic piston cap for a low heat loss engine"; University of Bath ; 1988.

28) Pilkington PLC. internal report
"CARE progress report for meeting at Bath University" ; 25 May 1988.

29) Manton S.M.
"Assesment of ceramic materials for thermally insulated reciprocating engines"; PhD. Thesis University of Bath ; 1986.

30) Shams O.M.A.
"Performance studies on a Petter PH1W direct injection diesel engine using a thermal barrier piston " ; MSc. Thesiss University of Bath ; 1985.

31) Moffat R.J.
"Gas temperature measurement " ; Temperature, its measurement and control in science and industry, Rienhold ; 1962.

32) Caton J.A.
"Comparisons of thermocouple, time averaged and mass averaged exhaust temperatures for a spark ignition engine." ; SAE 820050 ; 1982.

33) Lancaster J.K., Kreiger R.B. and Lienesch J.H.
"measurements and analysis of engine pressure data " ; SAE 750026 ; 1975.

34) Barker D.J., Prest P.H. and Packer J.
"High speed control and data acquisition system for a novel combustion rig " ; Eng. software 3, Proc. of third international conference, PP 666-678 ; April 1983.

35) Alkidas A.C.
"On the performance and emissions of an uncooled heavy-duty single-cylinder diesel engine " ; SAE 880013 ; 1988.

36) Rasihhan Y.
"Further developments in performance prediction techniques of adiabatic diesel engines " ; PhD. Thesis University of Bath ; 1990.

37) Tarabad M.
"Cycle simulation program CSP manual" ; University of Bath ; 1983.

38) Annand W.J.
"Heat transfer in the cylinders of reciprocating engines " ; Proc. I.Mech.E. Vol 177 No. 36 ; 1963.

39) Chen S.K. and Flynn P.F.
"Development of a single cylinder compression ignition research engine " ; SAE 650733 ; 1965

40) Watson N. and Kamel M.
"Thermodynamic efficiency evaluation of an indirect injection diesel engine " ; SAE 790039 ; 1979.

41) Kort R.T., Mansouri S.H., Heywood J.B. and Ekchian J.A.
"Divided chamber diesel engine, part II : Experimental validation of a predictive cycle simulation and heat release analysis " ; SAE 820274 ; 1982.

42) Hiroyasu H., Yoshimatsu A. and Arai M.
"Mathematical model for predicting the rate of heat release and exhaust emissions in IDI diesel engines " ; Proc. I.Mech.E. C102/82 PP 207-213 ; 1982.

43) Krieger R.B. and Borman G.L.
"The computation of apparent heat release for internal combustion engines " ; ASME 66-WA/DGP-4 ; 1966.

APPENDIX 1

Heat balance figures including the prechamber heat loss component.

FIGURE 4.38 ABSOLUTE HEAT REJECTION TO COOLANT VS. FUEL ENERGY INPUT FOR EXPERIMENTAL AND MATCHED RESULTS (STANDARD ENGINE CONFIGURATION.)

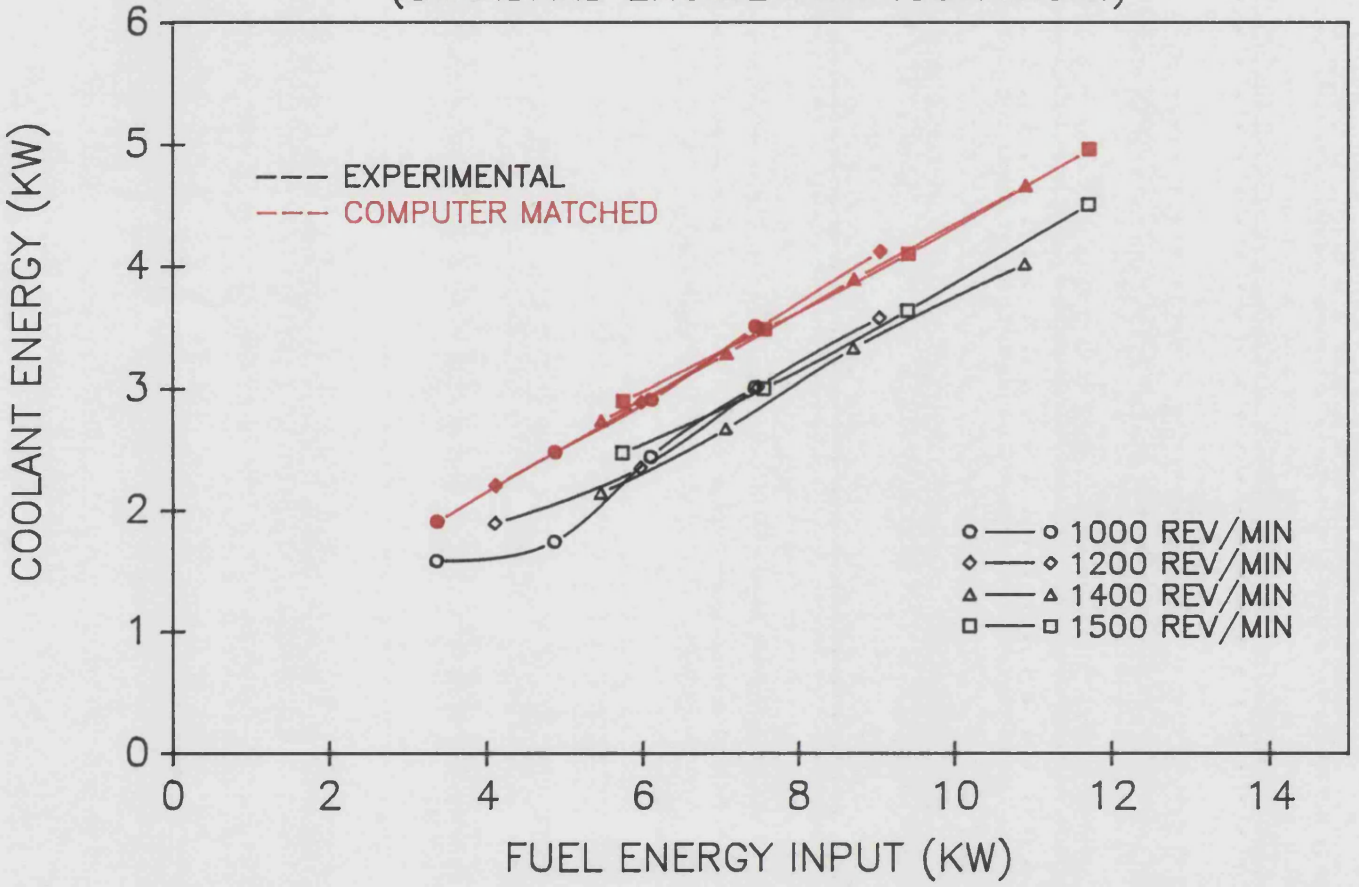

FIGURE 4.39 : PERCENTAGE HEAT REJECTION TO COOLANT VS. FUEL ENERGY INPUT FOR EXPERIMENTAL AND MATCHED RESULTS (STANDARD ENGINE CONFIGURATION.)

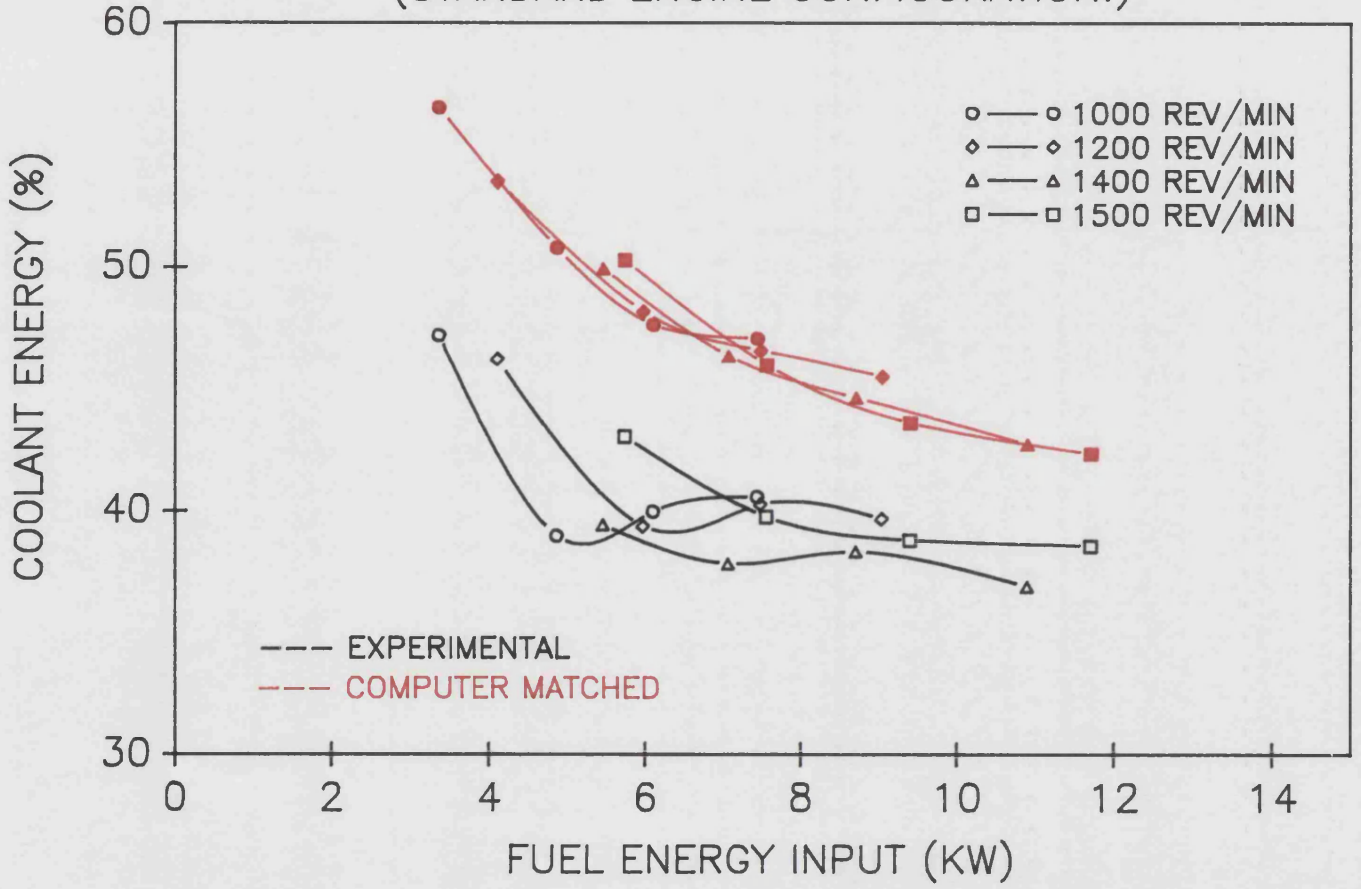

FIGURE 4.44 : ABSOLUTE HEAT REJECTION TO COOLANT VS. FUEL ENERGY INPUT FOR EXPERIMENTAL AND MATCHED RESULTS (INSULATED ENGINE CONFIGURATION.)

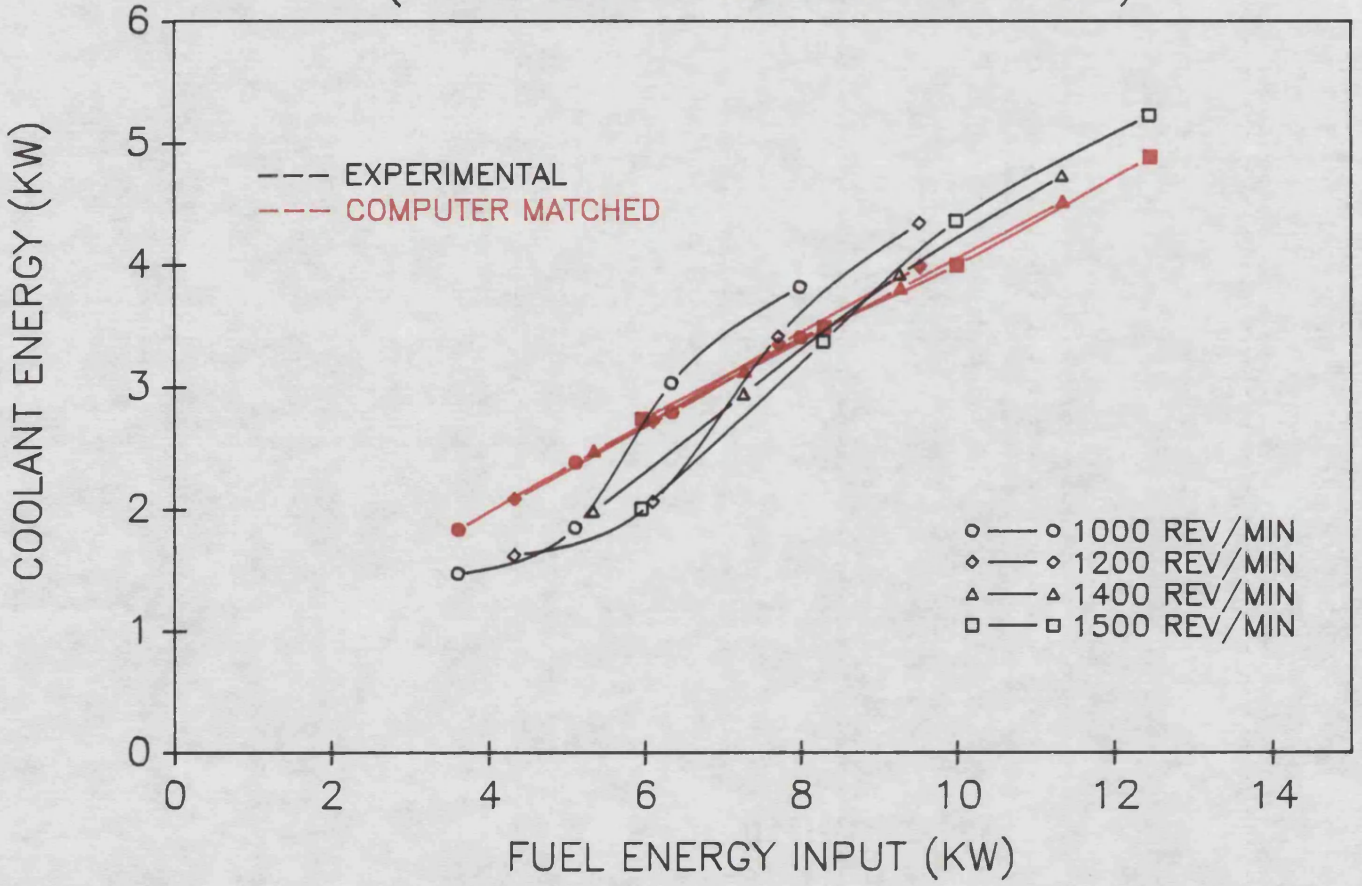

FIGURE 4.45 : PERCENTAGE HEAT REJECTION TO COOLANT VS. FUEL ENERGY INPUT FOR EXPERIMENTAL AND MATCHED RESULTS (INSULATED ENGINE CONFIGURATION.)

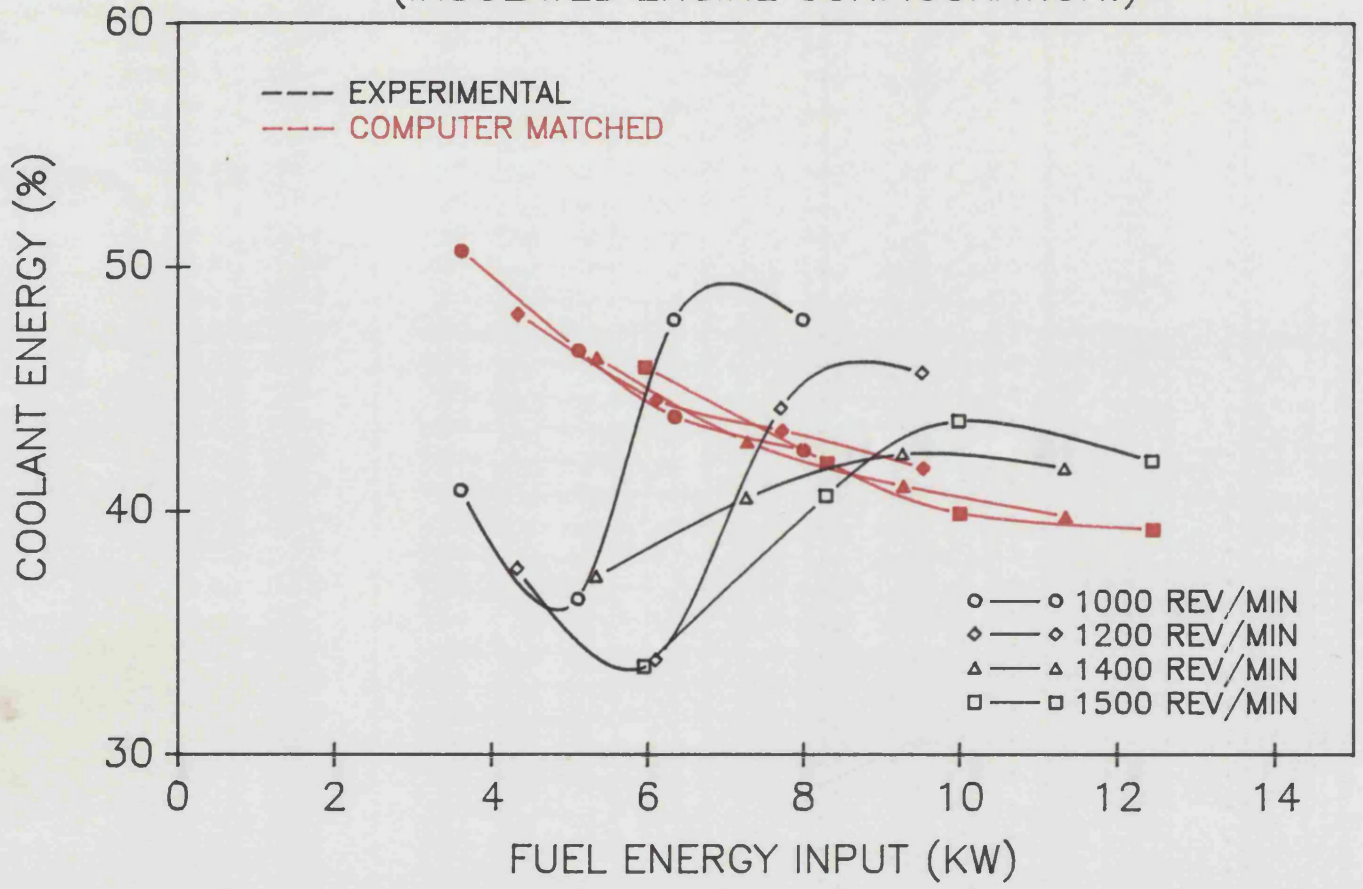

APPENDIX 2

Heat release results for the insulated engine.

FIGURE 6.45
MEASURED PRECHAMBER PRESSURE
VS. CRANK ANGLE FOR AN INSULATED ENGINE OPERATING
AT 1000 REV/MIN.

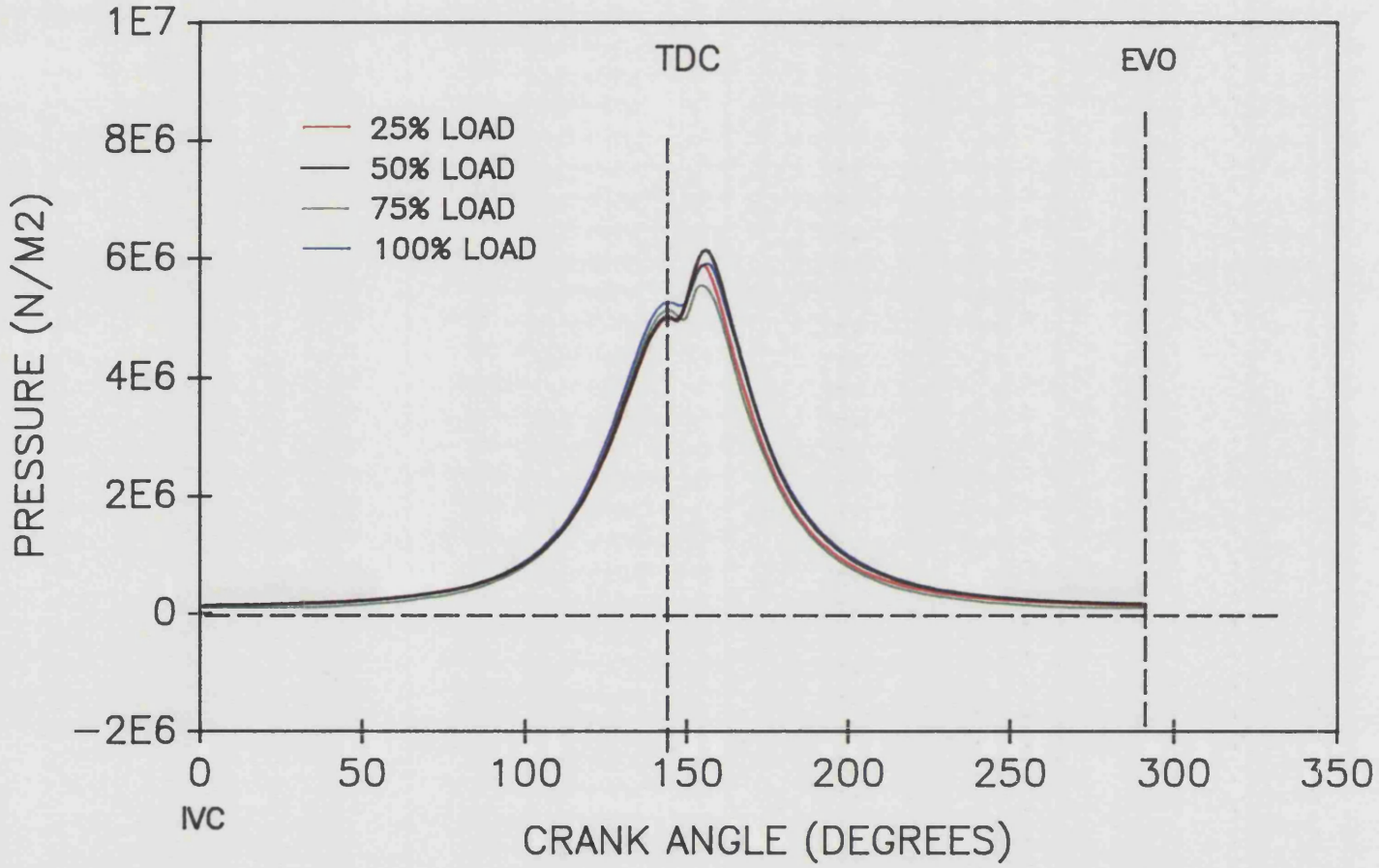

FIGURE 6.46
MEASURED PRECHAMBER PRESSURE
VS. CRANK ANGLE FOR AN INSULATED ENGINE OPERATING
AT 1200 REV/MIN

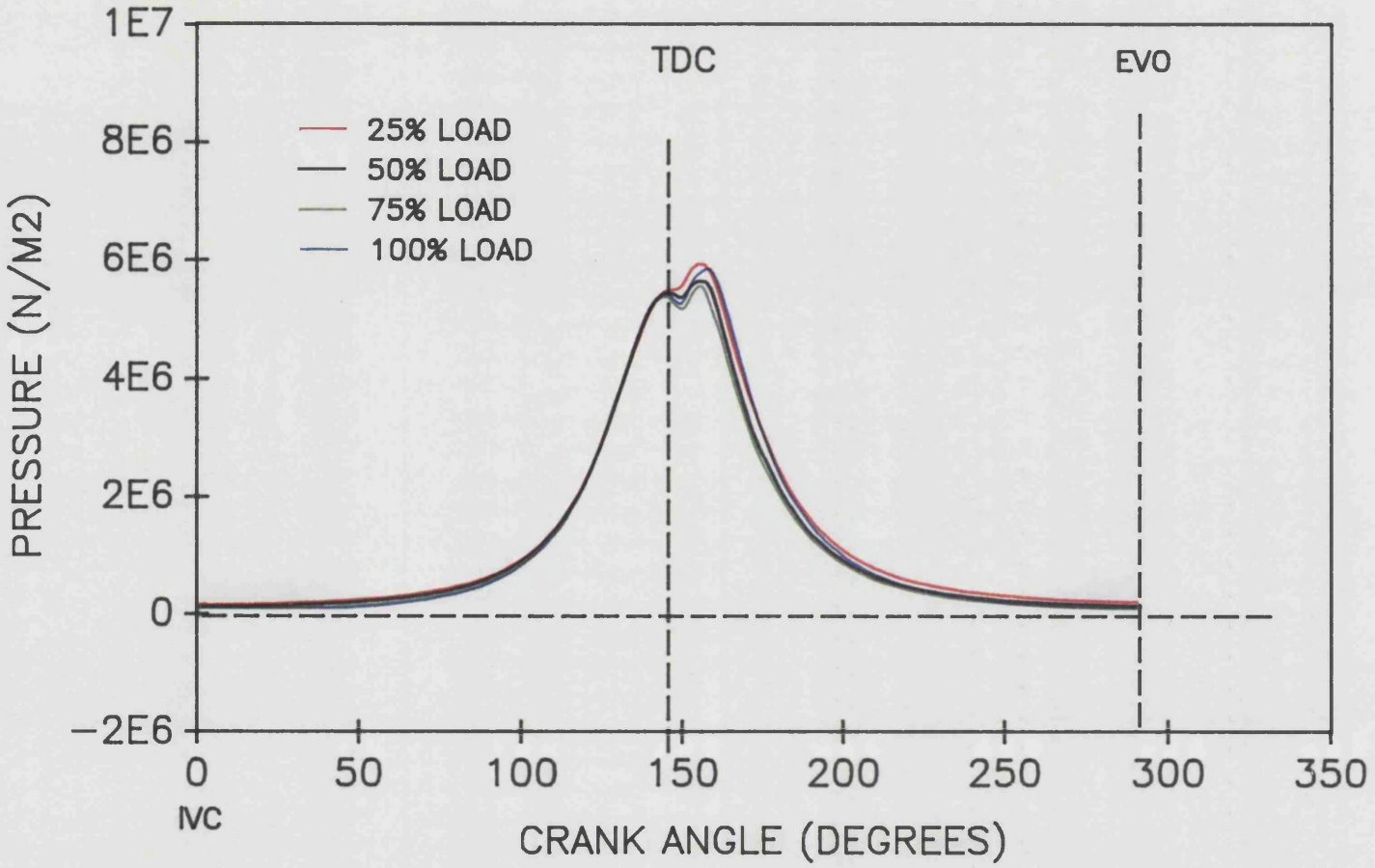

FIGURE 6.47
MEASURED PRECHAMBER PRESSURE
VS. CRANK ANGLE FOR AN INSULATED ENGINE OPERATING
AT 1400 REV/MIN.

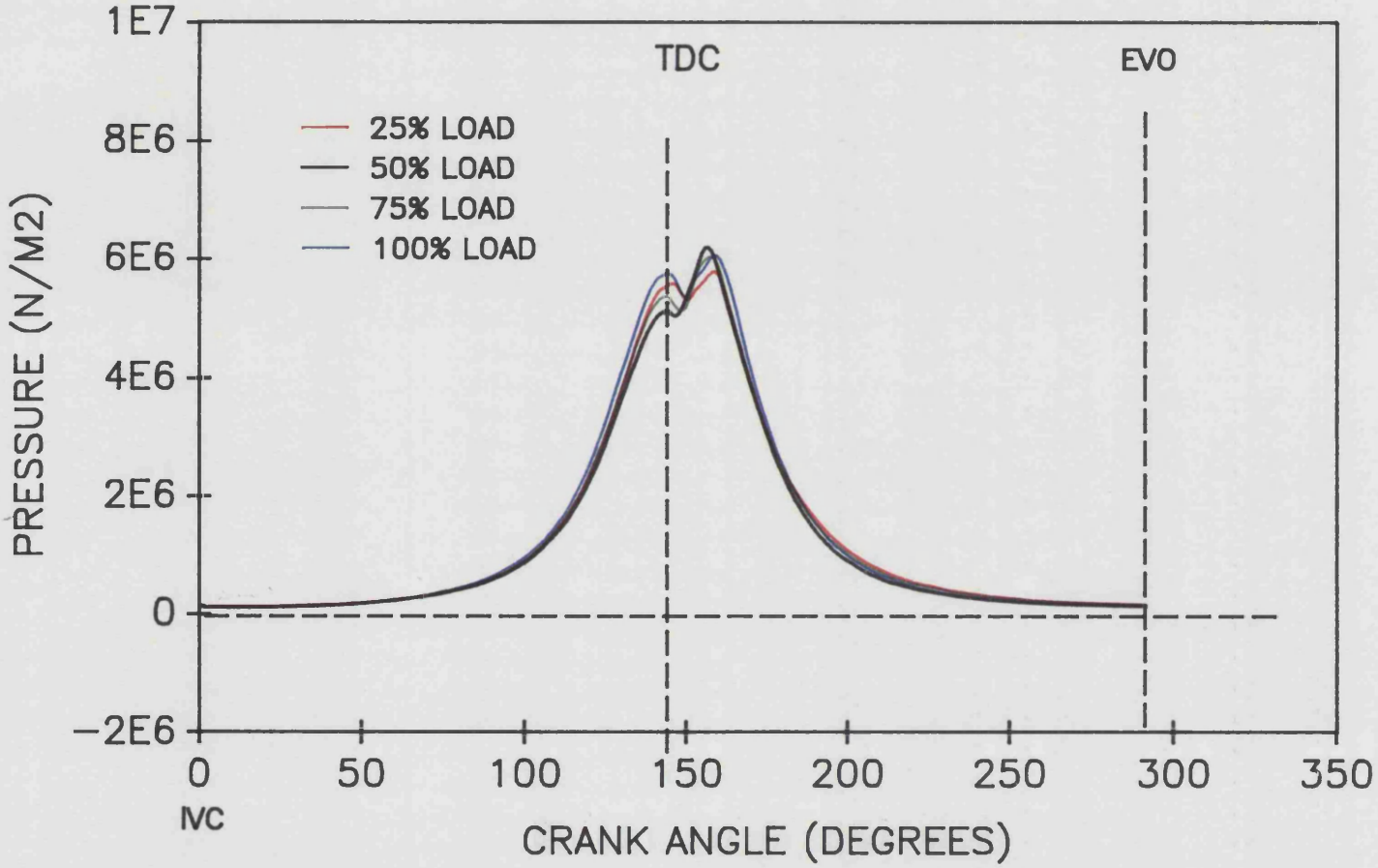

FIGURE 6.48
MEASURED PRECHAMBER PRESSURE
VS. CRANK ANGLE FOR AN INSULATED ENGINE OPERATING
AT 1500 REV/MIN.

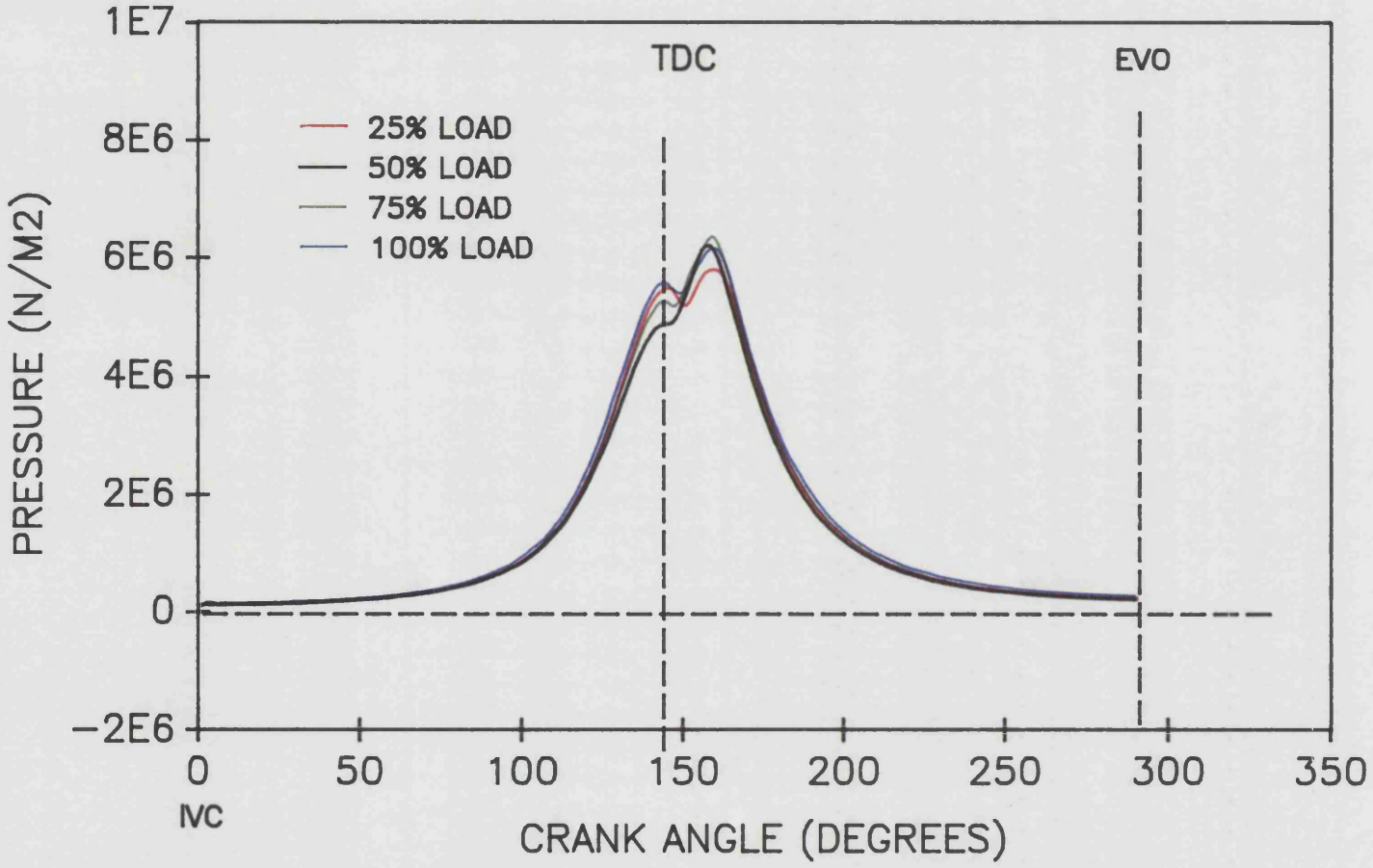

FIGURE 6.49
CALCULATED CYLINDER TEMPERATURE
VS. CRANK ANGLE FOR AN INSULATED ENGINE OPERATING
AT 1000 REV/MIN.

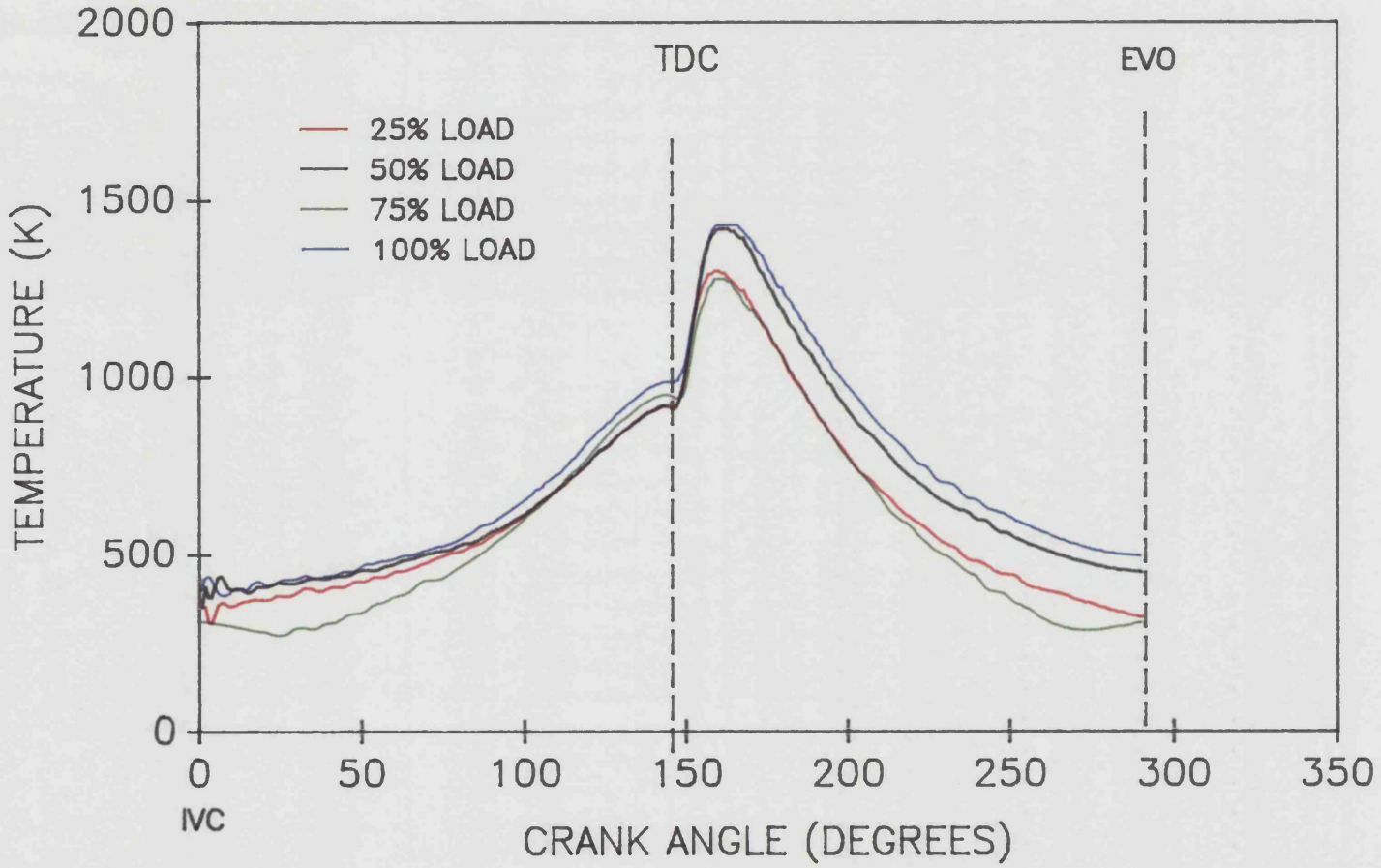

FIGURE 6.50
CALCULATED CYLINDER TEMPERATURE
VS. CRANK ANGLE FOR AN INSULATED ENGINE OPERATING
AT 1200 REV/MIN

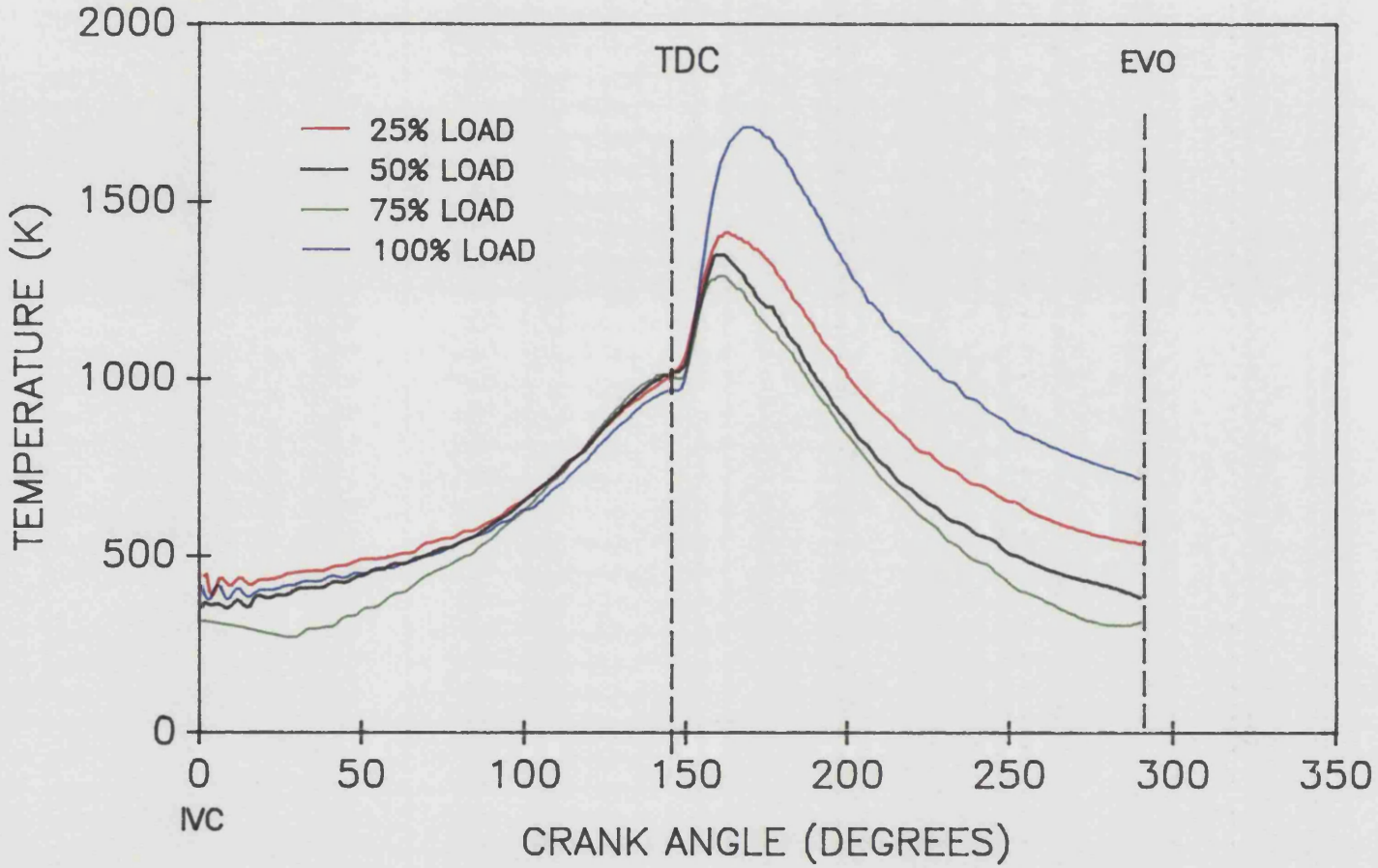

FIGURE 6.51
CALCULATED CYLINDER TEMPERATURE
VS. CRANK ANGLE FOR AN INSULATED ENGINE OPERATING
AT 1400 REV/MIN.

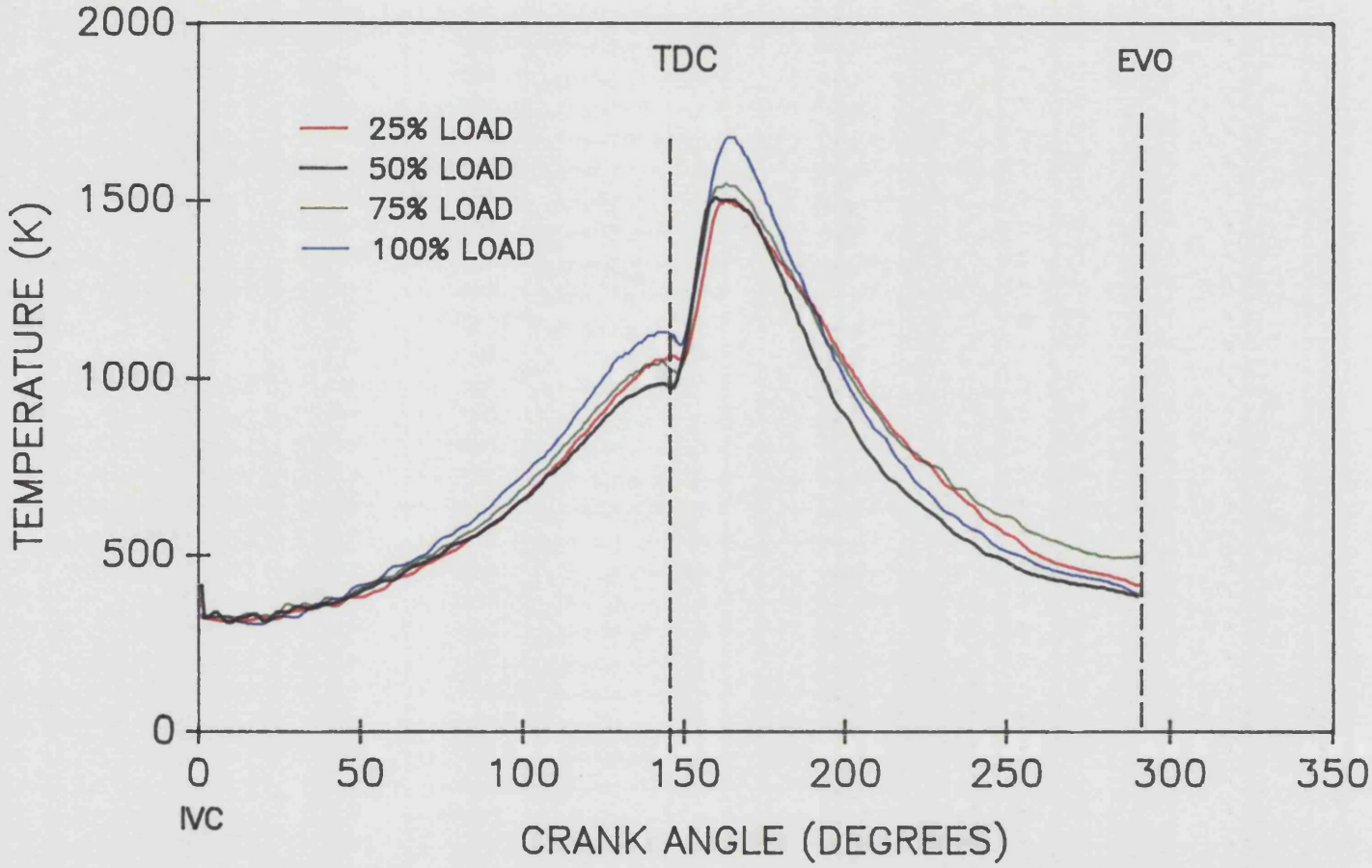

FIGURE 6.52
CALCULATED CYLINDER TEMPERATURE
VS. CRANK ANGLE FOR AN INSULATED ENGINE OPERATING
AT 1500 REV/MIN.

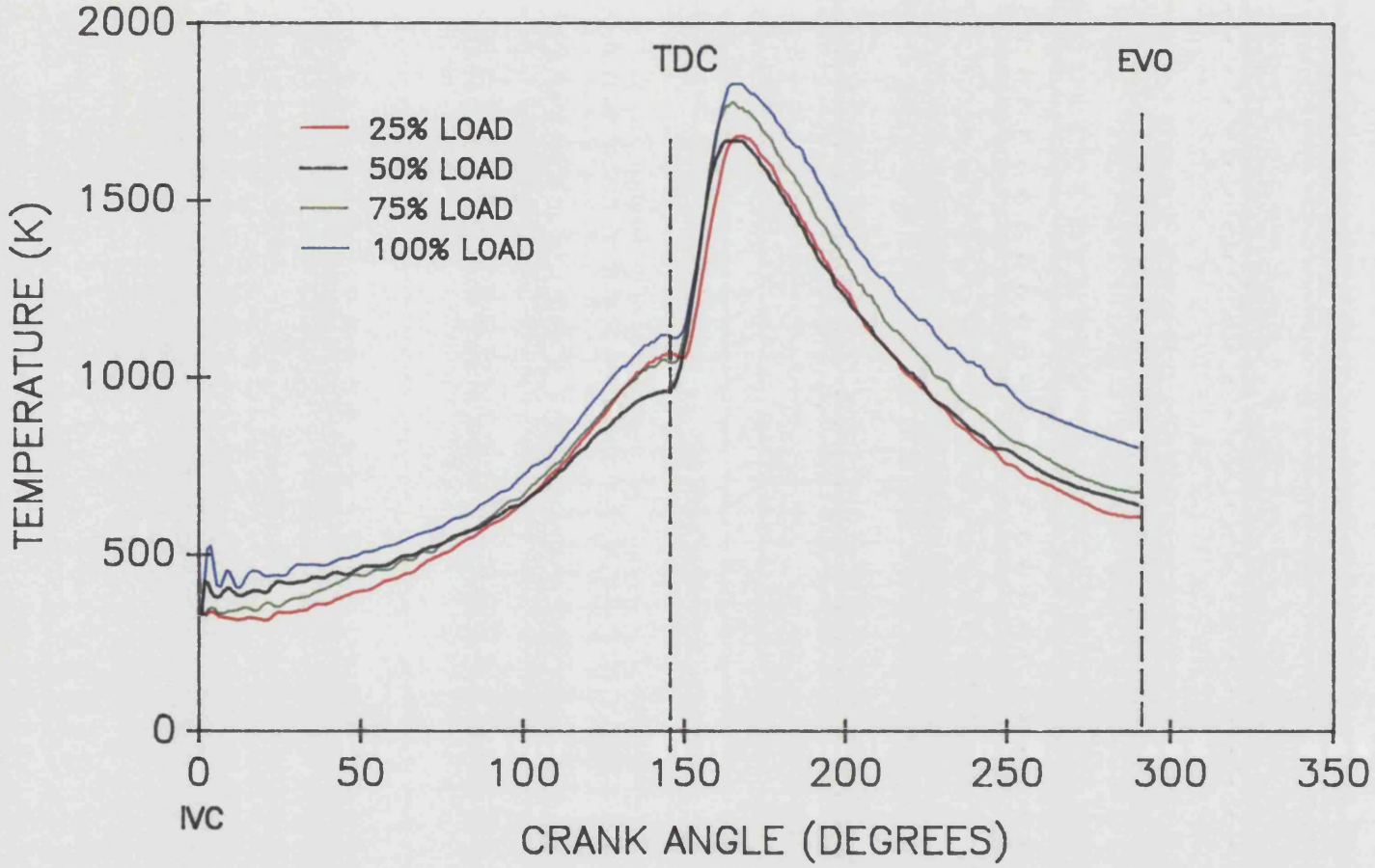

FIGURE 6.53
CUMULATIVE & RATE OF HEAT RELEASE (NETT & FUEL)
VS. CRANK ANGLE FOR AN INSULATED ENGINE OPERATING
AT 1000 REV/MIN 25% LOAD.

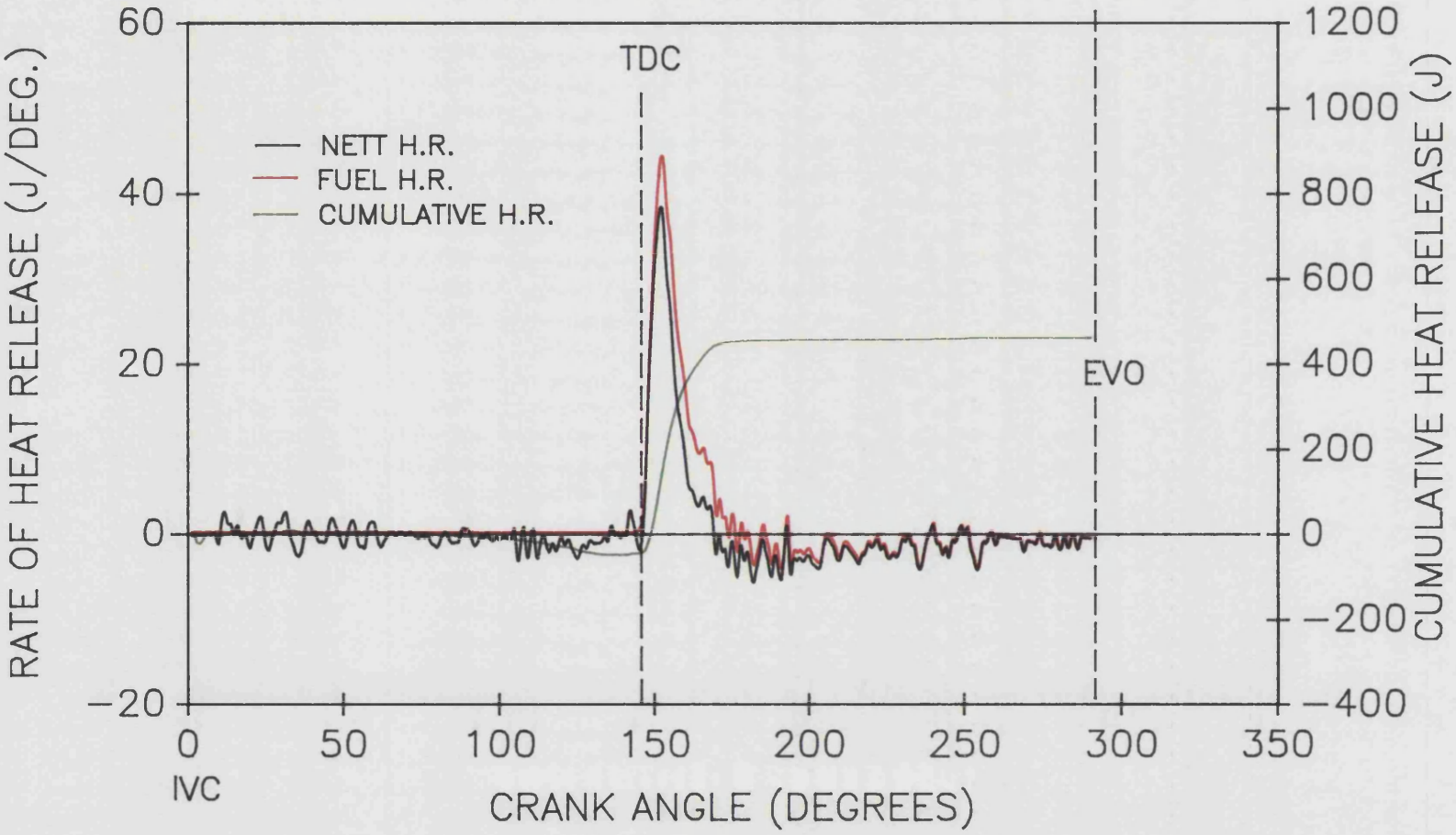

FIGURE 6.54
CUMULATIVE & RATE OF HEAT RELEASE (NETT & FUEL)
VS. CRANK ANGLE FOR AN INSULATED ENGINE OPERATING
AT 1000 REV/MIN 50% LOAD.

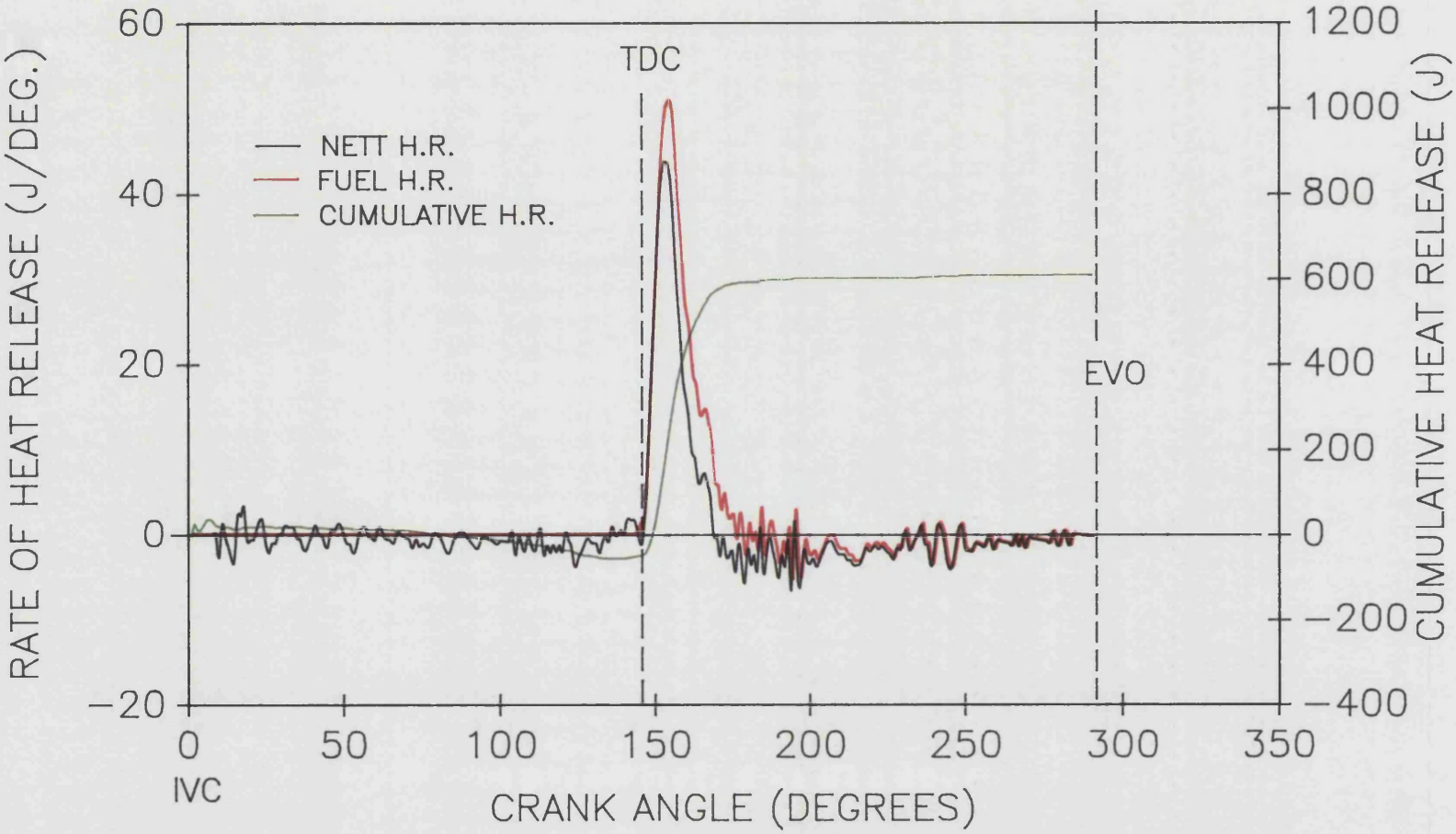

FIGURE 6.55
CUMULATIVE & RATE OF HEAT RELEASE (NETT & FUEL)
VS. CRANK ANGLE FOR AN INSULATED ENGINE OPERATING
AT 1000 REV/MIN 75% LOAD.

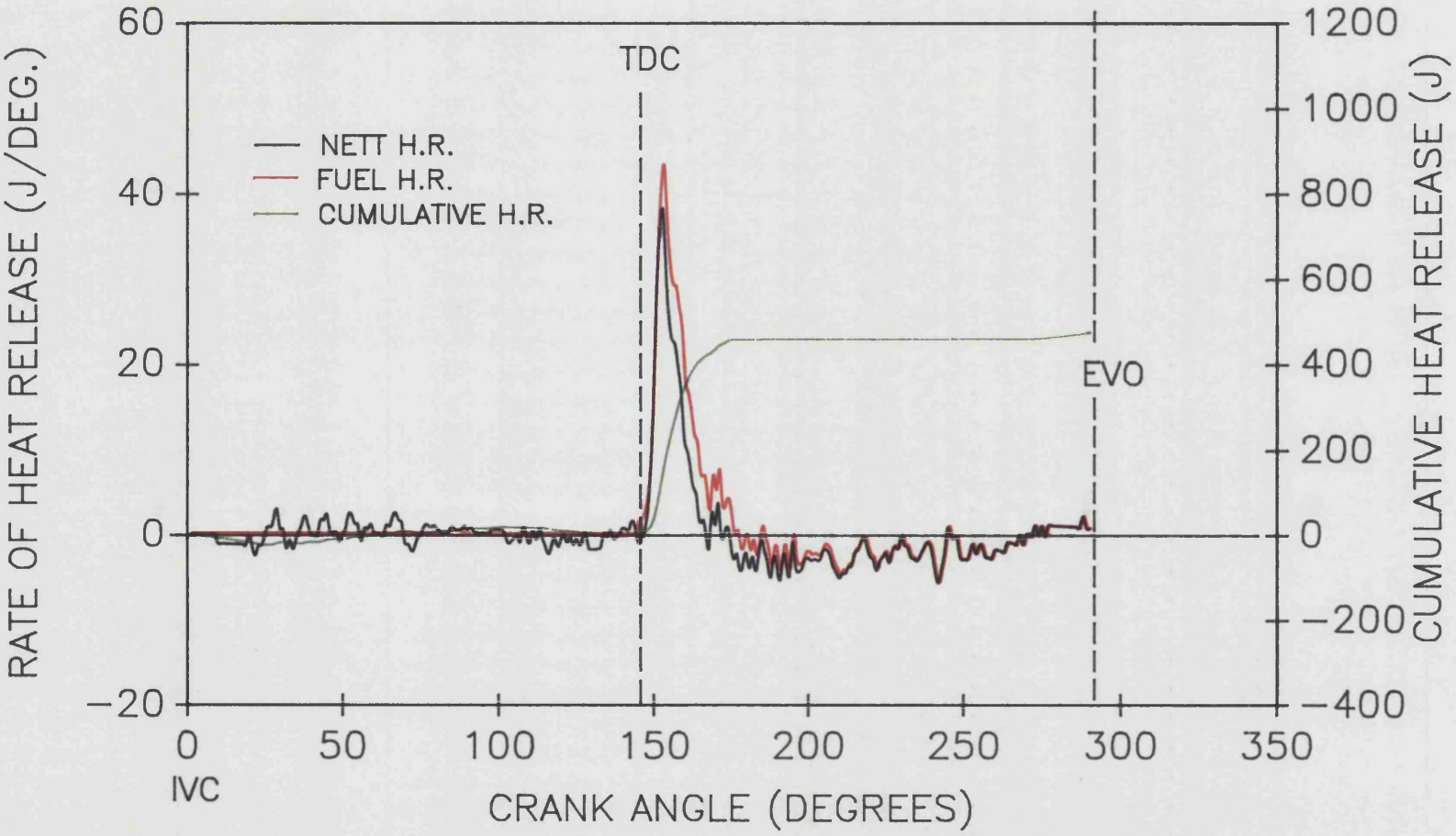

FIGURE 6.56
CUMULATIVE & RATE OF HEAT RELEASE (NETT & FUEL)
VS. CRANK ANGLE FOR AN INSULATED ENGINE OPERATING
AT 1000 REV/MIN FULL LOAD.

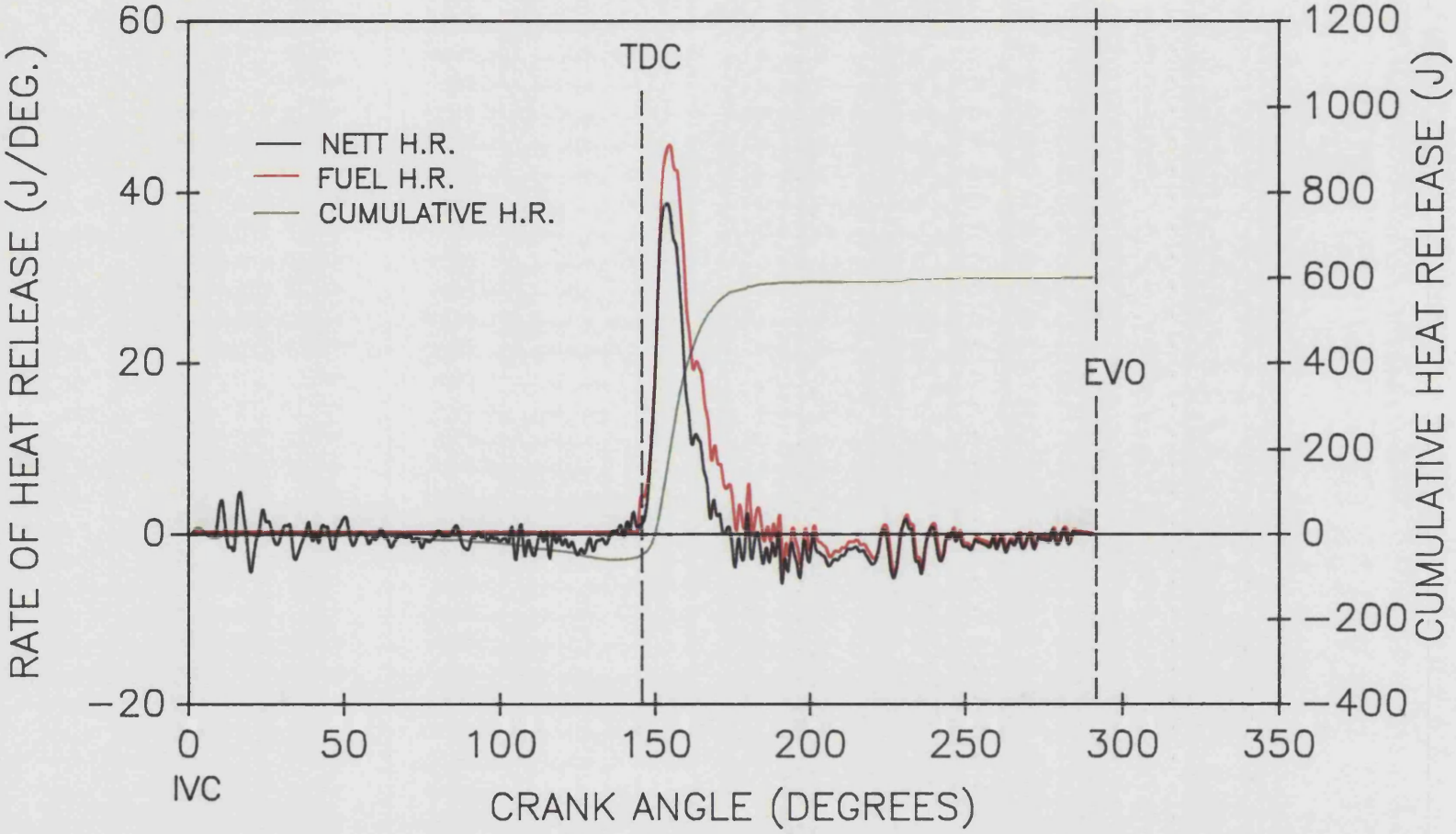

FIGURE 6.57
CUMULATIVE & RATE OF HEAT RELEASE (NETT & FUEL)
VS. CRANK ANGLE FOR AN INSULATED ENGINE OPERATING
AT 1200 REV/MIN 25% LOAD.

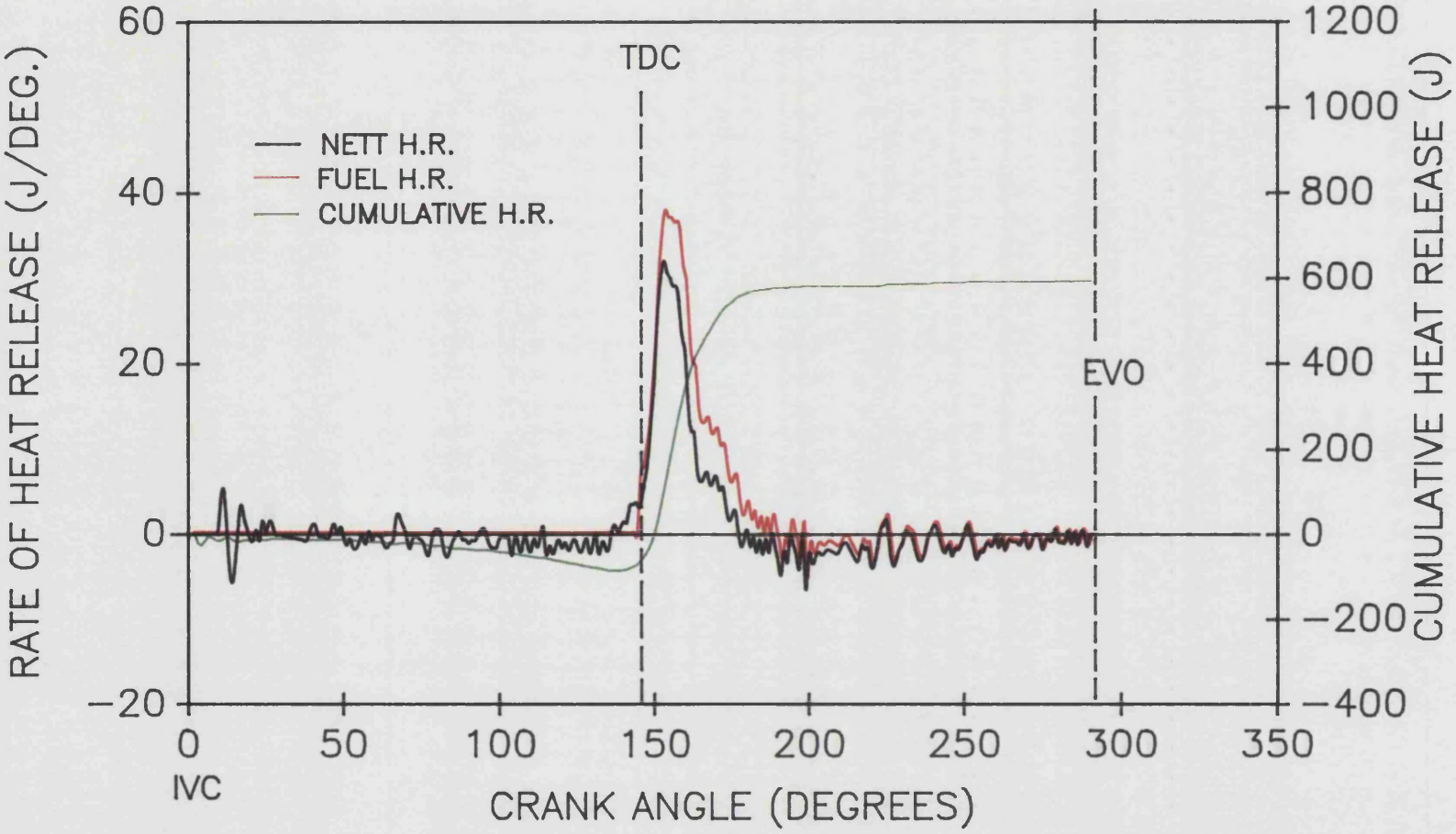

FIGURE 6.58
CUMULATIVE & RATE OF HEAT RELEASE (NETT & FUEL)
VS. CRANK ANGLE FOR AN INSULATED ENGINE OPERATING
AT 1200 REV/MIN 50% LOAD.

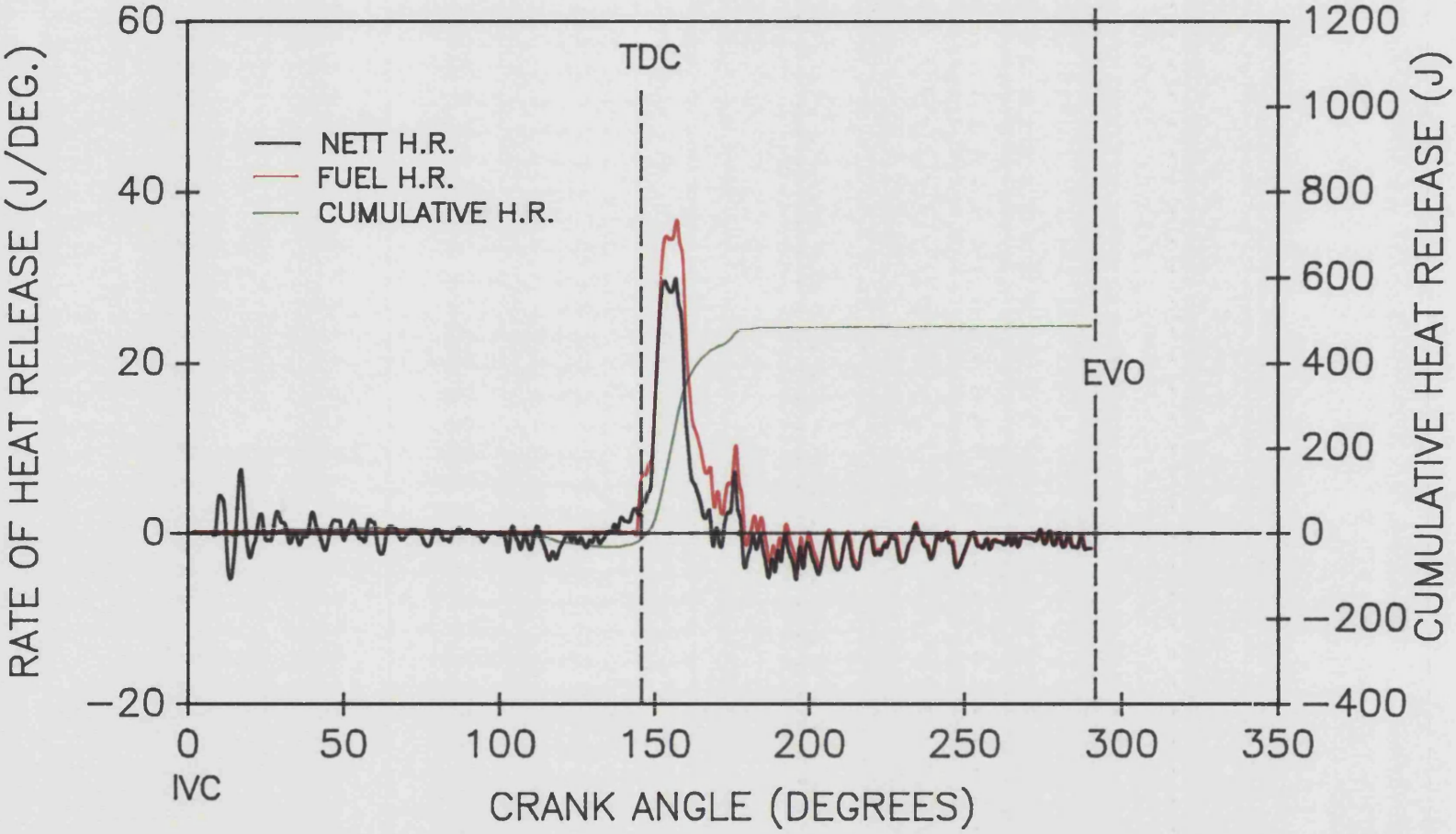

FIGURE 6.59
CUMULATIVE & RATE OF HEAT RELEASE (NETT & FUEL)
VS. CRANK ANGLE FOR AN INSULATED ENGINE OPERATING
AT 1200 REV/MIN 75% LOAD

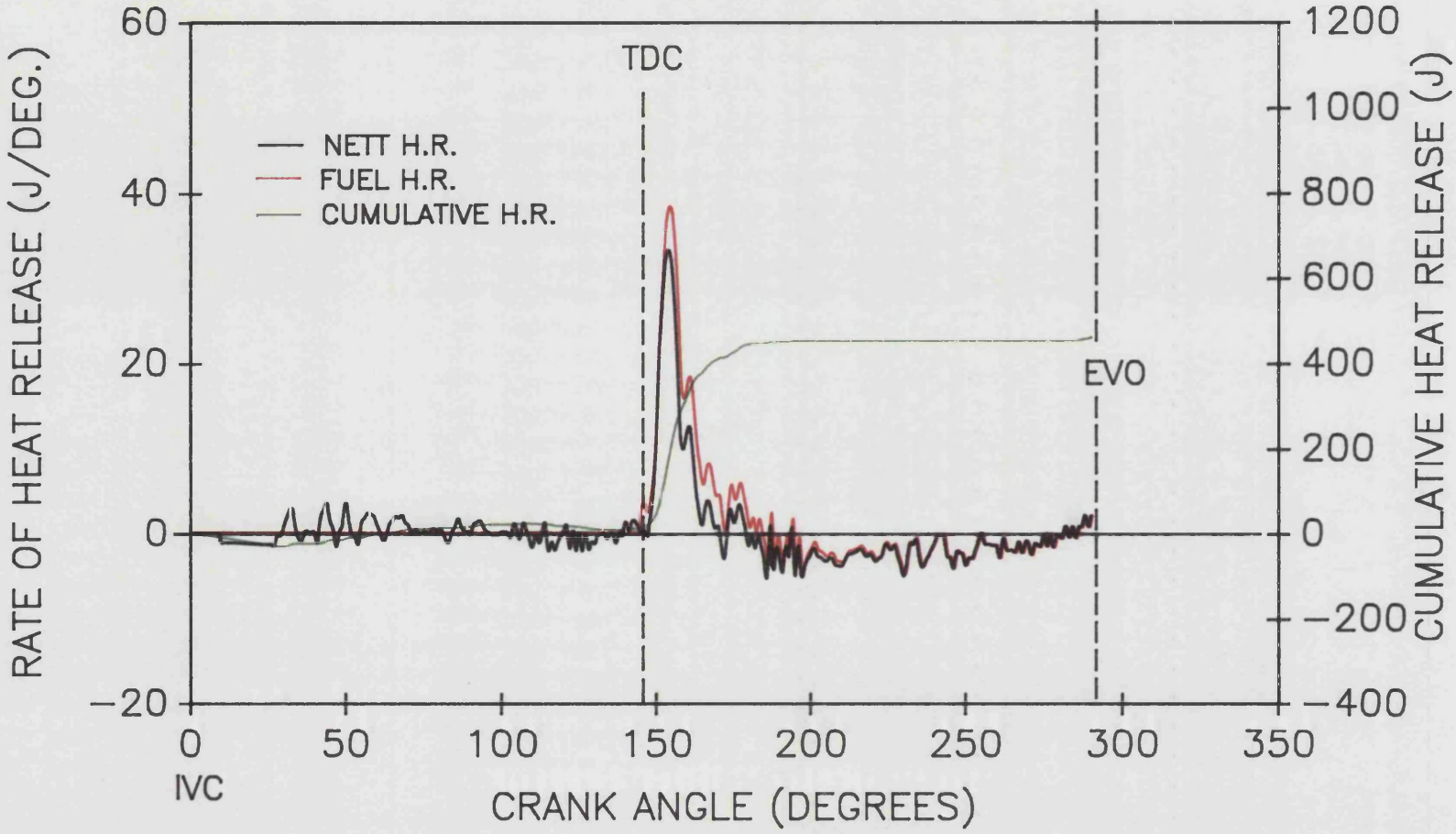

FIGURE 6.60
CUMULATIVE & RATE OF HEAT RELEASE (NETT & FUEL)
VS. CRANK ANGLE FOR AN INSULATED ENGINE OPERATING
AT 1200 REV/MIN FULL LOAD.

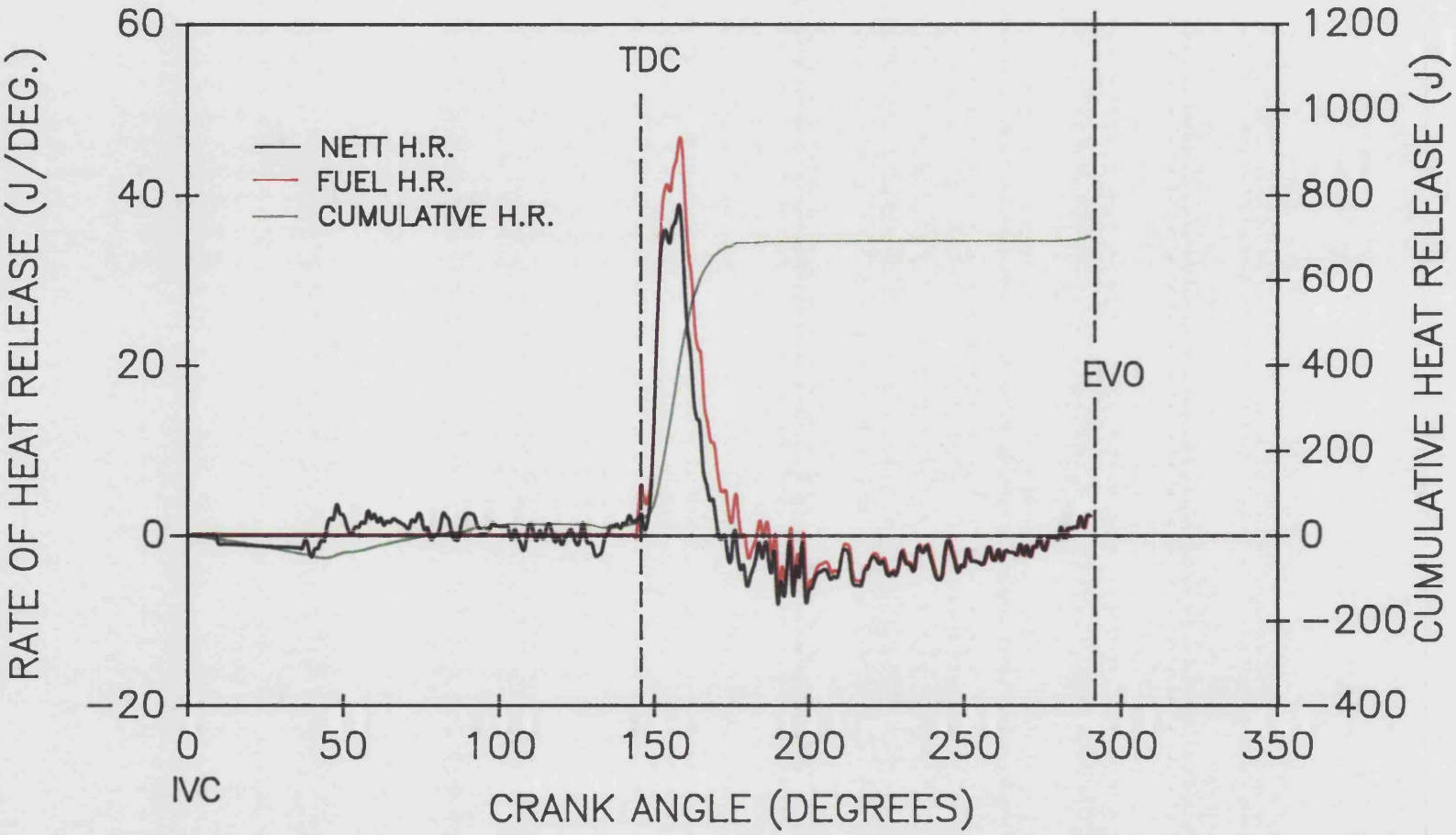

FIGURE 6.61
CUMULATIVE & RATE OF HEAT RELEASE (NETT & FUEL)
VS. CRANK ANGLE FOR AN INSULATED ENGINE OPERATING
AT 1400 REV/MIN 25% LOAD.

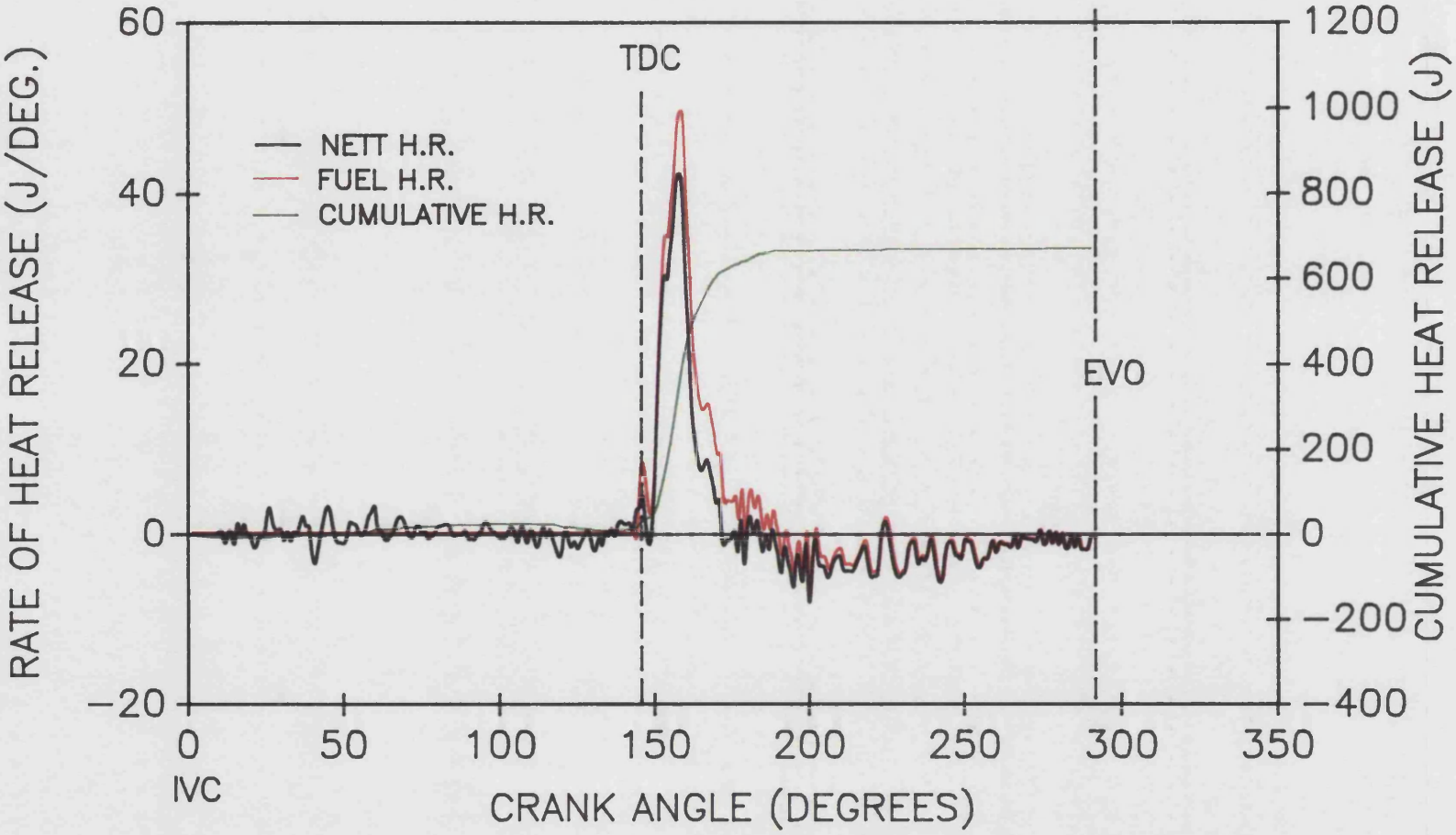

FIGURE 6.62
CUMULATIVE & RATE OF HEAT RELEASE (NETT & FUEL)
VS. CRANK ANGLE FOR AN INSULATED ENGINE OPERATING
AT 1400 REV/MIN 50% LOAD.

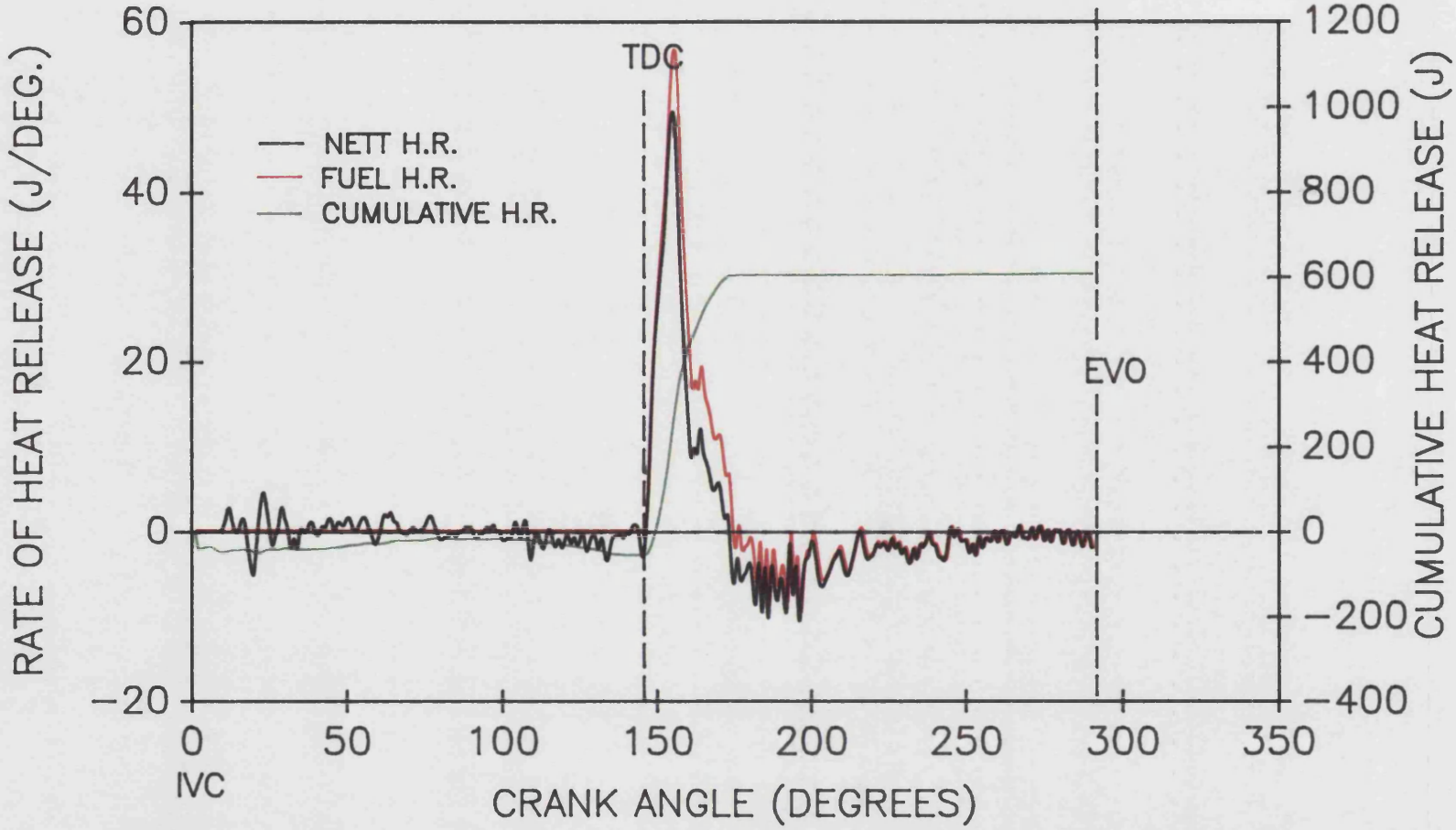

FIGURE 6.63
CUMULATIVE & RATE OF HEAT RELEASE (NETT & FUEL)
VS. CRANK ANGLE FOR AN INSULATED ENGINE OPERATING
AT 1400 REV/MIN 75% LOAD.

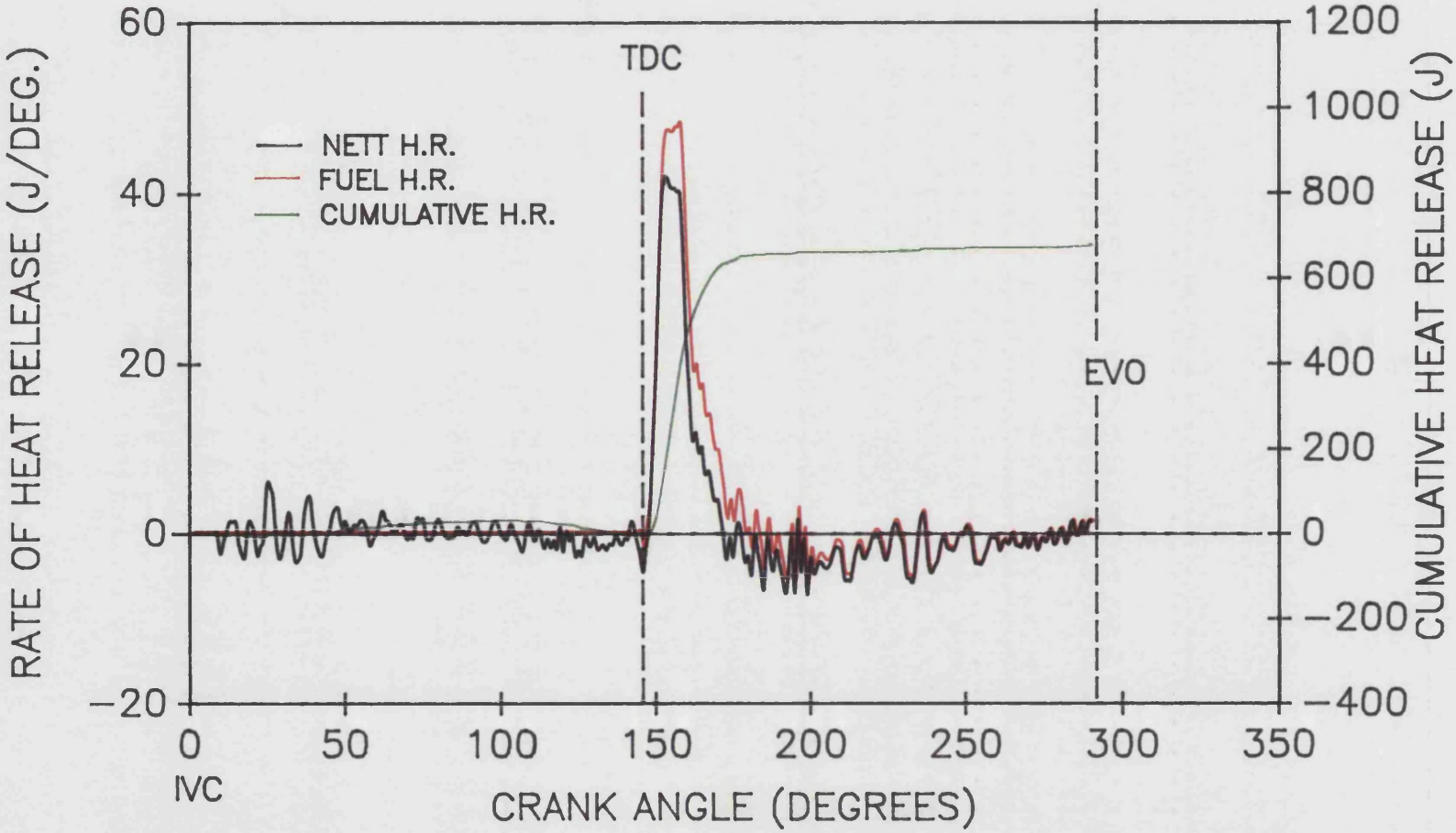

FIGURE 6.64
CUMULATIVE & RATE OF HEAT RELEASE (NETT & FUEL)
VS. CRANK ANGLE FOR AN INSULATED ENGINE OPERATING
AT 1400 REV/MIN FULL LOAD.

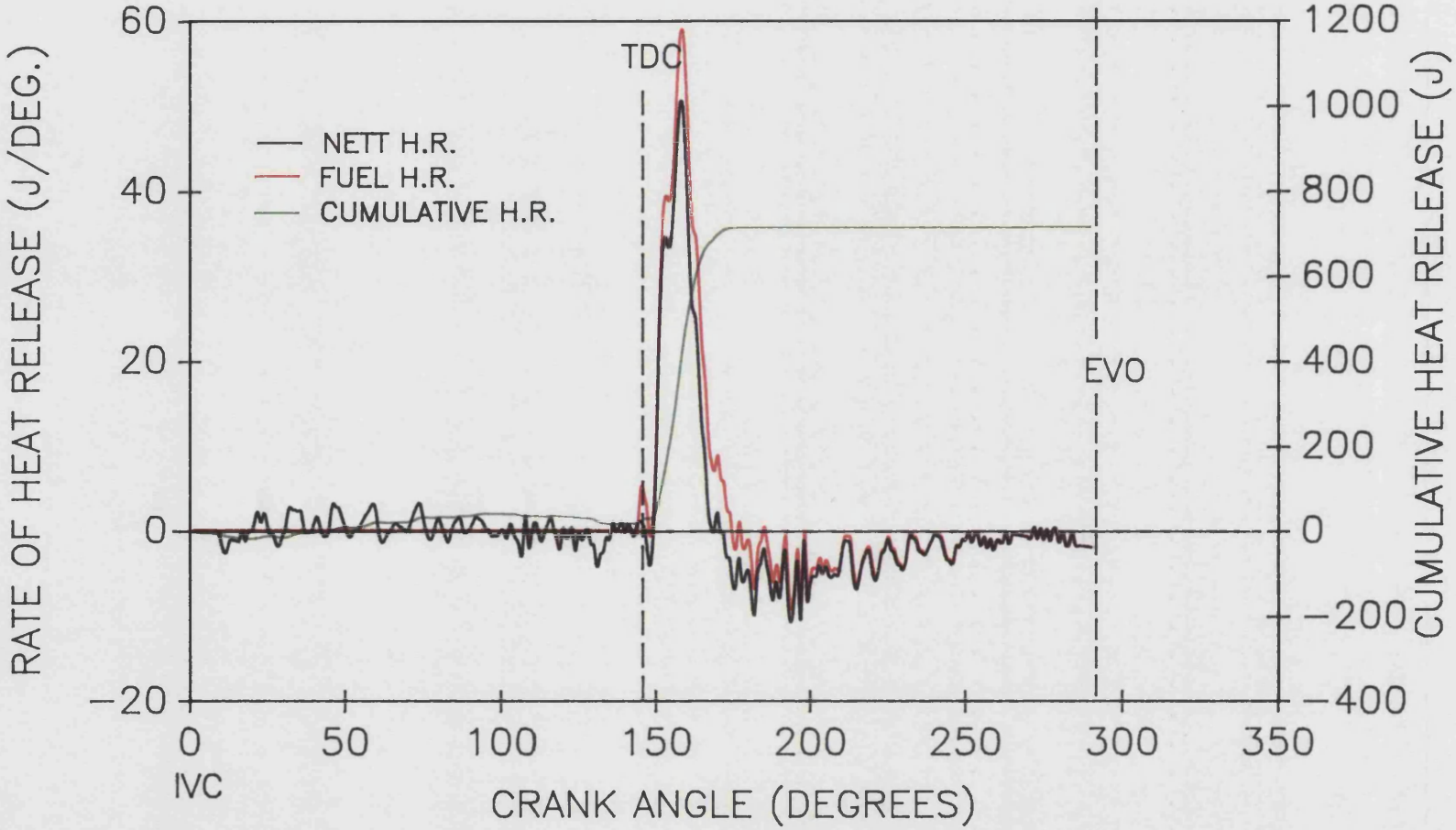

FIGURE 6.65
CUMULATIVE & RATE OF HEAT RELEASE (NETT & FUEL)
VS. CRANK ANGLE FOR AN INSULATED ENGINE OPERATING
AT 1500 REV/MIN 25% LOAD.

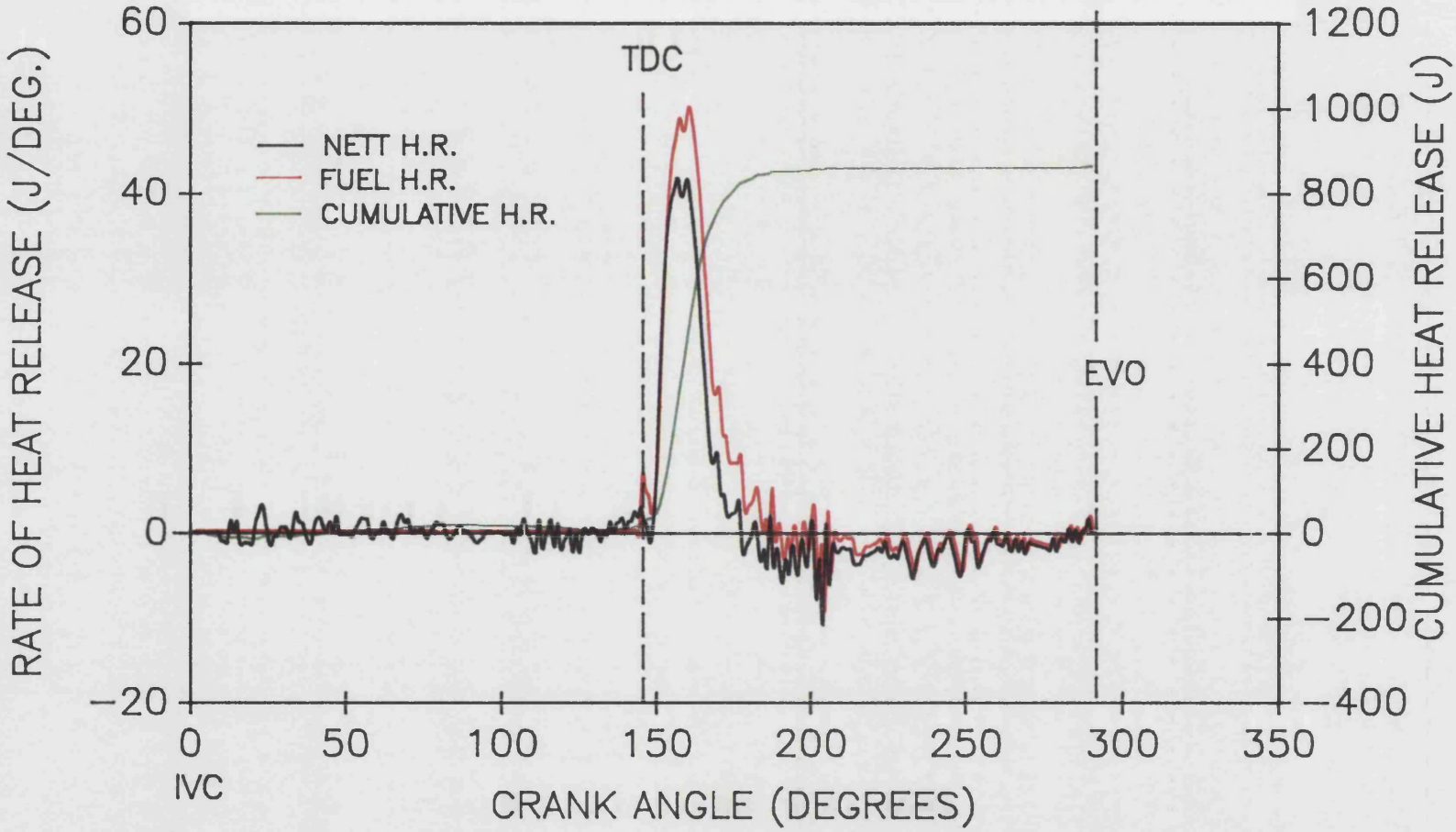

FIGURE 6.66
CUMULATIVE & RATE OF HEAT RELEASE (NETT & FUEL)
VS. CRANK ANGLE FOR AN INSULATED ENGINE OPERATING
AT 1500 REV/MIN 50% LOAD.

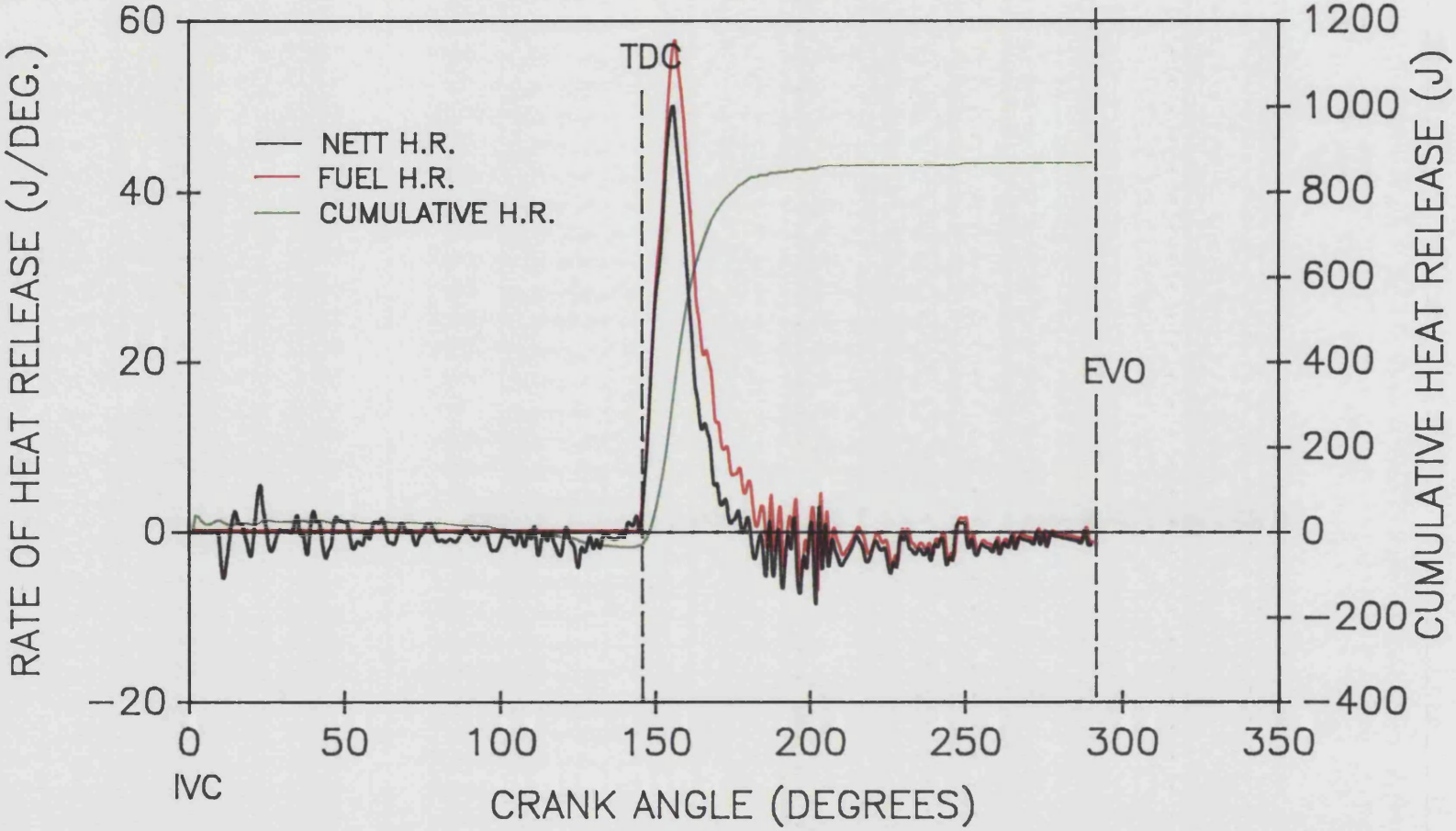

FIGURE 6.67
CUMULATIVE & RATE OF HEAT RELEASE (NETT & FUEL)
VS. CRANK ANGLE FOR AN INSULATED ENGINE OPERATING
AT 1500 REV/MIN 75% LOAD.

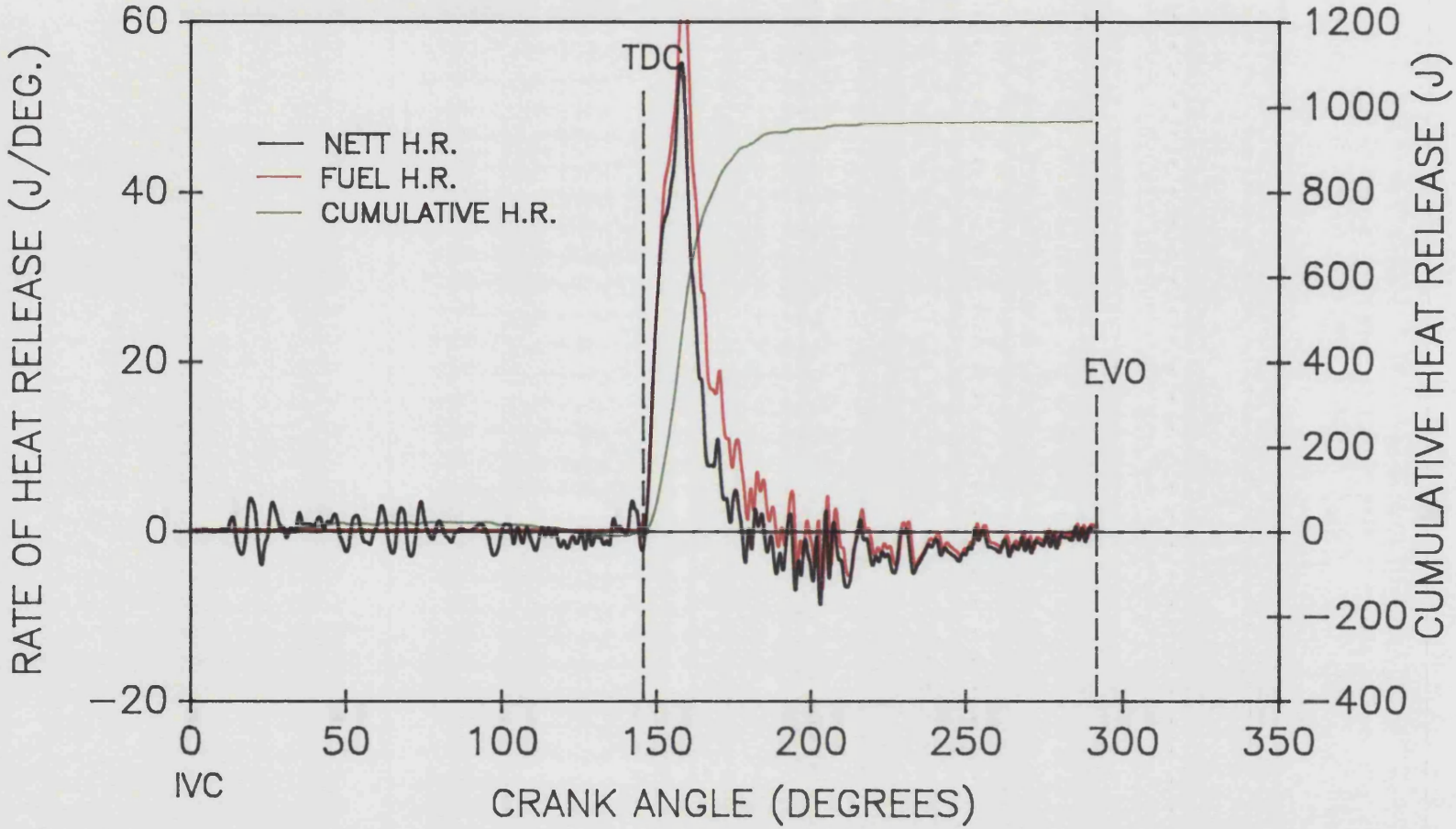

FIGURE 6.68
CUMULATIVE & RATE OF HEAT RELEASE (NETT & FUEL)
VS. CRANK ANGLE FOR AN INSULATED ENGINE OPERATING
AT 1500 REV/MIN FULL LOAD.

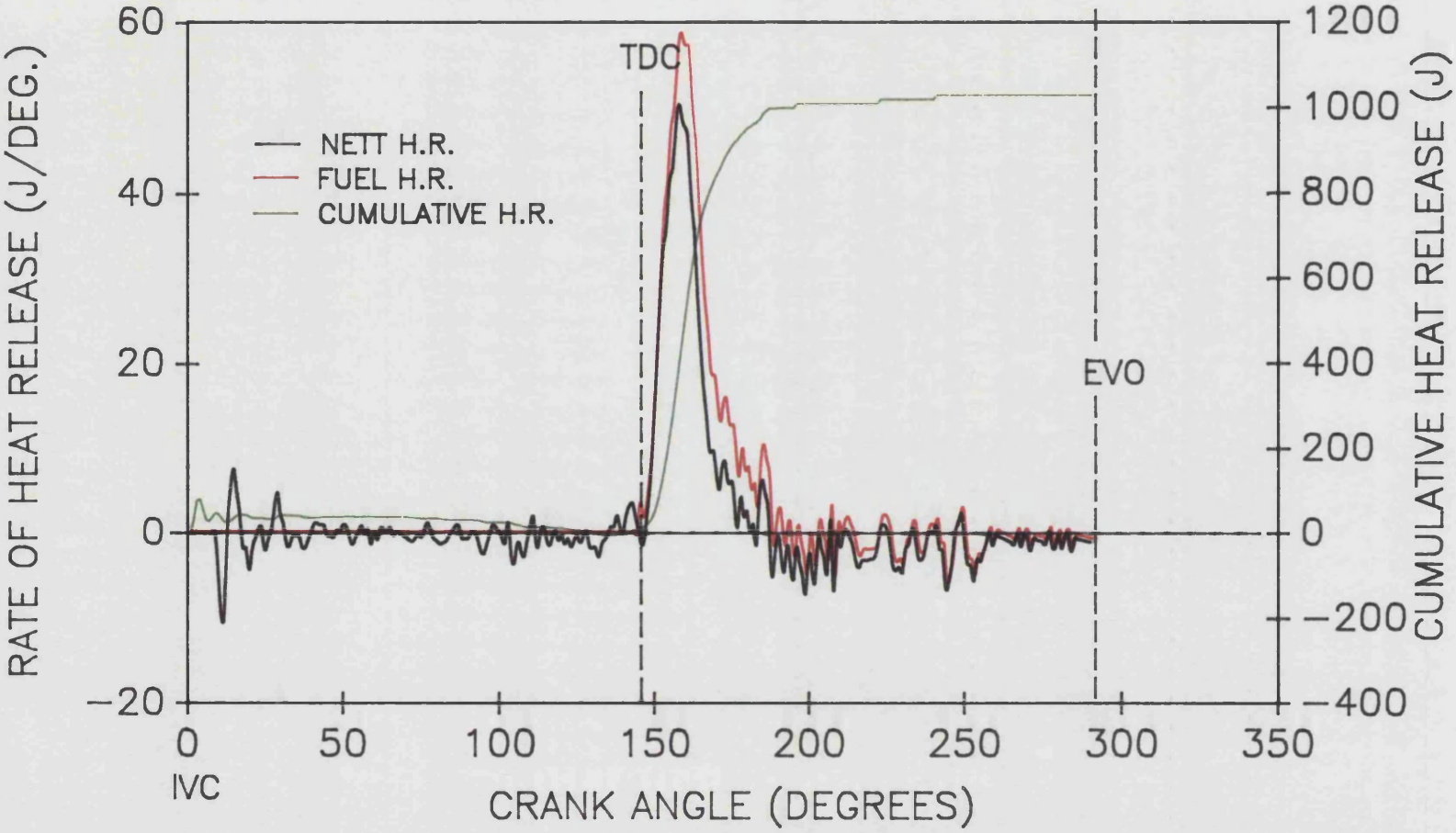

FIGURE 6.69
COMPUTED EQUIVALENCE RATIO & MASS OF FUEL
VS. CRANK ANGLE FOR AN INSULATED ENGINE OPERATING
AT 1000 REV/MIN.

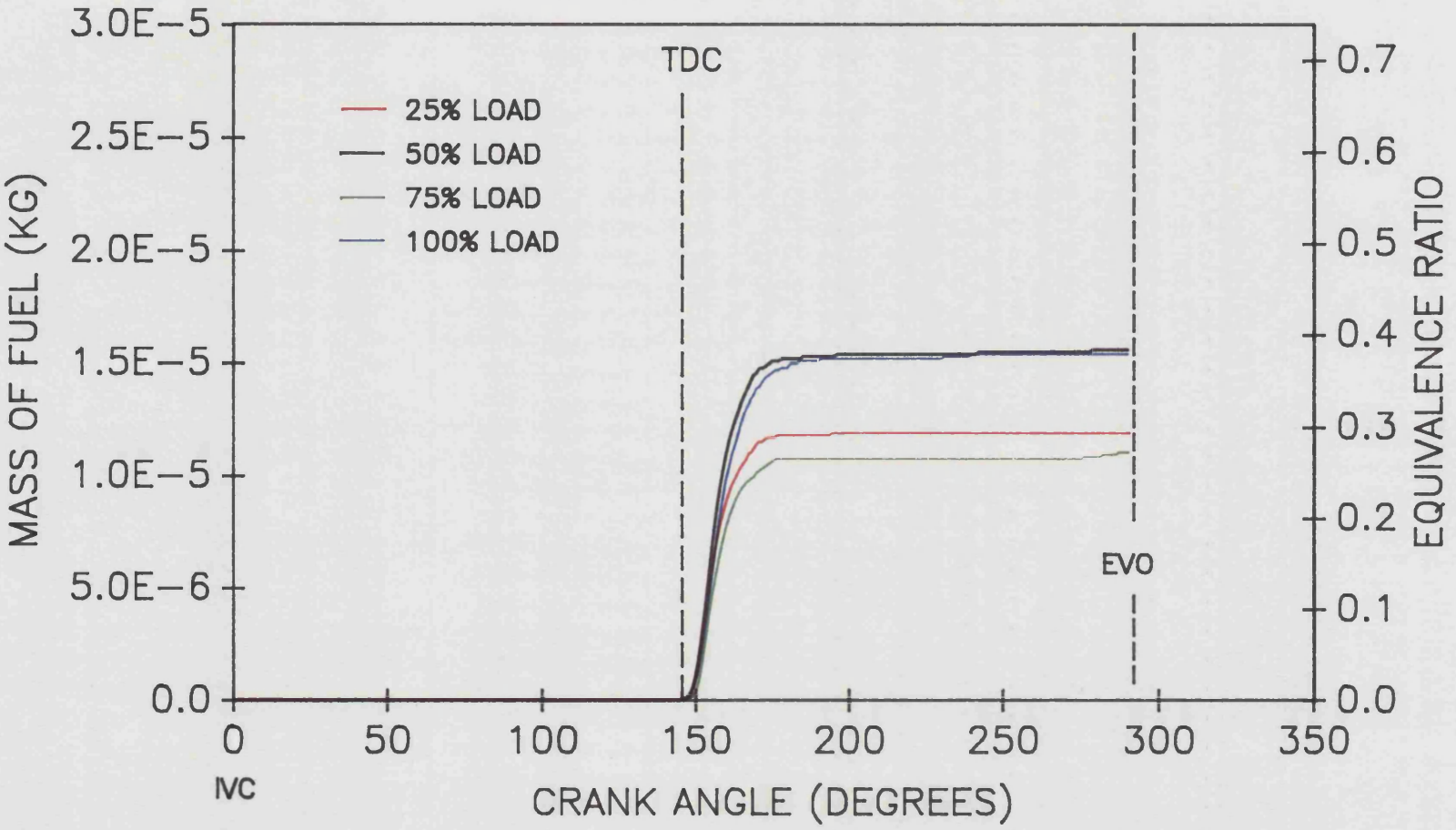

FIGURE 6.70
COMPUTED EQUIVALENCE RATIO & MASS OF FUEL
VS. CRANK ANGLE FOR AN INSULATED ENGINE OPERATING
AT 1200 REV/MIN.

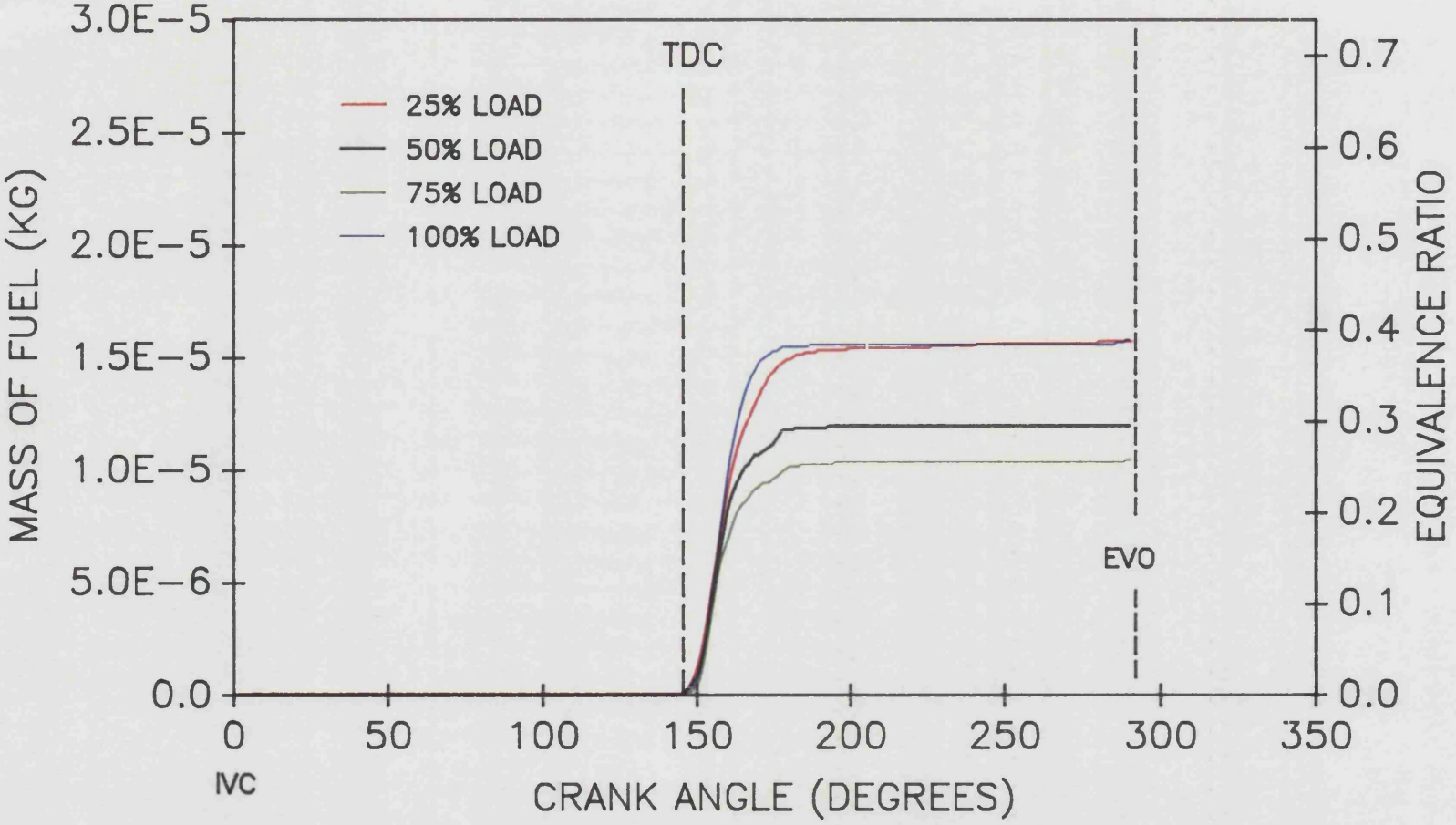

FIGURE 6.71
COMPUTED EQUIVALENCE RATIO & MASS OF FUEL
VS. CRANK ANGLE FOR AN INSULATED ENGINE OPERATING
AT 1400 REV/MIN.

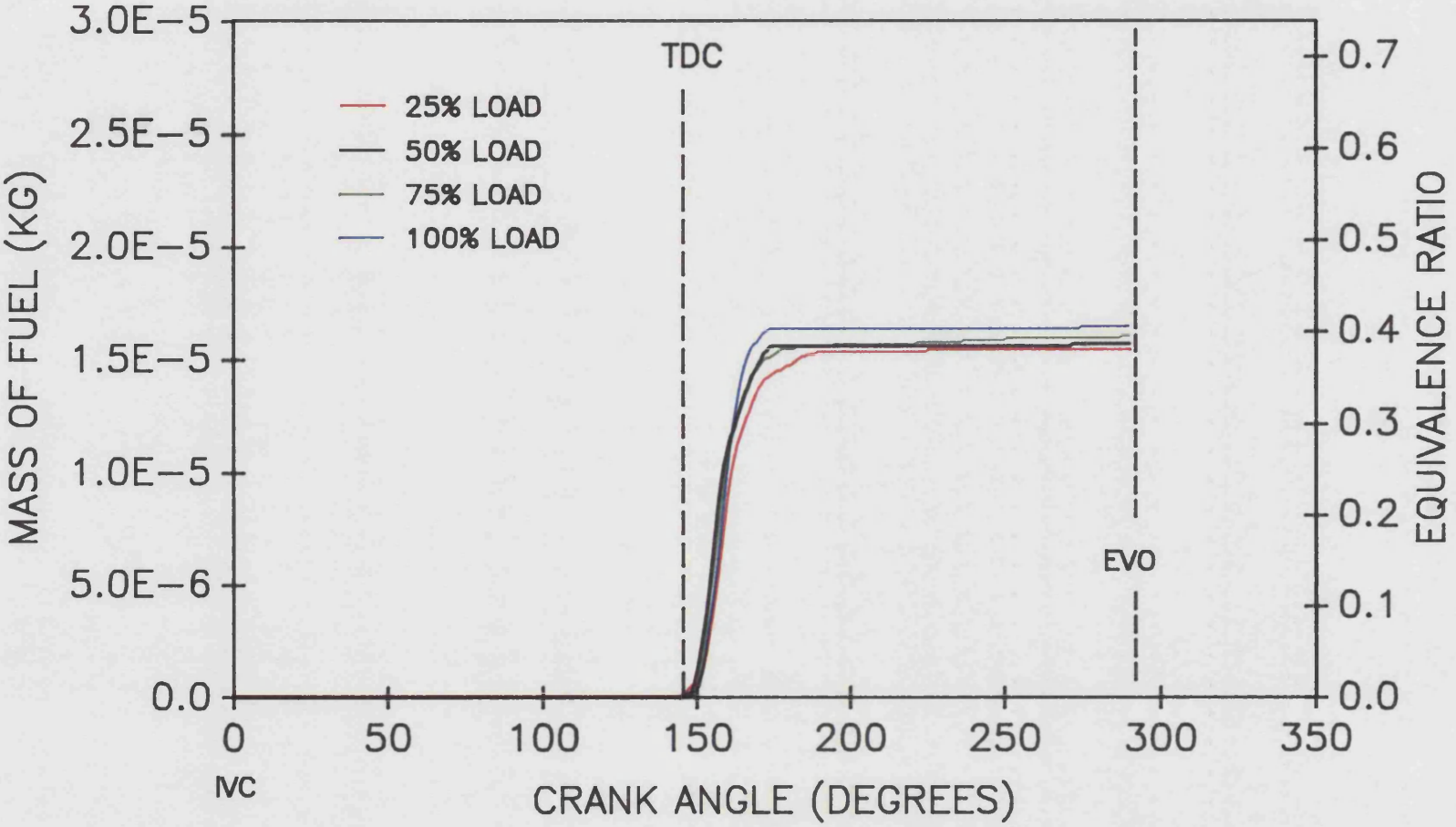

FIGURE 6.72
COMPUTED EQUIVALENCE RATIO & MASS OF FUEL
VS. CRANK ANGLE FOR AN INSULATED ENGINE OPERATING
AT 1500 REV/MIN .

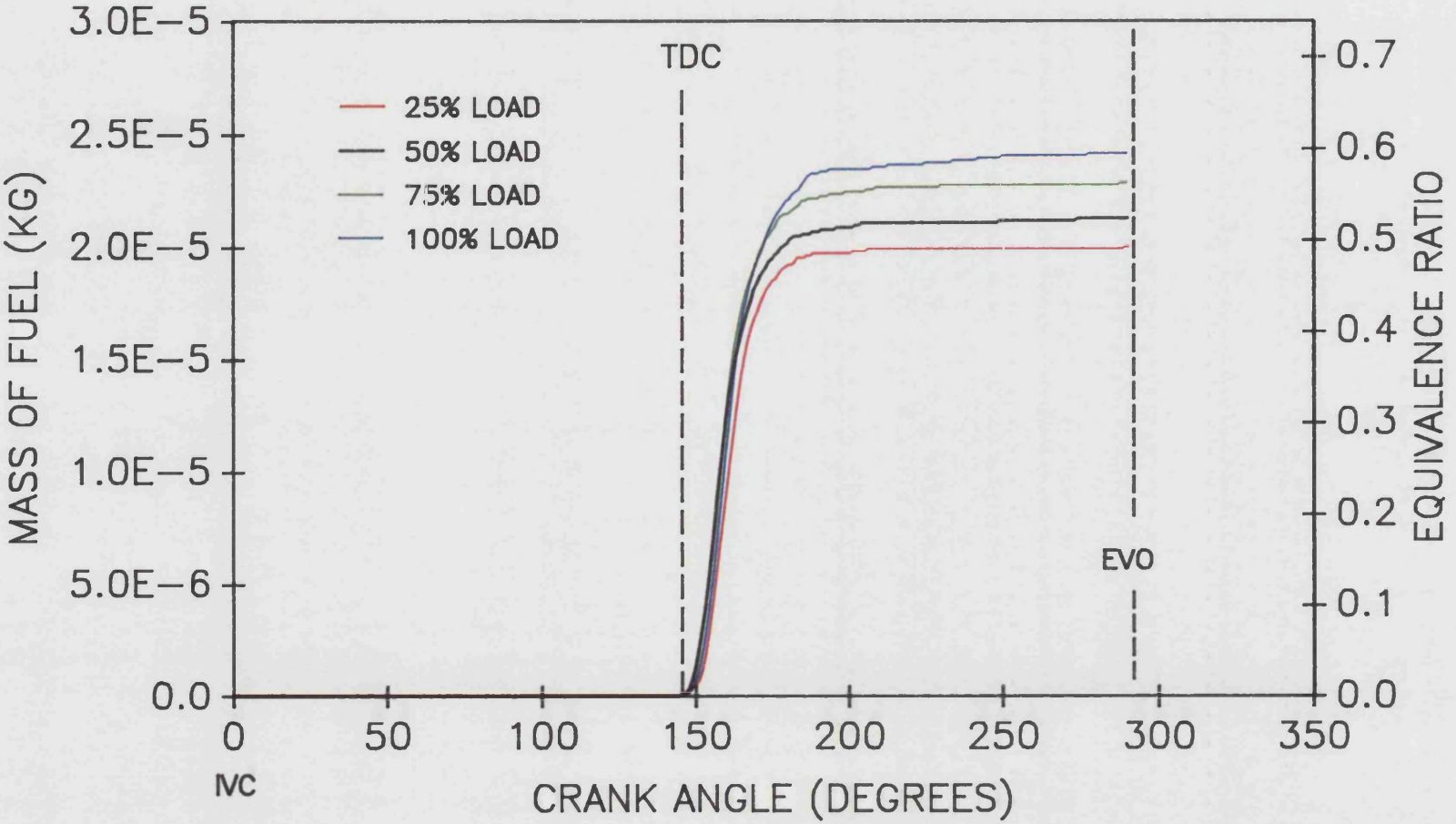

FIGURE 6.73
RATIO OF ACTUAL MASS OF FUEL MEASURED
EXPERIMENTALLY TO THAT CALCULATED USING
THE ANALYSIS PROGRAM SPA FOR THE STANDARD ENGINE.

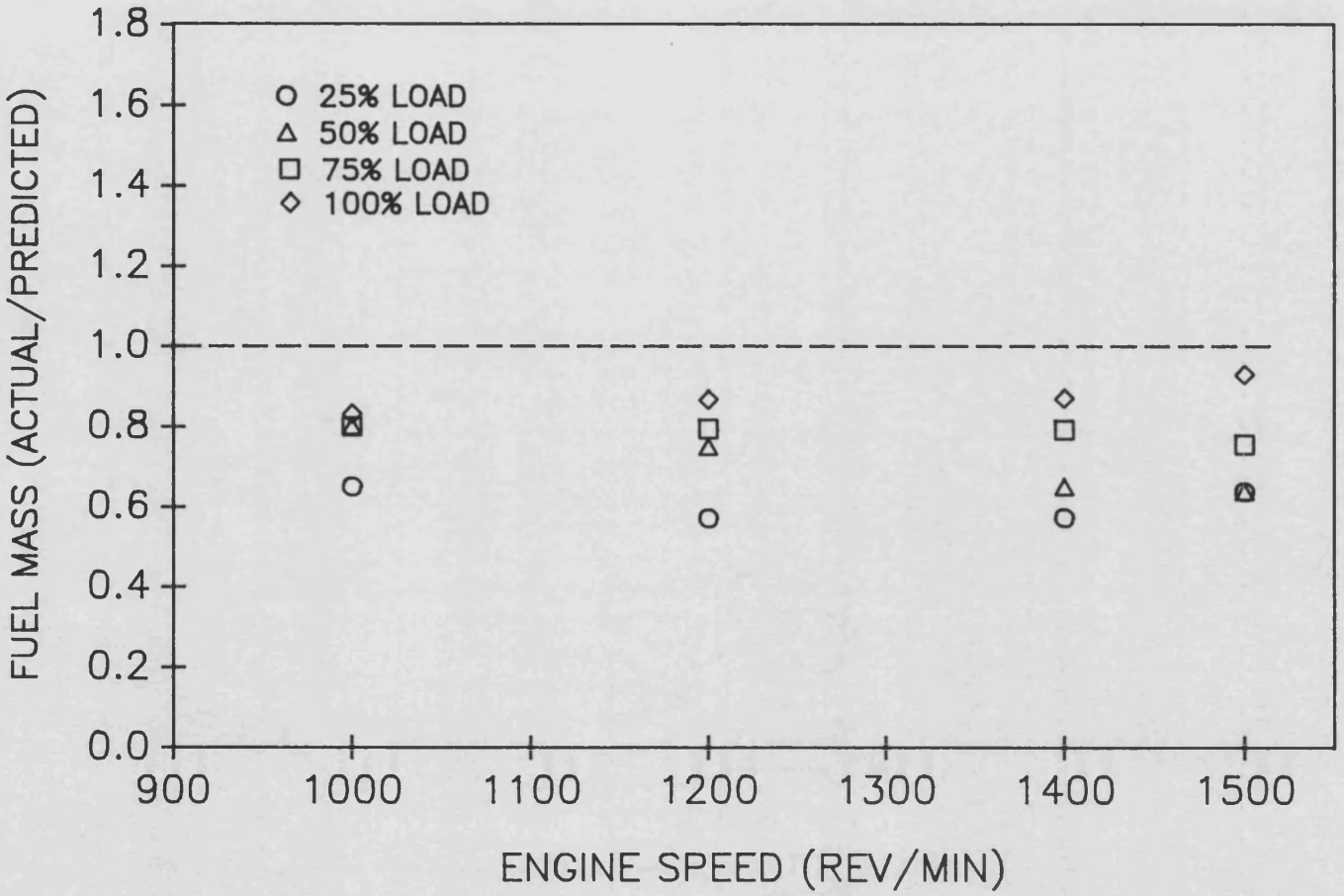

FIGURE 6.74
RATIO OF ACTUAL MASS OF FUEL MEASURED
EXPERIMENTALLY TO THAT CALCULATED USING
THE ANALYSIS PROGRAM SPA FOR THE INSULATED ENGINE.